AD-A062 905 IIT RESEARCH INST CHICAGO ILL F/G 11/2
PROPERTY SCREENING AND EVALUATION OF CERAMIC VANE MATERIALS.(U)
OCT 77 D C LARSEN, G C WALTHER F33615-75-C-5196
UNCLASSIFIED IITRI-D6114-ITR-24 NL

1 OF 4
ADA
062905

PROPERTY SCREENING AND EVALUATION
OF CERAMIC VANE MATERIALS.

(12) 374 p.

AIR FORCE MATERIALS LABORATORY/Code FY-1457
Task No. 8952, Assignment No. A8952
Wright-Patterson AFB
Dayton, Ohio 45433

Author: AFML/LLM/Dr. R. Ruh

(9) Interim technical rept. no. 4

Prepared by:
A. C. [illegible] & A. C. [illegible]

[illegible] RESEARCH INSTITUTE
[illegible] 35th Street
[illegible], Illinois 60616

LEVEL II

TABLE OF CONTENTS

TABLE OF CONTENTS (Cont'd)

LIST OF FIGURES

LIST OF FIGURES (Cont'd)

LIST OF FIGURES (Cont'd)

LIST OF FIGURES (Cont'd)

LIST OF FIGURES (Cont'd)

LIST OF FIGURES (Cont'd)

LIST OF FIGURES (Cont'd)

LIST OF TABLES

LIST OF TABLES (Cont'd)

LIST OF TABLES (Cont'd)

PROPERTY SCREENING AND EVALUATION OF CERAMIC VANE MATERIALS

Interim Technical Report #4

1.0 INTRODUCTION

During recent years significant progress has been made in the development of silicon-base ceramic materials for turbine engine applications. Silicon nitride and silicon carbide, in hot pressed, reaction bonded, and pressureless sintered forms, have shown the most potential. In order for these materials to be used by component designers, comprehensive property characterization must be accomplished.

A wide variety of silicon nitride and silicon carbide materials are continually emerging. The Interagency Coordination Group for the Application of Ceramics to Turbine Engines recognized the need for a valid comparison of such materials through an independent laboratory using controlled techniques and test parameters. The Air Force initiated the present program (Contract F33615-75-C-5196) two years ago with IIT Research Institute (IITRI) to fulfill this need.

The overall objective of this program is to select and characterize silicon nitride and silicon carbide materials for use as ceramic components in high temperature gas turbines. Various thermal and mechanical properties are being generated, together with interpretation with respect to microstructure, purity, flaws, and secondary phases. This evaluation is comprehensive in that property behavior is related to pre-test NDE characterization and post-test fractographic failure mode analysis. Additionally, statistical analysis and data correlation techniques are being applied to the generated data.

Process-related effects are studied through measurement of batch-to-batch variability of the materials that are produced in commercial quantities. Environmental effects are being studied through exposure to static oxidation conditions. Additionally, simulated gas turbine exposure is being accomplished through hot gas exposure and fatigue testing at NASA-Lewis Research Center. This work is a beginning effort to establish a computerized information storage and retrieval data base system for candidate ceramic gas turbine materials.

Initially this program entailed a four phase effort that involved 1) screening evaluation of four candidate materials, 2) comprehensive property data generation on selected candidates, 3) effect of scale up to vane size on material properties, effect of simulated turbine environment on properties, and evaluation of properties on samples taken from components which have been rig tested, and 4) screening evaluation of promising new materials, not necessarily in current production. The scope of the program has recently been altered, however, due to 1) the unavailability of a concurrent engine program to supply vane components, and 2) a current Air Force need for a screening evaluation on a much broader range of materials.

Therefore, this program now has two phases. The first phase is the original phase I screening evaluation of the thermal and mechanical properties of Norton hot-pressed and reaction sintered Si_3N_4, Norton siliconized SiC, and Kawecki-Berylco reaction sintered Si_3N_4. Phase I work is nearing completion. Phase II is currently in progress. The screening and characterization work in this phase is broader. A wide variety of silicon-base materials is being investigated, ranging from additional commercially available ones to promising

new materials. Potential turbine materials being characterized are not limited to those used for vanes, but also include lower temperature components such as bearings and seals. In particular, Phase II is directed to evaluating materials that had previously been developed in-house or contractually by members of the Interagency Coordination Group for the Application of Ceramics to Turbine Engines. Phase II samples have been supplied for characterization by Kyocera International (hot-pressed and sintered Si_3N_4), Carborundum (sintered SiC), General Electric (sintered SiC), and the Naval Research Laboratory (hot-pressed Si_3N_4/ZrO_2 additives). Other materials are presently in various stages of procurement.

This interim technical report covers the following areas: 1) brief review of previous mechanical property results with addition of fractographic failure mode analysis where currently available, impurity and microstructure characterization, 2) extensive thermal property information on Phase I materials, and 3) limited mechanical property data on Phase II materials.

2.0 MATERIALS STUDIED

Phase I materials are shown in Table 2.1 and consist of: Norton NC-132 hot-pressed Si_3N_4, Norton NC-435 siliconized SiC, Norton NC-350 reaction sintered Si_3N_4, and Kawecki-Berylco reaction sintered Si_3N_4. The rationale for selecting these materials and further descriptive processing information was presented in previous interim technical reports[1,2].

Phase II samples have been supplied for testing by Kyocera International (hot-pressed and sintered Si_3N_4), Carborundum (sintered SiC), General Electric (sintered SiC), and Naval Research Laboratory (hot-pressed Si_3N_4-ZrO_2 additive). Specific description of these materials is presented in Tables 2.2 and 2.3. Batch-to-batch variability is not being included in the broad Phase II work as it was in Phase I, in order to look at additional tests and a much wider variety of materials. In general Phase II samples are not readily available since most are developmental, and not commercial materials.

Other organizations who are currently preparing samples to be included in Phase II include: Ceradyne (hot-pressed Si_3N_4), Kawecki-Berylco (reaction bonded Si_3N_4), Ford Motor Company (reaction bonded Si_3N_4), GTE Sylvania (sintered Si_3N_4), Garrett/AiResearch (reaction bonded Si_3N_4), Norton (hot-pressed Si_3N_4-Y_2O_3 additive), Harbison-Walker (hot-pressed Si_3N_4-Ceria additive), Raytheon (reaction sintered Si_3N_4), Fiber Materials (hot-pressed Si_3N_4), British Nuclear Fuels (SiC), and Associated Engineering (reaction sintered Si_3N_4). Additional materials are being considered as they become available.

TABLE 2.1

PHASE I MATERIALS

MATERIAL	DESIGNATION	SUPPLIER	DESCRIPTION
Si_3N_4	NC-132	Norton	Hot Pressed
Si_3N_4	KBI	Kawecki-Berylco	Reaction Sintered
Si_3N_4	NC-350	Norton	Reaction Sintered
SiC	NC-435	Norton	Reaction Sintered and Densified by Silicon Impregnation (siliconized SiC)

TABLE 2.2

SECOND PHASE MATERIALS CURRENTLY BEING CHARACTERIZED

MATERIAL	DESIGNATION	SUPPLIER	DESCRIPTION
Si_3N_4	SN-3	Kyocera	Hot Pressed
Si_3N_4	SN-201	Kyocera	Sintered
Si_3N_4	SN-205	Kyocera	Sintered
SiC	-	Carborundum	Sintered (α)
SiC	-	General Electric	Sintered (β), boron doped
Si_3N_4-ZrO_2	-	Naval Research Laboratories	Various Hot-Pressed Si_3N_4 Compositions w/ 4-16 w/o ZrO_2 Additions. (See Table III)

TABLE 2.3

NRL MATERIALS - Expect ~200 samples eventually

HP Si_3N_4 + ZrO_2

FIRST NRL SET OF Si_3N_4 SPECIMENS FOR IITRI MATERIALS TESTING

COMPOSITION	HOT PRESSING #	# OF BARS	SPECIMEN DESIGNATION
4 w/o ZrO_2	SIN-VH3-120 AME-85; Tam Mono ZrO_2 Wet Milled Al_2O_3	8	R1F1-8
8 w/o ZrO_2	SIN-VH3-121 AME-85; Y_2O_3 Stab ZrO_2 Wet WC Milled	3	R2F1-3
8 w/o ZrO_2	SIN-VH3-123 AME-85; C.E. min ZrO_2 Wet WC Milled	10	R3F1-10
12 w/o ZrO_2	SIN-VH3-128 AME-85; Tam Mono ZrO_2	3	R4F1-3
16 w/o ZrO_2	SIN-VH3-129 AME-85; Tam Mono ZrO_2	5	R5F1-5

3.0 EVALUATION MATRICES

All samples that have been evaluated on this program have beer machined by the supplier. Prior to testing each specimen is subjected to various evaluations as shown in Table 3.1. Additionally, AFML conducts microstructural analysis, phase identification, and impurity analysis on each material studied. Post-test activities include fractographic failure mode analysis (performed in Phase I by M. Mendiratta of Systems Research Laboratories, P. L. Land and R. Ruh of AFML, and R.W. Rice of NRL; to be performed jointly by AFML and IITRI personnel for subsequent materials in Phase II), correlation of property data generated, and statistical analysis of data.

Phase I materials (NC-132, NC-435, NC-350, and KBI RSSN) were evaluated in air at various temperatures from 25° to 1500°C for flexural strength (including stress-strain behavior), flexural creep, creep rupture, fracture toughness, thermal expansion, thermal diffusivity, thermal shock, and hot gas exposure/fatigue as shown in Table 3.2. Detailed methods were presented elsewhere[1,2].

The general tests being conducted in the broad second phase effort are shown in Table 3.3. Specific test plans for the materials currently in-house are presented in Tables 3.4-3.7 Specific tests and conditions are determined based on the expected performance characteristics of each material, and the number of test samples available. All test material for the broad second phase effort have been and are expected to continue to be supplied at no charge by the manufacturer. In some cases IITRI or AFML will arrange to have test samples machined from supplied material billets.

TABLE 3.1

PRE-TEST EVALUATION

- Visual inspection (surface damage, features)
- Surface finish (<20 RMS μ-in. being the generally applied acceptance criterion)
- Density, Porosity characterization
- X-radiographic inspection (at AFML)
- Ultrasonic NDE (through transmission or pulse echo) Phase I materials only.

POST-TEST EVALUATION

- Fractographic analysis
- Data correlation/statistical analysis

TABLE 3.2

PHASE I TEST MATRIX/BATCH*
Contract F33615-75-C-5196

Test	25°C	1200°C	1350°C	1500°C
• Flexural Strength, Modulus, Stress-Strain (Ground)	10	10	10	10
• Flexural Strength, and Modulus (As Fired)	10/Material	NC-350		
• Creep(Flexural)	-	-	3	3
• Fracture Toughness (Double Torsion)	3	-	3	-
• Creep Rupture (Flexural)	-	-	3	3
• NDE	Density, Porosity, Surface Finish (20 Micro In.) Ultrasonic Scan on All Specimens X-radiography on All Specimens (AFML)			
• Microstructural Examination, Phase Identification, Impurity Analysis	by AFML: 2 Specimens/Batch			
• Thermal Expansion	Room Temperature→1500°C, 3 Specimens			
• Thermal Diffusivity	2 Directions (h.p. only): 3 Specimens Each RT, 1000→1500°C			
• Thermal Shock	Quench at various ΔT, Monitor internal friction change			
• Hot Gas Exposure and Fatigue	3 Spec/Batch (NASA-Lewis to perform testing on Mach 1 Burner Rig)			

*

- 4 materials to be studied in Phase I, Screening.
- 3 batches of each material to be included, except NC-132 which has 2 batches.
- Numbers in Table indicate number of specimens per batch at each temperature.

TABLE 3.3

SECOND PHASE - GENERAL MATRIX

1. Flexural Strength and Modulus
   RT + 3 elevated T's (1500°C max)
   7 samples per condition

2. Controlled Flaw Fracture Toughness
   RT + 3 elevated T's (1500°C max)
   3 samples per condition

3. Room Temperature Flexure Strength After Long Term, High Temperature Anneal under Oxidizing Conditions

4. Thermal Shock (water quench, internal friction)

5. Creep, 1400-1500°C

6. Thermal Expansion, RT → 1500°C

7. Thermal Diffusivity, RT → 1500°C

TABLE 3.4

KYOCERA MATERIALS

I. MATERIALS

1. SN-3 HP Si_3N_4

2. SN-201 Sintered Si_3N_4

3. SN-205 Sintered Si_3N_4

II. TEST MATRIX

	No. of Samples
1. Flexural Strength/Modulus, 25°C	7
2. Controlled Surface Flaw Fracture Tough., 25°C	2
3. Flexural Tests at 750°C, 1000°C, 1125-1250°C	5 each
Total	24

TABLE 3.5

CARBORUNDUM SINTERED α-SiC

TEST MATRIX

	TEST	NO. SAMPLES
1.	Flexural Strength/Modulus 25°C + 3 elevated T's	7 per condition
2.	Controlled Flaw Fracture Toughness 25°C + 3 elevated T's	3 per condition
3.	25°C Flexural Strength After Long Term, High Temperature Anneal under Oxidizing Conditions	4
4.	Thermal Shock Water Quench, Internal Friction	5
5.	Thermal Expansion 25°-1500°C	3
6.	Creep + Creep Rupture Various T, σ	7
7.	Thermal Diffusivity	3

TABLE 3.6

GENERAL ELECTRIC BORON-DOPED
SINTERED β-SiC

TEST MATRIX

	TEST	NO. SAMPLES
1.	Flexural Strength/Modulus 25°C + 3 elevated T's	7 per condition
2.	Controlled Flaw Fracture Toughness 25°C + 3 elevated T's	3 per condition
3.	25°C Flexure Strength After Long Term, high temperature anneal under oxidizing conditions	4
4.	Thermal Shock Water Quench, Internal Friction	5
5.	Thermal Expansion 25°-1500°C	3
6.	Creep + Creep Rupture Various T, σ	7
7.	Thermal Diffusivity	3

TABLE 3.7

NAVAL RESEARCH LABORATORY MATERIALS

PRELIMINARY TEST MATRIX

1. Flexural Strength and Modulus
   25°, 1200, 1350, 1500°C

2. Thermal Expansion
   25°-1500°C
   Heating and Cooling Cycle

3. Creep Rupture

4. Thermal Diffusivity

Future tests to be conducted on this program are not limited to those previously mentioned. Additional studies planned or being considered depend on the material/application, but include: controlled flaw fracture toughness, low and high cycle fatigue, ballistic impact, effect of various oxidation exposures on strength, tensile properties, slow crack growth, torch/air blast thermal shock/fatigue, and life prediction/proof testing. A more complete listing is provided in Table 3.8.

For all materials studied to date, the specimen identification scheme is presented in Tables 3.9 and 3.10.

TABLE 3.8

ADDITIONAL TESTS TO BE CONSIDERED
FOR FUTURE WORK - NEW MATERIALS - VARIATIONS ON OLD

1. Controlled Flaw Fracture Toughness
2. Low and High Cycle Fatigue (+0-, fully reversed (SCG).
3. Ballistic Impact (SEM, residual σ, ΔQ^{-1})
4. Effect of Oxidation Exposure on Strength
   a) optimize heat treatment, b) long term degradation
5. Tensile properties (strength, creep)
6. Slow crack growth (double torsion-load relaxation)
7. Creep + Creep Rupture (stepwise)
   including SEM/TEM microstructural analysis of crept specimens
8. Torch/Air Blast Thermal Shock/Fatigue
9. Thermal Fatigue
10. Life Prediction
11. Proof Testing

TABLE 3.9

SAMPLE DESIGNATION SCHEME

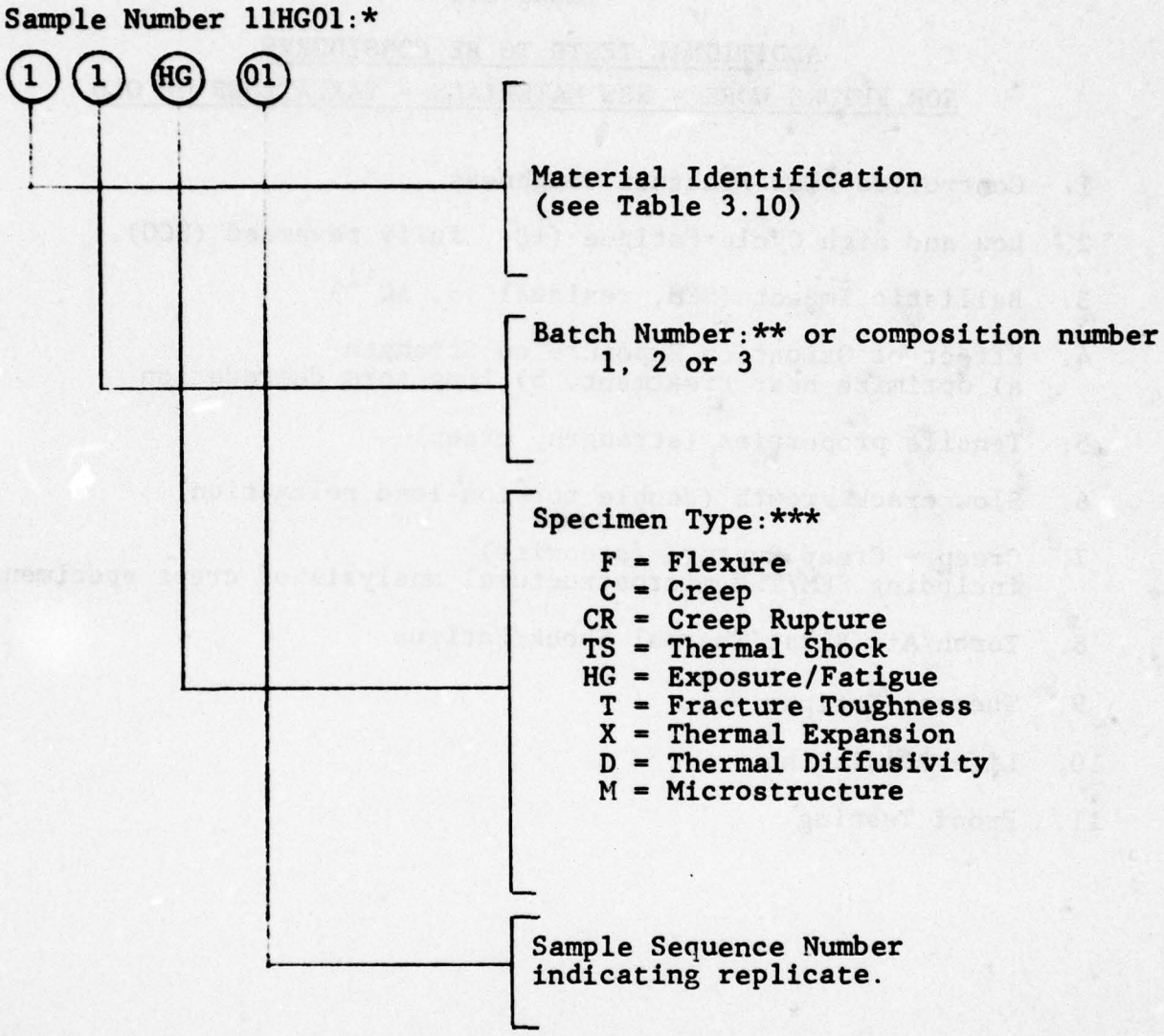

*The sample number shown as an example represents an exposure/fatigue sample from batch one (1) of NC-132. It has a sample sequence number of one (1), indicating replication.

**Only for Phase I materials. Composition number for NRL materials.

***Most Second Phase samples used the "F" designation, even though they were used for creep, thermal expansion, and fracture toughness evaluation as well as flexural strength and deformation tests.

TABLE 3.10

MATERIAL DESIGNATION

FIRST CHARACTER OF SAMPLE CODE	MATERIAL	
0		
1	Norton NC-132	HP Si_3N_4
2	Kyocera SN-205,	Sintered Si_3N_4
3	Norton NC-350	RS Si_3N_4
4	Norton NC-435	Siliconized SiC
5		
6		
7		
8	Carborundum	Sintered (α) SiC
9		
A	Kyocera, SN-3	HP Si_3N_4
B	Kyocera, SN-201	Sintered Si_3N_4
C		
D		
E		
F		
G	GE	Boron-Doped Sintered (β) SiC
H		
I		
J		
K	KBI	Reaction Sintered Si_3N_4
L		
M		
N		
O		
P		
Q		
R	Naval Research Lab	HP Si_3N_4/ZrO_2 Compositions
S		
T		
U		
V		
W		
X		
Y		
Z		

4.0 MATERIALS CHARACTERIZATION

Materials pre-test characterization consisted of density/porosity measurement, microstructural analysis, metallic impurity determination by spectrographic analysis, phase identification by x-ray diffraction, oxygen content (performed at AMMRC) by Neutron Activation Analysis, and x-radiographic inspection. Varying degrees of characterization are currently completed for each material.

Spectrographic analyses were accomplished at AFML using a Jarrell Ash 3.4 meter Ebert spectrometer. Impurities were determined using standards with known concentrations of the elements and comparing line intensities. Phase identification was accomplished using General Electric XRD-5 and Phillips XRG-3000X-ray diffractometers and a scanning speed of 2° 2θ/min. Oxygen analyses were accomplished using the USAMMRC Neutron Activation Analysis system which employs a 14 MeV Neutron generator. X-radiographic inspection was performed with a Norelco 150 unit with a 2.5 mm spot and berylium window. Specimens were x-rayed at a distance of 48 inches, accelerating voltage of 50 Kv, and current of 9 ma for times of from 30 seconds to 2-1/2 minutes depending on sample thickness. Type M Kodak film was used.

4.1 Characterization for Density/Porosity, Purity, and Crystalline Form

Detalied characterization is available for the Phase I materials: NC-132 hot-pressed Si_3N_4, NC-435 Siliconized SiC, NC-350 reaction sintered Si_3N_4 and KBI reaction sintered Si_3N_4. Norton NC-132 hot-pressed Si_3N_4 was longitudinally ground by the manufacturer to an average RMS surface finish of ~10 µin. Density variations were small and there was virtually no open porosity. Percent theoretical density was 98-99% as shown in Figure 4.1 compared to other materials. NC-132 contained ~3%

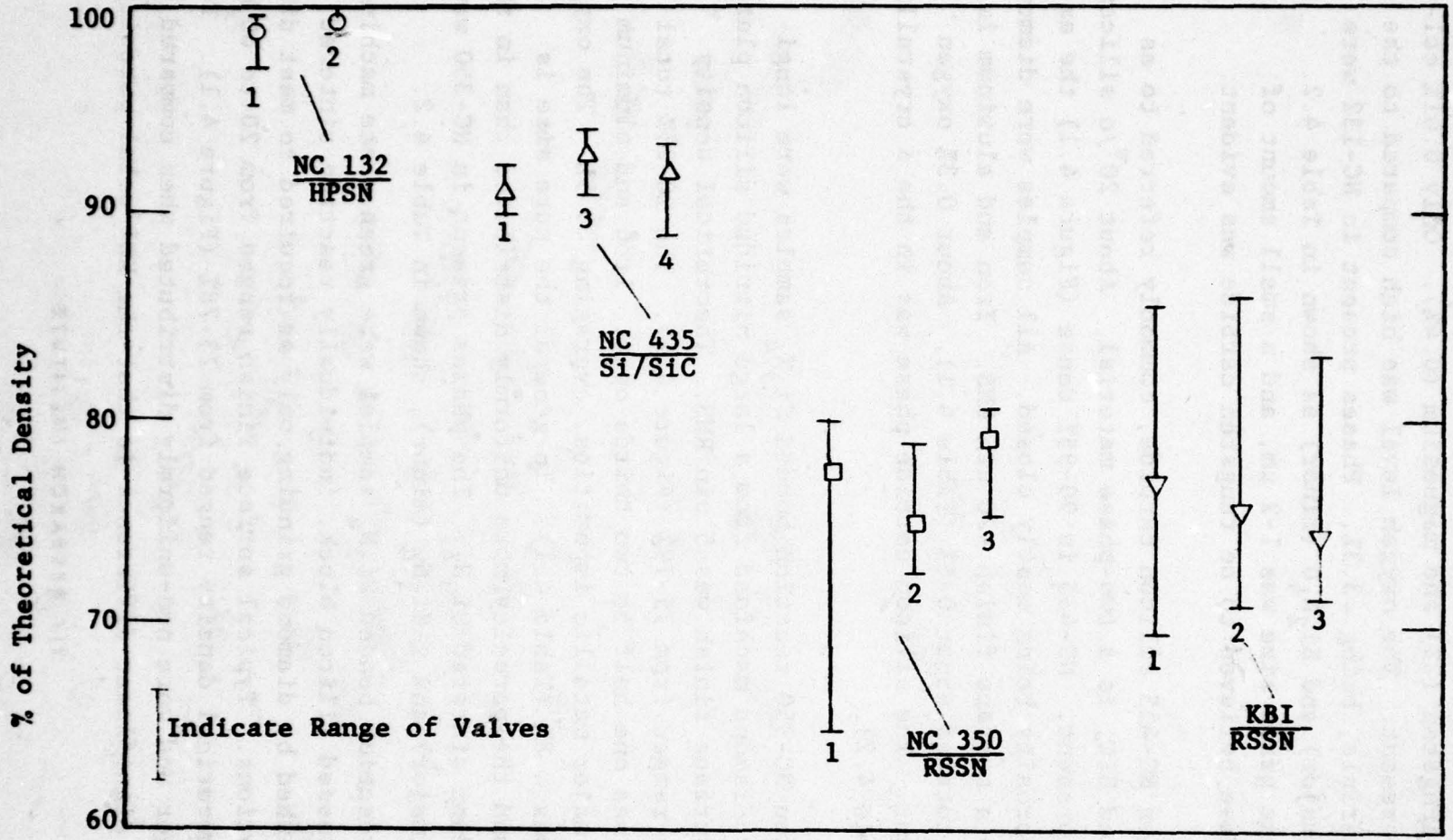

FIGURE 4.1 COMPARISON OF DENSITIES FOR DIFFERENT BATCHES OF PHASE I MATERIALS

metallic impurities including W, Mg, Fe, and Al (Table 4.1). Most was tungsten (2%) and magnesium (0.4%). Only 0.01% calcium was present. The oxygen level was high compared to the other materials, being ~3.3%. Phases present in NC-132 were β-Si_3N_4 (major) and Si_2N_4O (minor) as shown in Table 4.2. The average grain size was 1-2 μm, and a small amount of second phase believed to be tungsten carbide was evident.

Norton NC-435 silicon carbide, commonly referred to as siliconized SiC, is a two-phase material. About 20 v/o silicon phase is present. NC-435 is 90-95% dense (Figure 4.1) the exsisting porosity being mostly closed. All samples were diamond ground to a surface finish <20 μin RMS. Iron and aluminum impurities totaled about 0.6% (Table 4.1). About 0.3% oxygen was present. The silicon carbide phase was in the α crystalline form (Table 4.2).

Norton NC-350 reaction bonded Si_3N_4 samples were longitudinally diamond machined from a large nitrided silicon plate. Typical surface finish was 5 μin RMS. Theoretical density typically ranged from 75-79% (Figure 4.1). The 20-25% total porosity was one half to two thirds open. Iron and aluminum were the major metallic impurities, averaging ~0.5%. The oxygen content was ~.8% (Table 4.1). In general the pore size is smaller and the porosity more uniformly distributed than in the KBI reaction sintered Si_3N_4. The phases present in NC-350 were α-Si_3N_4 (major) and β-Si_3N_4 (minor), shown in Table 4.2.

KBI reaction bonded Si_3N_4 samples were green-state machined from a cold-pressed silicon block, individually reaction sintered, and then finished by diamond grinding only as required to meet dimensional specifications. Typical surface finish ranged from 20 to 60 μin RMS. Theoretical density ranged from 73-78% (Figure 4.1). Pores were larger and more non-uniformly distributed when compared to NC-350. The most significant difference is that the KBI total porosity (~25%)

TABLE 4.1

IMPURITY ANALYSIS

MATERIAL	METALLIC IMPURITIES (WT %)* BATCH I	BATCH II	BATCH III	AVERAGE	MAJOR	OXYGEN (WT %)** AVERAGE
RB Si_3N_4 (NC 350)	0.45	0.54	0.46	0.48	Fe,Al	0.84
RB Si_3N_4 (KBI)	0.73	0.68	0.64	0.68	Fe,Al	-
HP Si_3N_4 (NC 132)	3.15	3.08	-	3.12	W,Mg,Fe,Al	3.33
Siliconized SiC (NC 435)	0.49	0.58***	0.68	0.58	Fe,Al	0.34

* Spectrographic Analysis

** Neutron Activation Analysis (USAMMRC H. Priest)

*** Batch IV

TABLE 4.2

IDENTIFICATION OF PHASES PRESENT*

MATERIAL	PHASES PRESENT
RB Si_3N_4 (NC 350)	α-Si_3N_4 (Major) + β-Si_3N_4 (Minor)
RB Si_3N_4 (KBI)	β-Si_3N_4 + α-Si_3N_4 (~ Equal Amounts)
HP Si_3N_4 (NC 132)	β-Si_3N_4 (Major) + Si_2N_4O (Minor)
Siliconized SiC (NC 435)	α-SiC (Major) + Si (Minor)

*X-ray Diffraction Analysis

was mostly open (~90% open) as compared with the more evenly divided open and closed porosity of NC-350 reaction sintered Si_3N_4. Figures 4.2 and 4.3 illustrate this difference in porosity distribution between the two RSSN's. The KBI material was found to have somewhat lower purity, the total iron and aluminum content being ~0.7% (Table 4.1). Oxygen content data are not currently available for KBI RSSN. Sometimes a slight amount of silicon phase was observed, but not in all cases. The KBI material contained roughly equal amounts of α and β Si_3N_4 phases, in contrast to the NC-350 reaction sintered Si_3N_4 which was mostly α-Si_3N_4 (Table 4.2).

Characterization is currently in progress for the other materials tested to date: Kyocera hot pressed Si_3N_4 and two forms of sintered Si_3N_4, Carborundum sintered (α) SiC, and General Electric boron-doped sintered (β) SiC. The Kyocera hot pressed Si_3N_4, SN-3, is ~96% dense with virtually no open porosity. Kyocera SN-201 sintered Si_3N_4 is 93-94% dense, also containing very little open porosity (~.1%). Kyocera SN-205 sintered Si_3N_4, however, is ∽88% dense, containing ~7% open porosity and ~5% closed porosity.

Carborundum sintered (α) SiC is 98-99% dense, with virtually all of the existing 1-2% porosity being closed. The General Electric boron-doped sintered (β) SiC is ~95% dense, with about 80% of its total porosity being closed. The development of the Carborundum material has been described by Coppola and McMurtry[3]. The GE material is said to contain a small amount of boron nitride and carbon[4].

4.2 X-Radiographic Inspection

X-radiographic inspection is made of all test samples at AFML. The results for all material batches tested to date are contained in Appendix A. X-radiography is more of a qualitative characterization than a quantitative one.

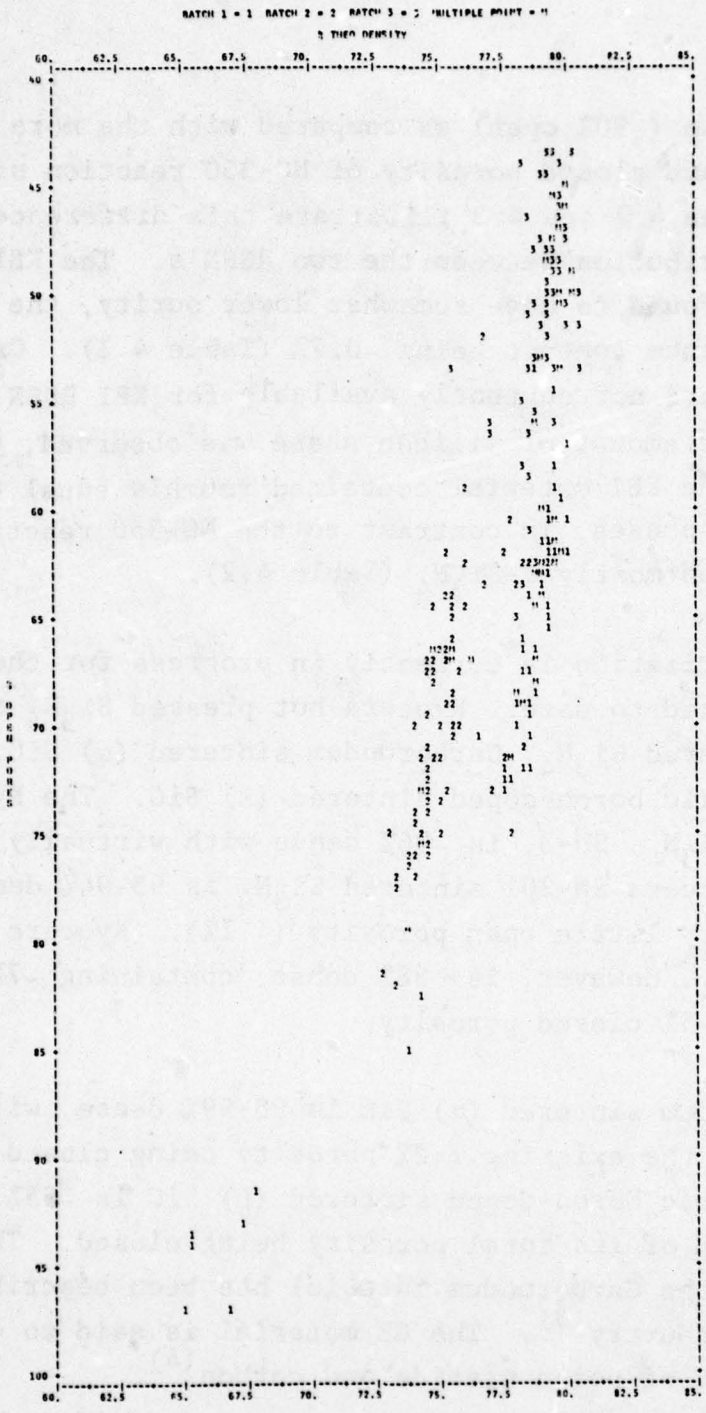

FIGURE 4.2 PERCENT THEORETICAL DENSITY VS % OF TOTAL POROSITY THAT IS OPEN FOR NC 350 (RSSN) (numbered data points refer to individual samples of the indicated batch)

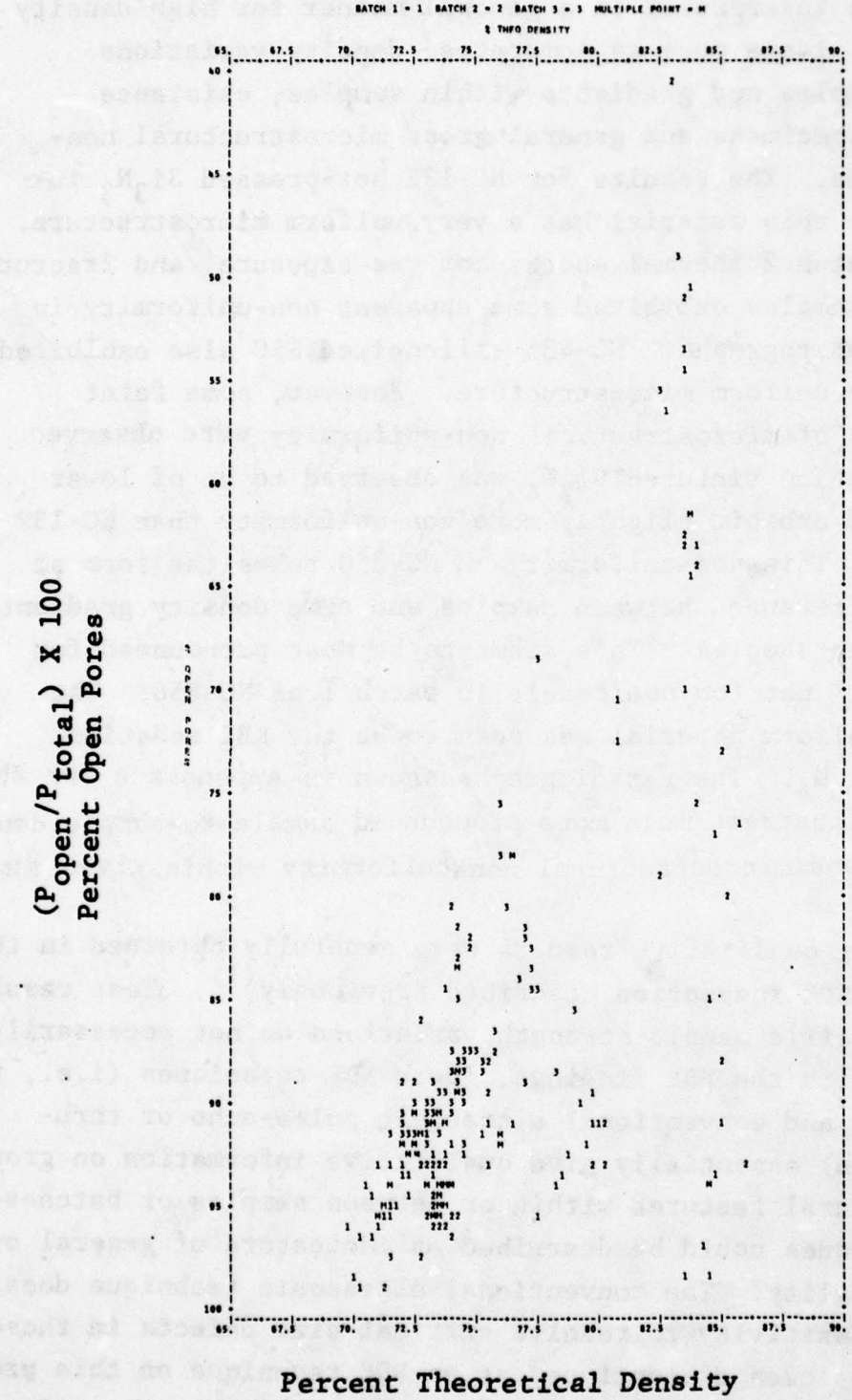

FIGURE 4.3 PERCENT THEORETICAL DENSITY VS % OF TOTAL POROSITY THAT IS OPEN FOR KBI-RSSN (numbered data points refer to individual samples of the indicated batch)

Results are interpreted in a general manner for high density inclusions, large pore agglomerates, density variations between samples and gradients within samples, existance of broken specimens and general gross microstructural non-uniformities. The results for NC-132 hot-pressed Si_3N_3 indicate that this material has a very uniform microstructure. However, batch 2 thermal shock, hot gas exposure, and fracture toughness samples exhibited some apparent non-uniformity in the x-ray photographs. NC-435 siliconized SiC also exhibited a generally uniform microstructure. However, some faint indications of microstructural non-uniformity were observed. NC-350 reaction sintered Si_3N_4 was observed to be of lower density and exhibit slightly more non-uniformity than NC-132 or NC-435. This non-uniformity in NC-350 takes the form of density differences between samples and some density gradients within given samples. This seems to be most pronounced for batch 2, but not too noticeable in batch 1 of NC-350. The most non-uniform material was seen to be the KBI reaction sintered Si_3N_4. The x-radiographs shown in Appendix A for this material illustrate much more pronounced sample-to-sample density variation and microstructural non-uniformity within given samples.

Similar qualitative results were generally obtained in the ultrasonic NDE inspection described previously[1]. Test results such as specific sample strength variations do not necessarily correlate with the NDE findings. Both NDE techniques (i.e., x-radiography and conventional ultrasonic pulse-echo or thru-transmission) essentially give qualitative information on gross microstructural features within or between samples or batches. Thus both techniques could be described as indicators of general overall material quality. The conventional ultrasonic technique does not have the sensitivity to resolve critical size defects in these materials and has been discontinued as an NDE technique on this program. X-radiographic inspection provides essentially the same information and is more amenable to rapid interpretation and easily

presentable results. For this reason, x-radiographic inspection of all sample batches will continue. Results will be presented as in Appendix A to document overall microstructural quality on a routine basis for reference purposes.

4.3 Microstructural Characterization

Microstructural characterization was accomplished at AFML.

A representative microstructure of NC-132 hot pressed Si_3N_4 is seen in Figure 4.4, which is a replica of an etched surface at 5000X. NC-132 exhibits a fine elongated grain structure of near theoretical density which accounts for high strength at low temperatures.

A typical microstructure of the NC-435 silicon densified SiC is seen in Figure 4.5, which is a polished surface at 250X. While this material has very low porosity, it has a high volume of Si phase, which is the light phase in the figure.

A microstructure of the Norton reaction bonded Si_3N_4 is given in Figure 4.6, which is a polished surface at 250X. This material has approximately 25% porosity, but the silicon nitride phase is quite uniform and the porosity is quite uniformly distributed.

A microstructure of the Kawecki-Berylco reaction sintered Si_3N_4 is seen in Figure 4.7, which is also a polished surface at 250X. This material has about the same amount of porosity as the Norton material but the porosity is not as uniformly distributed.

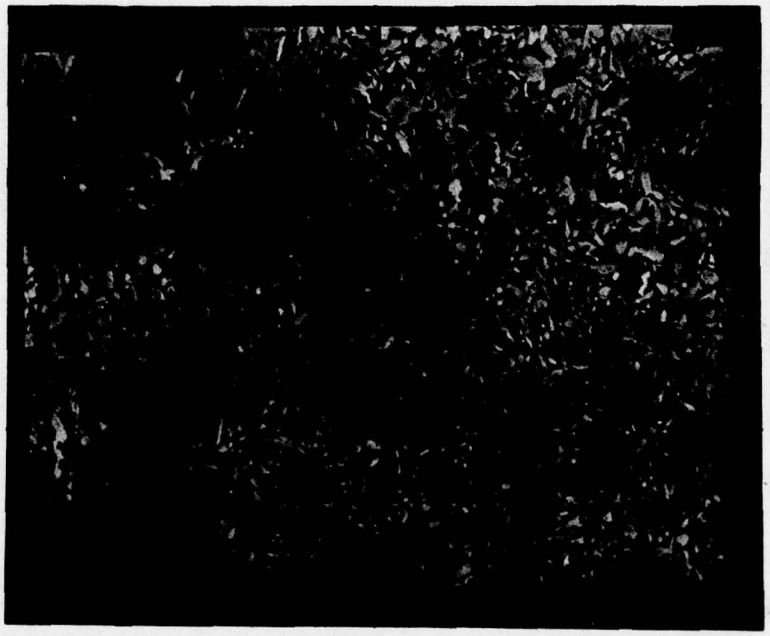

FIGURE 4.4 TEM MICROGRAPH OF NC-132 HP Si_3N_4 (5000X)

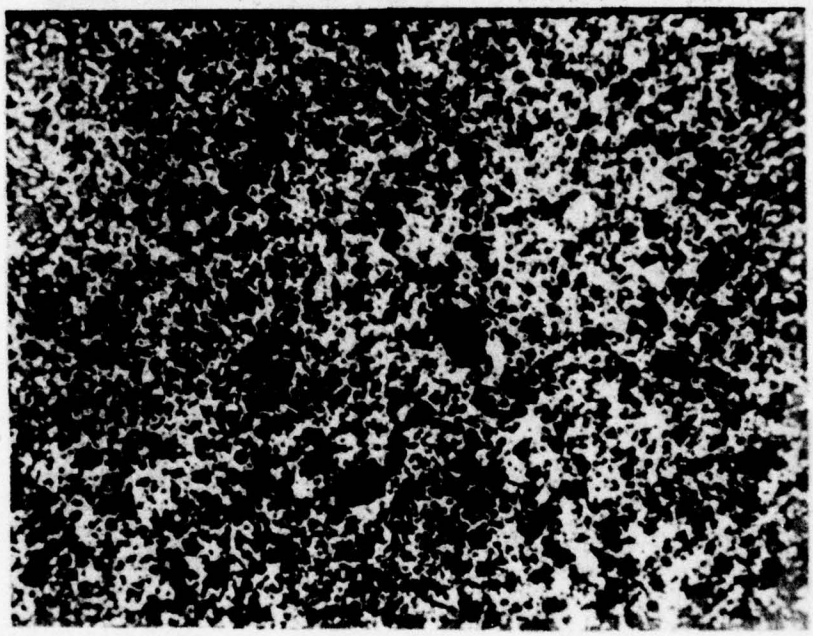

FIGURE 4.5 OPTICAL MICROGRAPH OF NC-435 SILICONIZED SiC (250X)

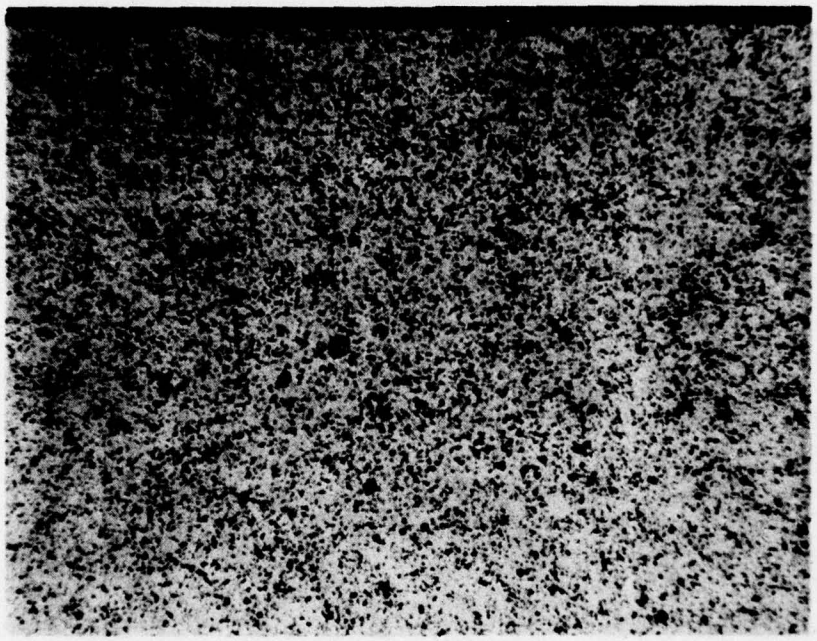

FIGURE 4.6 OPTICAL MICROGRAPH OF NC-350 RS Si_3N_4 (250X)

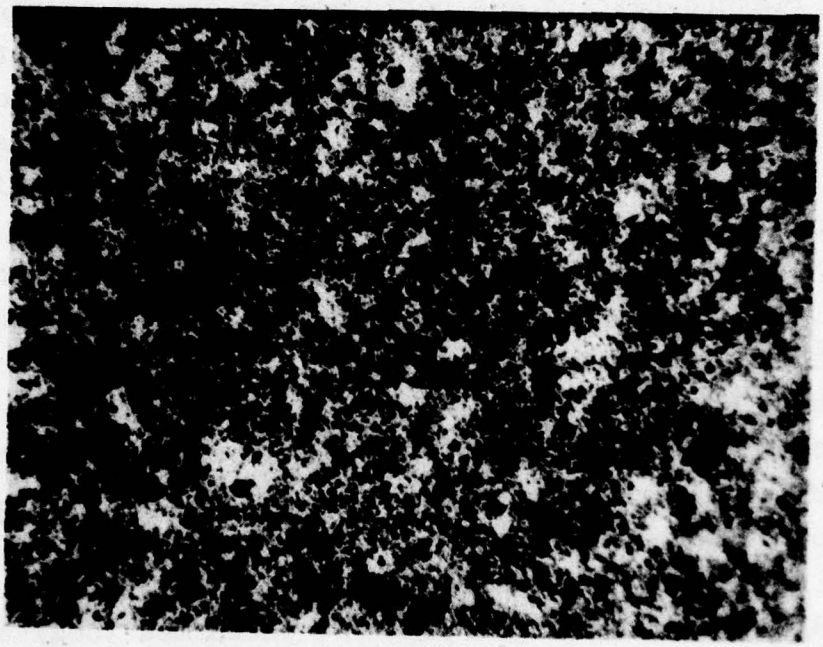

FIGURE 4.7 OPTICAL MICROGRAPH OF KBI RS Si_3N_4 (250X)

5.0 MECHANICAL PROPERTY TESTS

Flexural strength/modulus/stress-strain behavior, creep, and fracture toughness results are presented in this section. Since these tests constitute a part of a continuing program, varying amounts of data are reported for each material.

5.1 Flexural Strength/Modulus/Stress-Strain/Failure Mode Analysis

All flexure testing was performed in air on as-received samples in four-point flexure. Tests were conducted at various temperatures from 25° to 1500°C at a cross-head speed of 0.02 in/min. Specific temperatures were chosen based on the expected behavior of each material. Specimen cross-sectional dimensions were .125 X .250 $\pm$ .001 inch. Specimen lengths were 2.25 inches for all Norton, Carborundum, and Kyocera materials. General Electric and NRL samples were 2.0 inches in length. For these materials the upper and lower support pin spans were 0.875 and 1.75 inches, respectively. The Kawecki-Berylco materials were 1.500 inches in length. The upper and lower spans were 0.500 and 1.000 inches, respectively. NC-132 hot-pressed Si_3N_4 samples were oriented such that the tensile axis was normal to the hot-pressing direction (i.e. "strong" direction). For all materials except KBI RSSN, diamond grinding was performed longitudinally, i.e., parallel to the tensile axis. The KBI materials were essentially as-nitrided, only minimal machining conducted on each specimen to bring within dimensional specifications. The following sections discuss results obtained to-date for each material. Tabular results for all samples are presented in Appendix B.

5.1.1 Norton NC-132 Hot Pressed Si_3N_4

Detailed results for Norton NC-132 hot-pressed Si_3N_4 were presented in the last interim technical report[2].

Detailed fractographic failure mode analysis and fracture mechanics calculations are currently being conducted. To maintain continuity and provide for comparison with other materials, the results for NC-132 are reviewed in this section. NC-132 HP Si_3N_4 is often used as a baseline material when assessing the properties of new developing materials.

Figures 5.1 and 5.2 illustrate the strength and elastic modulus vs. temperature of all materials tested to date. NC-132 is seen to be the strongest silicon nitride material ($T \leq 1200°C$) owing to its high density and uniformity. At room temperature the strength was lower than expected for one batch of material as shown in Figure 5.3. (Norton claims ~120 ksi)[5], and data scatter was large[2]. Preliminary fractography studies[6] indicated primarily intergranular fracture originating at surface machining flaws. Data at elevated temperatures more closely agreed with literature values[9]. These observations suggest that the machining flaws may be healed at elevated temperatures where exposure time in air before load application was ~30 min. Similar behavior in hot pressed Si_3N_4 has been observed by Petrovic and Jacobson[7]. Kossowsky, et.al.[8] have speculated that this phenomenon is the result of crack tip blunting caused by an oxidation mechanism.

Representative flexural stress-strain behavior for NC-132 is illustrated in Figure 5.4. It is seen that this material exhibits linear elastic behavior to failure up to 1200°C but has a large non-linear component at 1350°C and 1500°C. This behavior can be explained by the presence of an impurity grain boundary phase resulting from the use of magnesia as a densification aid[10-13]. This behavior is similar to that found for HS-110 and HS-130 hot pressed Si_3N_4 by Kossowsky[8] who concluded that the deformation was controlled by a grain boundary

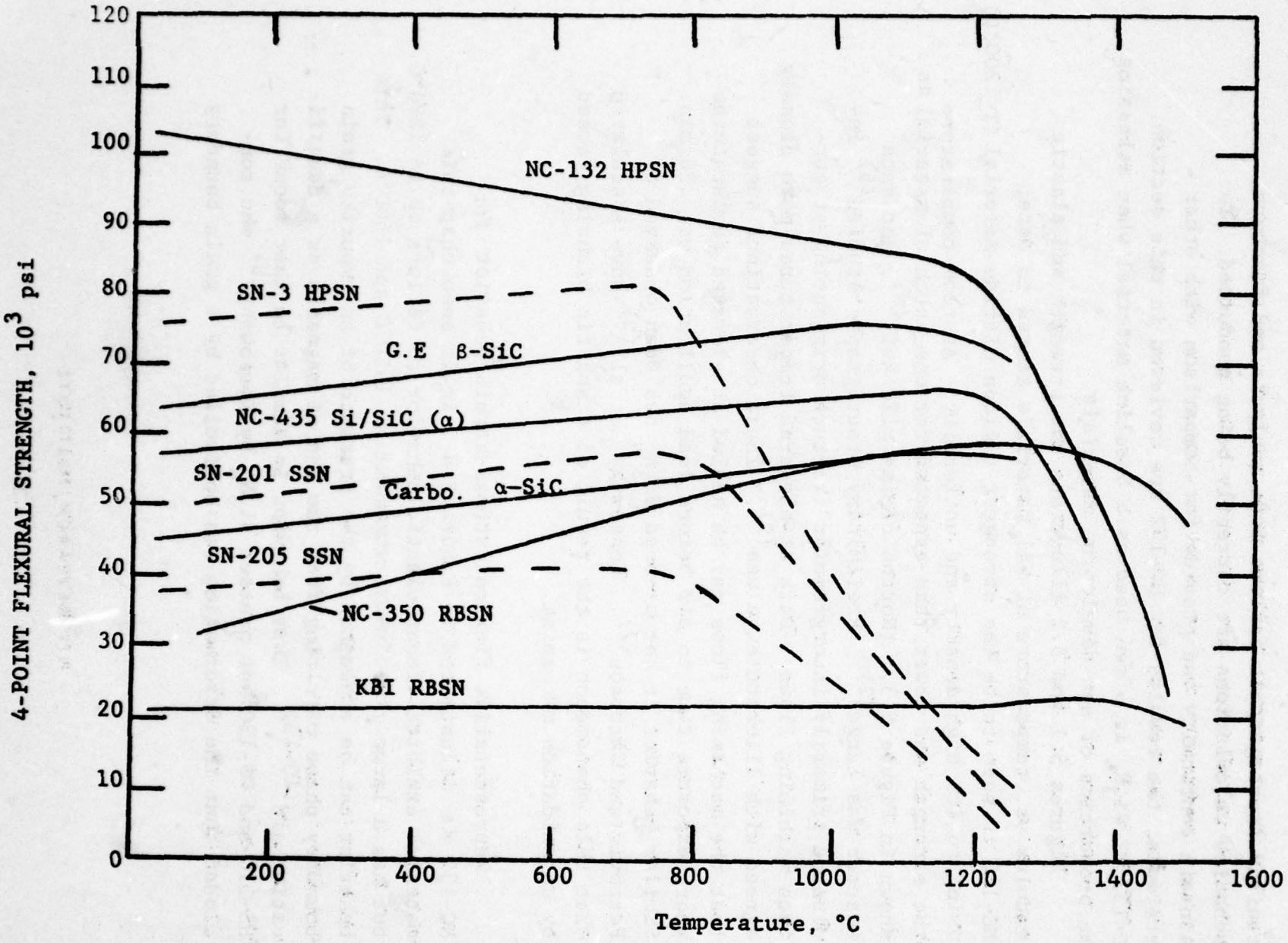

FIGURE 5.1 REPRESENTATIVE 4-POINT FLEXURAL STRENGTH OF Si_3N_4 AND SiC MATERIALS

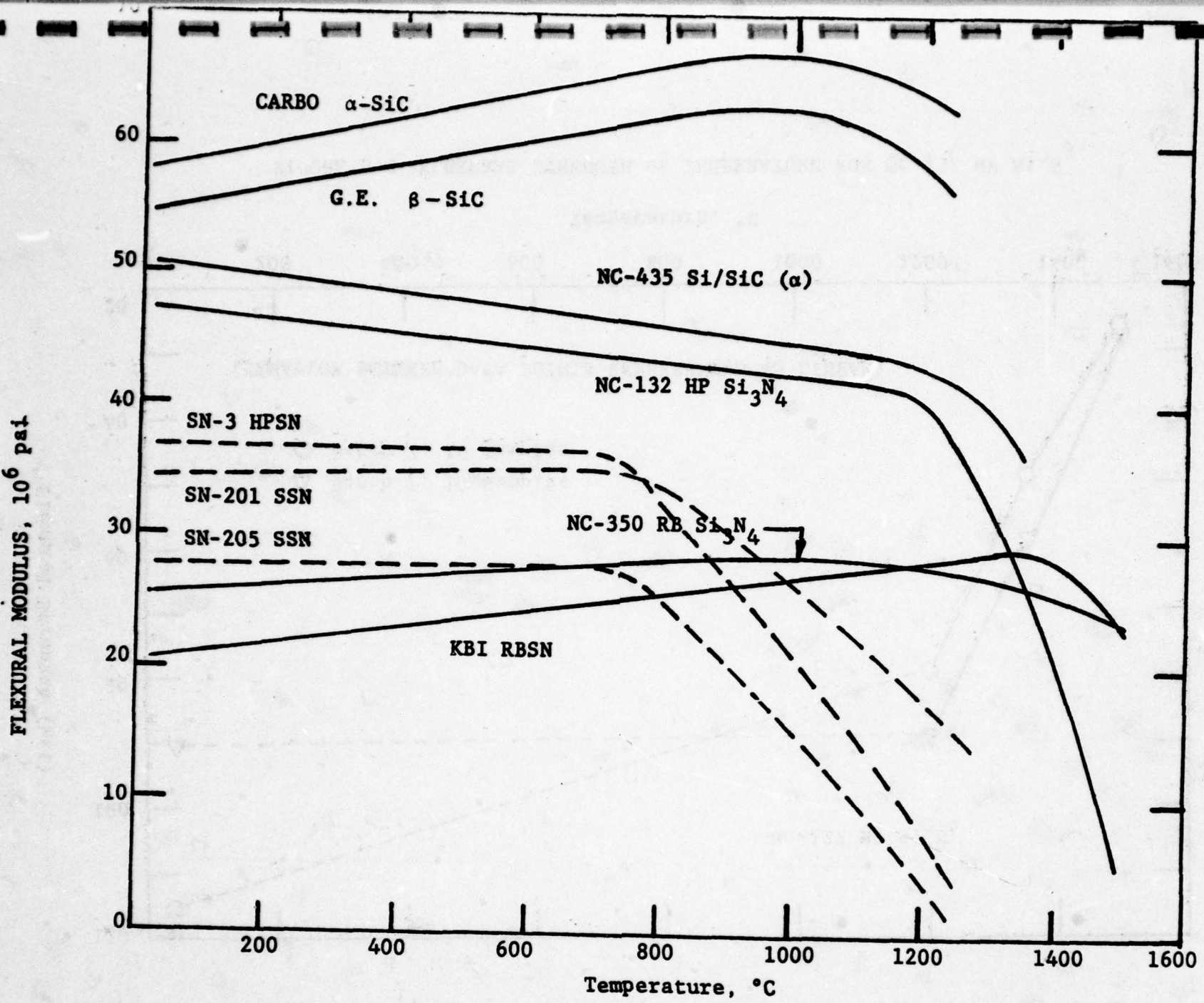

FIGURE 5.2 FLEXURAL ELASTIC (Secant) MODULUS OF Si_3N_4 AND SiC MATERIALS

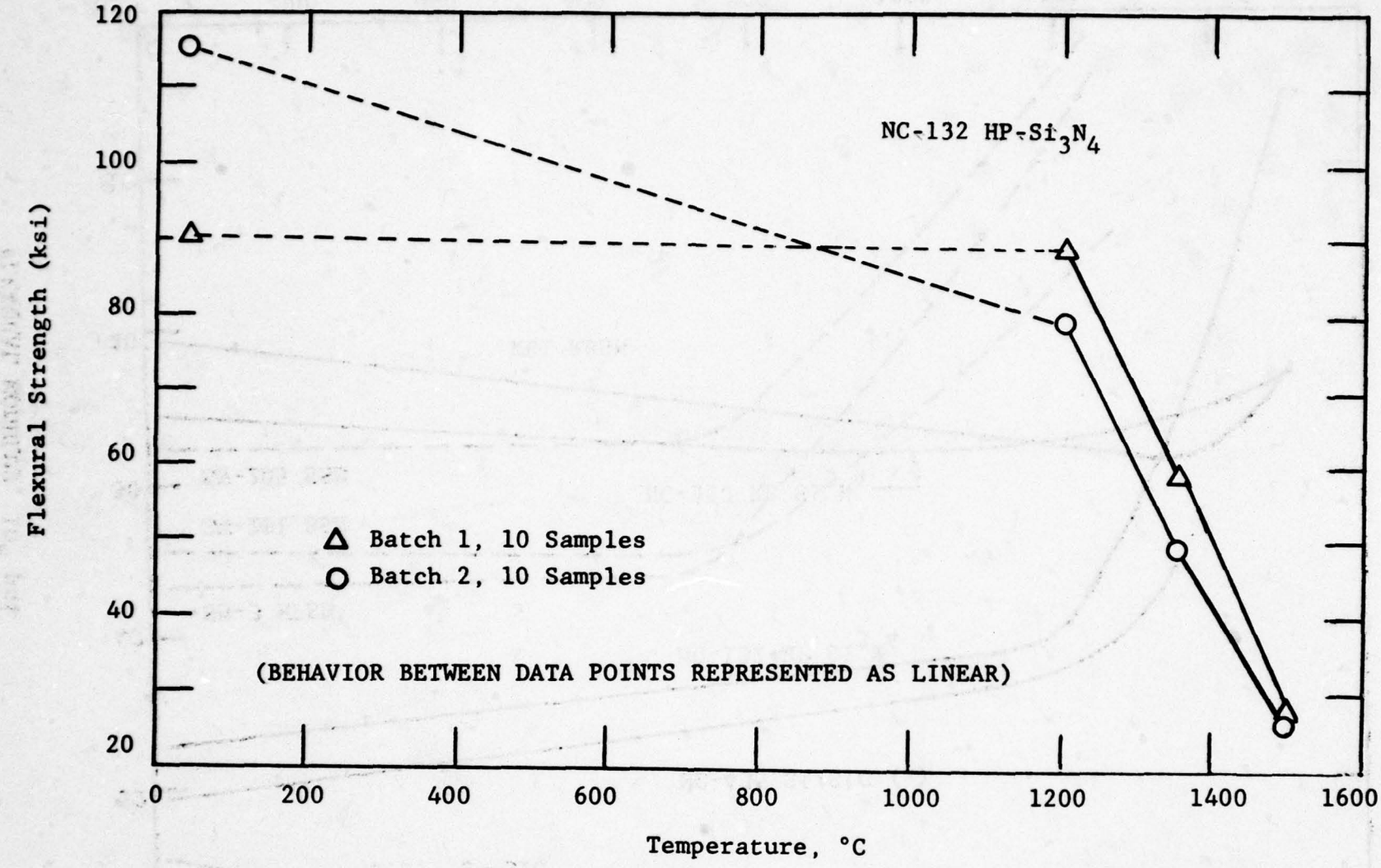

FIGURE 5.3 FLEXURAL STRENGTH vs TEMPERATURE FOR NC-132 HP Si_3N_4

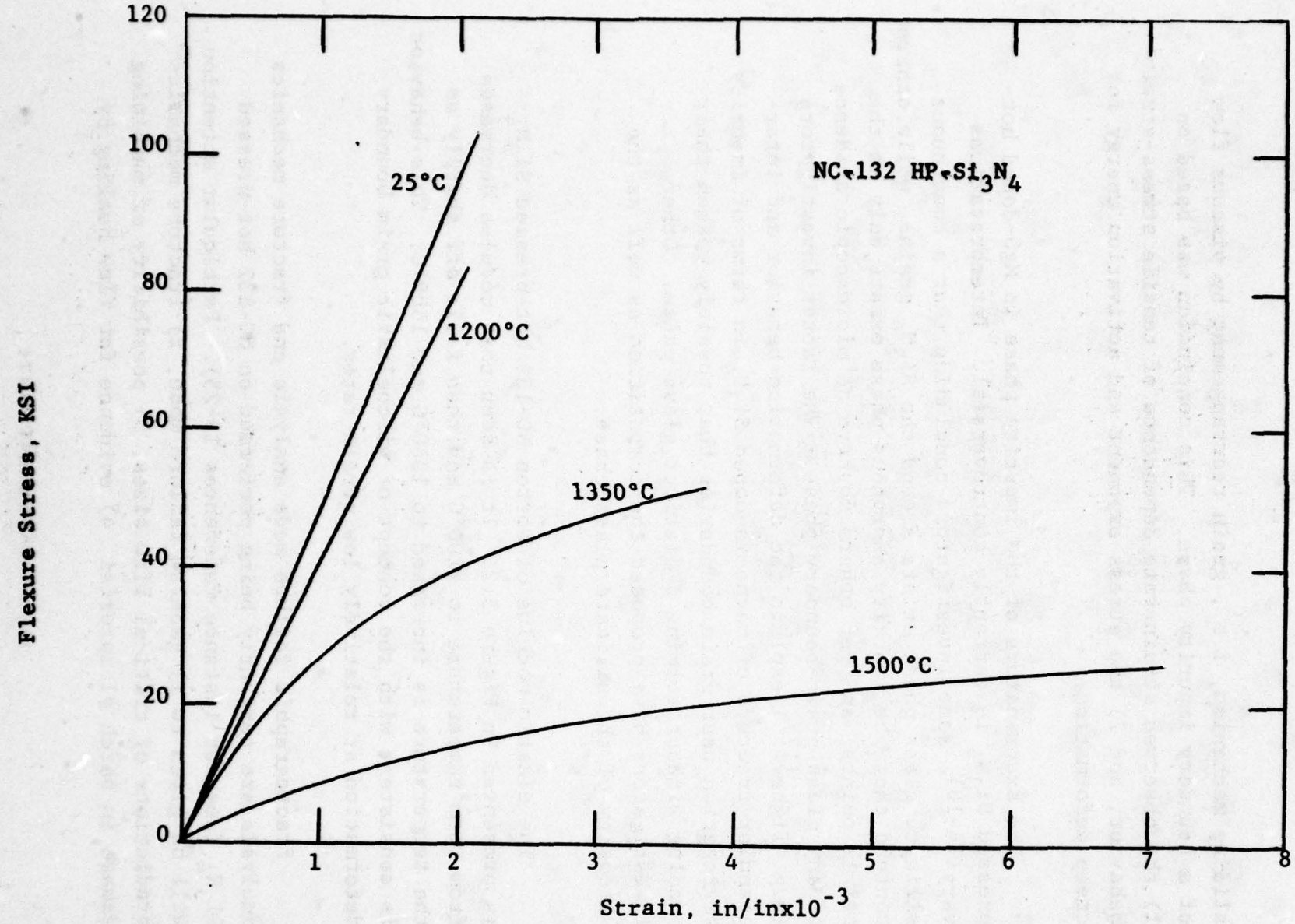

FIGURE 5.4 REPRESENTATIVE FLEXURAL STRESS-STRAIN BEHAVIOR OF NC-132, HP Si_3N_4

sliding mechanism, i.e., grain rearrangement by viscous flow of a boundary impurity phase. This conclusion was based on 1) the observed strain-rate dependence of tensile stress-strain behavior, and 2) the stress exponent and activation energy for creep deformation.

The exact nature of the impurity phase in MgO-doped hot-pressed Si_3N_4 is currently controversial. Interpretations vary[14-18]; some investigators concluding that a continuous silicate glass phase exists around the Si_3N_4 grains, while others contend that the impurity amorphous phase exists only at the triple points, and yet others observe no microscopic evidence of any glass grain-boundary phase. The latter investigators (e.g. Tighe[17]) explain the deformation behavior and intergranular fracture of magnesia-doped Si_3N_4 in terms of impurity segregation near grain boundaries that possibly weaken their bonding without forming a distinct glass phase. Other investigators have proposed the composition as well as the viscosity of the silicate glass phase.

The elastic modulus of Norton NC-132 hot-pressed Si_3N_4 is presented in Figure 5.2. It is seen that modulus decreases from room temperature to 1200°C and then falls off sharply as the temperature is increased to 1350°C and 1500°C. This behavior is consistent with the concept of viscoelastic grain boundary deformation at relatively low strain rates.

Fractographic failure mode analysis and fracture mechanics analysis are currently being performed on NC-132 hot-pressed Si_3N_4 (see for instance references 19-25). Particular attention will be given to 1) general failure mode, 2) fracture mechanics predictions of critical flaw sizes, 3) possibility of machining damage in batch #1 material, 4) evidence for flaw healing by

oxidative crack-tip blunting , and 5) evidence of subcritical crack growth. Lange[26] has reported the evidence of slow crack growth in hot-pressed Si_3N_4. Rice, et. al.[27] have found the fractographic evidence of slow crack growth phenomena at temperatures $\geq$ 1350°C in NC-132. Edington, et.al.[28] explain how the rapid fall in strength in hot-pressed Si_3N_4 at some critical temperature, T_c > 1200°C, is related to sub-critical crack growth promoted by grain boundary sliding which in turn arises from the onset of plasticity in the intergranular glassy phase. Essentially, it is believed that sub-critical crack growth permits flaw growth during load application, which permits the critical stress intensity, K_{IC}, to be attained at a lower macroscopic stress than if the cracks had been unable to grow.

5.1.2 Norton NC-435 Siliconized SiC

Norton NC-435 SiC, commonly refered to as siliconized SiC, is a fine-grain sintered product densified by silicon impregnation[9]. The 1410°C melting point of the 20^{v}/o silicon phase limits use temperatures to $\leq$ 1350°C. Figures 5.1 and 5.2 present the flexural strength and modulus of NC-435 SiC, compared to the other materials. NC-435 exhibited strength increases to 1200°C, whereafter a rapid degradation in strength occurred. Similarly the elastic modulus decreased gradually to 1200°C, and fell off rapidly at higher temperatures. Stress-strain behavior is shown in Figure 5.5. Elastic behavior is only seen at 25°C. The strength increase from 25° to 1200°C may be the result of machining damage that lowers the room temperature strength, but that is subsequently healed by an oxidation mechanism at 1200°C. Lange[29] has reported this phenomenon for other SiC materials, but for oxidation for much longer times (10-100 hr.) at higher temperatures (1400°C). The contribution of the 20^{v}/o silicon-rich phase in NC-435 to possible surface flaw healing is not known at present.

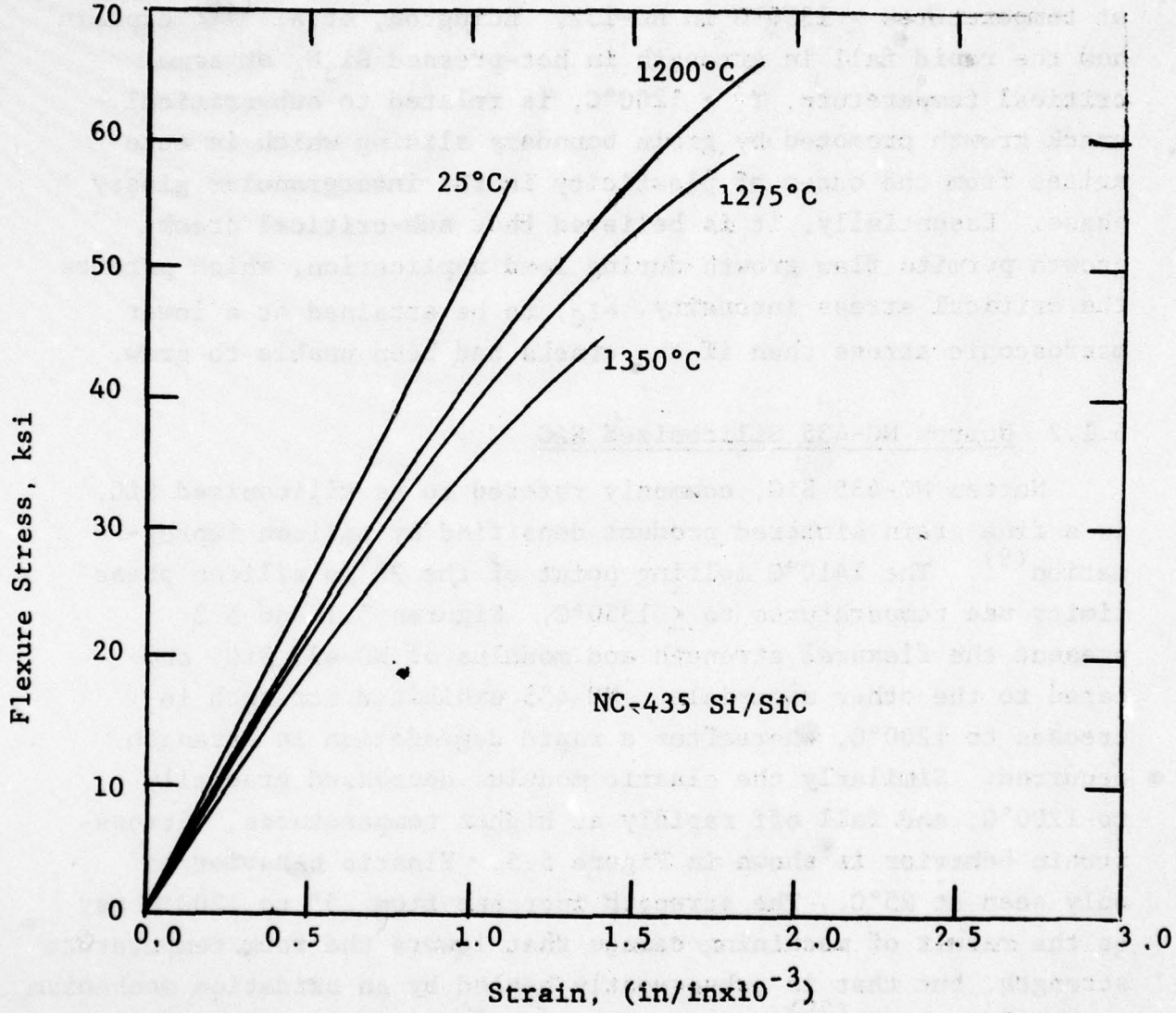

FIGURE 5.5 **REPRESENTATIVE FLEXURAL STRESS-STRAIN BEHAVIOR OF NC-435 Si/SiC**

The rapid fall off in properties at about 1200°C and general increase in anelasticity throughout the temperature range may be due to softening of the silicon phase, or a silicon-rich grain boundary phase. Differences in strength between three batches of NC-435 at 25°C and 1200°C (shown in Figure 5.6) were found to correlate with the semi-quantitative determination of silicon-rich phase by x-ray diffraction analysis[30]. Higher strengths were found for lower silicon content. Rice et. al.[27] indicate that fractographic analysis of this material has not provided definitive results mainly due to the heterogeneous nature of this siliconized SiC material. Current fractographic work at AFML will re-examine this material.

5.1.3 Norton NC-350 Reaction Bonded Si_3N_4

Results of 4-point flexural testing of Norton NC-350 reaction bonded Si_3N_4 were presented in the last interim technical report[2]. Detailed fractographic failure mode analysis and fracture mechanics analysis are currently in progress on this material. To maintain continuity and to make comparisons with other materials which will be subsequently investigated, the behavior of NC-350 is reviewed in this section. Additionally, preliminary fractographic evicence is presented, and the effect of oxidation on strength is discussed.

The development and properties of NC-350 reaction sintered Si_3N_4 are discussed in several publications by Norton Company personnel[9,31-34]. Figures 5.1 and 5.2 illustrate the strength and modulus of this material as a function of temperature. All 4-point flexure testing was performed in air on our current program. It is observed that this material is the strongest tested thus far at 1500°C, the flexure strength being ~50 ksi. This illustrates the potential of NC-350 reaction sintered Si_3N_4 for high temperature gas turbine use and thus our interest

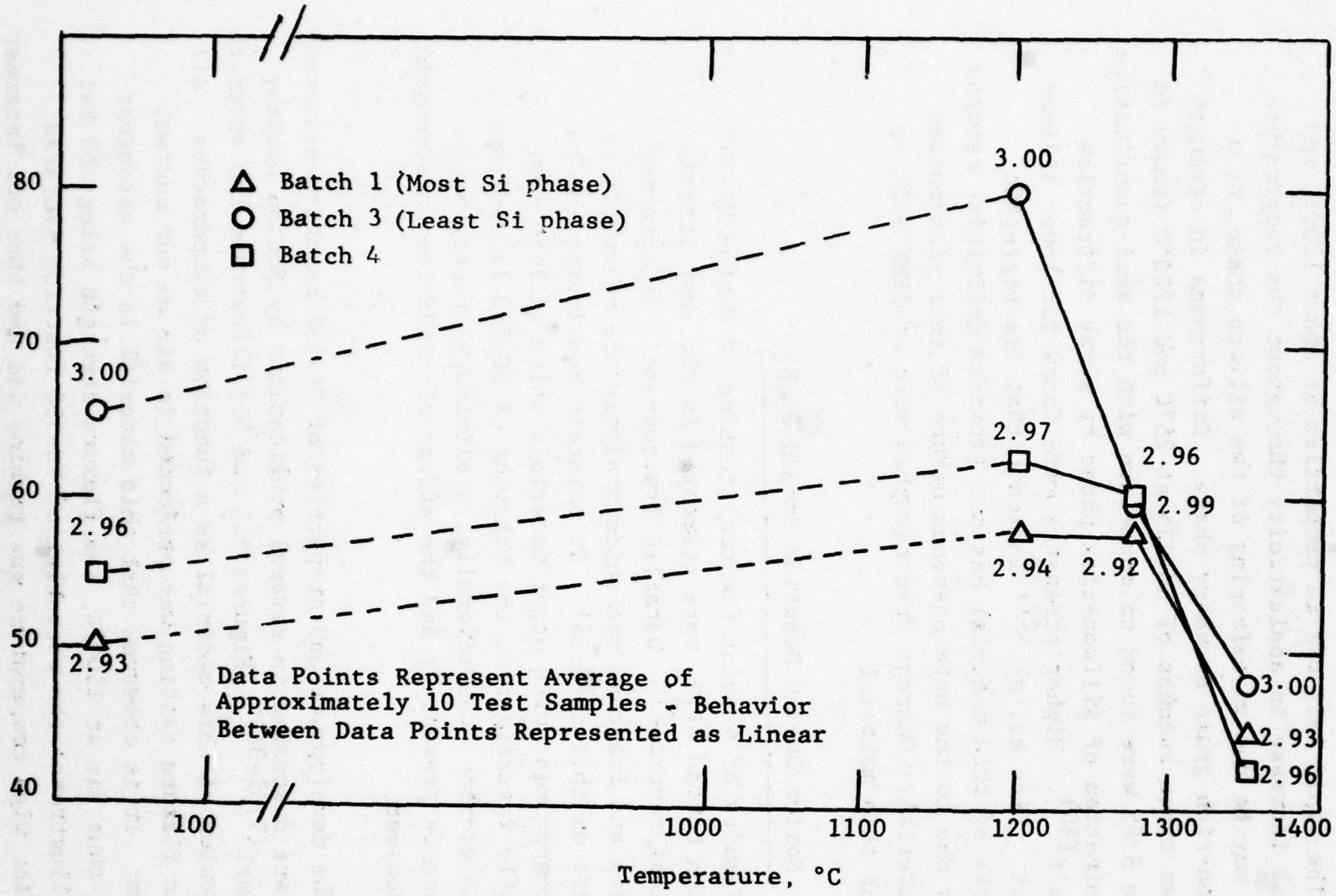

FIGURE 5.6 FLEXURAL STRENGTH vs TEMPERATURE FOR NC-435 Si/SiC

in a comprehensive characterization of its properties and behavior.

NC-350 reaction sintered Si_3N_4 exhibits low room temperature flexural strength and modulus when compared to the hot pressed silicon nitrides (see Figures 5.1 and 5.2). This is due to the higher porosity in reaction sintered Si_3N_4. NC-350 exhibited a large strength variability at room temperature that correlated with a density variation from 2.4 to 2.54 gm/cc, as illustrated in Figure 5.7. The room temperature 4-point flexure strength vs. bulk density for all samples of NC-350 RS Si_3N_4 is presented in Figure 5.8. The batch variability and general trend of increasing strength with increasing density for NC-350 is illustrated. The large scatter, however, would seem to indicate that the distribution and size of porosity is also important in controlling strength. This was confirmed by subsequent fractographic analysis, as discussed below, which indicated many fracture origins to be large pores or pore agglomerates. The presence of a few pore clusters would be expected to add data scatter to an otherwise well-behaved strength-density relation.

Rice[35,36] has investigated application of the exponential form of porosity dependence ($S = S_o e^{-bP}$, where S = strength at volume fraction porosity P, and S_o = strength at P = 0) for a wide variety of silicon nitride materials. Data are presented in a semi-log plot of strength vs. volume fraction porosity. Figure 5.9 illustrates such a plot of the present NC-350 room temperature 4-point flexure data. The straight line representation is a least squares fit of the individual data points shown by symbols referring to batch number. The terms S_o and b refer to strength at zero porosity and slope, respectively. The values obtained for NC-350 in the present investigation are higher than Rice[35] has indicated for a wide variety of Si_3N_4

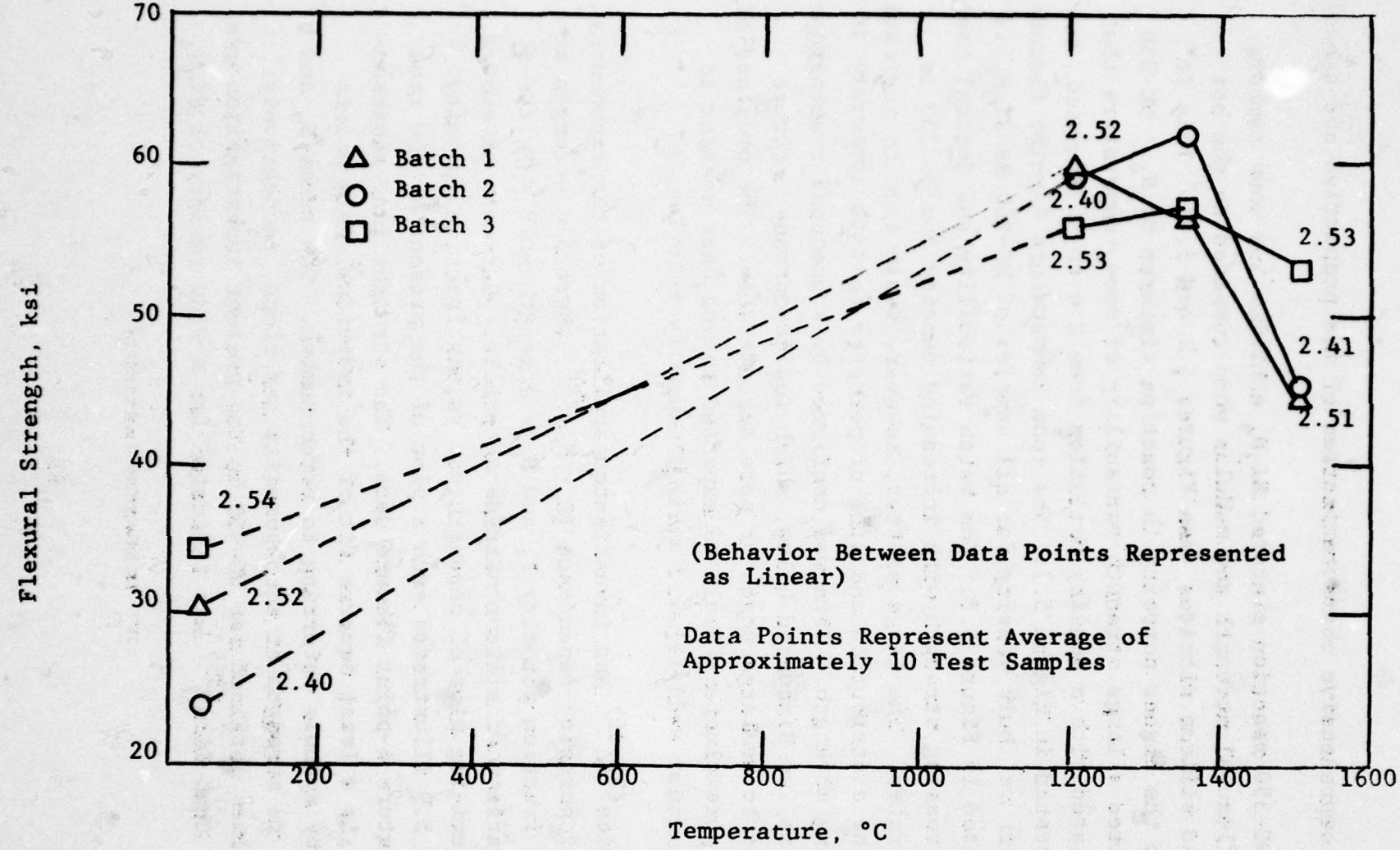

FIGURE 5.7 FLEXURAL STRENGTH vs TEMPERATURE FOR NC-350 RB Si_3N_4

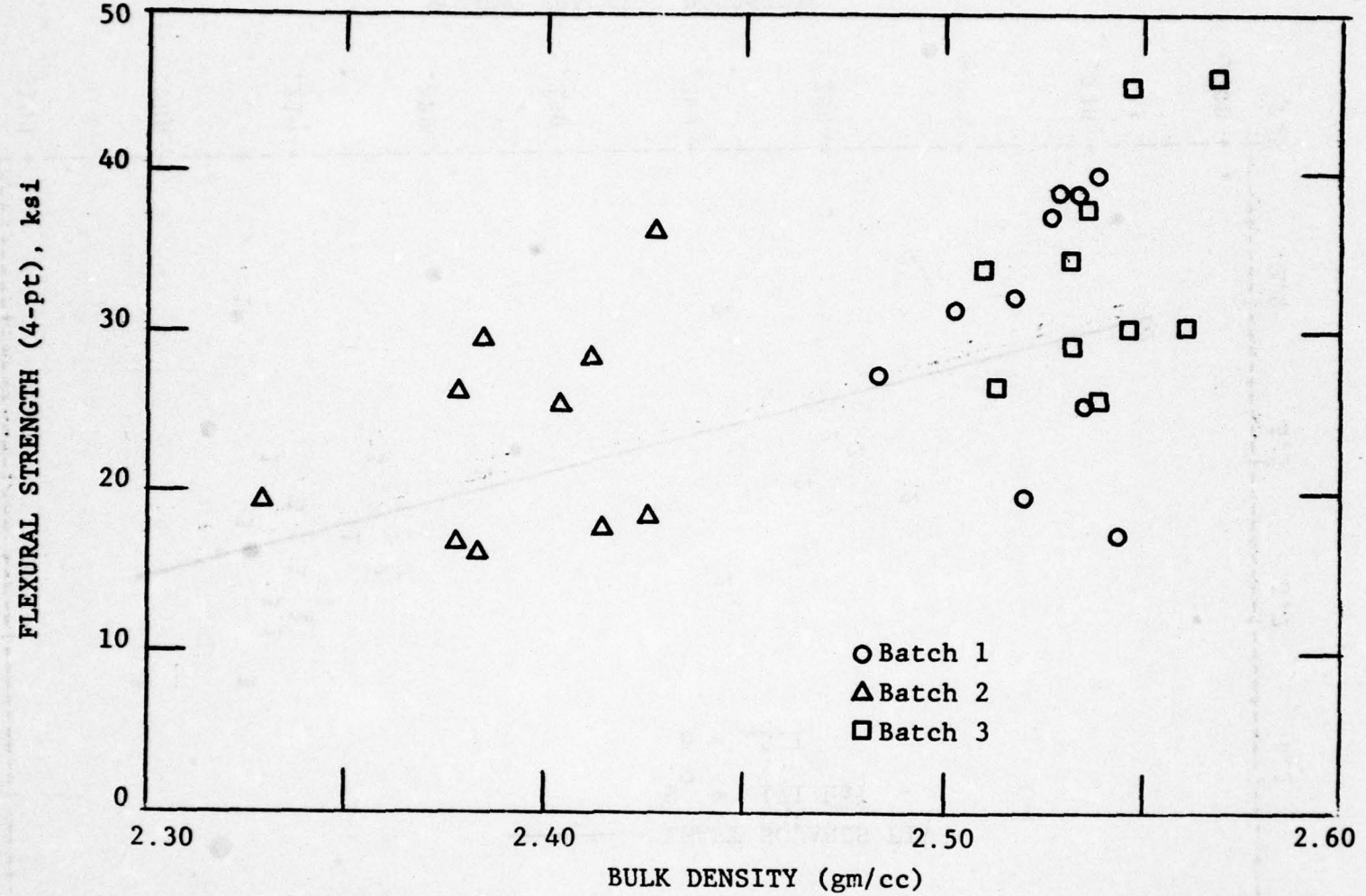

FIGURE 5.8 FLEXURE STRENGTH VS DENSITY FOR NC-350 RS Si_3N_4 AT ROOM TEMPERATURE

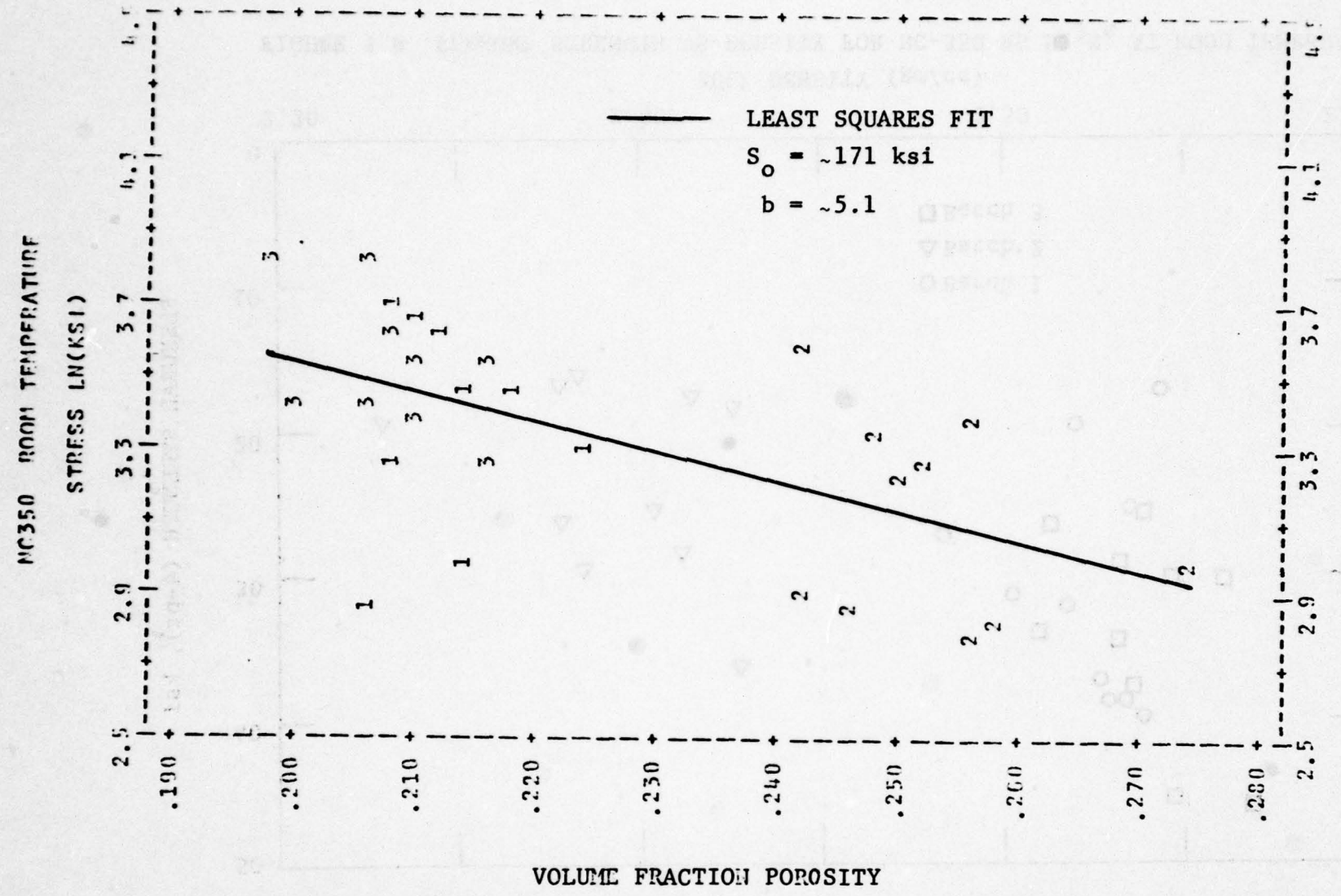

FIGURE 5.9 SEMI-LOGARITHMIC PLOT OF ROOM TEMPERATURE 4-POINT FLEXURE STRENGTH OF NC-350 RS Si_3N_4 AS A FUNCTION OF POROSITY.

materials, as shown in Figure 5.10, although current NC-350 data is in general agreement with the main trend of the literature data and falls within the scatter band. The reason for any disagreement shown is most probably the limited range of porosity covered by the current NC-350 data.

The strength of Norton NC-350 reaction sintered Si_3N_4 increases significantly from room temperature to 1200°C-1350°C then falls off somewhat at 1500°C, as shown in Figures 5.1 and 5.7. Linear elastic stress-strain behavior to failure is exhibited at all temperatures, including 1500°C, as shown in Figure 5.11. This can be explained by the lack of a significant impurity phase, as is present in hot pressed silicon nitrides (using MgO as a densification aid). The relative purity levels (metallic + oxygen) of NC-350 and NC-132 is shown in Table 5.1. Note that at 1500°C NC-350 exhibits strength of almost 50 ksi, which is almost twice the room temperature flexural strength.

It is anticipated that fractographic analysis can provide reasons for 1) the ~25% lower room temperature strength observed for NC-350 in comparison to Norton data[31] for samples with similar density and surface finish, and 2) the strength increase with temperature observed for NC-350 tested in flexure in air at $T \geq 1200°C$ (and its relation to porosity, the correlation with which is shown in Figure 5.7).

Preliminary results by Rice, et. al[27] indicate that at room temperature the most definitive fracture origins are process related - large pores and clusters of pores. However, probable machining flaws were identified in ~80% of the test bars. It should be noted that this may be a matter of interpretation, since in some instances the probable machining flaws were in regions of higher porosity, which would be process related.

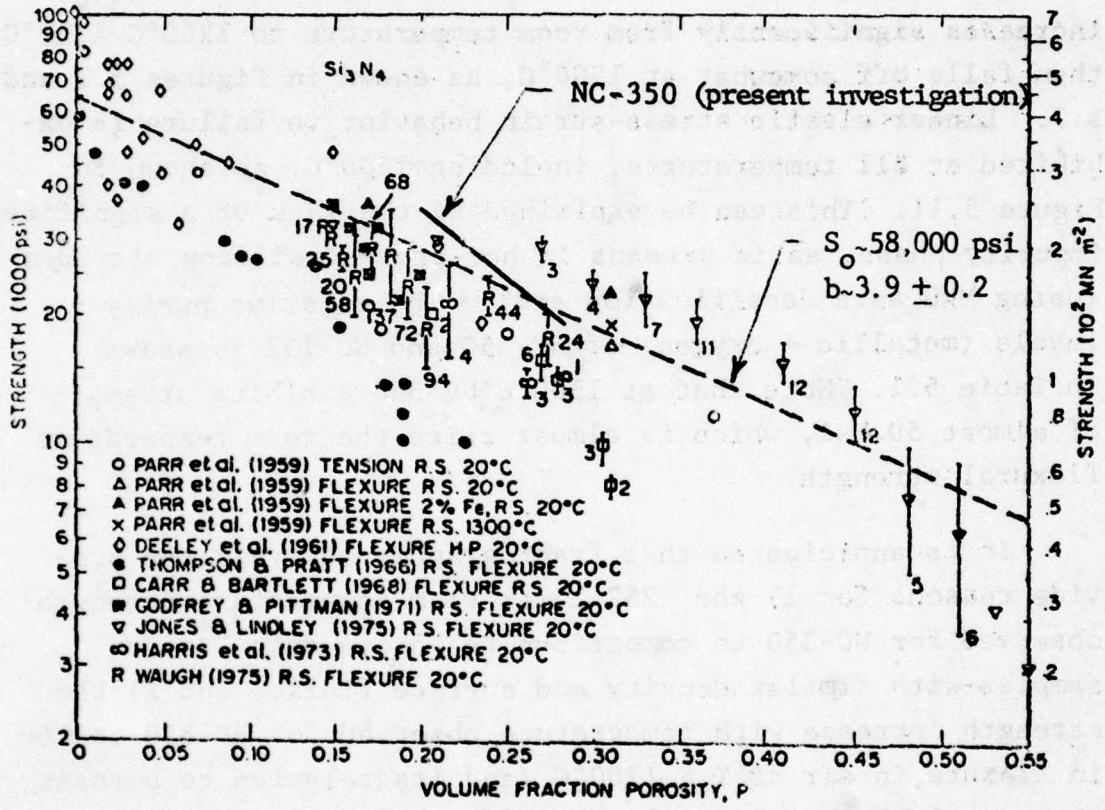

FIGURE 5.10 SEMI-LOGARITHMIC PLOT OF STRENGTH (25°C) of Si_3N_4 AS A FUNCTION OF POROSITY (TAKEN FROM RICE[35]) SHOWING PRESENT DATA TREND FOR NC-350 RSSN OVER THE POROSITY RANGE INDICATED.

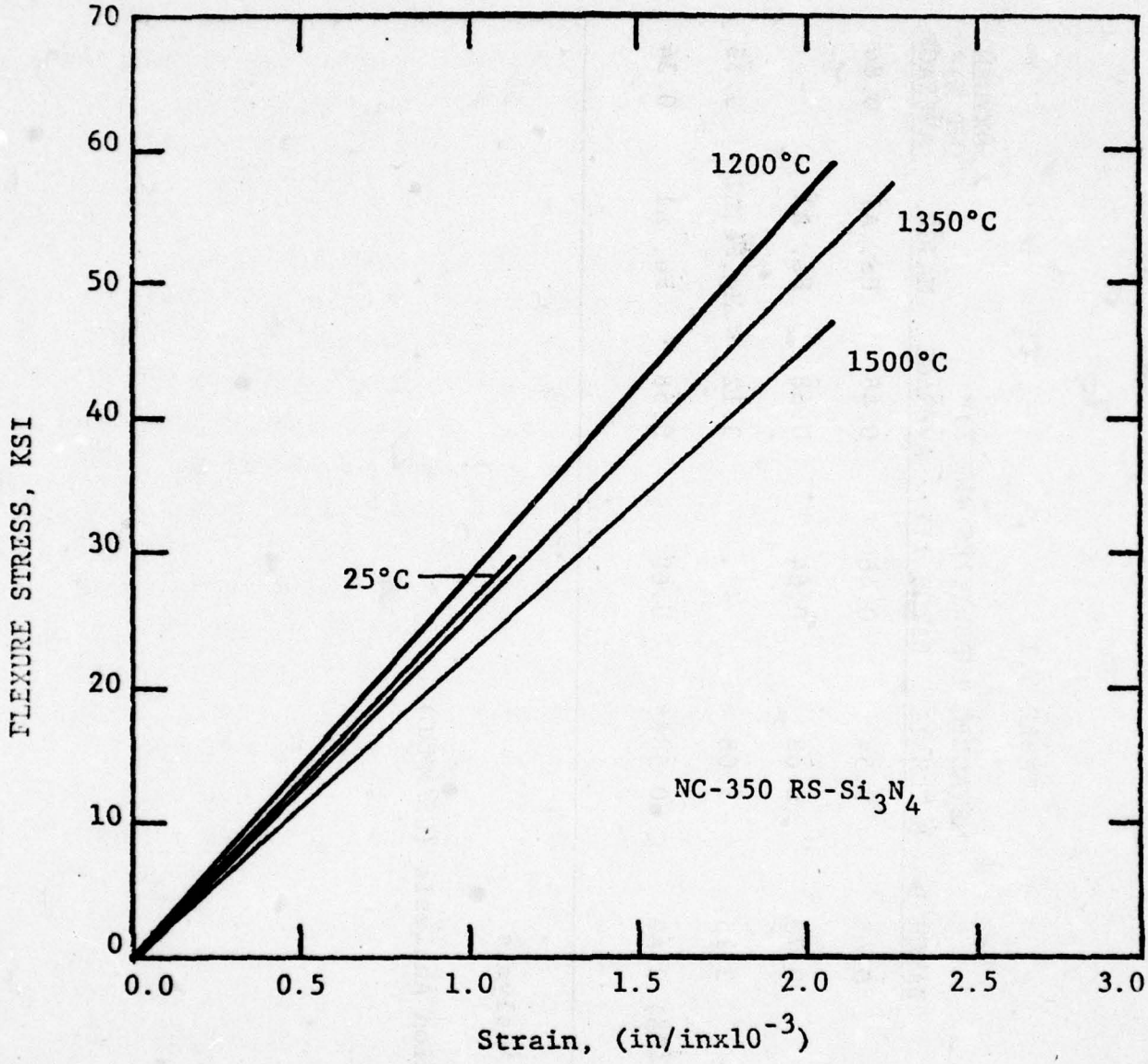

FIGURE 5.11 REPRESENTATIVE FLEXURAL STRESS-STRAIN BEHAVIOR OF NC-350 REACTION SINTERED Si_3N_4

TABLE 5.1

MATERIAL	METALLIC IMPURITIES (WT %)* BATCH I	BATCH II	BATCH III	AVERAGE	MAJOR	OXYGEN (WT %)** AVERAGE
RB Si_3N_4 (NC 350)	0.45	0.54	0.46	0.48	Fe, Al	0.84
RB Si_3N_4 (KBI)	0.73	0.68	0.64	0.68	Fe, Al	-
HP Si_3N_4 (NC 132)	3.15	3.08	-	3.12	W,Mg,Fe,Al	3.33
Siliconized SiC(NC 435)	0.49	0.58**	0.68	0.58	Fe, Al	0.34

* Spectrographic Analysis

** Neutron Activation Analysis (USAMMRC)

*** Batch IV

At elevated temperatures multiple fracturing was the limiting factor in determining fracture origins. Oxidation of fresh fracture surfaces is another factor that has thus far limited the identification of specific fracture origins in elevated temperature samples [27,37].

A detailed fractographic failure mode analysis and fracture mechanics analysis is currently being conducted at AFML[37]. Only preliminary results are available at this time. NC-350 4-point flexure bars broken at room temperature exhibited uniform, planar features representing a transgranular fracture mode. This can be observed in Figure 5.12, an SEM micrograph of a region of the fracture surface of NC-350 tested at 25°C far away from the fracture origin. The most dominant fracture-originating flaws thus far identified have been pores and pore agglomerates near the tensile surface of the bend bar. NC-350 generally exhibited a relatively uniform distribution of 1-2 μm pores; however isolated larger pores and pore agglomerates of ~10 μm size are being frequently encountered (locations A and B in Figure 5.12). Location of a fracture origin near the tensile surface does not necessarily imply machine-induced damage, since in bending the local stress is highest at the surface. Obviously, the spatial distribution of the large pore agglomerates will greatly influence the strength distribution. Specific fracture initiating origins are currently being tabulated for this material and fracture mechanics calculations are being performed.

Attention is being given to the significant strength increase with temperature observed in testing NC-350 in air in four-point flexure (Figure 5.1, 5.7). Davidge, et. al[38] indicate that this has been observed in reaction-sintered Si_3N_4 previously, and discuss how oxidation can either reduce the flaw size or increase the fracture surface energy to account for the strength increase. Wiederhorn[39] has shown how prolonged oxidation can decrease

FIGURE 5.12 FRACTURE SURFACE SHOWING MICROSTRUCTURE OF NC-350 RS Si_3N_4. BEND BAR FRACTURED AT ROOM TEMPERATURE. SECONDARY ELECTRON SEM MICROGRAPH.

strength by producing new flaws. Rice[27] presents fractographic evidence that shows surface pitting to degrade the strength of NC-132 HP Si_3N_4 oxidized for long times prior to testing.

Figure 5.7 illustrates that for Batch 2, the 4-point flexure strength of NC-350 tested at IITRI is 23,500 psi, whereas at 1200°C the strength of a virgin sample tested in air is 58,600 psi. One possibility for the strength increase is oxidative flaw tip blunting at elevated temperature. The flaws could be either machining damage or porosity resulting from fabrication. The most common fracture mechanism in reaction sintered Si_3N_4 found in the literature is extension of the largest pores. Thus, for oxidation to effect strength, the distribution and relative amounts of open and closed porosity become important. For instance, some materials may exhibit uniform oxidation throughout the specimen thickness, whereas others have their surface pores sealed off thus preventing in-depth oxidation[41].

To investigate these possibilities, several NC-350 Batch 2 flex samples were pre-oxidized at 1200°C, and then tested at 25°C for flexural strength. Care was taken to ensure that the environmental exposure was identical to that experienced during previous elevated temperature tests on virgin samples. The results are illustrated in Table 5.2, and compared with previous results for virgin samples. It is observed that the room temperature strength of the pre-oxidized samples (43,900 psi) is significantly higher than for the virgin material (23,500 psi) but slightly lower than that for virgin material tested at 1200°C (58,600 psi). The density of all materials was ~2.4 gm/cc. The conclusion from these data is that exposure of NC-350 reaction-sintered Si_3N_4 in air at 1200°C for ~15-30 minutes does have a significant "crack healing" effect. The reason that the pre-oxidized samples did not exhibit strengths quite as high as

TABLE 5.2A

FLEXURAL TEST RESULTS: NC 350 (2)
PRE-OXIDIZED AT 1200°C TESTED AT 25°C

Sample	Bulk Density (gm/cc)	Strength (psi)	Strain-to-Failure (in/in x 10^{-3})	Secant Modulus (10^6 psi)
32F41	2.414	45,080	2.00	22.4
32F42	2.385	45,790	2.10	21.8
32F43	2.340	33,900	1.60	22.5
32F44	2.417	50,850	2.15	23.6
Mean	2.389	43,910	1.96	22.6
Std.Dev.		7,150	0.25	0.7
Max.		50,850	2.15	23.6
Min.		33,900	1.60	21.8

TABLE 5.2B

PREVIOUS* FLEXURAL TEST RESULTS: NC 350 (2)
VIRGIN SAMPLES TESTED IN AIR

Test Condition	Avg.Bulk Density (gm/cc)	Mean Strength (psi)	Strain-to-Failure (in/in x 10^{-3})	Elastic Modulus (10^6 psi)
25°C	2.40	23,530	0.99	23.5
1200°C	2.40	58,620	2.47	23.1

*See Appendix Tables for Details

the virgin materials tested at 1200°C can possibly be explained by considering the series of experiments conducted by Evans and Davidge[40]. It was found that cristobalite formed at 1200°C-1400°C, modifying internal and external pores and increasing strength, except when the sample was subsequently cooled to <250°C, at which point surface cracking would occur in the cristobalite layer due to the volume decrease accompanying the α-β phase inversion, thereby reducing the strength. In subsequent work, Davidge et. al.[38] showed that at 1200°C most of the oxidation was complete in the first 15 minutes, a time consistent with the exposure times in our present experiments at IITRI. Subsequent fractography on our samples will attempt to confirm the validity of these possibilities, although it is realized that any existing oxide layers might be to thin to distinguish by SEM. Davidge, et.al.[38] caution that explanation of the strength behavior of oxidized reaction-sintered silicon nitride is complex due to 1) the fact that two distinct stages of oxidation are possible, and 2) that both internal and external oxide layers may be either strained or cracked.

Preliminary results are available for the detailed fractographic/fracture mechanics analyses being conducted at AFML. Fracture surfaces of NC-350 bend bars broken in air at 1200°C exhibited a marked difference in appearance as compared to room temperature fracture surfaces. The 1200°C fracture surface did not show uniform, planar features; rather it showed diffused, undefined features as illustrated in Figure 5.13. From the appearance it is difficult to judge whether the fracture mode is transgranular or intergranular. However, as compared to the room-temperature fracture appearance, (i.e., uniform planar features), the fracture mode has definitely changed.

To check whether oxidation of the fresh fracture surface at 1200°C might be obscuring the fracture features to give this result, two bend bars were broken at AFML in four-point flexure

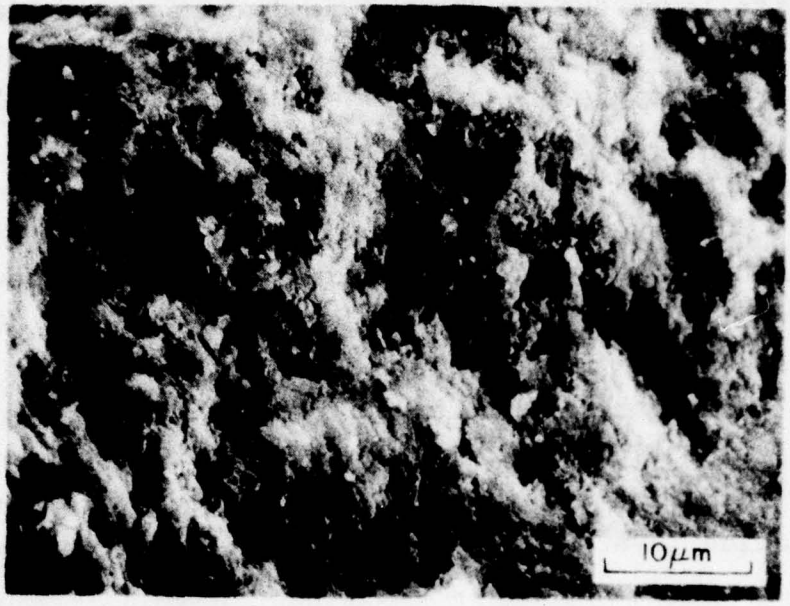

FIGURE 5.13

FRACTURE SURFACE SHOWING MICROSTRUCTURE OF NC-350 RS Si_3N_4. FRACTURED AT 1200°C IN AIR. SECONDARY ELECTRON SEM MICROGRAPH.

in a vacuum of 10^{-4} torr. The fracture surface appearance of bend bars broken at 1200°C in vacuum was very similar to those broken at 1200°C in air (Figure 5.13). The oxidation at 1200°C, therefore, did not obscure the appearance of the fresh fracture surfaces, and it is concluded that there is a definite change in fracture mode at elevated temperatures, regardless of whether the environment is air or vacuum. This change is thus solely a function of temperature, but is not responsible for the strength increase found in 1200°C air testing, as discussed below.

The strength data obtained for the 1200°C vacuum tests is shown in Table 5.3. The 34 ksi strength obtained in vacuum at 1200°C is very close to the strength obtained in air at room temperature (see Appendix Tables B1-3, $\bar{\sigma} \cong 30$ ksi). This would tend to indicate that the large strength increases observed in 1200°C tests in air are somehow caused by the air environment. It is tempting to conclude that it is oxidation-e.g., flaw tip blunting or some chemical effect related to the presence of oxygen. However, if the strength increases at 1200°C in air were caused by oxidation, then it is not presently understood how the 1200°C/air and 1200°C/vacuum fracture surface features would be so similar, and so different than the fracture surface appearance of a sample broken at 25°C in air. Of course, the possibility exists for two mechanisms to be operative, e.g., one associated with oxidation (resulting in the strength increase observed in elevated temperature air tests), and another solely associated with temperature. It is emphasized that these results are only preliminary, and that detailed fractographic determination of strength-controlling flaws and fracture modes, together with the application of fracture mechanics techniques are currently in progress.

The strength decreases for NC-350 reaction sintered Si_3N_4

TABLE 5.3

FOUR-POINT FLEXURAL STRENGTH AT 1200°C
FOR NC-350 Si_3N_4

Oxidation Treatment	Test Atmosphere	Average Strength
None	Air	65 ksi (IITRI)
None	Vacuum	34 ksi (AFML)

between 1200°C and 1500°C (Figure 5.1). If significant plastic deformation were observed at 1500°C, it could be inferred that a significant oxygen impurity was present resulting in a slight intergranular glassy phase which could cause strength degradation. Since Figure 5.11 indicates no plastic deformation at 1500°C, another mechanism must be found. Noakes and Pratt[42] suggest that this can be explained by the breakdown of intergranular cohesion.

Young's modulus data for NC-350 reaction bonded Si_3N_4 obtained in flexure are presented in Figure 5.2. Values at room temperature are in good agreement with reported values[32] 25-29x10^6 psi. A modulus of 41x10^6 psi is obtained for theoretically dense material if data are corrected for porosity using the MacKenzie[43] relation $E=E_0[1-1.9P+0.9P^2]$. Other modulus-density models will be investigated also. This compares favorably with the value of 47x10^6 psi obtained for the hot-pressed material NC-132. The change in modulus with temperature to 1200°C can be correlated with density. Materials with a density of 2.4 gm/cc exhibited no modulus change, whereas the other NC-350 samples with densities of > 2.5 gm/cm^3 had increasing moduli. Noakes and Pratt[42] also observed increasing moduli with temperature for reaction bonded Si_3N_4 with density $\geq$ 2.5 gm/cm^3. The physical reason for this is not known at present.

5.1.4 Kawecki-Berylco Reaction-Sintered Si_3N_4

The strength and elastic modulus of KBI RS Si_3N_4 are presented in Figures 5.1 and 5.2. It is observed in Figure 5.1 that the strength is much lower than NC-350 reaction sintered Si_3N_4 at all test temperatures, and that the strength does not increase with temperature. Recall that the porosity was slightly greater and less uniform for the KBI material and that most of the porosity was open. However, the KBI materials had an average density of 2.4 gm/cc, and their strength and modulus

agreed reasonably well with results of Batch 2 of NC-350 reaction-sintered Si_3N_4 samples that also had a bulk density of 2.4 gm/cc.

Figures 5.14 and 5.15 illustrate the strength and modulus vs temperature relation for all three batches of KBI-RS Si_3N_4. Note the direct correlation between room temperature strength and batch density. This correlation does not necessarily exist at high temperature, however. Figure 5.16 shows the individual sample room temperature 4-point flexural strength vs bulk density. As discussed above for NC-350, plotting ln (fracture stress) vs volume fraction porosity permits application of the exponental porosity dependence relation $S = S_o e^{-bP}$, as discussed by Rice[35,36]. Figure 5.17 illustrates this for the KBI RSSN room temperature data. Figure 5.18 shows these data compared with Rice[35] for a wide variety of silicon nitride materials. The present KBI room temperature strength data are in excellent agreement with the main trend of data shown, both for slope and strength at zero porosity (56,000 psi). Recall that NC-350 reaction sintered Si_3N_4 did not give such good agreement, most probably due to a more restricted range of porosity to fit to the exponetial strength-porosity relation.

KBI reaction sintered Si_3N_4 exhibits linear stress-strain behavior to failure at all test temperatures, including 1500°C. This is illustrated in Figure 5.19, and indicates that despite it's low strength, there is apparently no significant grain boundary impurity phase in this material.

Preliminary SEM micrographs of general features of the fracture surface of room temperature KBI RSSN flex bars are available.

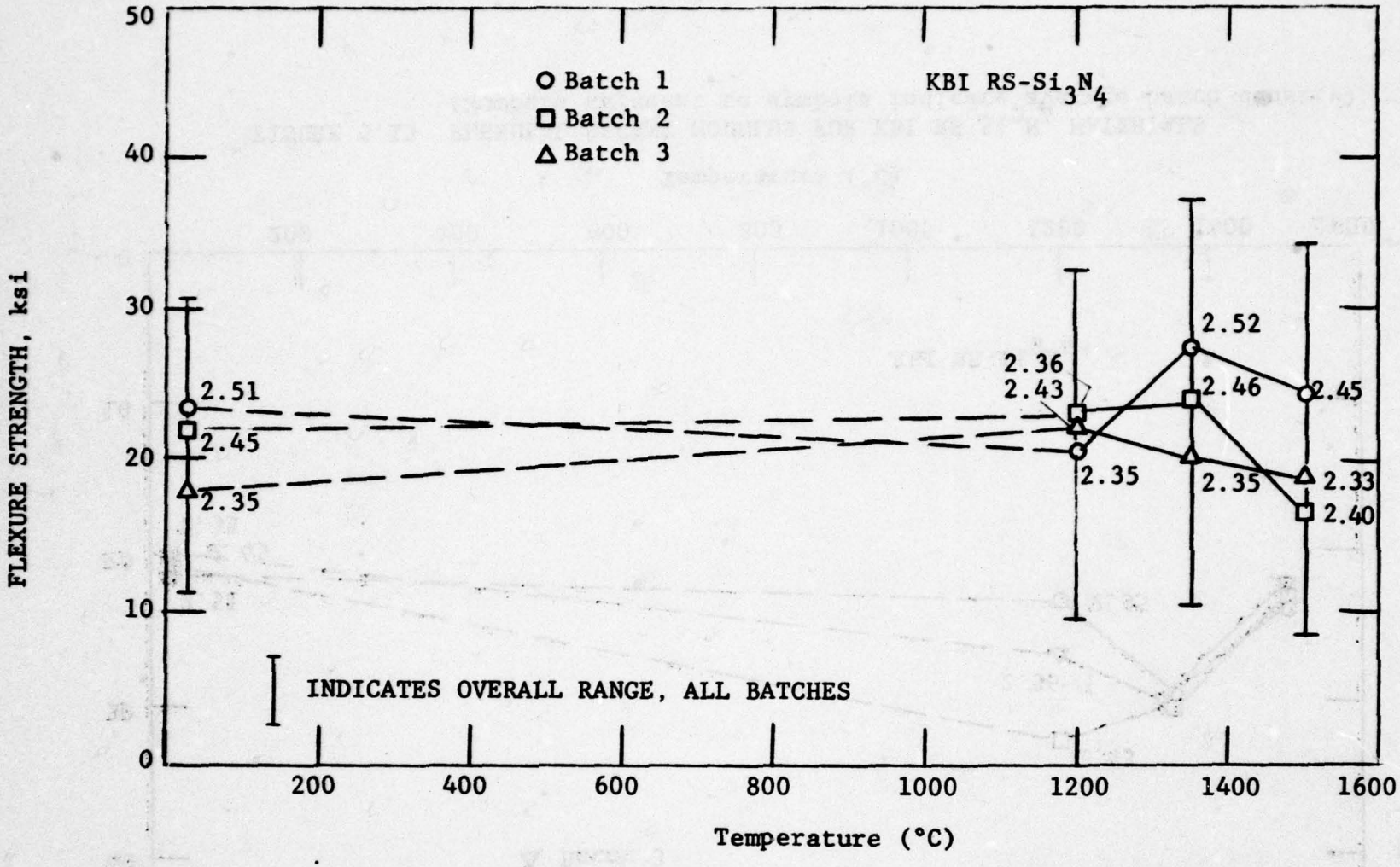

FIGURE 5.14 4-POINT FLEXURAL STRENGTH OF KBI RSSN MATERIAL

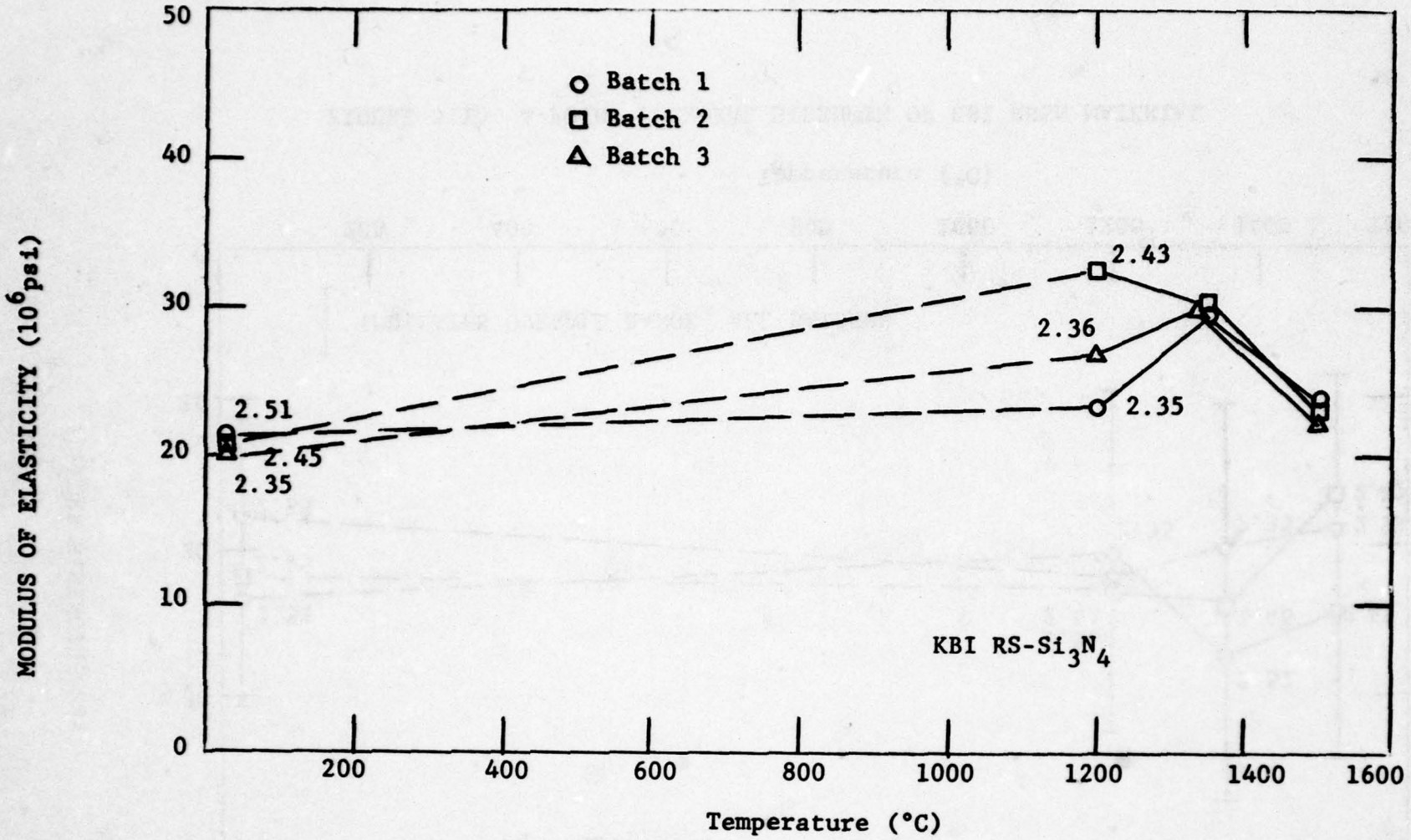

FIGURE 5.15 FLEXURAL SECANT MODULUS FOR KBI RS Si_3N_4 MATERIALS
(Numbers adjacent to symbols indicate average batch density)

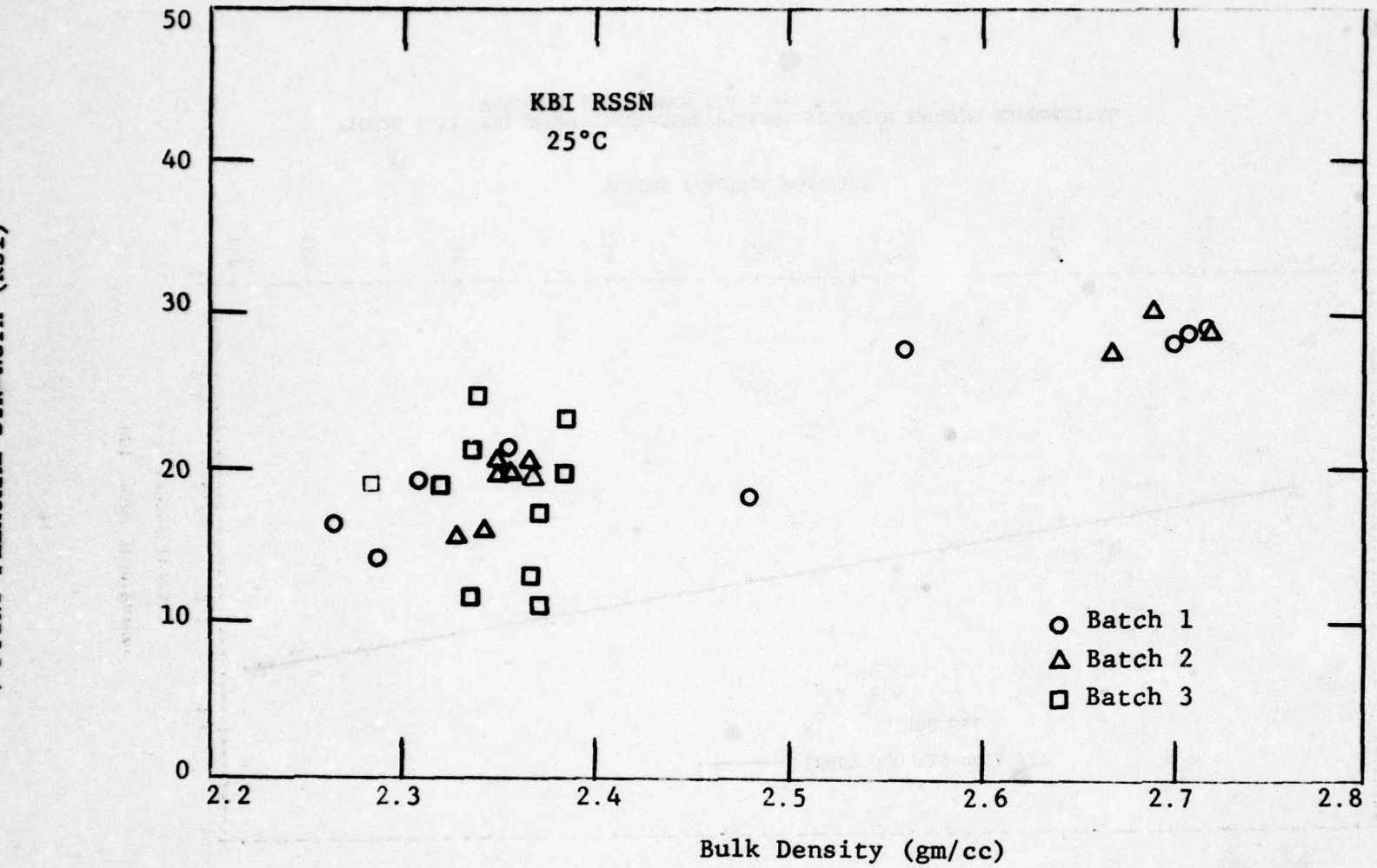

FIGURE 5.16 FLEXURE STRENGTH vs. DENSITY FOR KBI RS Si_3N_4 AT ROOM TEMPERATURE

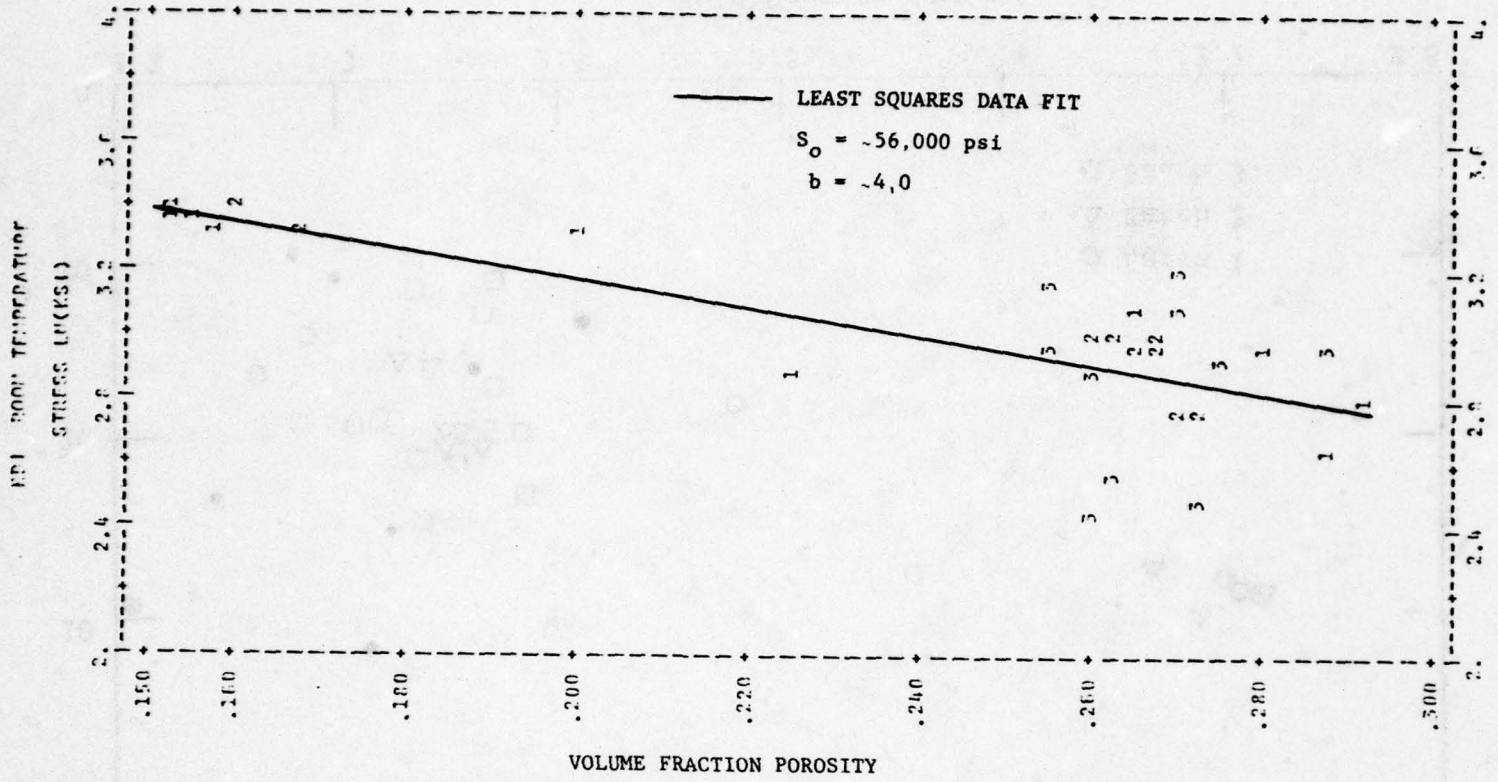

FIGURE 5.17 KBI ROOM TEMPERATURE FLEXURE STRENGTH SHOWING EXPONENTIAL POROSITY DEPENDENCE (ln σ vs. P)

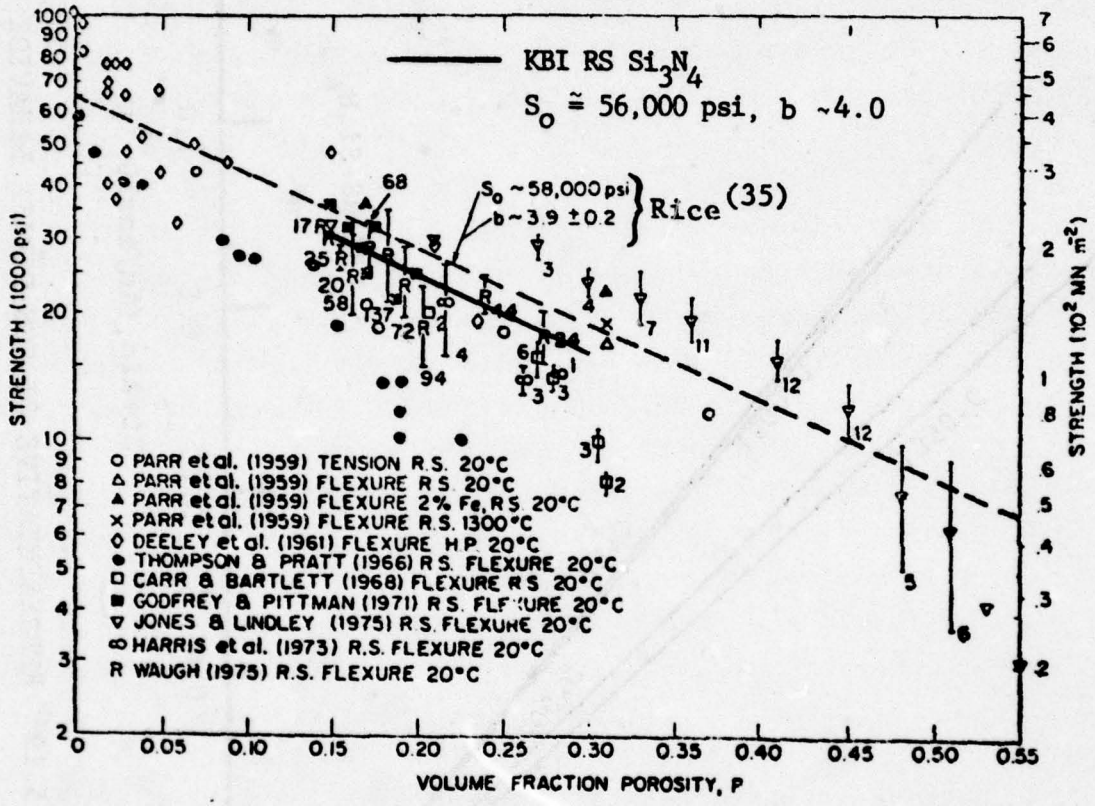

FIGURE 5.18 SEMI-LOG PLOT OF STRENGTH (25°C) OF Si_3N_4 AS A FUNCTION OF POROSITY (TAKEN FROM RICE[35]) SHOWING PRESENT DATA TREND FOR KBI-RSSN OVER THE POROSITY RANGE INDICATED

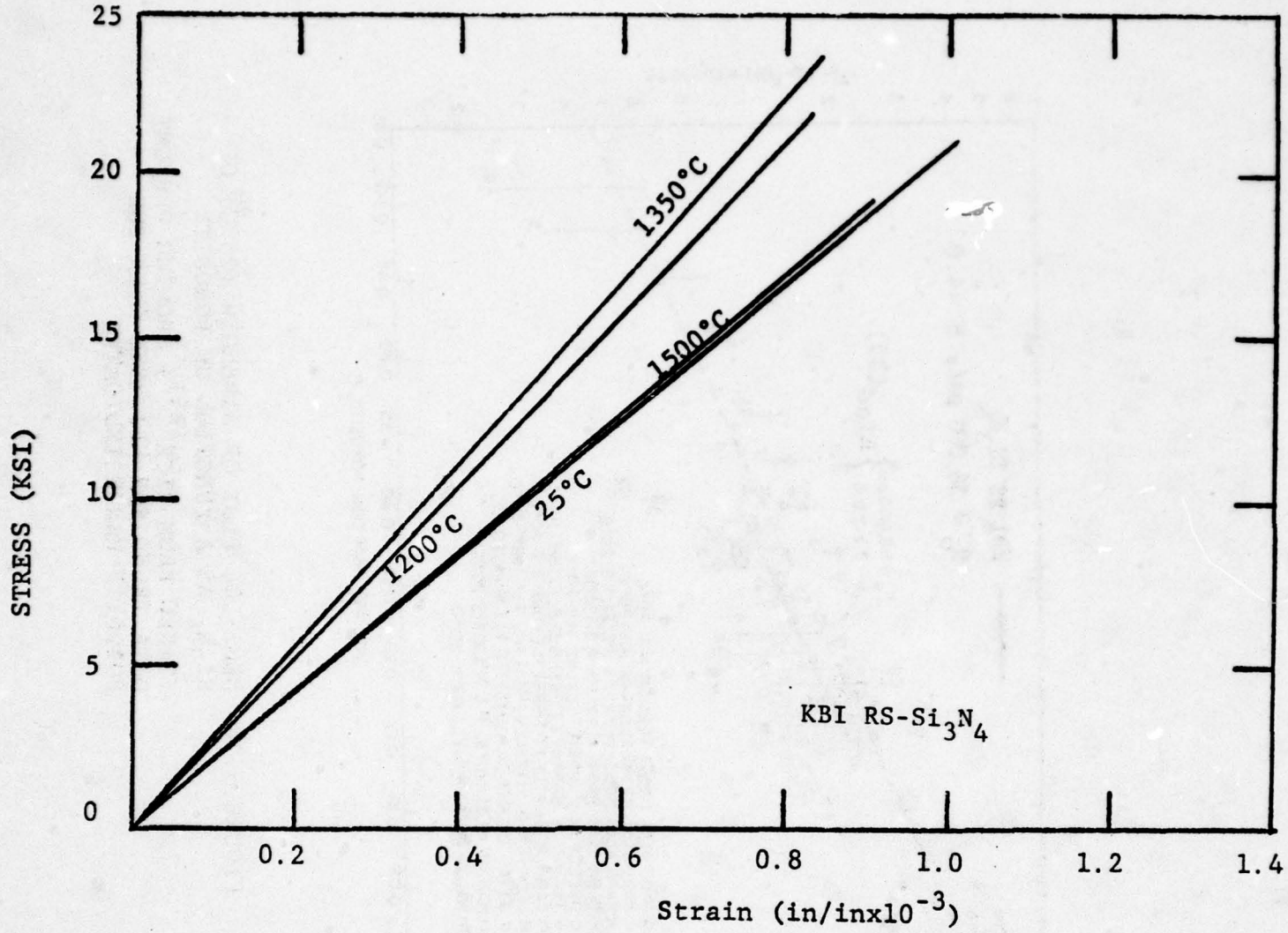

FIGURE 5.19 REPRESENTATIVE STRESS-STRAIN BEHAVIOR OF KBI REACTION SINTERED Si_3N_4

In contrast to the relatively sharp fracture features in NC-350 fractured at 25°C, the KBI material revealed diffused non-uniform fracture features. This is shown in Figures 5.20(a) and (b). Figure 5.20(a) illustrates ill-defined features giving a wooly appearance; it is difficult to determine whether the fracture is transgranular or intergranular. Small pores having a size range of ~2-5 μm can be seen in the micrograph. Many large pores showing unreacted material and having a size of ~50 μm were also frequently observed; an example of such a pore is shown in Figure 5.20 (b).

The fracture features for the NC-350 and KBI reaction sintered materials as described above were observed far away from the fracture originating flaws. These general features were common to most of the bend bars and, therefore, were independent of strength distribution. The more uniform fracture features, the flat transgranular fracture mode, and the smaller, more uniform porosity in NC-350 materials indicate that this material has sintered more completely than KBI material. For this reason NC-350 should exhibit less scatter in strength values and a higher mean strength value than that exhibited by the KBI material. The strength data in the Appendix and summarized in Figure 5.1 indicate that indeed such is the case.

The KBI reaction sintered Si_3N_4 exhibited no strength increase with temperature as did the NC-350 material by virtue of the proposed oxidative crack-tip blunting mechanism discussed above (refer to Figure 5.1). The conclusion to be deduced from this is that possibly the larger pores of the KBI material were not affected as much by the same oxidative exposure. Fractographic analysis of the high temperature KBI flexure bars is currently in progress.

Table 5.4 presents the Weibull modulus for the room temperature strength of all materials discussed to date. These data were

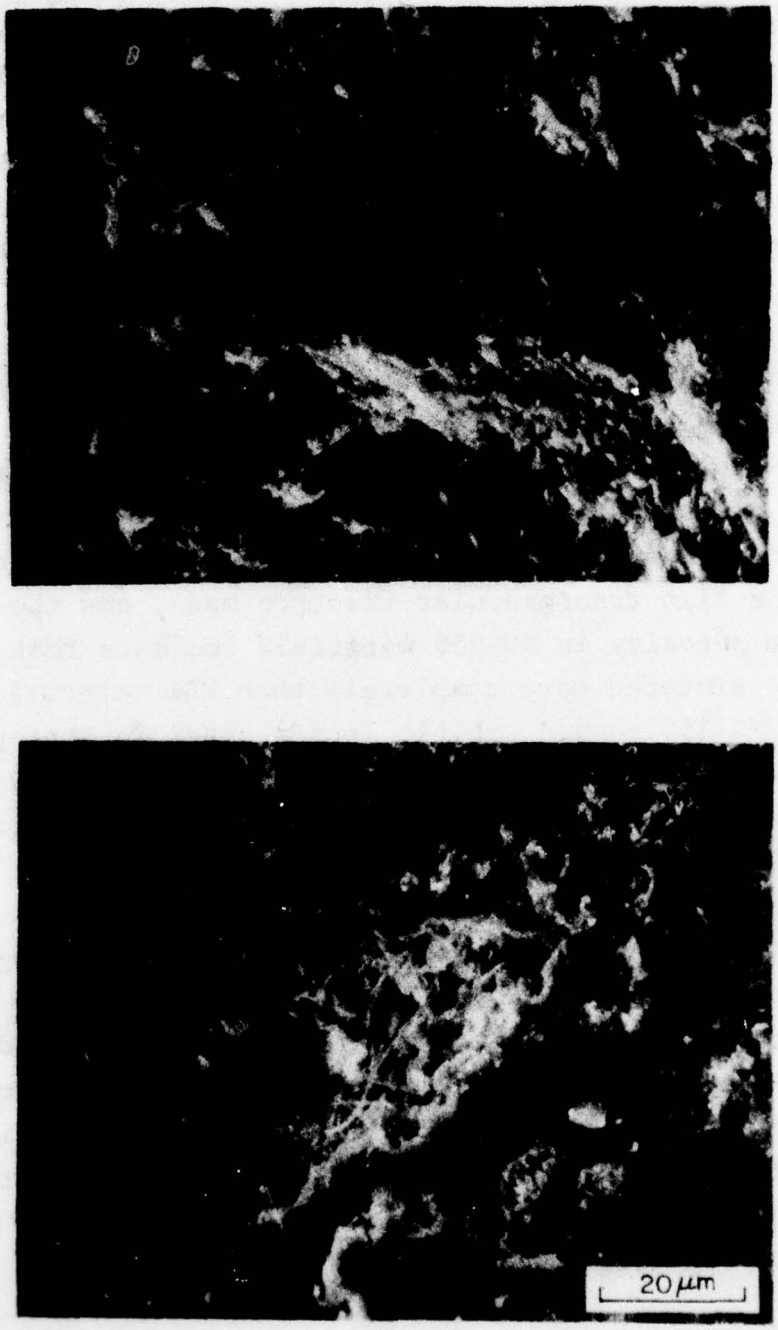

FIGURE 5.20 FRACTURE SURFACES SHOWING MICROSTRUCTURE OF KBI RS Si_3N_4. BEND BAR FRACTURED AT ROOM TEMPERATURE.

TABLE 5.4

WEIBULL MODULUS-FLEXURAL STRENGTH

MATERIAL/ TEMPERATURE °C	Batch 1	Batch 2	Batch 3	Batch 4	Combined
NC-132(HPSN)					
25	5.13	7.60	-	-	5.14
1200	11.58	17.21	-	-	11.61
1350	11.44	26.61	-	-	9.14
1500	8.26	30.63	-	-	10.29
NC-435(SiC)					
25	3.20	-	5.93	10.67	4.68
1200	6.22	-	16.41	13.55	6.28
1275	5.53	-	5.51	13.99	7.69
1350	5.38	-	7.40	19.73	7.87
NC-350(RBSN)					
25	3.35	3.34	4.65	-	3.67
1200	5.65	8.12	4.28	-	6.53
1350	7.52	11.12	5.23	-	7.79
1500	7.37	4.49	12.51	-	6.63
KBI (RBSN)					
25	3.51	3.89	3.52	-	4.01
1200	7.29	2.68	4.33		4.46
1350	2.51	3.16	2.12		2.97
1500	3.24	2.99	2.78		3.24

obtained on sample populations of ten using techniques described by Johnson and Prochazka[44]. Interpretation of these results for NC-132, NC-435, and NC-350 are contained in our last interim technical report[2]. However, it is interesting to compare results for the KBI material with NC-350, the other reaction sintered material. The Weibull modulus of NC-350 is shown to increase and remain relatively constant at elevated temperatures compared to room temperature. This reduction in data scatter at elevated temperatures is consistent with the concept of high temperature oxidative porosity modification discussed above for NC-350. The KBI reaction sintered material, however, exhibits a lower room temperature Weibull modulus (see Table 5.4) that remains relatively constant with increasing temperature. This is consistent with increased data scatter, lower strength, and temperature independent strength exhibited by the KBI material. The relative Weibull modulus of NC-350 and KBI reaction sintered materials agree with the fractographic interpretation of NC-350 as a more completely reaction sintered material.

Table 5.5 summarizes the four-point flexural results of Norton NC-132, NC-435, NC-350, and KBI reaction bonded Si_3N_4.

5.1.5 Kyocera Materials

Four-point flexure tests have been performed on limited numbers of three Kyocera materials: SN-3 hot pressed Si_3N_4, and two sintered silicon nitrides SN-201 and SN-205. These materials are being developed for high volume production of low temperature components, and were supplied by Kyocera International. Strength and modulus data are shown in Figures 5.21 and 5.22. Stress-strain data are provided in Figures 5.23 and 5.25. Figures 5.1 and 5.2 compare data with other materials in this program. Detailed impurity, microstructural, and fractographic analyses are not yet available for these materials.

TABLE 5.5 SUMMARY OF 4-POINT FLEXURE RESULTS*

TEMPERATURE °C	BATCH No.	NORTON NC-132 $HPSi_3N_4$			NORTON NC-350 $RBSi_3N_4$			BATCH No.	NORTON NC-435 Si/SiC			BATCH No.	KBI RB Si_3N_4		
		σ_f** (psi)	STD DEV***	E**** (10^6psi)	σ_f (psi)	STD DEV	E (10^6psi)		σ_f (psi)	STD DEV	E (10^6psi)		σ_f (psi)	STD DEV	E (10^6psi)
25	1	90,910	18,150	48.4	30,870	8150	25.5	1	50,460	13,210	53.9	1	23,270	5970	21.5
	2	115,210	14,210	45.7	23,530	6790	23.5	3	65,980	10,770	49.5	2	21,800	5340	21.1
	3	X	x	x	33,960	7155	27.7	4	55,150	5020	48.8	3	18,080	4650	20.0
1200	1	88,190	7440	42.8	59,970	8550	32.5	1	57,400	8520	46.4	1	20,500	2680	23.2
	2	79,240	4360	39.2	58,620	7030	23.1	3	79,660	4620	39.7	2	23,020	6880	32.5
	3	X	X	X	56,320	10,350	28.7	4	62,390	4430	43.4	3	22,040	4410	26.9
1275	1	X	X	X	X	X	X	1	57,820	10,180	40.6	1	X	X	X
	2	X	X	X	X	X	X	3	59,010	9890	39.1	2	X	X	X
	3	X	X	X	X	X	X	4	60,200	4130	42.8	3	X	X	X
1350	1	58,620	4900	30.8	54,480	7000	26.9	1	44,120	6890	36.1	1	27,350	6940	29.2
	2	48,800	770	22.7	62,130	5360	23.5	3	48,310	6120	35.0	2	24,030	8660	30.0
	3	X	X	X	57,140	8600	25.5	4	42,090	1940	37.7	3	20,190	5110	30.1
1500	1	27,770	2920	7.7	46,150	5850	23.7	1	X	X	X	1	24,190	6970	23.9
	2	25,210	790	6.5	45,430	9130	20.5	3	X	X	X	2	16,460	4130	23.0
	3	X	X	X	53,060	3950	28.8	4	X	X	X	3	18,760	4260	22.4

* All data represent averages of approximately 10 samples

** σ_f denotes fracture stress
*** STD DEV denotes strength standard deviation
**** E denotes secant modulus

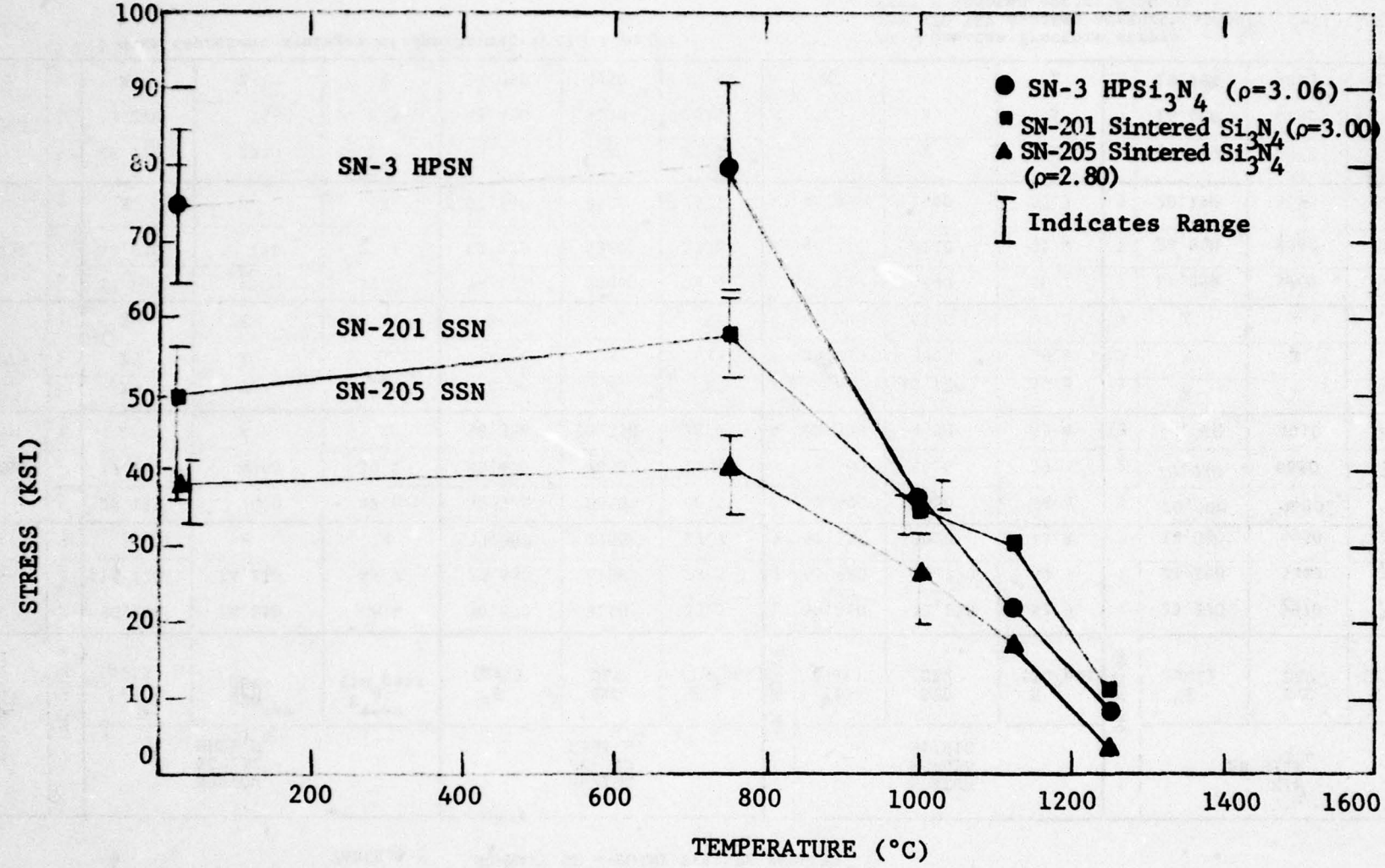

FIGURE 5.21 4-POINT FLEXURAL STRENGTH OF KYOCERA MATERIALS

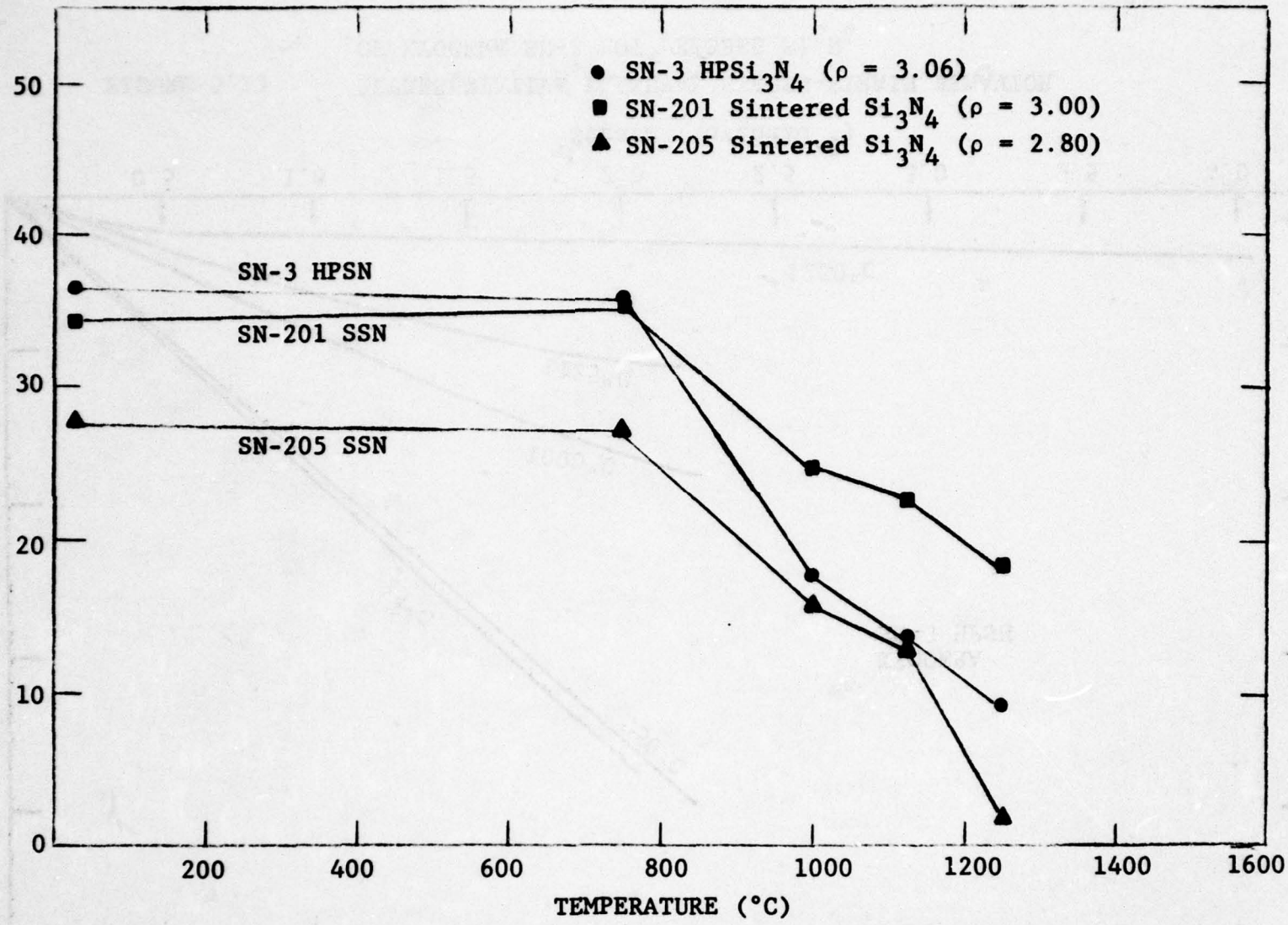

FIGURE 5.22 FLEXURAL SECANT MODULUS OF KYOCERA MATERIALS

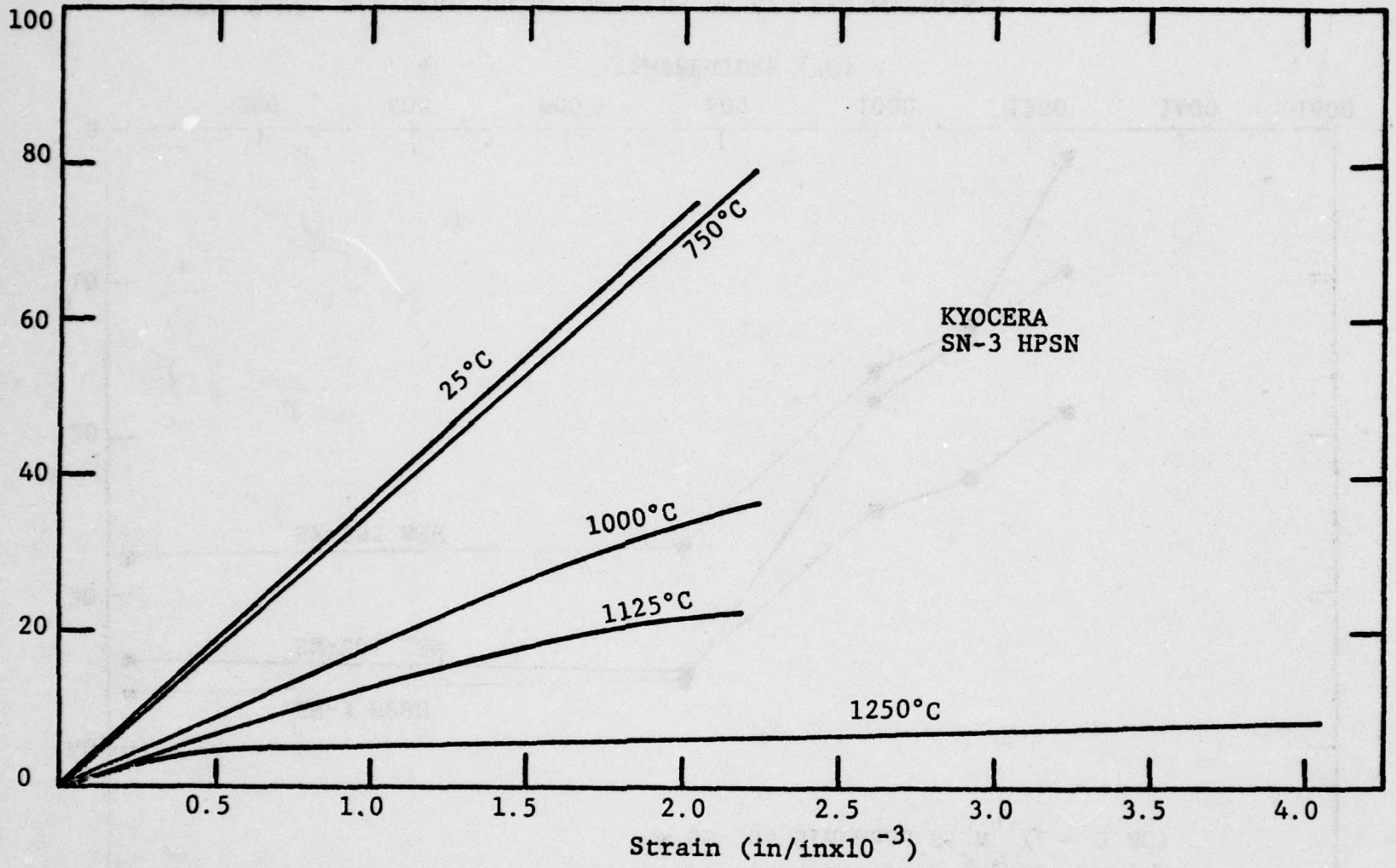

FIGURE 5.23 REPRESENTATIVE FLEXURAL STRESS-STRAIN BEHAVIOR OF KYOCERA SN-3 HOT PRESSED Si_3N_4

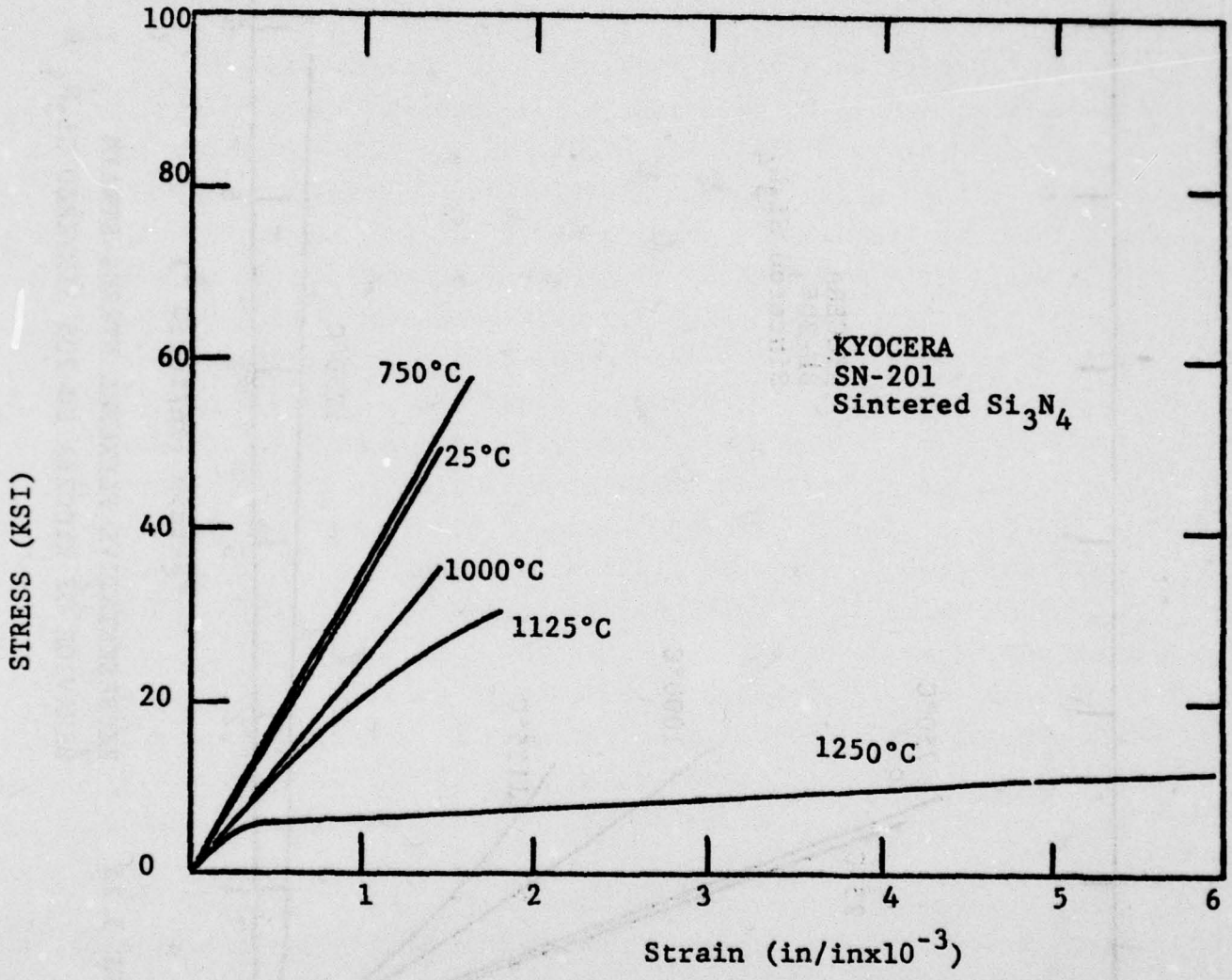

FIGURE 5.24 REPRESENTATIVE FLEXURAL STRESS-STRAIN BEHAVIOR OF KYOCERA SN-201 SINTERED Si_3N_4

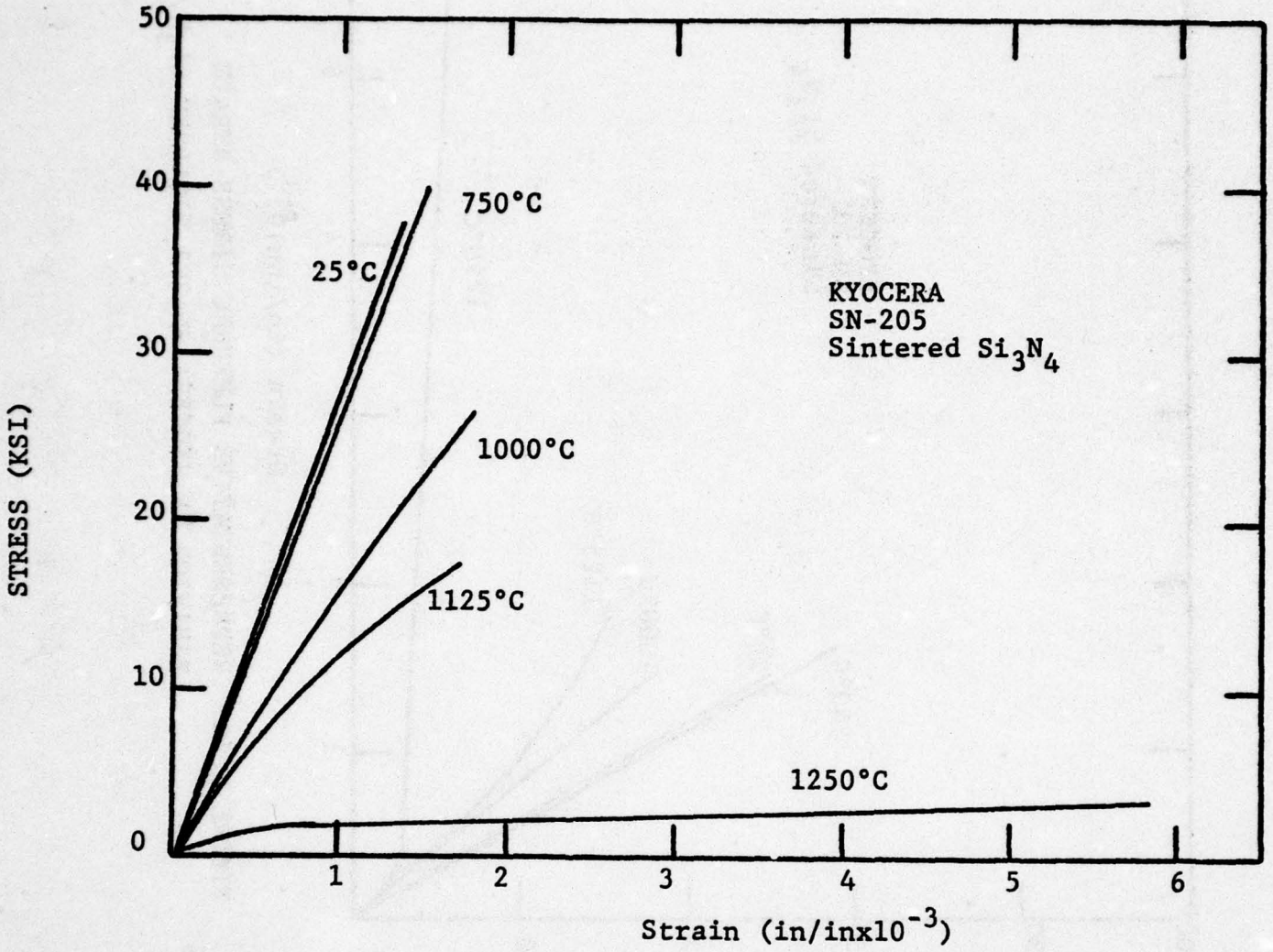

FIGURE 5.25 REPRESENTATIVE FLEXURAL STRESS-STRAIN BEHAVIOR OF KYOCERA SN-205 SINTERED Si_3N_4

Thus, interpretation of the property data is somewhat speculative at this point.

SN-3 hot pressed Si_3N_4 is seen to be significantly weaker at room temperature than NC-132 hot-pressed Si_3N_4. Additionally, the strength falls off at ~800°C for SN-3, whereas NC-132 retains good strength until ~1200°C. The elastic modulus data shown in Figure 5.2 and 5.22 exhibits similar trends. The lower density of the Kyocera material is perhaps the main cause of the low room temperature strength. It is believed that less pure precursor powders may have been used in hot pressing the Kyocera material. The type and amount of densification aid employed for the hot pressed SN-3 is unknown at present. However, the loss of high temperature properties at such a low temperature would imply a large impurity content in the hot pressed product. The stress-strain behavior of SN-3 hot-pressed Si_3N_4 (Figure 5.23) exhibits linear elastic behavior to failure only at 750°C and below, consistent with the strength and modulus data. The properties of SN-3 hot-pressed Si_3N_4 are consistent with the mechanisms of deformation discussed above for NC-132 (i.e., viscoelastic intergranular phase), but much more pronounced due to apparently higher oxide impurity.

Kyocera SN-201 and SN-205 are pressureless sintered Si_3N_4 materials. The room temperature strength and modulus of these conventionally sintered materials are higher than that of the Norton and KBI reaction bonded materials, probably due to their higher density (refer to Figures 5.1 and 5.2). SN-201 has slightly better properties than SN-205 since it has higher

density and much less open porosity. These sintered Kyocera materials also, like SN-3 hot pressed Si_3N_4, lose their room temperature strength and modulus at ~750°C. The loss of elastic stress-strain behavior above 750°C is shown in Figures 5.24 and 5.25. The reason for this sudden degradation of properties with temperature in SN-201 and SN-205 is that, unlike the reaction bonded silicon nitrides, oxide additions are made to enhance sintering[45]. Thus, a significant intergranular glassy phase would be expected. The resulting product would exhibit many of the behaviorial trends of hot-pressed silicon nitrides employing oxide densification aids.

Note that in general the strength of the Kyocera materials increases between 25° and 750°C. Referring to Figure 5.21, the reader is cautioned, however, that the trends referred to are averages of data sets that exhibit a wide spread of values. However, NC-132 HP Si_3N_4 does not exhibit this slight strength increase at T<1000°C. The difference may be due to greatly different oxidation rates resulting from differences in purity.

5.1.6 Sintered SiC Materials

Initial data are available on two sintered SiC materials that were supplied by the manufacturer: Carborundum α-SiC and General Electric boron-doped β-SiC. Initial characterization and description of these materials is contained in Section 4 of this report. Coppola and McMurtry[3] describe the development of the Carborundum material. The development of the General Electric material is described in a series of G.E. reports to the Navy by Prochazka et.al.[46]. The test plan for these materials was presented in Section 3 of this document. Detailed impurity, microstructural, and fractographic analyses are currently in progress.

Flexure testing has been performed in air at selected temperatures from room temperature to 1250°C. Strength and modulus data are plotted as a function of temperature in Figures 5.26 and 5.27. Behavior is compared with other materials in Figures 5.1 and 5.2. It is observed that the strength of both G.E. and Carborundum materials increased with temperature to 1250°C.

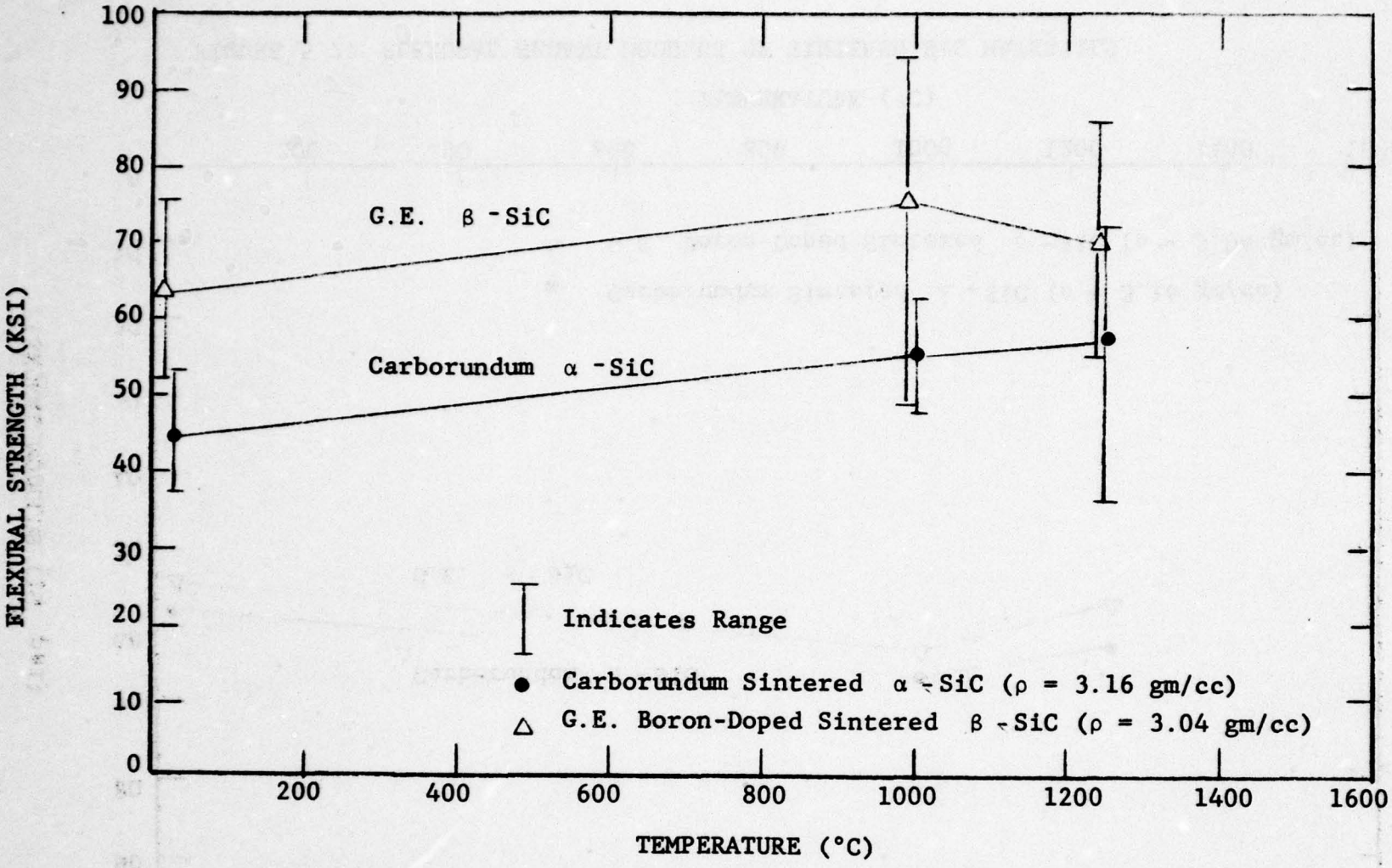

FIGURE 5.26 4-POINT FLEXURAL STRENGTH OF SINTERED SiC MATERIALS

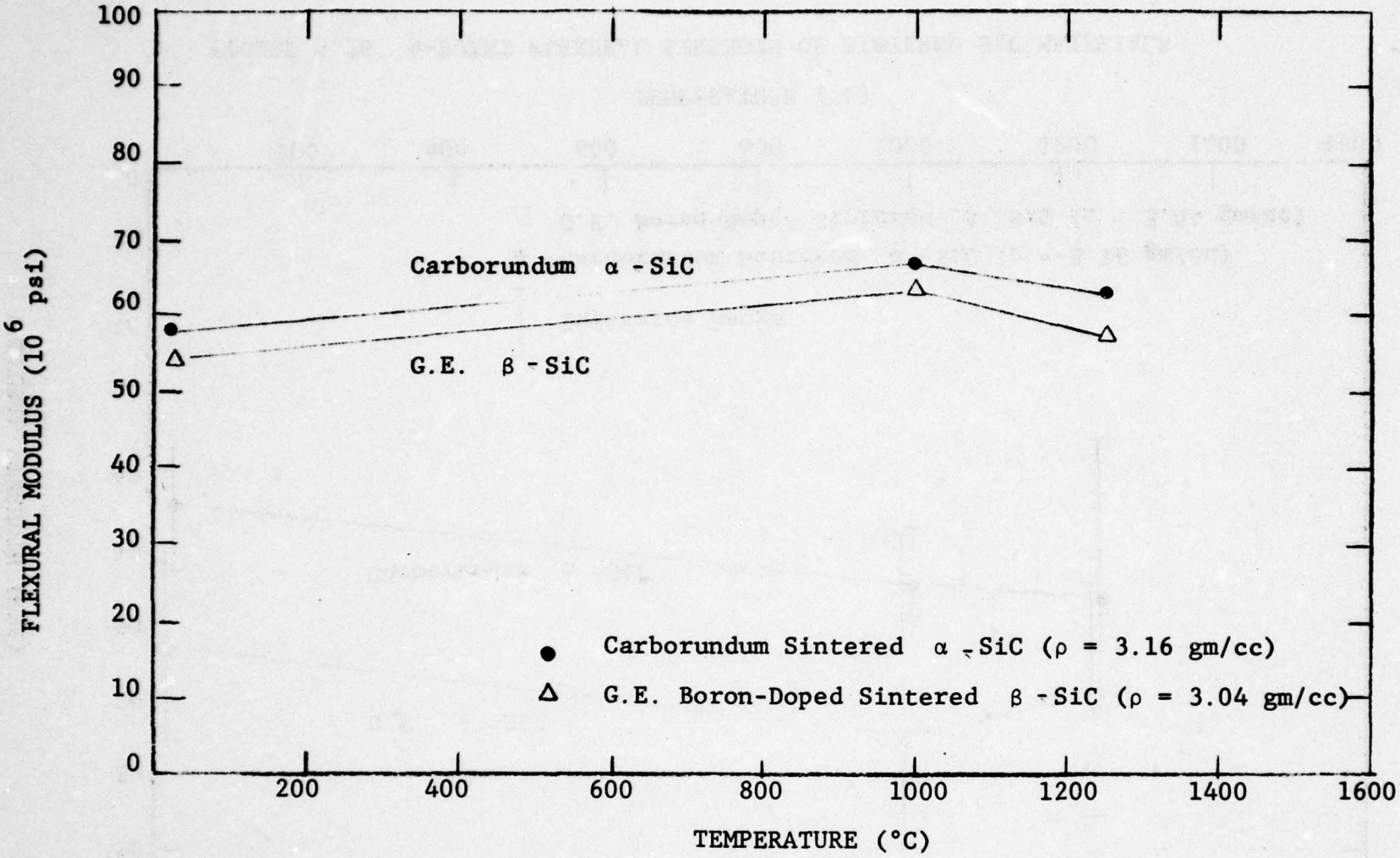

FIGURE 5.27 FLEXURAL SECANT MODULUS OF SINTERED SiC MATERIALS

Both materials exhibited linear elastic stress-strain behavior to failure at temperatures up to and including 1250°C, as illustrated in Figures 5.28 and 5.29. Both materials exhibit the high modulus typical of silicon carbide. However, as shown in Figure 5.27 the static modulus determined during flexure testing[1] is shown to increase slightly with temperature. This is unlike the behavior obtained by dynamic resonance methods for these two materials by Coblenz[47] and Kraft[48] where a slight linear decrease with temperature was observed. At room temperature the static IITRI data are ~2-10% lower than these dynamic modulus data. Room temperature data are currently being compared with AFML data on these same materials using the resonant sphere technique[50]. Preliminary data[51] indicate good agreement (within ~2%) with the IITRI static data at room temperature. No physical reason is known, however, for the modulus increasing slightly with temperature as determined by our present static data. There may be a small systematic error in the high temperature static measurement of such high modulus materials as observed by the trend of the Carborundum and G.E. data shown in Figure 5.27. We are currently preparing our own dynamic resonance system[49] to use on this program to investigate this discrepancy further.

Further interpretation will be made of the results for these sintered SiC materials when testing, characterization, and fractography are complete.

5.1.7 NRL Si_3N_2-ZrO_2 Materials

The U.S. Naval Research Laboratory is currently investigating the use of ZrO_2 additives for hot-pressed Si_3N_4 which both promote densification and form a more refractory silicate grain-boundary phase, thus improving high temperature strength and creep resistance[52,53]. R. W. Rice has supplied samples of various Si_3N_4-ZrO_2 compositions to our IITRI/AFML program. The test plan for these materials is con-

AD-A062 905 IIT RESEARCH INST CHICAGO ILL F/G 11/2
PROPERTY SCREENING AND EVALUATION OF CERAMIC VANE MATERIALS.(U)
OCT 77 D C LARSEN, G C WALTHER F33615-75-C-5196
UNCLASSIFIED IITRI-D6114-ITR-24 NL

2 OF 4
ADA
062905

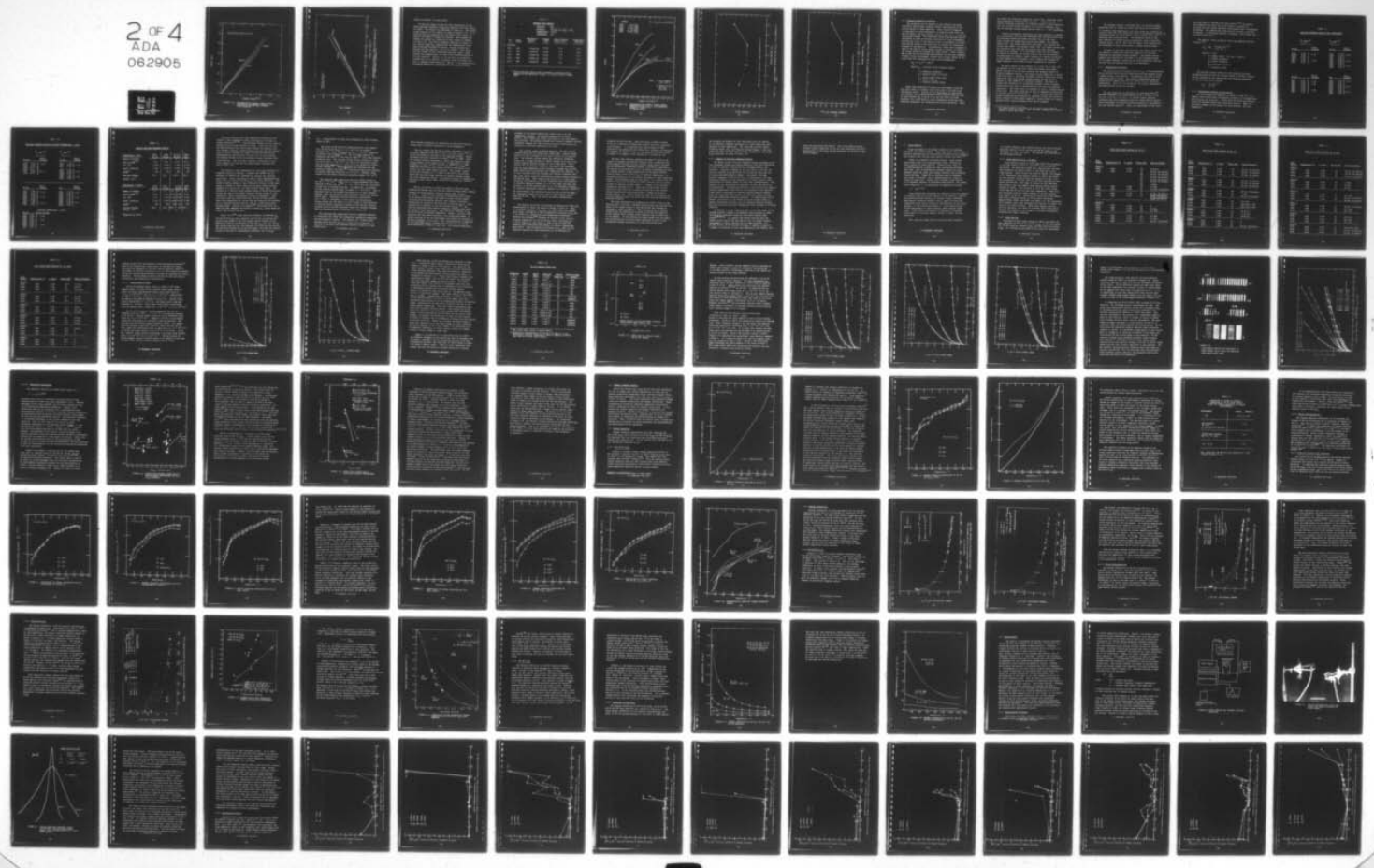

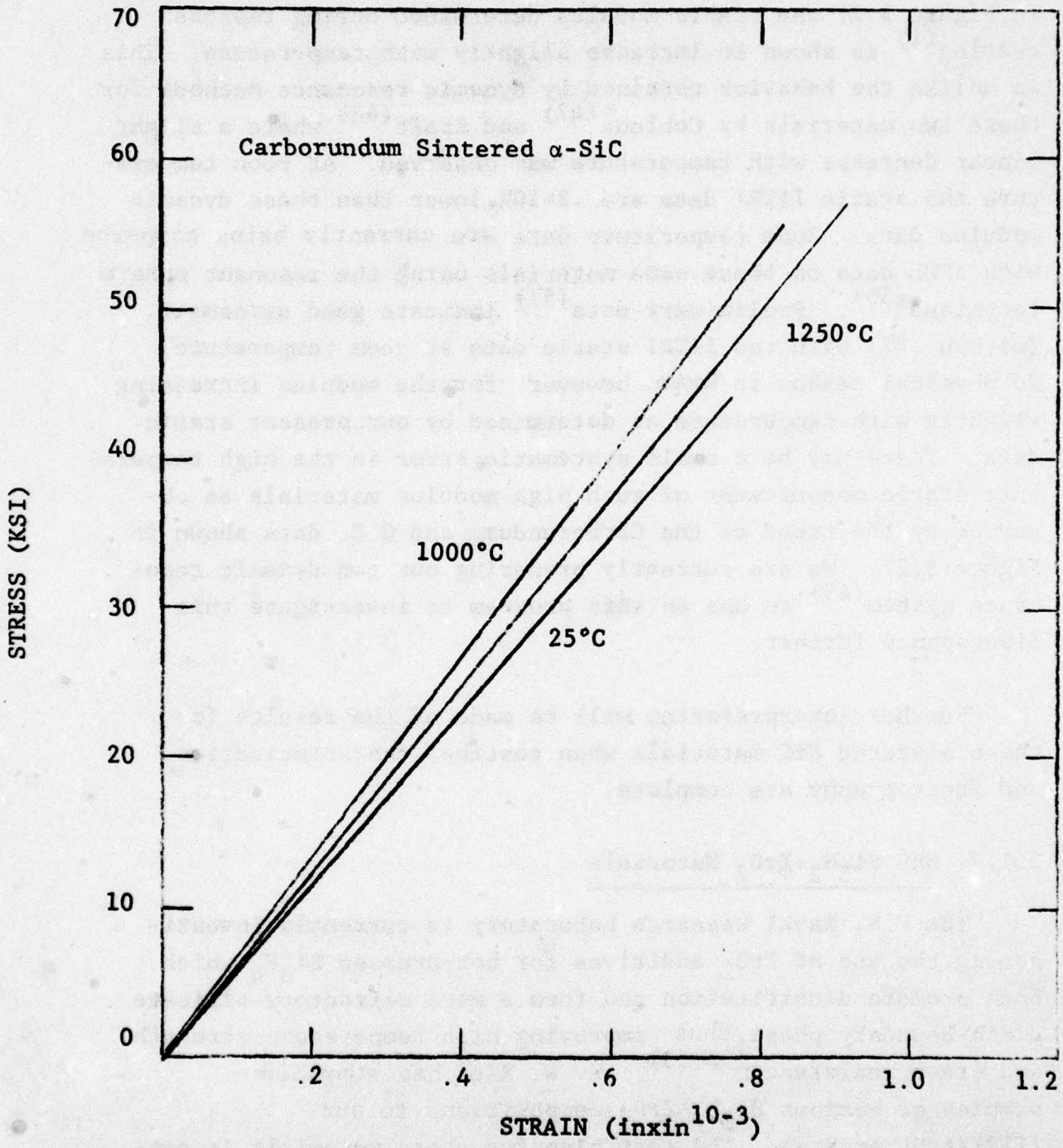

FIGURE 5.28 REPRESENTATIVE FLEXURAL STRESS-STRAIN BEHAVIOR OF CARBORUNDUM SINTERED α-SiC MATERIAL

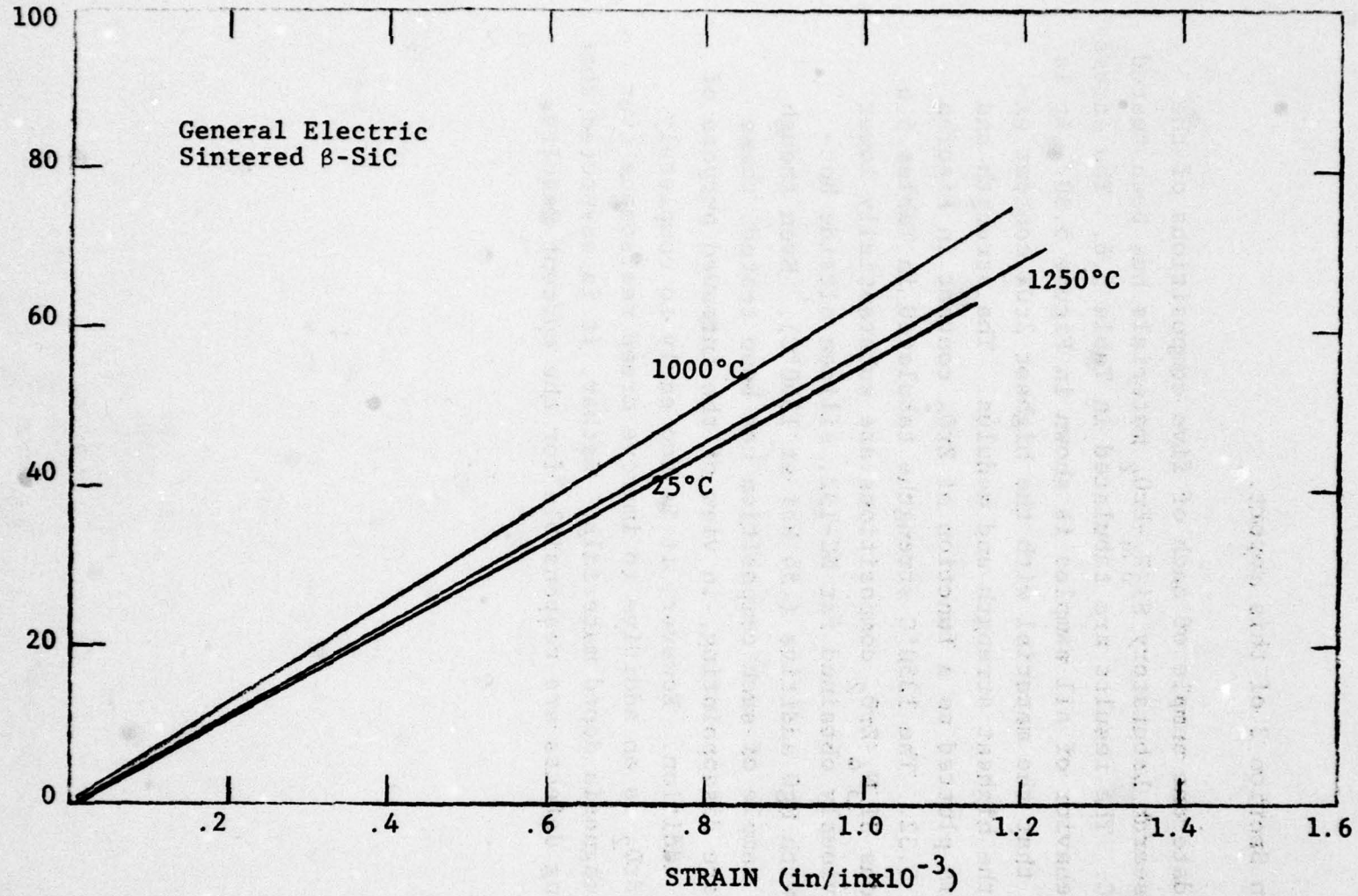

FIGURE 5.29 REPRESENTATIVE FLEXURAL STRESS STRAIN BEHAVIOR OF G.E. BORON-DOPED SINTERED β-SiC

tained in Section 3 of this report.

To date one sample of each of five compositions of the Naval Research Laboratory Si_3N_4-ZrO_2 materials has been tested at 1350°C. The results are tabulated in Table 5.6. The stress-strain behavior of all samples is shown in Figure 5.30. It is observed that the material with the highest ZrO_2 content exhibited the highest strength and modulus. The strength and modulus is plotted as a function of ZrO_2 content in Figures 5.31 and 5.32. The 1350°C strengths tabulated in Tables 5.6 for various Si_3N_4-ZrO_2 compositions are substantially lower than previously obtained for NC-132, silicon nitride hot-pressed with MgO additive (~54 ksi at 1350°C). Even though only one sample of each composition has been tested, these results are disappointing, in view of the intended purpose of the ZrO_2 addition. However, it is too early to completely condemn ZrO_2 as an additive to improve creep resistance over that of magnesia doped materials. Rather, it is suspected that processing defects are responsible for the current results.

TABLE 5.6

FLEXURAL TEST RESULTS

SUPPLIER: NRL
MATERIAL: Various HP Si_3N_4 + ZrO_2
TEMPERATURE: 1350°C
ATMOSPHERE: Air

W/O Si_3N_4/ZrO_2	Sample	Bulk Density * (gm/cc)	Strength (psi)	Strain-To-Failure (in/in x 10^{-3})	Secant Modulus (10^{+6} psi)
96/4	R1F1	3.105(95.3%)	52,010	1.62	34.4
92/8	R2F1	3.360(101%)	36,560	2.38	32.3
92/8	R3F1	3.291(99.2%)	41,530	1.90	31.3
88/12	R4F1	3.097(91.7%)	36,940	1.55	33.1
84/16	R5F1	3.401(98.8%)	63,760	1.51	54.2

* Percent theoretical density shown in parentheses; theoretical density computed for each composition, (ρSi_3N_4 = 3.2; ρZrO_2 = 5.73) on a volume basis.

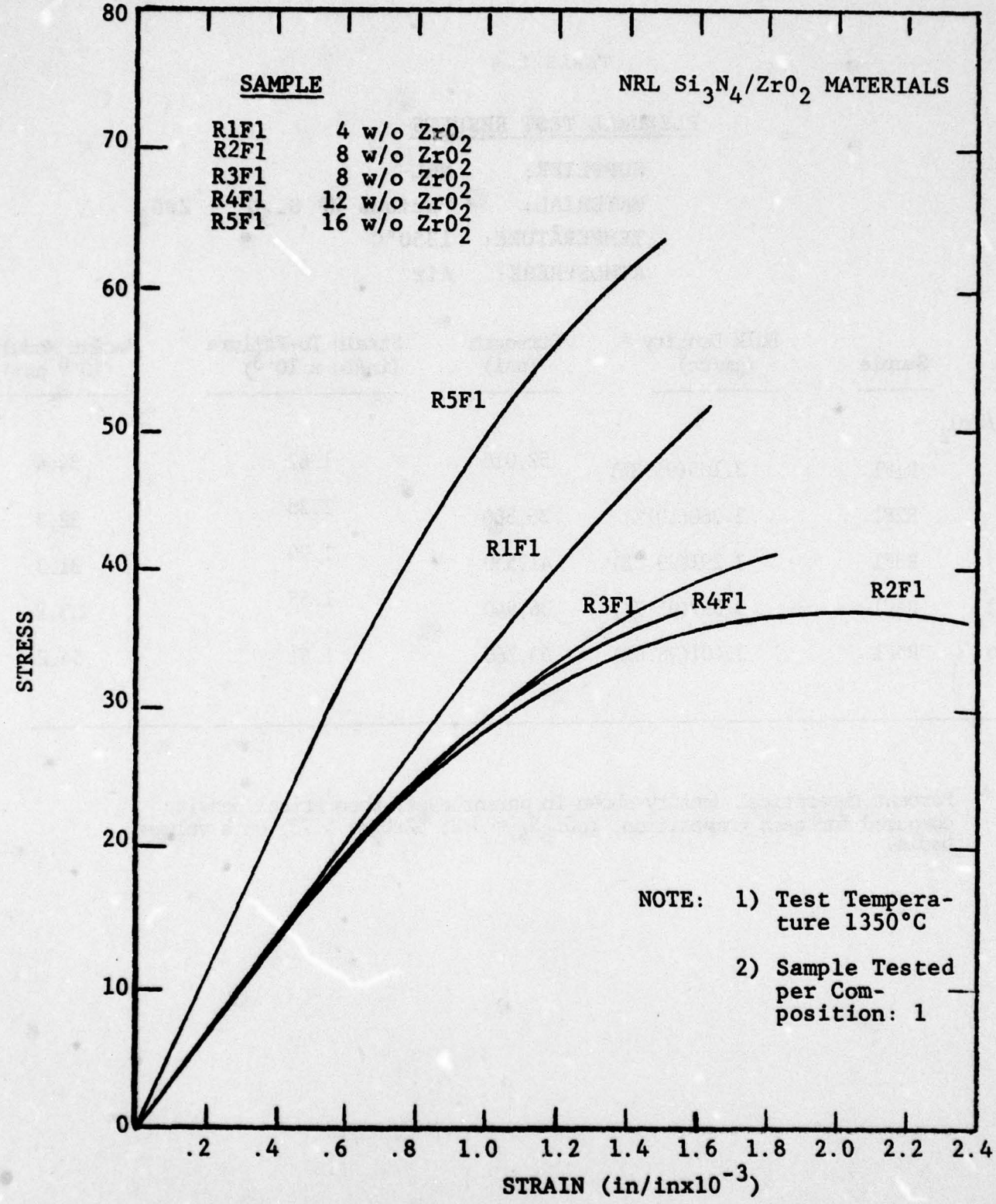

FIGURE 5.30 REPRESENTATIVE FLEXURAL STRESS-STRAIN BEHAVIOR OF NRL Si_3N_4 + ZrO_2 MATERIALS TESTED AT 1350°C (1 Sample Each)

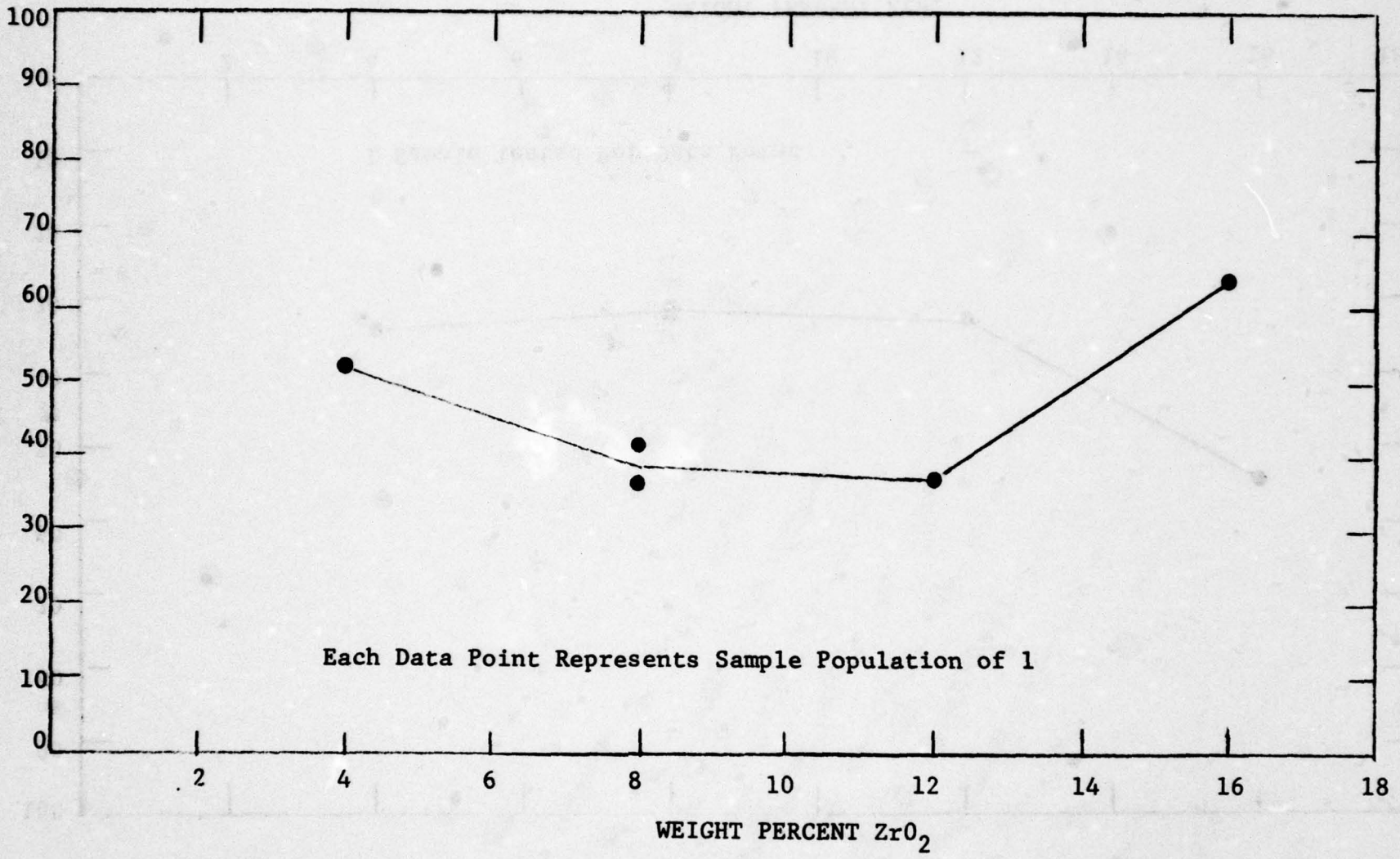

FIGURE 5.31 4-POINT FLEXURAL STRENGTH OF NRL Si_3N_4 + ZrO_2 MATERIALS AT 1350°C

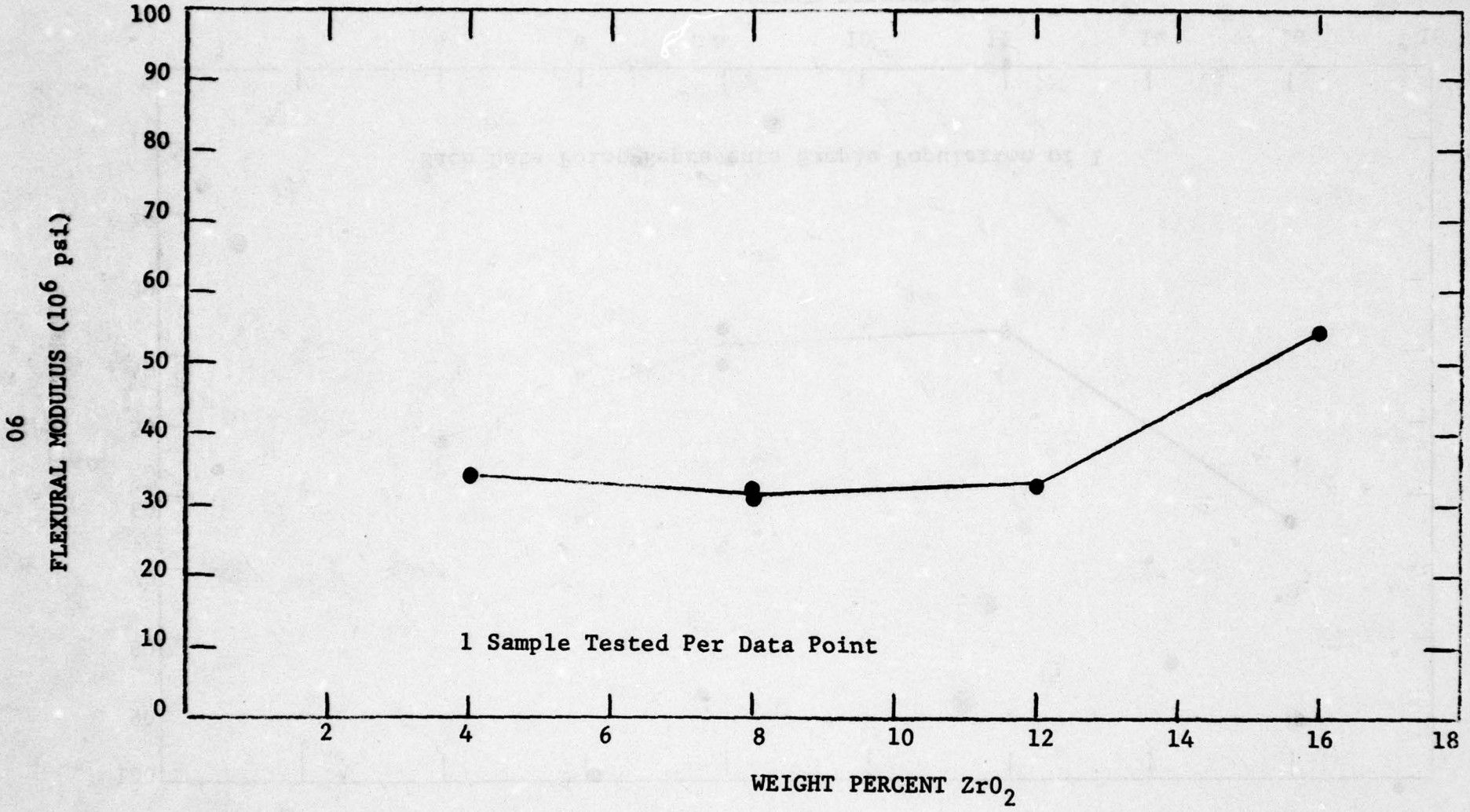

FIGURE 5.32 FLEXURAL SECANT MODULUS OF NRL Si_3N_4 + ZrO_2 MATERIALS AT 1350°C

5.2 Fracture Toughness Parameters

The potential use of ceramics in gas turbines and other structural applications requires careful consideration of the brittle nature of these materials. Their fracture toughness or resistance to crack propagation is generally much lower than that of metals, and when failure occurs it does so in a rapid and catastrophic manner. The conditions controlling fracture may be considered in terms of fracture initiation or crack propagation. Fracture may occur if the applied stress is increased or intensified locally around a flaw such that it exceeds the theoretical strength of the material. Alternatively, cracks will propagate as long as the rate of strain energy release is greater or equal to the energy needed for forming new crack surface. These concepts may be seen in the following relationships for fracture toughness in mode I crack displacement (wherin only stresses normal to the crack plane are considered to cause crack propagation):

$$K_{I_C} = Y \sigma_f a^{\frac{1}{2}} = (2E\gamma)^{\frac{1}{2}}$$

where K_{I_C} = critical stress intensity factor

Y = geometric parameter

σ_f = applied stress at failure

a = crack length (flaw size)

E = Young's modulus

γ = fracture surface energy

Under some conditions of stress and environment cracks may also grow slowly in ceramics until they reach a critical size and failure occurs. Because of this phenomenon of subcritical crack growth, the relation between stress intensity and the rate of crack advance (K_I vs da/dt or v) and the level of stress intensity (K_o) below which no crack propagation occurs are also important parameters for designing with brittle materials. These

are useful for predicting potential service life, especially under cyclic mechanical and/or thermal stresses. However, in the current screening evaluation of candidate ceramic turbine materials, only the critical stress intensity (or fracture toughness), K_{IC}, and the fracture surface energy derived from it, γ, were determined.

Several experimental techniques have been developed to measure these parameters, but each has advantages and limitations such that no particular method has found universal favor at this time. These include the single edge notched beam (SENB), the compact tension (CT), the double cantilever beam (DCB), the tapered cantilever beam (TCB), the constant moment (CM), the double torsion (DT), the controlled flaw (CF) and the natural flaw (NF) specimen geometries or methods. It is desireable that the test simulate as closely as possible the stress state at the tip of naturally occuring flaws in ceramics, permit testing in a variety of hostile or high temperature environments, have a simple and inexpensive sample geometry, and provide as much information as possible.

The exact nature of the stresses at a crack tip or flaw, and the geometry of the crack front before and during crack propagation continue to be the most nebulous and ambigous feature of fracture toughness testing. The double torsion sample has a curved crack front that is receiving increased critical attention as being invalid for slow crack growth studies because it may not be a constant K_I test geometry as originally thought.* The shape of natural and controlled (or artifically induced) flaws is usually semielliptical but must be established by post-test fractographic examination. The other tests are presumed to have a straight-through crack front. The exact shape may in fact be dependent on machining or fatigue-generated flaw geometry. Various opinions have been expressed concerning the necessity of creating a sharp crack front by cyclic fatigue or other means compared to results based on a simple machined notch, where machining flaws may be adequate.

---

* The double torsion crack front is also quite large compared to actual flaws in ceramics, thus removing inhomogeneity-related effects from DT test data.

The constant tension, cantilever beam, and constant moment geometries must be loaded in tension and hence are not amenable to testing at high temperature (the other tests are conducted in bending). Tests in high temperature hostile environments usually preclude monitoring the crack advance during testing, as is required by the CT and DCB tests. The advancing crack is also more difficult to follow in porous materials, such as reaction sintered Si_3N_4. The CT, DCB, and TCB samples also require careful machining of their notch and/or a complex tapered shape.

In light of the above considerations the double torsion and the natural or controlled flaw tests appear to be the most promising for potential turbine ceramics. The double torsion geometry was selected for the Phase I of this program because of its simple geometry, capability for high temperature testing, and that only the applied load had to be monitored.

5.2.1 Experimental Procedure

The critical stress intensity factor, K_{I_C}, of the as-machined NC-132, NC-435, NC-350 and KBI RSSN materials was measured using a double torsion test geometry. Measurements were made at room temperature and at 1350°C. The elevated temperature tests for several NC-435 samples were made at 1410°C due to a defective thermocouple. When this was recognized the correct temperature was measured with an optical pyrometer.

The test apparatus was described in a previous report[2]. Specimen dimensions were approximately 64 mm x 25 mm x 2.5 mm (2.5 in. x 1.0 in. x 0.1 in.). To achieve proper fracture initiation and crack propagation down the sample groove necessitated development of the final machined geometry as discussed in the last interim report[2]. Since the environment of the crack

has been shown to influence the test results,[54] the samples were washed in hot water for 15-20 minutes to remove the grinding aid used during machining (the manufacturer's recommended procedure). All samples were then dried in an oven at 80°C for 15 minutes. A cross-head speed of 0.5 mm/min. (0.02 in/min) was utilized during tests.

The critical stress intensity factor was computed from the relation:[55]

$$K_{I_C} = PW_m \left[\frac{3\ (1 + \nu)}{W\ t^3\ d_n}\right]^{1/2}$$

where P = Load

W = sample width = 25.4 mm = 1.000 in.

t = sample thickness

d_n = Groove thickness

W_m = 9.525 mm = 0.375 in.

ν = Poisson's ratio

The fracture surface energy for each material was also determined using the data for average values of flexural modulus and K_{I_C} obtained in this program and the following expression for K_{I_C} in plane-strain bending:

$$K_{I_C} = \left[\frac{2\ \gamma\ E}{1 - \nu^2}\right]^{1/2}$$

5.2.2 Experimental Results and Discussion

The test results are tabulated in Tables 5.7 and 5.8. All samples tested experienced catastrophic failure at all temperatures once fracture was initiated. Tests where the crack path did not follow the machined groove were considered invalid. Table 5.9 provides a summary of the results for each material and test temperature.

TABLE 5.7

FRACTURE TOUGHNESS RESULTS ROOM TEMPERATURE

NC-132	K_{I_C} $MNm^{-3/2}$	Batch Average
11T9	6.55	4.48
11T10	4.34	
11T11	5.54	
12T1	4.18	5.04
12T3	5.44	
12T4	5.50	

NC-435	K_{I_C} $MNm^{-3/2}$	Batch Average
41T1	3.72	3.93
41T2	4.14	
41T3	3.94	
43T1	3.61	3.92
43T2	4.58	
43T3	3.56	
44T1	3.74	3.40
44T3	3.36	
44T4	3.11	

NC-350		Batch Average
31T1	1.63	1.88
31T3	2.12	
32T1	2.25	2.16
32T2	2.28	
32T3	1.94	
33T1	2.31	2.08
33T2	1.91	
33T3	2.02	

KBI		Batch Average
K1T1	2.17	2.35
K1T2	2.41	
K1T3	2.47	
K2T1	2.03	2.08
K2T2	2.04	
K2T3	2.17	
K3T1	2.29	2.21
K3T2	2.19	
K3T3	2.15	

TABLE 5.8

FRACTURE TOUGHNESS RESULTS ELEVATED TEMPERATURE: 1350°C

NC-132	K_{IC} MNm$^{-3/2}$	Batch Average
11T6	8.41	8.55
11T7	9.02	
11T8	8.22	
12T5	10.2	10.4
12T6	11.3	
12T7	9.66	
12T8	10.5	

NC-435	K_{IC} MNm$^{-3/2}$	Batch Average
41T4	7.76	7.30
41T7	6.97	
41T8	7.16	
43T8	6.16	7.20
43T9	9.66	
43T10	5.54	
44T8	7.42	6.30
44T9	6.86	
44T10	4.63	

NC-350		Batch Average
31T4	3.44	3.10
31T6	2.03	
31T7	3.83	
32T4	3.18	2.73
32T6	1.78	
32T7	3.23	
33T4	2.98	2.54
33T5	1.67	
33T6	2.97	

KBI		Batch Average
K1T4	1.92	2.16
K1T5	2.33	
K1T6	2.22	
K2T4	2.17	2.22
K2T5	2.17	
K2T6	2.32	
K3T4	2.52	2.41
K3T5	2.22	
K3T6	2.49	

ELEVATED TEMPERATURE: 1410°C

NC-435		Batch Average
41T5	2.98	2.83
41T6	2.67	
43T4	1.22	1.61
43T5	1.65	
43T6	1.97	
44T5	2.14	1.95
44T6	1.87	
44T7	1.83	

TABLE 5.9

AVERAGE FRACTURE TOUGHNESS RESULTS

Temperature = 20°C	HPSN NC-132	RSSN NC-350	Si/SiC NC-435	RSSN KBI
Number of Samples	6	8	9	9
Mean K_{IC}, $MNm^{-3/2}$	5.25	2.06	3.75	2.21
Std. Dev.	0.968	0.224	0.408	0.150
Coeff. Variation	0.186	0.109	0.109	0.068
E, GNm^{-2}	324	176	349	144
Fracture Surface Energy γ Jm^{-2}	37.1	11.3	19.3	15.8

Temperature = 1350°C	HPSN NC-132	RSSN NC-350	Si/SiC NC-435		RSSN KBI
Number of Samples	6	9	9	8	9
Mean K_{IC}, $MNm^{-3/2}$	9.46	2.79	6.91	2.40*	2.26
Std. Dev.	1.17	0.772	1.43	0.560	0.182
Coeff. Variation	0.123	0.277	0.207	0.233	0.080
E, GNm^{-2}	184	195	254	254	207
Fracture Surface Energy γ Jm^{-2}	233.5	19.2	88.6	10.9	12.7

*measured at 1410°C

The data obtained from room temperature testing are comparable to data obtained by other investigators for these or similar materials[56-64]. The agreement between the two reaction bonded silicon nitride materials is good. Also note that the KBI RSSN exhibited very little data scatter (in contrast with flex strength results), which supports the fact that the induced flaw in the DT technique is larger than the process-related inhomogeneities and intrinsic critical flaw in this material. The standard deviation for all materials tested increased with increasing K_{I_C}. The relatively constant coefficient of variation suggests the test was not significantly influenced by failure load level.

The results at room temperature for the Si_3N_4 materials are primarily related to density. Strength and modulus are proportional to density and influence K_{I_C} through the relations given above. Flaws consisting of pores or pore agglomerates are larger than the typical flaw found in the denser materials. The fracture surface energy is also affected by density in that more energy is needed to create crack area through a dense material compared to a porous one, all other factors being equal. The presence of a distinct grain boundary phase in NC-132 should also account for some of its higher fracture surface energy at room temperature, where intergranular fracture predominates. Thus, the porous reaction bonded materials, NC-350 and KBI, exhibit lower room temperature K_{I_C} values than the denser NC-132 material due to increased porosity and the lack of a significant grain boundary phase. Claussen and Lahmann[64] fabricated their own HPSN using MgO additions and obtained similar K_{I_C} values using the single edge notched beam test.

Wills, et.al[59] state that the difference in measured K_{I_C} for NC-350 RS Si_3N_4 and a material like NC-435 siliconized SiC would be due mainly to the much higher elastic modulus of SiC. Additional factors contributing to the high K_{I_C} and γ for NC-435 may include high density, the presence of silicon and the elastic discontinuity between the Si and SiC phases, and that the fracture process in SiC may be intrinsically different than in Si_3N_4

(i.e., intergranular in Si_3N_4 and transgranular along cleavage planes in SiC).

The value of the fracture surface energy at room temperature for NC-132 HP Si_3N_4 (γ = 37.1 Jm^{-2}) is in excellent agreement with values for Norton HS-130 (γ = 39 Jm^{-2}) reported by Petrovic and Jacobson[60,61], who cite work reported by Wiederhorn and Evans[62] and also by Lange[63] from other fracture mechanics tests. The fracture surface energy obtained at IITRI for NC-435 SiC (γ = 19.3 Jm^{-2}) at 25°C is in qualitative agreement with data reported (γ = 16.35 Jm^{-2}) for NC-203 hot pressed silicon carbide[58]. Better agreement was obtained with the results of Coppola and Bradt[66] using the notched beam technique on another reaction bonded SiC (γ = 19 Jm^{-2}). However, their results for the double cantilever beam were higher (30.7 Jm^{-2}).

The computed room temperature fracture surface energy of NC-350 (γ = 11.3 Jm^{-2}, Table 5.9) is in good agreement with data reported by Wills, et. al[59] (γ = 10.2 Jm^{-2}) from the controlled surface flaw in bending technique. By comparison, the results for KBI reaction bonded Si_3N_4 are higher (γ = 15.8 Jm^{-2}). This is apparently due to the inverse contribution of a lower flexural modulus, since the critical stress intensity factors are approximately equal. Subsequent fracture mechanics calculations will attempt to determine if this higher room temperature surface energy for KBI RSSN is at all related to the difference in fracture surface appearance between NC-350 and KBI reaction sintered silicon nitride materials tested for flexural strength that was discussed above in Sections 5.1.3 and 5.1.4.

The observed high temperature fracture toughness behavior is consistent with other high temperature mechanical properties and fractographic evidence. The presence of a viscous grain boundary phase and the healing of flaws during oxidation, in addition to porosity, may influence material behavior at high temperatures.

These provide mechanisms for absorption of additional fracture energy and so increase resistance to crack propagation.

The K_{I_C} results for NC-132 at 1350°C (see Table 5.9) are in excellent agreement with the CF work of Petrovic et.al.[61] on HS-130 and showed an increase of 82% over 25°C values. Similar increases have been observed by others[62,63] for HPSN. Since the flexural modulus decreased at 1350°C and fracture surface energy depends on the square of K_{I_C}, a large value of γ was obtained (γ = 233.5 Jm^{-2}). Petrovic et al[61] and Lange[65] suggested subcritical crack growth occurs in HPSN which could account for this large energy increase. The viscous nature of the grain boundary at T > 1200°C in NC-132 is the primary reason for the very large increase in fracture surface energy over room temperature values. Considerable energy is expended and absorbed in the viscous layer during the intergranular fracture process.

The K_{I_C} for NC-350 at 1350°C increased by 35% over room temperature averages and the fracture surface energy almost doubled. Strength and fractographic evidence suggest some oxidation of pores occurs in this material at temperature when tested in air which would explain the higher fracture surface energy calculated for this porous material (the concept of porosity modification by oxidation was discussed in Section 5.1.3). These results are in contrast to the work of Wills et al.[59], who used the controlled flaw fracture toughness technique and tested in vacuum at high temperature. They reported a decrease in K_{I_C} for NC-350 with increasing temperature. However, our work would indicate that this result was due to the vacuum environment, or rather the lack of the air environment that caused the increase in fracture toughness in our tests. This interpretation is supported by the IITRI/AFML static strength data in both air and vacuum shown previously in Table 5.3 and 5.2B. The elevated temperature

strength of air-tested samples was almost double the room temperature strength. At elevated temperature in vacuum, however, the strength was almost equivalent to the room temperature strength. The present strength and fracture toughness results, therefore, support the idea of microstructural modification by oxidation in elevated temperature air tests.

The critical stress intensity factor K_{I_C} for KBI reaction sintered Si_3N_4 did not change with temperature. Similar values (Table 5.9) were obtained at 25°C and at 1350°C in air environment. The fracture surface energy was similarily unaffected except for a slight decrease at 1350°C thought to be due to the modest flexural modulus increase at this temperature. These results for the fracture toughness (K_{I_C} and γ) are consistent with the high temperature static flexural strength data for KBI RSSN, where very little change with temperature was observed. It is thus concluded from the strength and fracture toughness data, that very little structure modification occurred during oxidation in the KBI RS Si_3N_4. This could be due either to 1) a much lower oxidation rate compared to NC-350 (oxidation rate very sensitive to specific impurity content) or to 2) the larger and more open porosity in the KBI material that is not as profoundly affected by elevated temperature oxidative exposure as in NC-350. Graham[41] has found however that oxidation rates for KBI and NC-350 RSSN's are comparable (rates very low, rate for KBI slightly greater than for NC-350). Thus, the latter hypothesis appears more plausible.

The results for NC-435 siliconized SiC measured at 1350°C and inadvertantly at 1410°C are shown in Tables 5.8 and 5.9. There is an initial increase in K_{I_C} and γ at 1350°C over room temperature values, followed by a rapid degradation (decrease in K_{I_C} and γ) at 1410°C to a level below room temperature performance. Petrovic and Jacobson[58] obtained an increase in K_{I_C} with increasing temperature for NC-203 HP SiC (with 4 wt% Al_2O_3 and 4 wt% W) similar to that found at IITRI on NC-435 when they annealed their controlled flaw samples at various temperatures above 600°C. They attributed the increase in K_{I_C} that was subsequently measured at room temperature to the influence of

oxidation on flaw healing. They also found a modest increase in K_{I_C} as a function of temperature without the prior annealing heat treatment. It is possible that some healing of flaws occurred in the present NC-435 Si/SiC also, although the decreases in strength and modulus found for this material at 1350°C (refer to Figure 5.1) suggest it was limited if it occurred at all.

The fact that fracture toughness increased in spite of decreases in strength and modulus indicates that a mechanism that could markedly increase fracture surface energy and/or increase plastic deformation (absorbing energy) is primarily responsible. The silicon in the structure could be solely responsible for this in a manner similar to the contribution of the grain boundary impurity phase in NC-132 HP Si_3N_3 at elevated temperature, i.e., increasing plasticity of the silicon-rich phase at high temperature. However, the mechanism might be more subtle. For instance the increase in K_{I_C} of NC-435 Si/SiC at 1350°C could be due to a large increase in fracture surface energy, γ, caused by the elevated temperature exposure in air. There may be some change in composition at the crack tip or along the crack path that permits energy absorbtion by slow crack growth, a change in fracture surface energy, etc. Such a mechanism might be the formation of silicide compounds along the crack path with elevated temperature oxidative exposure.

The rapid degradation of properties at 1410°C, which is the melting point of silicon, probably occurs because the silicon-rich phase can no longer support a load and offers only minimum resistance to crack propagation. This interpretation is further supported by the observation of beads of silicon-rich material on the samples after testing (total exposure time at 1410°C was 15-30 minutes). As the silicon-rich phase exudes from the sample the microstructure of the SiC phase remaining to resist crack propagation becomes equivalent to a much more porous body.

The strength and modulus of this equivalent body are lowered so the fracture toughness decreases to a value lower than that measured at room temperature. The resulting critical stress intensity factor, K_{I_C}, and fracture surface energy, γ, for the porous SiC body are very close to those obtained for the porous Si_3N_4 materials (as shown in Table 5.9).

5.2.3 Summary of Fracture Toughness Results

The double torsion fracture toughness results obtained on the four candidate ceramic gas turbine materials have been interpreted in terms of porosity, microstructure, secondary phases, and oxidation. Fracture toughness at 25° and 1350°C is low for the reaction sintered Si_3N_4 materials due to high porosity and lack of energy absorbing impurity phases. Conversely, the high fracture toughness of NC-132 HP Si_3N_4 is attributed to its near theoretical density and the presence of a viscous impurity phase concentrated in regions along the crack path (intergranular). The behavior of the siliconized SiC material, NC-435, may not be as straightforward. Increasing plasticity to the silicon-rich phase at elevated temperature could lead to the increases in K_{IC} observed. A more subtle interpretation involves chemo-mechanical effects along the crack path that increase the fracture surface energy with high temperature oxidative exposure. At temperatures $\geq$1410°C however, the silicon in the Si/SiC structure becomes unable to support significant stresses, and the composite material behaves much like a porous body with accompanying rapid decrease in fracture toughness.

In Section 3 it was indicated that in the next phase of our program fracture toughness measurements would be made on other SiC and Si_3N_4 materials using the controlled surface flaw method[58,59,61]. To compare this method directly with the double torsion method the test matrix used for double torsion measurements is being repeated for the same materials, i.e. NC-132, NC-435, NC-350 and KBI RS Si_3N_4 (3 samples in each of 3 batches of material at both room temperature and 1350°C), but

using the controlled flaw method. This study should provide a valuable direct comparison of the two test techniques and their applicability to the Si_3N_4 and SiC materials of interest in gas turbine engines.

5.3 Creep Behavior

Creep resistance is of primary concern in the rotating components of a turbine engine. High creep rates lead to both excessive deformations and uncontrolled stresses in the transition zone between crept and non-crept material during cool-down.[106]

Creep is a thermally activated process. After stress application there is an instantaneous strain, followed by three regions of creep behavior. Primary creep (stage I) is characterized by a creep rate that continually decreases with time. This is followed by secondary (stage II) creep behavior where the creep rate remains constant with increasing strain and time. Stage III or tertiary creep is observed just prior to fracture, and is characterized by a rapid increase in creep rate. Steady state secondary creep behavior is of greatest interest in structural applications. The steady state creep rate, $\dot{\varepsilon}$, is governed by the empirical relation:

$$\dot{\varepsilon} = A\sigma^{n} e^{-E/kT} \qquad (1)$$

Creep deformation mechanisms are deduced in part by analysis of measured creep rates with respect to this relation, together with microstructural analysis of deformed (crept) specimens. Experimental schedules normally cover a range of stress and temperature which permit analytical determination of the stress exponent, n, and activation energy, E. Creep rupture tests involve measurement of time-to-failure under various steady loads. Creep rupture information is important in lifetime predictions in structural members subject to static fatigue conditions.

Both creep and creep rupture tests have been conducted

in 4-point flexure on the silicon nitride and silicon carbide materials (NC-132, NC-435, NC-350 and KBI RS Si_3N_4) in air atmosphere at 1350, and 1500°C. The results are discussed in the following sections.

5.3.1 Creep Rupture Tests - 50 Hours

Creep rupture results at 1350°C and 1500°C were presented in the last interim technical report[2] on NC-132, NC-435 and NC-350. No definitive trends were observed when the data were presented as rupture stress vs. log time due to very large scatter. These results are shown in Tables 5.10 through 5.12. Four-point creep rupture results at 1350°C and 1500°C for KBI reaction sintered Si_3N_4 are tabulated in Table 5.13. The performance of the KBI reaction sintered material was much poorer than NC-350. The times to failure for KBI RSSN were much shorter, the test samples often failing during initial loading at 1500°C. This occurred at 20-30 ksi lower stress levels than NC-350 for the same test temperature. These data are consistent with the lower strength of the KBI material with respect to NC-350. Comparing the densities of KBI samples with time to failure results in fairly good correlation. Samples K1CR2, K3CR1, and K3CR2 (see Table 5.13) are exceptions, but in general only those specimens with density >2.6 gm/cc survived to (or near) 50 hours. These creep rupture data for the four materials will again be evaluated when fractographic analyses are complete in an attempt to correlate flaws/microstructure with time to failure.

5.3.2 Creep Testing

Four-point 50 hour creep testing at 1350°C and 1500°C has been completed for NC-132 hot-pressed Si_3N_4, NC-435 siliconized SiC, NC-350 reaction sintered Si_3N_4, and KBI reaction sintered Si_3N_4. All testing was performed in air using the dead-weight

TABLE 5.10

FOUR POINT CREEP RUPTURE ON NC-132

Spec. Number	Temperature °C	ρ, gm/cc	Stress, KSI	Time-to-Failure
Batch 1				
11CR1	1350	3.184	40	15.6 hrs.
11CR2	1350	3.178	10	65 hrs. No Failure
			20	50 hrs. No Failure
			30	50 hrs. No Failure
			40	67 hrs. No Failure
			50	50 hrs. No Failure
			60	6 hrs.
11CR3	1350	3.183	50	2.5 hrs.
11CR4	1350	3.182	40	170 hrs. No Failure
11CR5	1500	3.178	10	51 hrs. No Failure
11CR6	1500	3.179	15	Large Deformation 50 hrs. No Failure Large Deformation
Batch 2				
12CR1	1350	3.190	40	0
12CR2	1350	3.190	35	0.6 hrs.
12CR3	1350	3.185	30	0.7 hrs.
12CR4	1500	3.175	15	0.2 hrs.
12CR5	1500	3.179	10	1.1 hrs.
12CR6	1500	3.178	2.5	50 hrs. No Failure

TABLE 5.11

FOUR POINT CREEP RUPTURE ON NC-435

Spec. Number	Temperature °C	ρ, gm/cc	Stress, KSI	Time-to-Failure
Batch 1				
41CR4	1200	2.939	40	50 hrs. No Failure
41CR5	1200	2.924	40	50 hrs. No Failure
41CR6	1200	2.942	40	50 hrs. No Failure
Batch 3				
43CR4	1200	2.989	40	50 hrs. No Failure
43CR5	1200	2.993	40	50 hrs. No Failure
43CR6	1200	2.982	40	50 hrs. No Failure
Batch 4				
44CR4	1200	2.971	40	50 hrs. No Failure
44CR5	1200	2.958	45	3 hrs.
44CR6	1200	2.957	45	50 hrs. No Failure
Batch 1				
41CR1	1350	2.906	40	11.9 hrs.
41CR2	1350	2.924	40	Less Than 1 Min.
41CR3	1350	2.935	40	Less Than 1 Min.
Batch 3				
43CR1	1350	2.993	35	46.32 hrs.
43CR2	1350	2.984	35	3.61 hrs.
43CR3	1350	2.985	35	10.98 hrs.
Batch 4				
44CR1	1350	2.964	35	0
44CR2	1350	2.945	35	0
44CR3	1350	2.955	25	50 hrs. No Failure

TABLE 5.12

FOUR POINT CREEP RUPTURE ON NC-350

Spec. Number	Temperature °C	ρ, gm/cc	Stress, KSI	Time-to-Failure
Batch 1				
31CR1	1350	2.516	35	50 hrs. No Failure
31CR2	1350	2.521	35	50 hrs. No Failure
31CR3	1350	2.548	35	50 hrs. No Failure
Batch 2				
32CR1	1350	2.434	40	.9 Min.
32CR2	1350	2.441	35	50 hrs.
32CR3	1350	2.506	35	50 hrs.
Batch 3				
33CR1	1350	2.550	35	33.5 Min.
33CR2	1350	2.522	35	50 hrs. No Failure
33CR3	1350	2.544	35	50 hrs. No Failure
Batch 1				
31CR4	1500	2.488	25	50 hrs. No Failure
31CR5	1500	2.507	30	37.7 hrs.
31CR6	1500	2.542	30	35.3 hrs.
Batch 2				
32CR4	1500	2.389	30	45.9 hrs.
32CR5	1500	2.343	30	10.8 hrs.
32CR6	1500	2.398	30	37.4 hrs.
Batch 3				
33CR4	1500	2.540	30	Less Than 1 Min.
33CR5	1500	2.577	30	50 hrs. No Failure
33CR6	1500	2.572	30	50 hrs. No Failure

TABLE 5.13

FOUR POINT CREEP RUPTURE ON KBI RBSN

Spec. Number	Temperature °C	ρ, gm/cc	Stress, KSI	Time-to-Failure
Batch 1				
K1CR1	1350	2.282	14.9	1.6 hrs.
K1CR2	1350	2.287	10	50 hrs.
K1CR3	1350	2.282	12.1	14.2 hrs.
Batch 2				
K2CR1	1350	2.351	11.5	4.5 hrs.
K2CR2	1350	2.677	10	50 hrs.
K2CR3	1350	2.360	10.7	3.5 hrs.
Batch 3				
K3CR1	1350	2.305	11.2	29 hrs.
K3CR2	1350	2.307	10.7	35.7 hrs.
K3CR3	1350	2.371	10.2	5.8 hrs.
Batch 1				
K1CR4	1500	2.679	10	50 hrs.
K1CR5	1500	2.554	9.9	12 hrs.
K1CR6	1500	2.748	9.9	50 hrs.
Batch 2				
K2CR4	1500	2.754	10.2	50 hrs.
K2CR5	1500	2.359	10.4	0
K2CR6	1500	2.342	9.8	0
Batch 3				
K3CR4	1500	2.383	8.5	0
K3CR5	1500	2.353	8.4	0
K3CR6	1500	2.379	6	0

loading/3-point DCDT deflectometer system described previously[1]. Much of the steady-state creep strain vs time data for these materials was presented in the last interim technical report[2]. The reader is referred to Section 4.2.2.1 of that report for details. During the current reporting period testing was completed for Phase I materials. The following sections overview the data and discuss correlations and mechanistic interpretation.

5.3.2.1 Creep Strain vs Time

NC-132 hot-pressed Si_3N_4 tested at 1360°C ± 10°C under applied loads of 10 and 15 ksi attained second stage creep in about ten hours, and exhibited steady state creep rates of ~3.2 ± .2 x 10^{-4} hr^{-1}, and ~5.1 ± .4 x 10^{-4} hr^{-1}, respectively. At 1500°C, previously presented data for Batch 2 and new data for Batch 1 are shown in Figures 5.33 and 5.34. Applied stress levels varied from 1.5 to 2.5 ksi, and steady state creep was obtained in 10 hours. Creep rates varied fairly consistently over the applied stress range from 1 x 10^{-4} hr^{-1} to 2.2 x 10^{-4} hr^{-1}.

NC-435 siliconized SiC samples exhibited very low deformation rates at 1200°C, < 2 x 10^{-5} hr^{-1} for applied stresses of 30-35 ksi. Several samples tested at 30 ksi exhibited creep rates of ~6 ± 2 x 10^{-6} hr^{-1}. Compared to NC-132 a more gradual transition from primary to secondary creep was observed. This was also true for NC-435 samples tested at 1350°C. All samples from two batches of material tested at 1350°C survived the 50 hour creep test, exhibiting stage II rates of 4.5 ± 1.5 x 10^{-5} hr^{-1} at 30 ksi and creep rates of ~2.6 x 10^{-5} hr^{-1} at 20 ksi. At 20 ksi, however, large scatter was observed, the creep rates varying from 1.7 x 10^{-5} hr^{-1} to 4.7 x 10^{-5} hr^{-1}. The third batch of NC-435 samples tested at 1350°C (Batch 3) all failed in less than 10 hours under applied stresses ranging from 20-30 ksi.

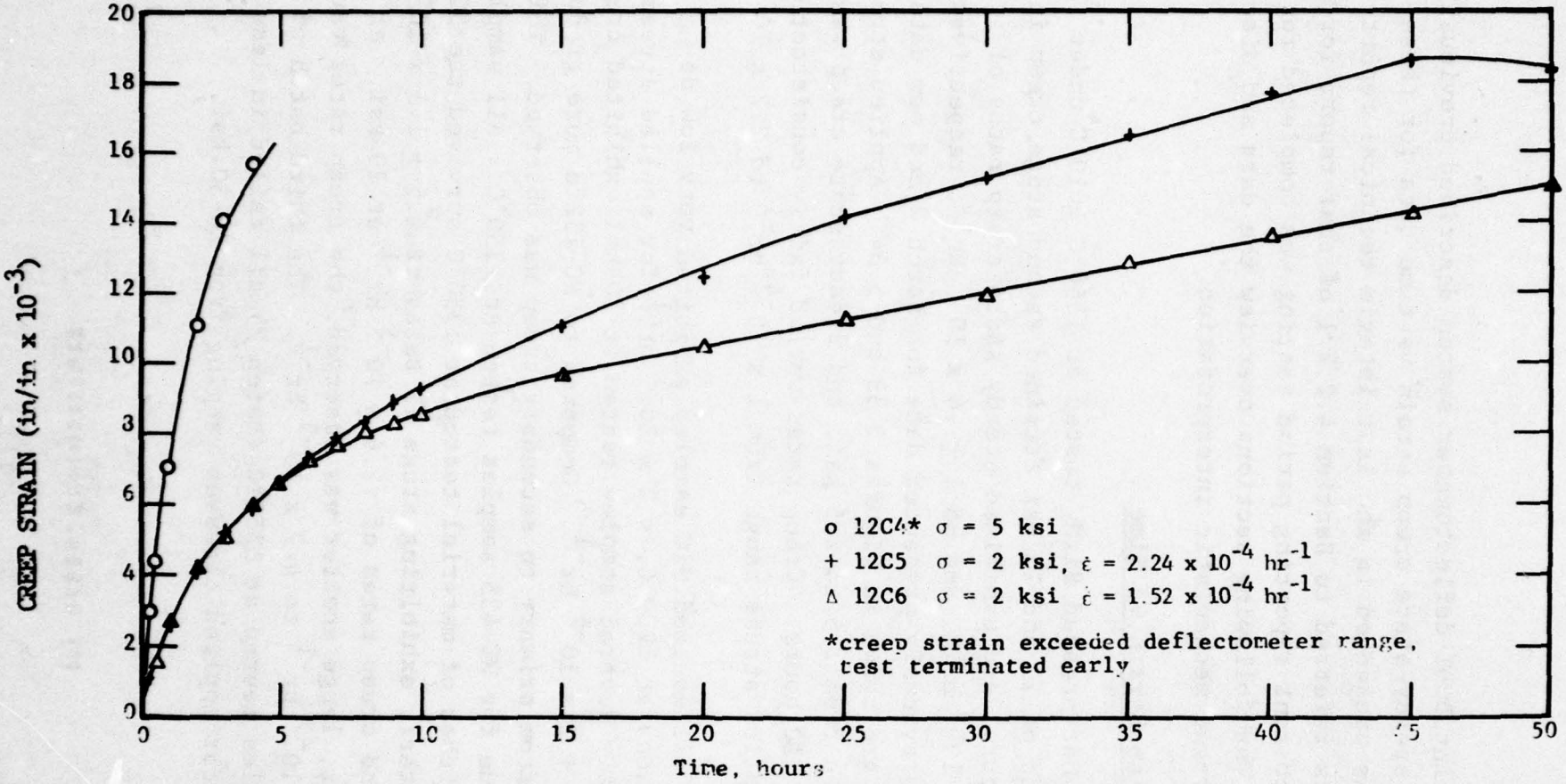

FIGURE 5.33 CREEP STRAIN VS TIME FOR NC-132 HP Si_3N_4 AT 1500°C (Batch 2)

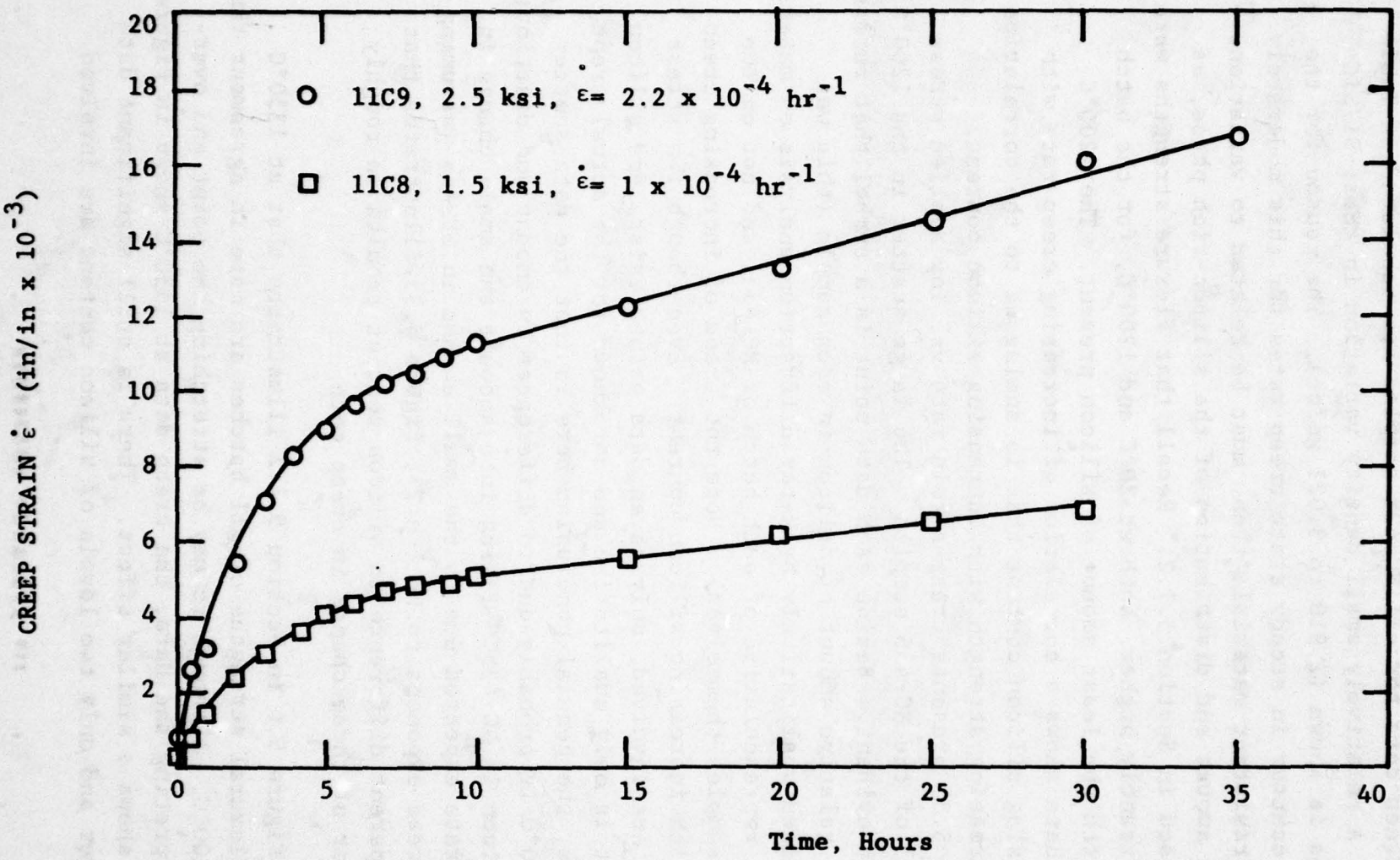

FIGURE 5.34 CREEP STRAIN vs. TIME FOR NC-132 HP Si_3N_4 (Batch 1) at 1500°C.

Creep data for all NC-435 samples are tabulated in Table 5.14. A relatively small density variation in these Si/SiC samples is shown (2.910 to 3.021 gm/cc). The reason for the large scatter in steady state creep rates for this moderately creep resistant material, then, must be related to variations in the amount and distribution of the silicon-rich phase, as discussed in Section 5.1.2. Recall that flexure strengths were significantly higher, both at 20°C and 1200°C, for the batch (#3) with the least amount of silicon present. The 1200°C creep data shows a correlation of increasing creep rate with increasing silicon content that is analagous to the correlation of decreasing strength with increasing silicon content. Figure 5.35 presents creep strain rate vs. log applied stress for all of the NC-435 samples. The large scatter in the 1200°C data is evident. Beside each data point is a symbol that refers to the relative amount of silicon in each sample (this was determined qualitatively by x-ray diffraction analysis on material judged representative of each batch of NC-435, and not on the creep samples themselves). Note the trend of increasing creep rate with increasing silicon content. Even though two stress levels are involved, only seven data points exist, and silicon content is only qualitative and not known for the actual crept samples, the general conclusion here is that the data scatter at 1200°C is probably due to differences in amount and distribution of silicon in NC-435. Taking into account the small change in creep rate expected due to the small change in stress (assuming the stress exponent to be $1<n<2$), Figure 5.35 illustrates that the apparent difference in silicon content results in roughly a factor of three change in creep rate.

Figure 5.6 in Section 5.1.2 illustrates that at 1350°C the flexural strengths of all batches are more in agreement than at 1200°C. Although it may be stretching the point and over-interpreting the data, the creep data at 1350°C shown in Figure 5.35 shows a similar effect. There is still significant data scatter and only two levels of silicon content are involved.

TABLE 5.14

NC-435 TABULAR CREEP DATA

TEMPERATURE °C	SAMPLE # *	DENSITY gm/cc	CREEP RATE $\dot{\varepsilon}$, hr^{-1}	APPLIED Stress, ksi	RELATIVE SILICON Content**
1200°C	41C5	2.918	$2x10^{-5}$	35	HIGH
1200°C	41C6	2.948	$2.1x10^{-5}$	35	HIGH
1200°C	41C4	2.928	Failed at t=0	40	HIGH
1200°C	43C4	3.021	$6.4x10^{-6}$	30	LOW
1200°C	43C5	3.007	$1.4x10^{-5}$	30	LOW
1200°C	43C6	2.983	$5.3x10^{-6}$	30	LOW
1200°C	44C5	2.943	$7.6x10^{-6}$	30	MODERATE
1200°C	44C6	2.963	$4.7x10^{-6}$	30	MODERATE
1350°C	41C1	2.910	$6.3x10^{-5}$	30	HIGH
1350°C	41C2	2.914	$3.9x10^{-5}$	30	HIGH
1350°C	41C3	2.932	$3.1x10^{-5}$	30	HIGH
1350°C	43C1	3.004	Failed at 10hr.	30	LOW
1350°C	43C2	2.972	Failed at 1hr.	30	LOW
1350°C	43C3	3.002	Failed at 9hr.	20	LOW
1350°C	44C1	2.988	$4.7x10^{-5}$	20	MODERATE
1350°C	44C2	2.953	$1.5x10^{-5}$	20	MODERATE
1350°C	44C3	2.945	$1.7x10^{-5}$	20	MODERATE

* The second digit refers to Batch Number.

** Qualitative determination of silicon rich phase by x-ray diffraction analysis conducted at AFML on samples of NC-435 that were not actual creep samples.

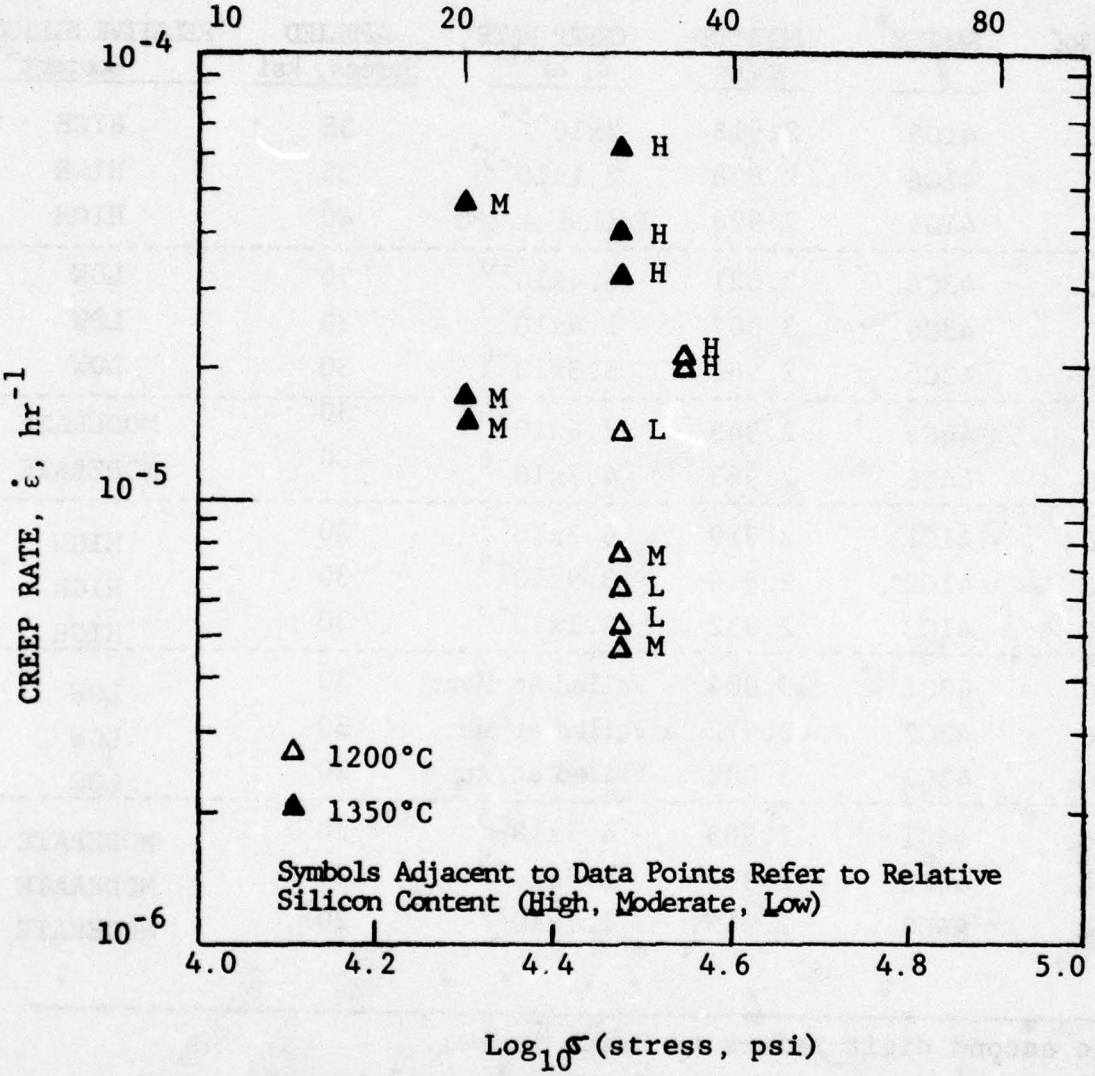

FIGURE 5.35 CREEP RATE VS. APPLIED STRESS FOR NC-435 SAMPLES

However, a more realistic stress exponent would be obtained at 1350°C (even though it cannot be accurately calculated due to the data scatter), indicating a reduction in the affect of silicon content on the creep behavior.

NC-350 reaction sintered Si_3N_4 was observed to be an extremely creep resistant material. No creep deformation was detectable after 50 hours exposure at 1350°C under an applied stress of 40 ksi. These results are consistent with behavior reported by Seltzer[67,68] for NC-350. At 1500°C NC-350 exhibited steady state creep rates of ~1 x 10^{-5} hr^{-1} at 25 ksi (for details refer to reference 2). For the nine samples tested, measured creep rates varied from 5 x 10^{-6} hr^{-1} to 1.9 x 10^{-5} hr^{-1}. This factor of four variation in creep rate could not be correlated with sample density differences (2.38 to 2.55 gm/cc). Thompson and Pratt[69] had previously reported creep strengths being related to porosity in reaction sintered silicon nitride over a density range 2.2 to 2.6 gm/cc.

Creep tests on KBI reaction sintered Si_3N_4 were conducted at 1350° and 1500°C. Creep strain vs time data for three samples in each of three batches of material tested at 1350°C are presented in Figure 5.36 through 5.38. Batch 1 material (Figure 5.36) was fairly well-behaved, exhibiting creep rates increasing from 5 x 10^{-6} hr^{-1} at 3 ksi to 1.6 x 10^{-5} hr^{-1} at 6 ksi. It is noted that roughly the same creep rates were observed for NC-350 RBSN at an applied stress of 25 ksi at 1500°C. Batch 2 KBI material tested at 1350°C (Figure 5.37) exhibited less predictable creep behavior compared to Batch 1. It is noted in Figure 5.37 that the highest creep rate was obtained at only 4.5 ksi. However, that particular sample possessed the lowest density of the three in Batch 2. That creep sample (K2C7) was extracted from material that was originally a thermal shock specimen (K2TS4).

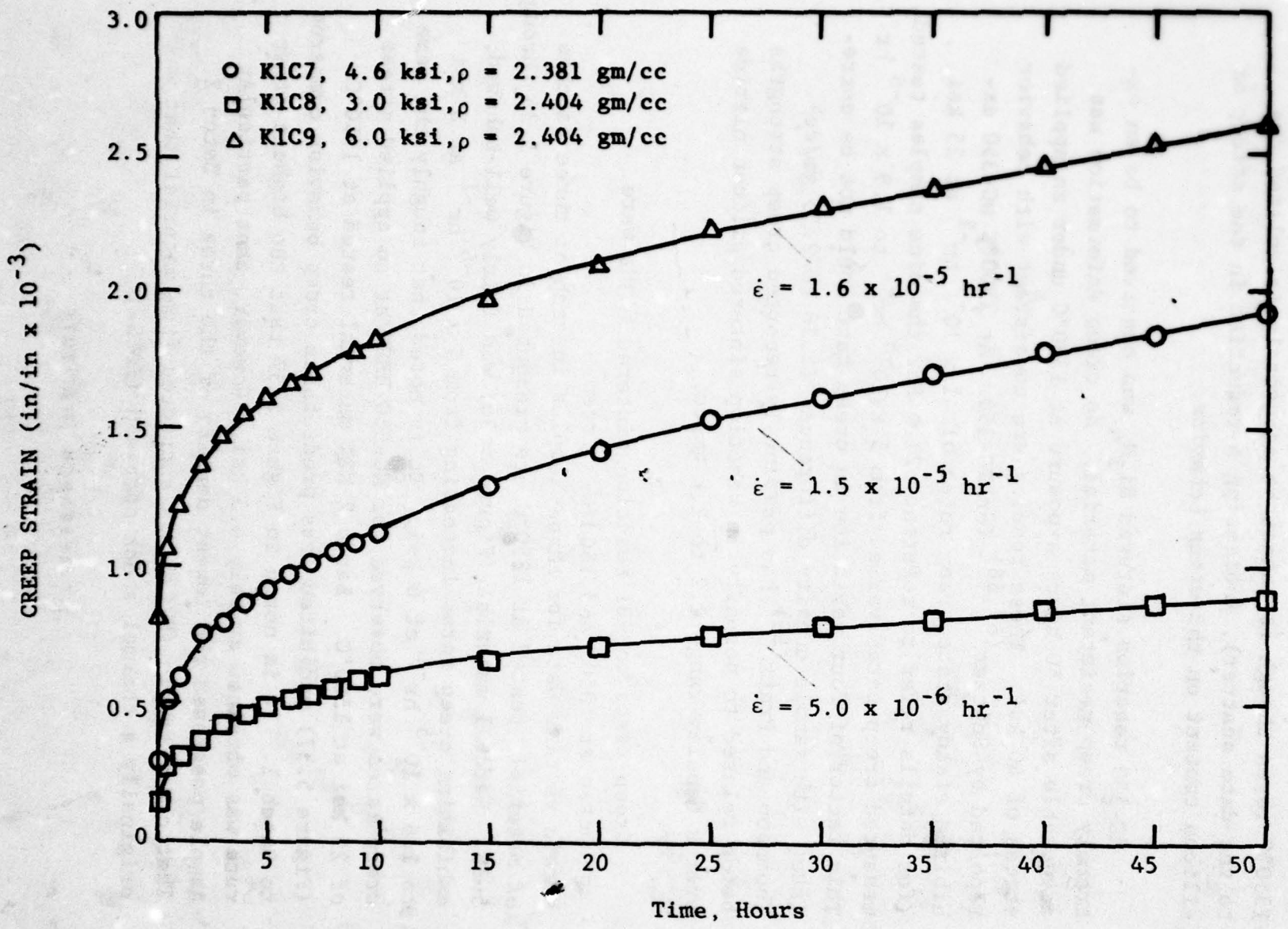

FIGURE 5.36 CREEP STRAIN vs. TIME FOR KBI RS Si_3N_4 BATCH 1 at 1350°C

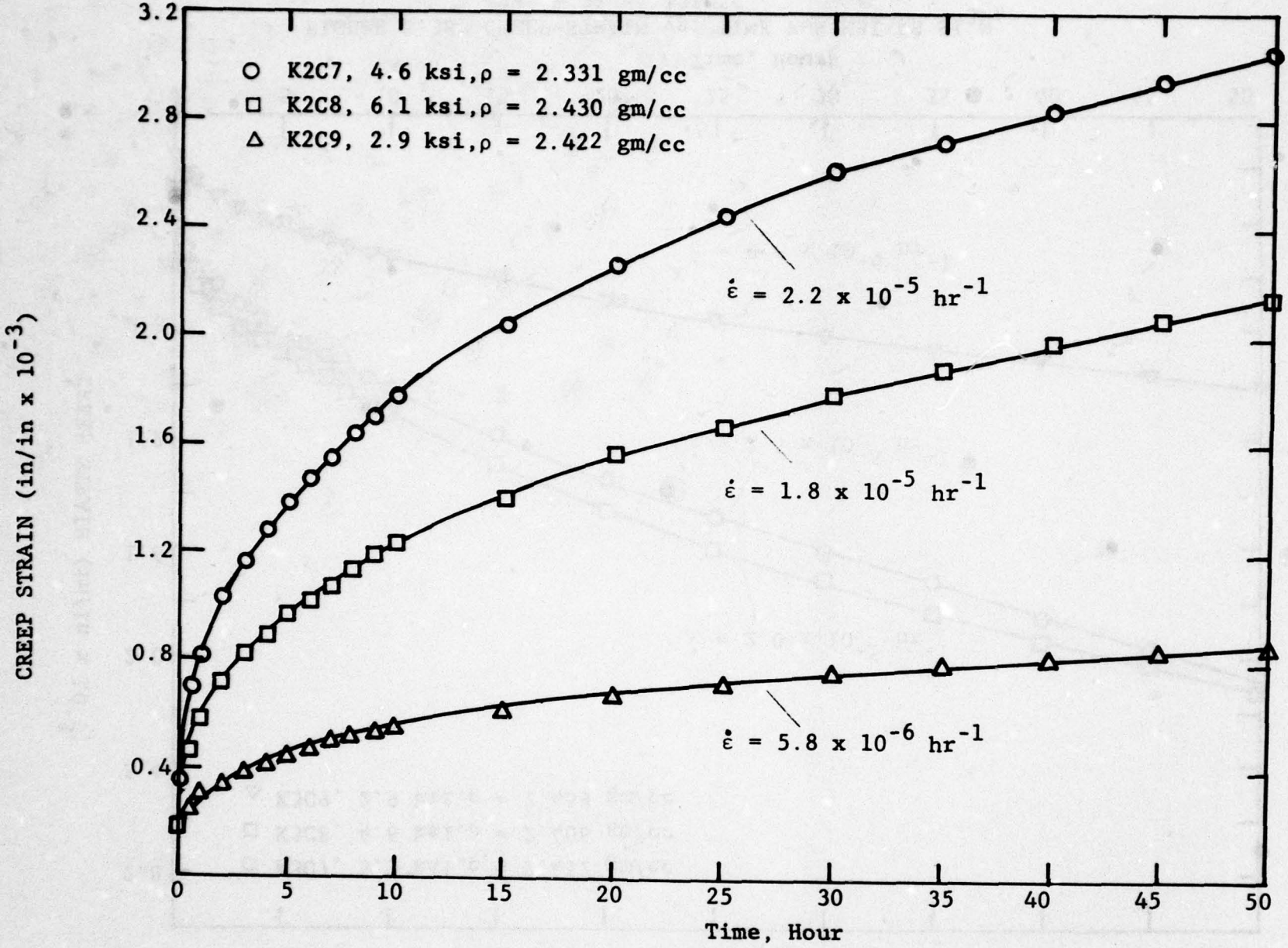

FIGURE 5.37 CREEP STRAIN vs. TIME FOR KBI RS Si_3N_4 (Batch 2) at 1350°C

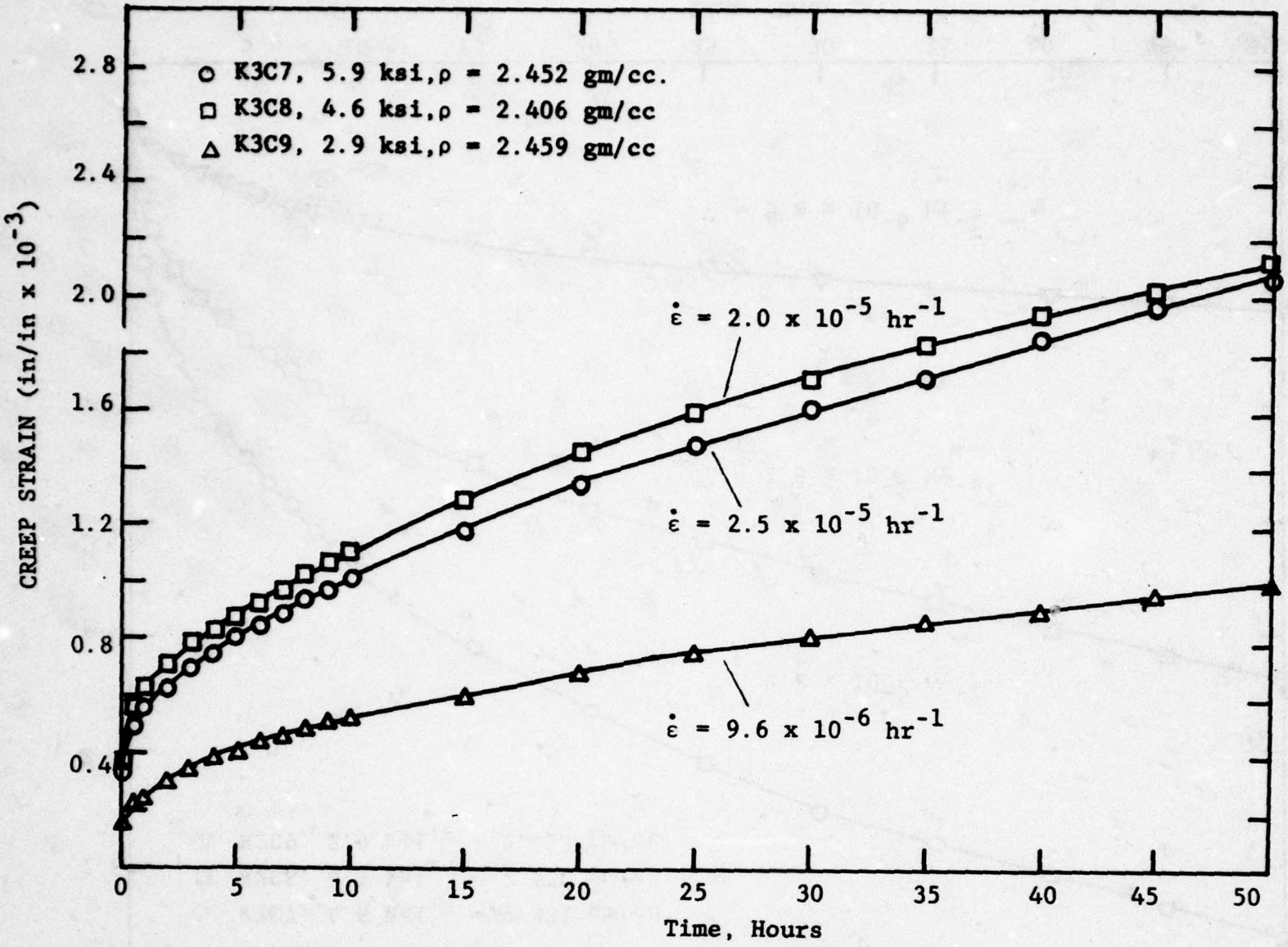

FIGURE 5.38 CREEP STRAIN vs. TIME FOR KBI RS Si_3N_4 (Batch 3) at 1350°C.

Figure 5.39 illustrates that particular 1 x 2-1/2 inch thermal shock sample to be the most non-uniform in x-radiographic inspection.

KBI creep-strain vs. time data for the three material batches tested at 1500°C is provided in Figure 5.40. Fairly consistent behavior is seen, but note the extremely low applied stress levels. NC-350 exhibited roughly the same creep rates at the same temperature for stresses a factor of twenty higher. Of the samples that failed upon load application at t = 0, it is significant to note that sample K2C10 came from the same original thermal shock sample (K2TS4) that was shown to be non-uniform as seen in the x-radiograph presented in Figure 5.39.

In comparing the 1350°C-1500°C creep strength of all four materials, the following general observations are made. The large creep deformation observed for NC-132 hot-pressed Si_3N_4 is consistent with the large anelasticity observed in its flexural stress-strain behavior at 1350°C and 1500°C. This has been attributed to the presence of a significant impurity phase in this material, which is thought to result in glassy grain boundary material which controls deformation. The good sample-to-sample agreement in creep behavior for NC-132 is consistent with its uniform density and microstructure. NC-435, siliconized SiC exhibited slightly improved creep resistance compared to NC-132, but exhibited a large amount of data scatter which is thought to be caused by variations in the amount and distribution of the silicon phase in this material. NC-350 reaction sintered Si_3N_4 exhibited excellent creep strength. This behavior is consistent with the linear stress-strain characteristics and superior strength of NC-350 at 1500°C, which result from the lack of major impurities in this material. The KBI reaction sintered material exhibited much lower creep resistance than NC-350. This is consistent with this materials lower strength, greater porosity, and generally lower microstructural uniformity and homogeneity.

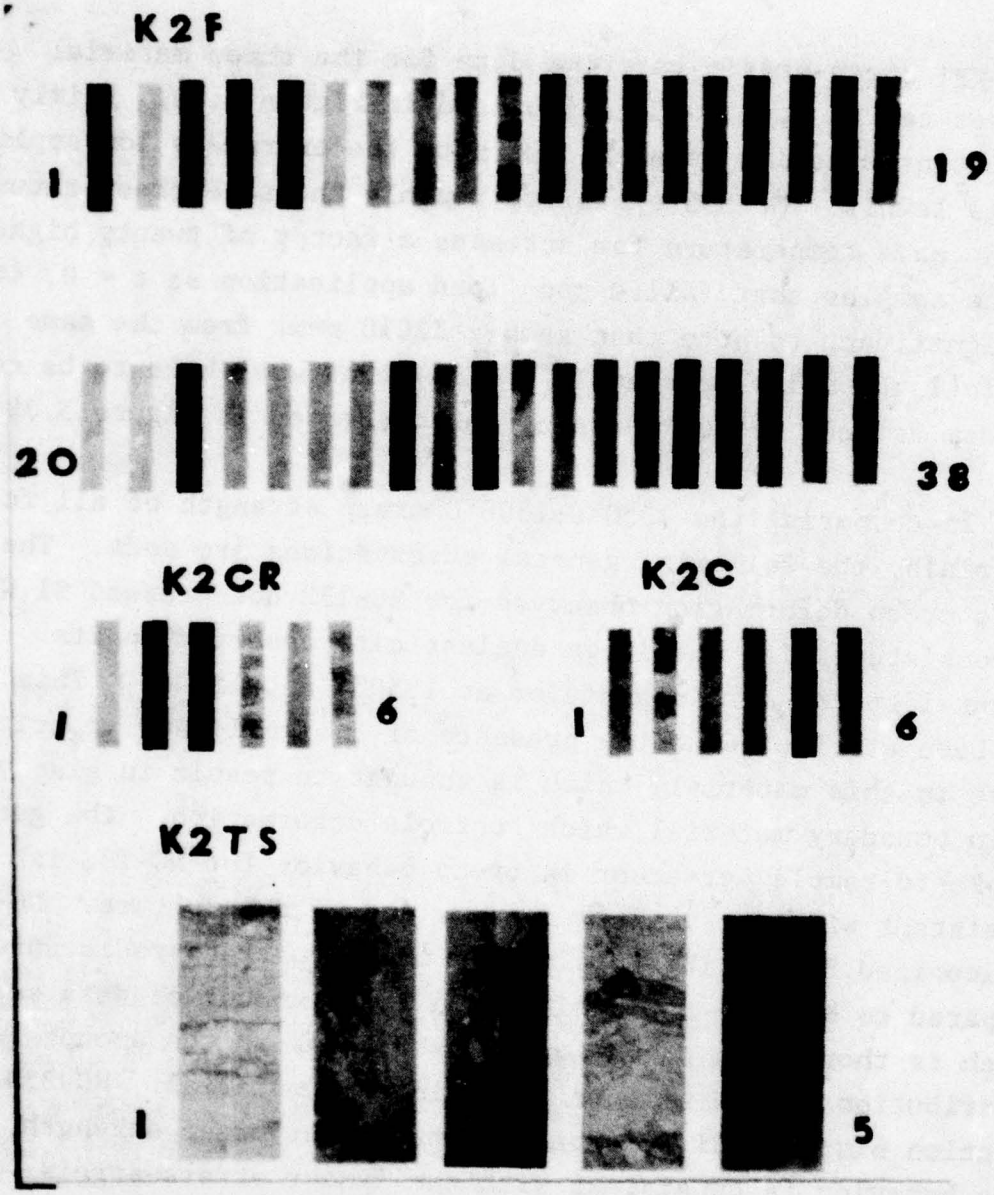

FIGURE 5.39
X-RADIOGRAPH SHOWING NON-UNIFORMITY IN CREEP SAMPLE (K2C7) WHICH WAS EXTRACTED FROM SAMPLE K2TS4 SHOWN.

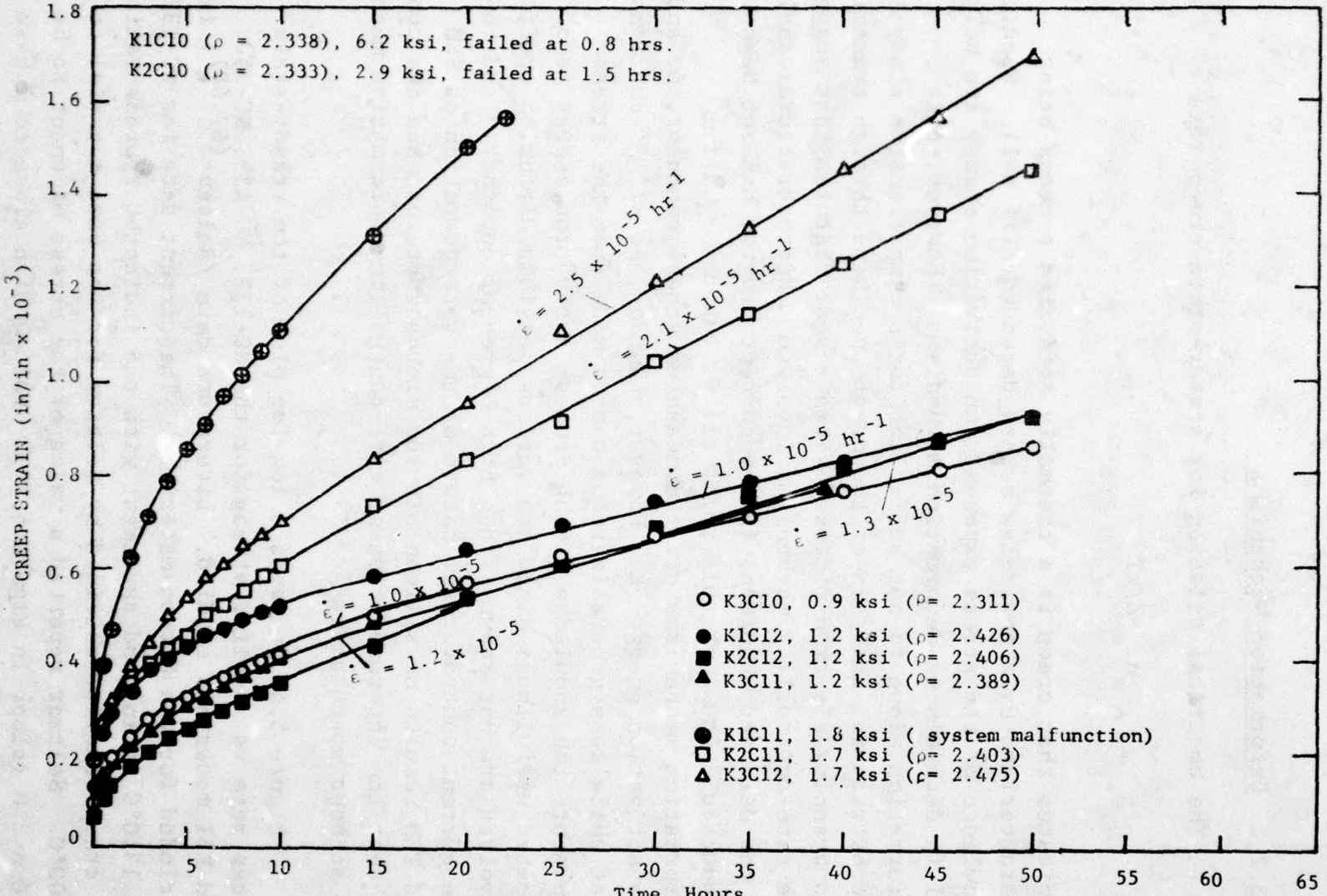

FIGURE 5.40 CREEP STRAIN vs. TIME FOR KBI RS Si_3N_4 AT 1500°C

5.3.2.2 Deformation Mechanisms

The empirical relation for steady-state creep rate $\dot{\varepsilon}$

$$\dot{\varepsilon} = A \sigma^n e^{-E/kT}$$

indicates that creep is a thermally activated process being characterized by a power-law stress dependence(if n>1). Specific knowledge of the stress exponent and activation energy are helpful in determining deformation mechanisms. However, this information alone is not sufficient for a comprehensive study; microstructural analysis of the crept specimens through transmission and scanning electron microscopy can reveal features that suggest the rate-controlling mechanisms involved. Microstructural analysis of the deformed specimens in the current program has not been conducted. Thus, at this point all we can use to infer deformation mechanisms are the measured stress exponent, n, and the activation energy, E. However, Langdon, et al[70] cautions that while some generalizations can be made from the stress exponent, the knowledge of the process activation energy is of limited usefullness since the various possible diffusion coefficients involved are not known with a high degree of accuracy. Add to this the current controversial nature of the interpretation of SEM and TEM results of silicon nitride microstructures, and the conclusion is that the interpretation of rate-controlling deformation mechanisms is at best speculative.

Figure 5.41 presents a log-log plot of the steady-state creep rate vs. applied stress for the NC-132, NC-435, NC-350, and KBI materials studied. Literature data (Seltzer[67,68]) is included for the Norton materials. The current data for NC-132 at 1350°C is in good agreement with the indicated representation of creep behavior obtained by Seltzer for the same material at 1400°C. Seltzer reported a value of the stress exponent to be 1.6<n<2.0 (slope in Figure 5.41). Values of n close to 2 have

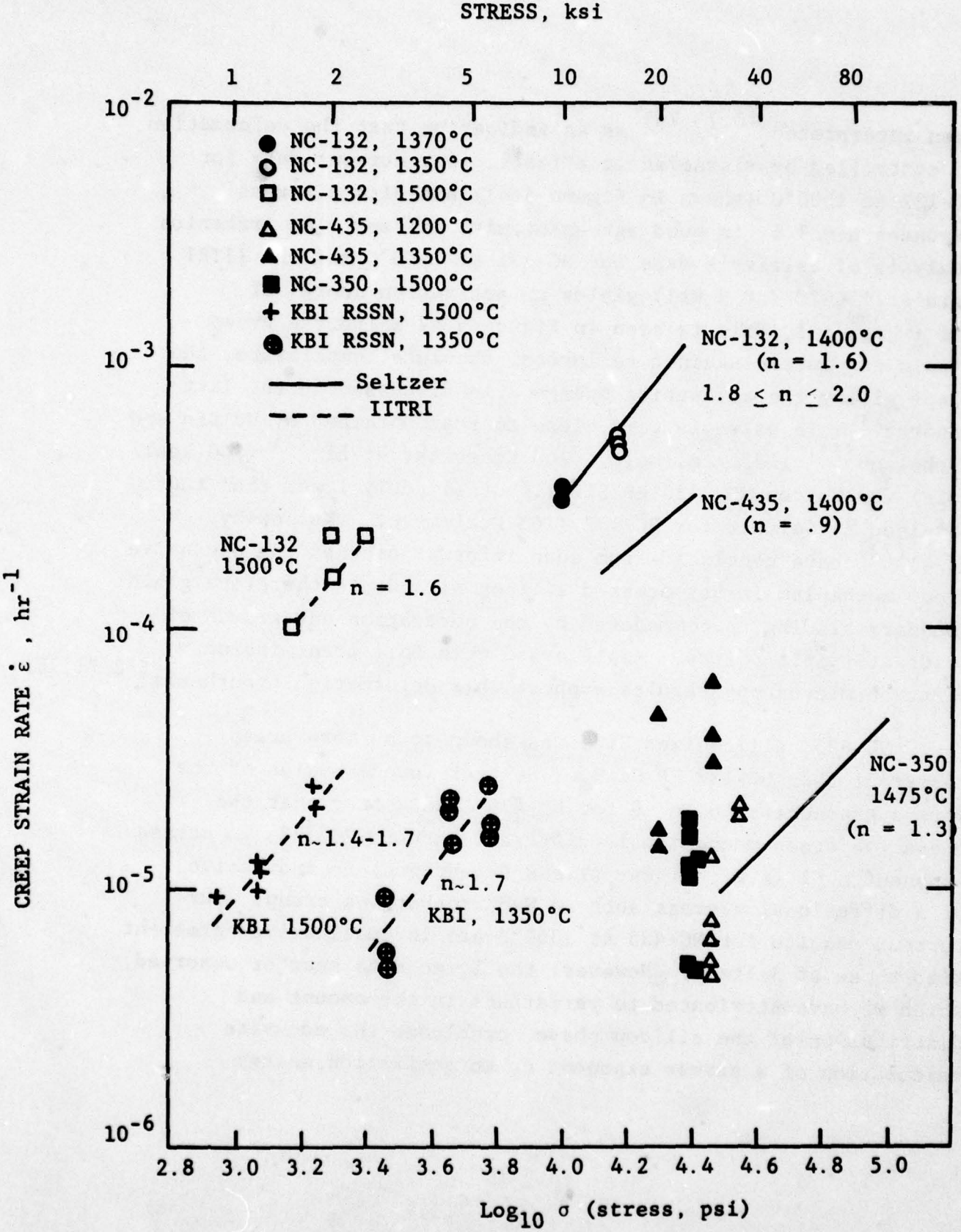

FIGURE 5.41 STEADY STATE FLEXURAL CREEP RATE VS. APPLIED STRESS FOR VARIOUS SiC and Si_3N_4 MATERIALS.

been interpreted[70,73,74] as an indication that the deformation is controlled by viscoelastic effects. Our current data for NC-132 at 1500°C (shown in Figure 5.41) exhibits a stress exponent n = 1.6, in good agreement with Seltzer. An Arrhenius analysis of Seltzer's data for NC-132 at 1400°C and the IITRI data at 1500°C (at 2 ksi) yields an activation energy of 130 $\pm$ kcal/mol. This is seen in Figure 5.42 where the creep strain is plotted against reciprocal absolute temperature, the slope giving the activation energy. As discussed in the last report[2] this value is very close to that obtained by Ud Din and Nicholson[71] (135 kcal/mole) and Kossowsky et al[72] (140 kcal/mole) for Norton HS- 130 HP Si_3N_4, but slightly lower than that obtained by Seltzer for NC-132 (168 kcal/mole). Kossowsky, et al[72] have concluded from such information that the operative creep mechanism in hot pressed silicon nitride is therefore grain boundary sliding, accommodated by the nucleation and growth of voids at triple points. Replica and thin foil transmission electron microscopy results support this deformation hypothesis[72,71,75].

NC-435, siliconized SiC, was shown to be more creep resistant than NC-132 HP Si_3N_4. Seltzer found a value of the stress exponent to be n ~.9 for NC-435, indicating that the operative creep mechanism is different than in NC-132. A stress exponent n ~ 1 (i.e., linear stress dependence) is indicative of a diffusional process such as Nabarro-Herring creep. Our current results for NC-435 at 1350°C are in qualitative agreement with those of Seltzer. However, the large data scatter observed, which we have attributed to variations in the amount and distribution of the silicon phase, precluded the accurate calculation of a stress exponent or an activation energy.

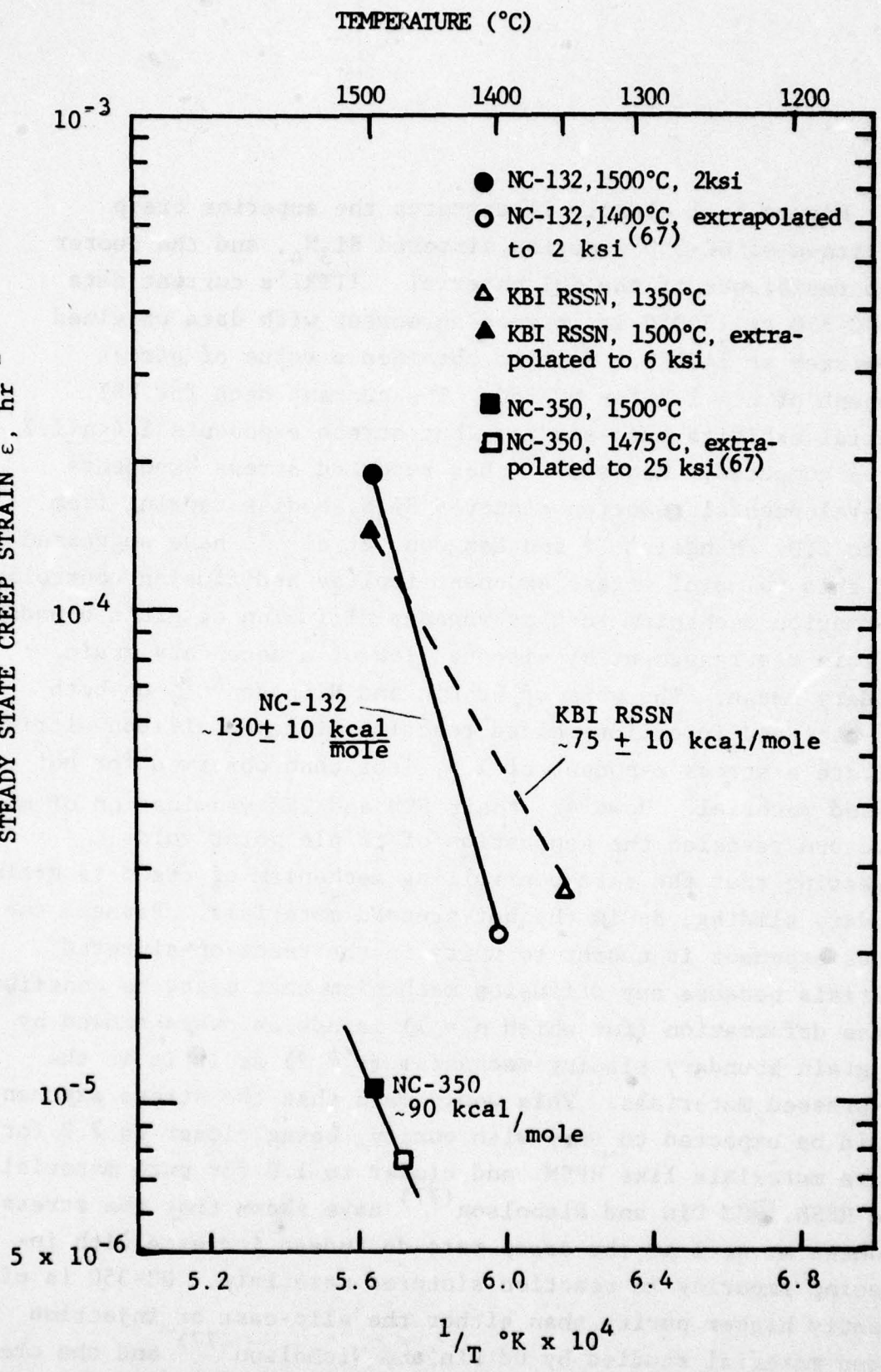

FIGURE 5.42 STEADY STATE CREEP RATE vs. RECIPROCAL ABSOLUTE TEMPERATURE

Figure 5.41 clearly illustrates the superior creep resistance of NC-350 reaction sintered Si_3N_4, and the poorer creep resistance of the KBI material. IITRI's current data for NC-350 at 1500°C is in good agreement with data obtained by Seltzer at 1475°C. Seltzer obtained a value of stress exponent of n = 1.3 for NC-350. The current data for KBI material exhibits much scatter, but stress exponents $1.4 \leq n \leq 1.7$ can be computed. Mangels[76] has reported stress exponents in developmental reaction sintered Si_3N_4 bodies ranging from 1.2 to 2.0. Mangels[76] and Langdon, et al[70] have suggested that this value of stress exponent implies a diffusion controlled deformation mechanism such as vacancy diffusion at grain boundaries, or grain rearrangement by viscous flow of a secondary grain boundary phase. The work of Ud Din and Nichoson[77] on both slip-cast and injection-molded reaction sintered silicon nitride indicate a stress exponent of 1.4, less than observed for hot pressed material. However, their SEM and TEM examination of microstructure revealed the generation of triple point voids, suggesting that the rate-controlling mechanism of creep is grain boundary sliding, as in the hot-pressed materials. Perhaps the stress exponent is nearer to unity in the reaction-sintered materials because any diffusion mechanism that might be contributing to the deformation (for which n = 1) is not as overshadowed by the grain boundary sliding mechanism ($n \cong 2$) as it is in the hot-pressed materials. This would mean that the stress exponent should be expected to vary with purity, being closer to 2.0 for impure materials like HPSN, and closer to 1.0 for pure materials like RSSN. Ud Din and Nicholson[77] have shown that the stress exponent as well as the creep rate do indeed increase with increasing impurity in reaction sintered materials. NC-350 is of slightly higher purity than either the slip-cast or injection molded material studied by Ud Din and Nicholson[77] and the creep rate and stress exponent are slightly lower for NC-350. NC-350

also contains a higher percentage of α-Si_3N_4 than either the slip-cast or injection molded material. Ud Din and Nicholson attribute higher α-Si_3N_4 content to higher creep resistance. The comments about higher purity and higher α-Si_3N_4 content resulting in lower creep rates may be applied to the differences shown in Figure 5.42 between NC-350 and the KBI material. The higher stress exponent and higher creep rates for the KBI material may be reflective of higher impurity content. It is already known that the KBI material has a higher β-Si_3N_4 content, which results in lower creep resistance. Of course, it is not known whether or not this behavior for KBI could also be due to its less well sintered condition as discussed in Section 5.14 (this could also lead to variations in α/β content). As illustrated in Figure 5.42, the reaction sintered materials (although exhibiting much scatter) exhibit activation energies lower than the hot pressed material. This is in agreement with Ud Din and Nicholson. At the moment it is not known whether this might be due partially to increased porosity or whether a different creep mechanism is operative.

6.0 THERMAL PROPERTY RESULTS

One of the reasons that Si_3N_4 and SiC are prime candidates for use in ceramic gas turbine applications is their low expansion coefficient (especially Si_3N_4) and high strength, which makes them less susceptible than many other ceramics to damage in thermal gradients. The other properties that determine thermal stress are thermal conductivity and thermal diffusivity. These thermophysical properties determine temperature distribution within a component and thus the thermal strain field. In this program the thermal expansion and thermal diffusivity are measured directly. Thermal conductivity is computed from thermal diffusivity and specific heat. Specific heat is not as variable with respect to impurities and microstructure as thermal conductivity. Thus, literature data for specific heat is being used. Thermal shock resistance is being determined both experimentally and analytically for all materials.

6.1 Thermal Expansion

Thermal expansion measurements have been completed for NC-132 HP Si_3N_4, NC-435 Si/SiC, NC-350 RS Si_3N_4 and KBI RS Si_3N_4. The apparatus and test conditions were described previously[2]. Current data consists of NC-132 (2), NC-435 (3,4), and KBI (2,3)*. All testing was conducted in air.

6.1.1 NC-132 HP Si_3N_4

Figure 6.1 presents linear thermal expansion behavior of NC-132 batch 2 material from 25° to 1500°C (heating cycle only). At 1000°C a 0.3% expansion is shown. This agrees well with previous data on batch 1 material[(2)]. This was expected since thermal expansion does not vary strongly with trace impurity content and flaw distribution, rather being a function of solid phase composition which for NC-132 is quite uniform.

*Numbers in parentheses refer to batch number

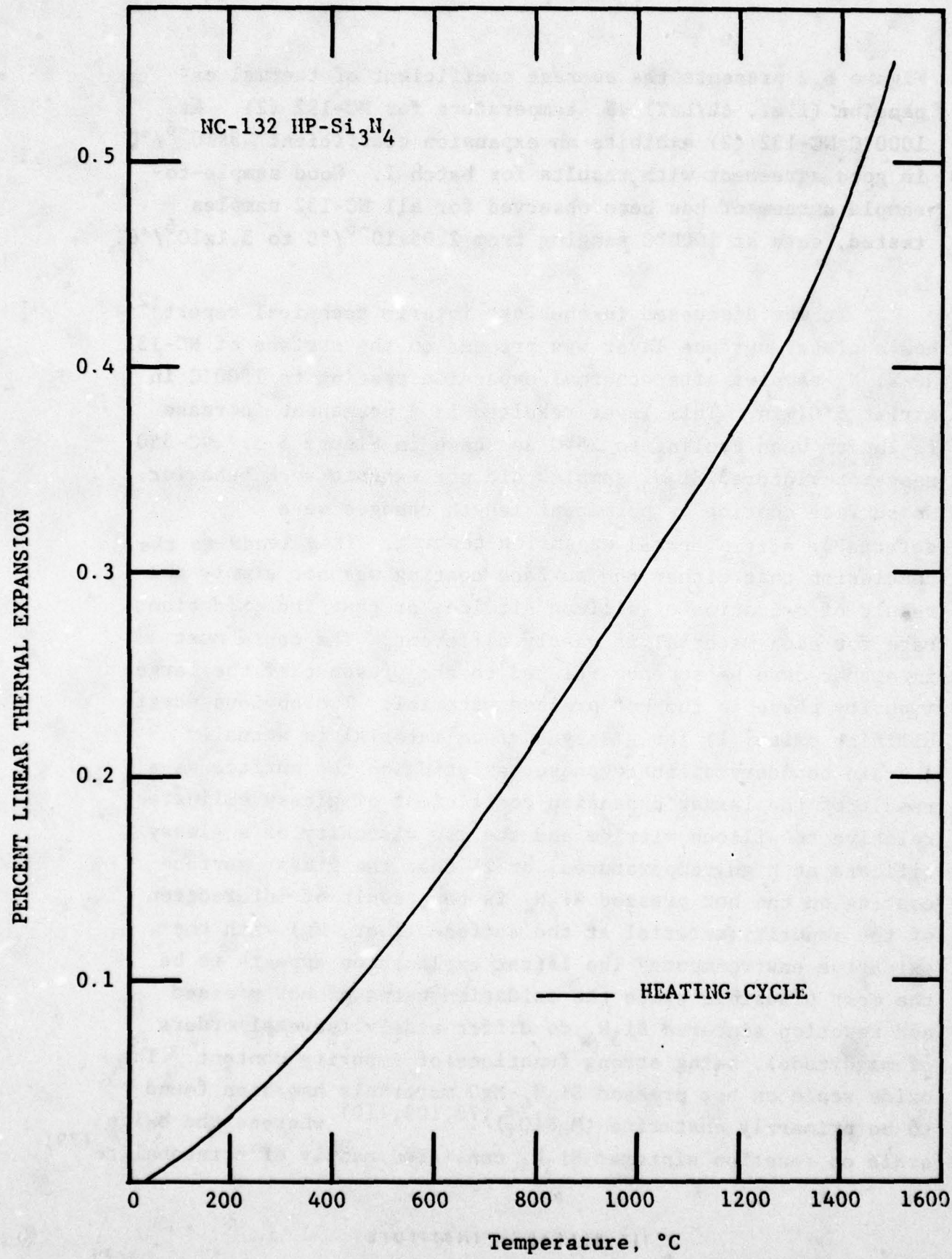

FIGURE 6.1 THERMAL EXPANSION BEHAVIOR OF NC-132 (2) HP Si_3N_4

Figure 6.2 presents the average coefficient of thermal expansion (i.e., $\Delta L/L\Delta T$) vs. temperature for NC-132 (2). At 1000°C NC-132 (2) exhibits an expansion coefficient ~3×10^{-6}/°C in good agreement with results for batch 1. Good sample-to-sample agreement has been observed for all NC-132 samples tested, data at 1000°C ranging from 2.95×10^{-6}/°C to 3.1×10^{6}/°C.

It was discussed in the last interim technical report[2] how a glassy surface layer was present on the surface of NC-132 HP-Si_3N_4 samples after thermal expansion testing to 1500°C in air at 5°C/min. This layer resulted in a permanent increase in length upon cooling to 25°C as shown in Figure 6.3. NC-350 reaction sintered Si_3N_4 samples did not exhibit such behavior. No surface coating or permanent length changes were detectable after thermal expansion testing. This leads to the conclusion that either the surface coating was not simply the result of oxidation of silicon nitride, or that the oxidation rate for each material is vastly different. The cause must in either case be somehow related to the presence of the large impurity phase in the hot pressed material. Two obvious possibilities exist: 1) the glassy surface material is actually a grain boundary silicate phase, existing on the surface as a result of the larger expansion coefficient of glassy silicates relative to silicon nitride and the low viscosity of a glassy silicate at high temperatures, or 2) that the glassy surface coating on the hot pressed Si_3N_4 is the result of interaction of the impurity material at the surface (i.e., Mg) with the oxidative environment. The latter explanation appears to be the most plausible since the oxidation rates of hot pressed and reaction sintered Si_3N_4 do differ widely (several orders of magnitude), being strong functions of impurity content. The oxide scale on hot pressed Si_3N_4-MgO materials has been found to be primarily enstatite ($MgSiO_3$)[78,109,110] whereas the oxide scale on reaction sintered Si_3N_4 consisted mainly of cristobalite[79].

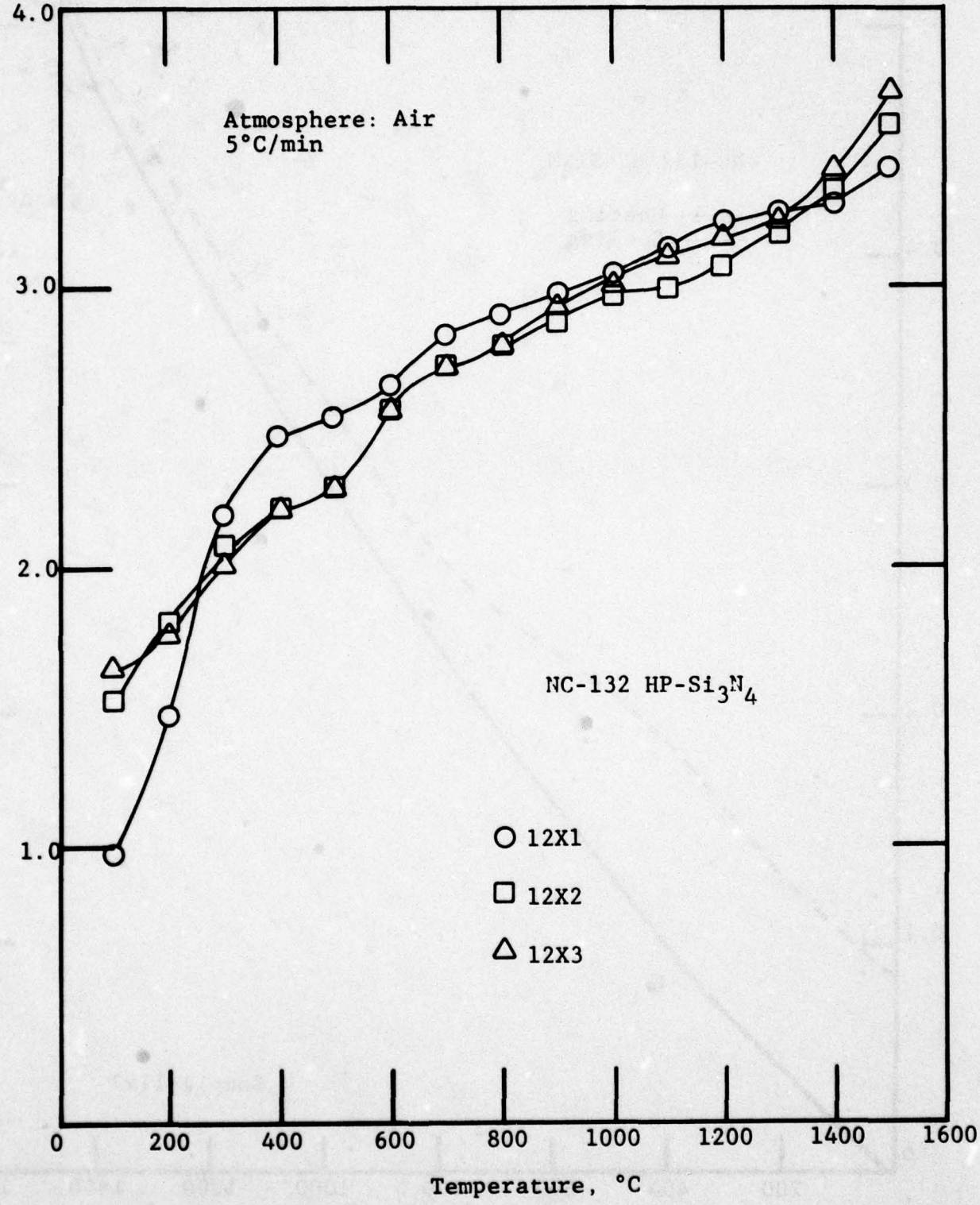

FIGURE 6.2 THERMAL EXPANSION COEFFICIENT OF NC-132 HP Si_3N_4, Batch 2

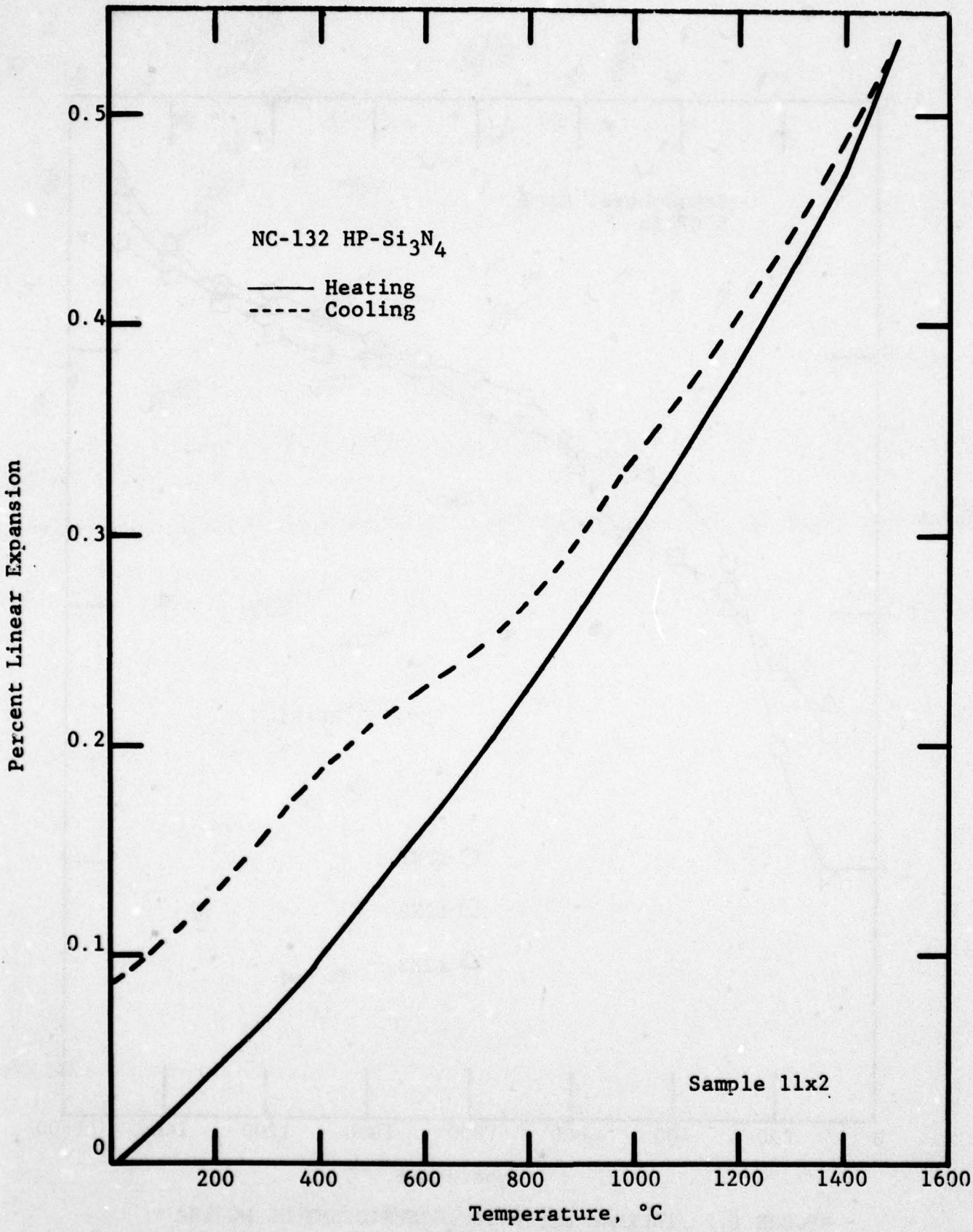

FIGURE 6.3 THERMAL EXPANSION OF NC-132 HP Si_3N_4

To investigate these effects further, additional tests were conducted during the current reporting period.

Thermal expansion tests were conducted up to 1500°C on NC-132 hot pressed Si_3N_4 in environments consisting of varying amounts of oxygen in an attempt to provide further empirical evidence from which to infer the origin of the glassy surface layer. These tests were conducted in dry nitrogen, oxygen-free nitrogen, and in a nitrogen -2% hydrogen mixture. The results are presented in Table 6.1, in terms of the permanent length changes as a function of environment. It is observed that for all nitrogen environments, roughly the same results were obtained as in air environment. The magnesia-doped hot pressed material tested in an inert atmosphere exhibited a glassy coating similar to that observed on air-tested samples. It would thus appear that the glassy coating and resultant length increases observed for the hot pressed material after 1500°C exposure in the expansion test is indeed the impurity silicate phase present at the grain boundaries, and is largely independent of environment. This phase apparently exudes from the sample at high temperature due to its relatively low viscosity and thermal expansion mismatch with the Si_3N_4 grains.

This empirical evidence of the apparent extent of the silicate impurity phase in MgO-doped (hot pressed) Si_3N_4 is entirely consistent with both the flexural strength and deformation behavior as well as the creep behavior of NC-132 relative to that of NC-350 reaction sintered material. The appearance of the scale formation as a relatively amorphous material (that starts to develop a dendritic crystalline form upon extended elevated temperature exposure) lends credence to the concept of deformation being controlled by a glassy grain boundary phase in MgO-doped Si_3N_4.

TABLE 6.1

COMPARISON OF CHANGE IN PHYSICAL DIMENSIONS OF NC-132 HPSN SAMPLES TESTED FOR THERMAL EXPANSION IN VARIOUS ENVIRONMENTS*

ENVIRONMENT	LENGTH CHANGE %
AIR	+.07 to +.18
DRY NITROGEN 99.7% N_2 (32 ppm Moisture Maximum)	+.07
OXYGEN-FREE NITROGEN (max O_2 = 0.5 ppm)	+.13
N_2 - 2% H_2	+.13

*For comparison, NC-350 RS Si_3N_4 exhibited a +.01% length increase in air

It is emphasized here that these results are preliminary and certainly not conclusive regarding the possible existence of a glassy impurity phase in HPSN. The conclusions are based on the presence of the glassy layer even after exposure in an "oxygen-free" environment. However, Tripp and Graham[109] have shown significant oxidation of HPSN down to 10^{-9} atm. P_{O_2}. Clearly, more basic work is required to determine the exact nature of the impurity phases in HP-Si_3N_4.

6.1.3 NC-435 Siliconized SiC

The thermal expansion coefficient of the remaining two batches of NC-435 siliconized SiC is presented in Figures 6.4 and 6.5. The data are similar to batch 1 behavior reported previously[2]. At 1000°C the coefficient of thermal expansion for NC-435 varies from 4.2×10^{-6}/°C to 4.5×10^{-6}/°C, the variation probably due to differences in silicon content as discussed previously. Norton product literature indicates a coefficient of thermal expansion at 1100°C of 4.8×10^{-6}/°C. Present data are lower than this ($4.3\text{-}4.5 \times 10^{-6}$/°C) probably reflecting the larger silicon content in the present material. Hot pressed silicon carbide exhibits an expansion coefficient of $\sim 5.1 \times 10^{-6}$/°C at 1100°C[80]. The expansion coefficient of silicon is lower (2.33×10^{-6}/°C) than that of high purity silicon carbide.[81]

6.1.4 Reaction Sintered Si_3N_4 Materials

The coefficient of thermal expansion for NC-350 reaction sintered Si_3N_4 is $2.8 \pm 0.1 \times 10^{-6}$/°C at 1000°C. Figure 6.6 illustrates the results for a typical NC-350 batch of three materials. In comparing this reaction sintered material with NC-132 HP Si_3N_4, note 1) the higher expansion coefficient throughout the temperature range, and 2) more rapidly increasing coefficient of expansion above 1350°C for the hot pressed material

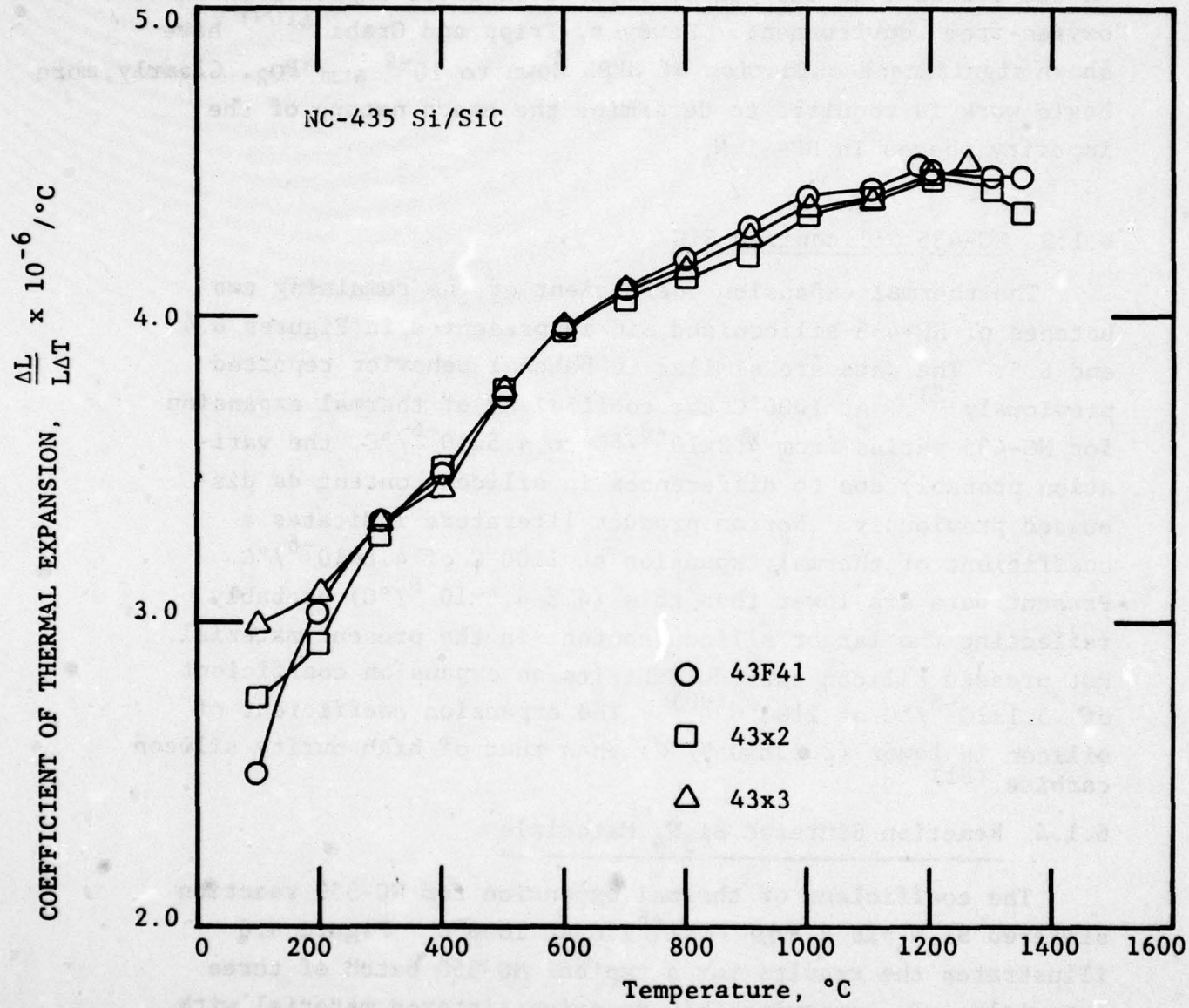

FIGURE 6.4 COEFFICIENT OF THERMAL EXPANSION OF NC-435 SILICONIZED SiC (Batch 3)

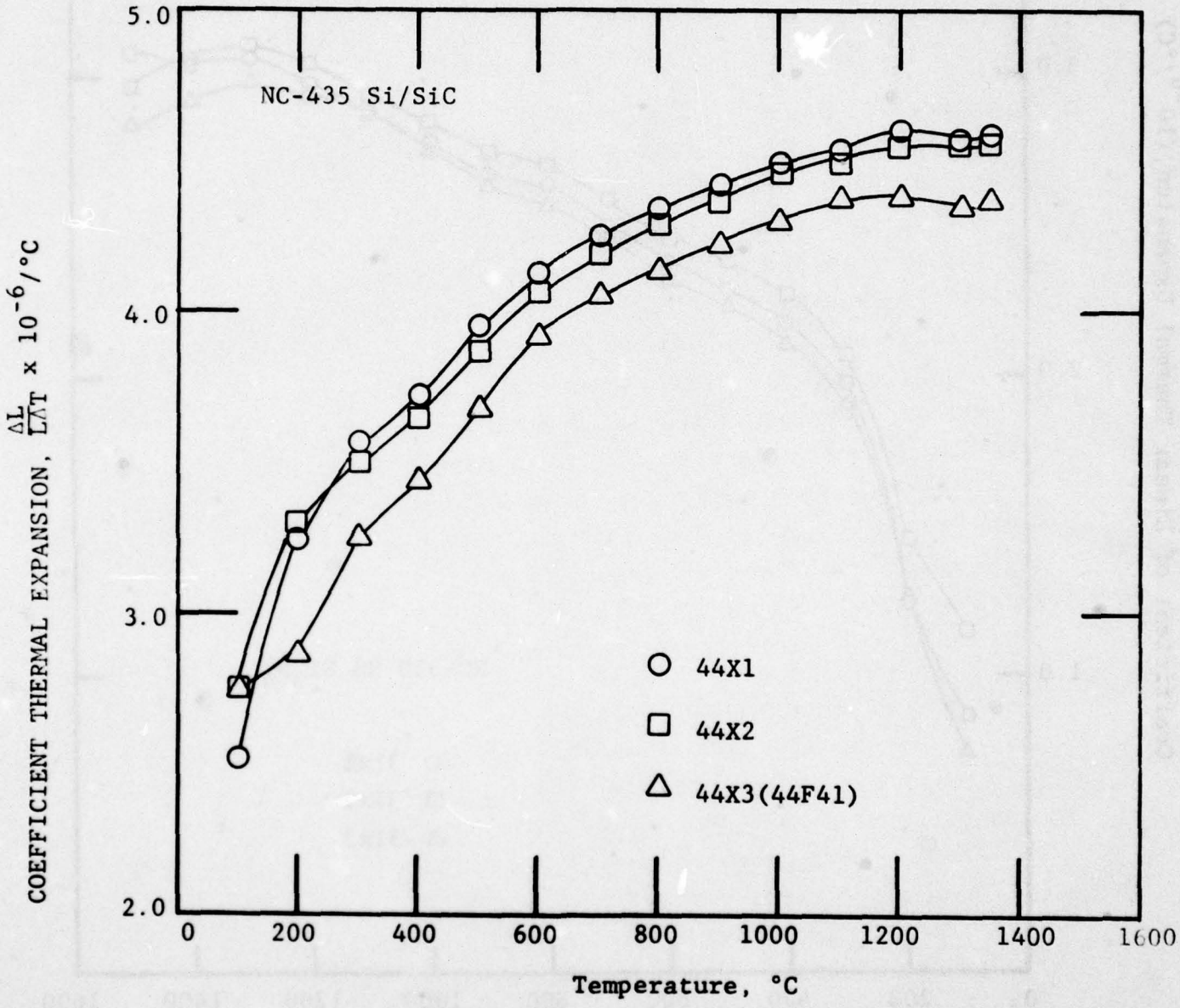

FIGURE 6.5 THERMAL EXPANSION COEFFICIENT OF NC-435 SILICONIZED SiC (Batch 4)

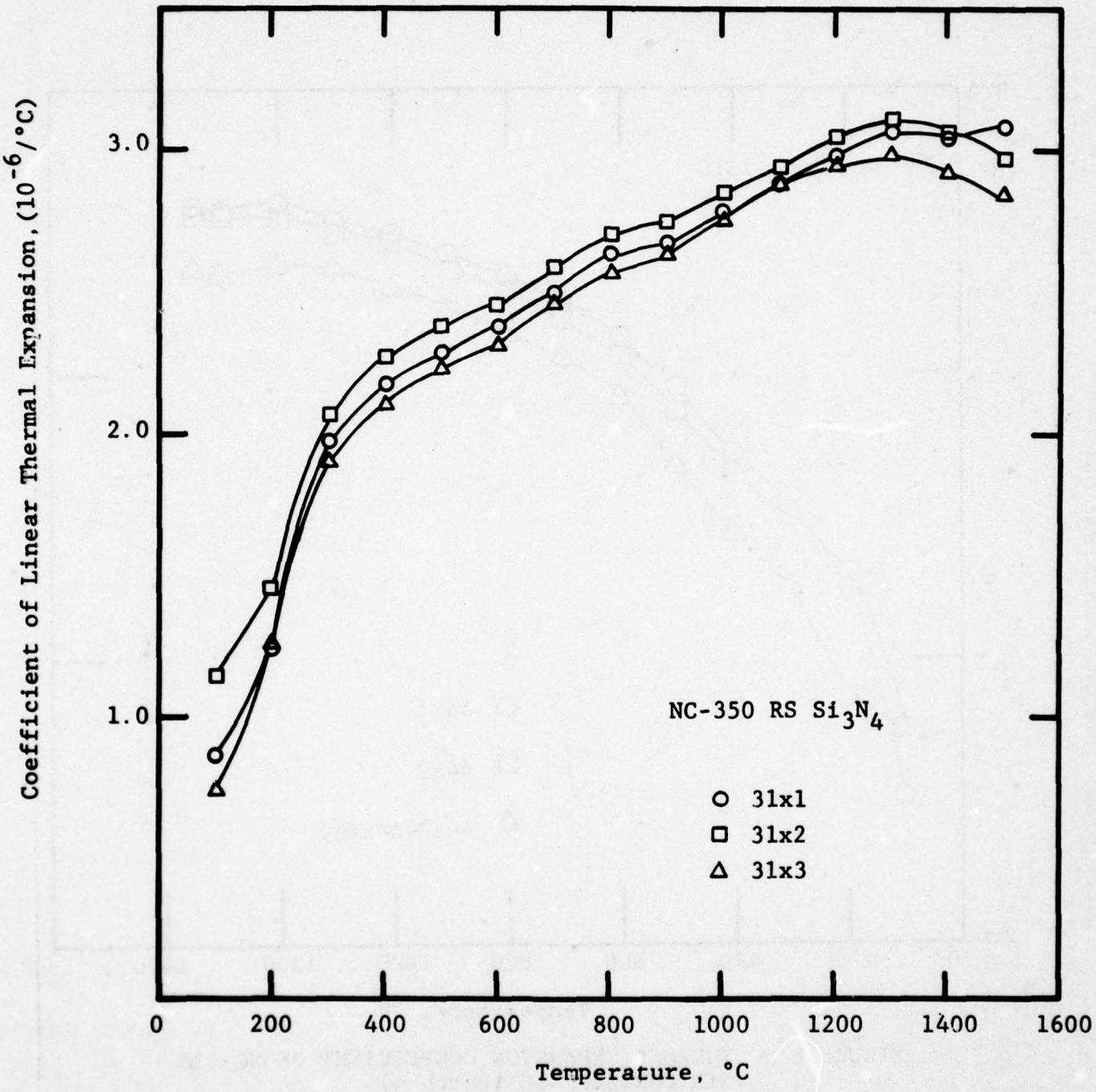

FIGURE 6.6 THERMAL EXPANSION COEFFICIENT OF NC-350 RBSN, BATCH 1

(see Figure 6.2). At 1000°C NC-132 exhibits an expansion of $3.0 \pm .05 \times 10^{-6}$/°C. Both of these aspects of the thermal expansion are apparently related to the silicate phase concentrated at the grain boundaries of the hot pressed material as discussed above.

Figures 6.7 through 6.9 present data for the KBI reaction sintered material. The expansion coefficient is seen to vary from 2.6 to 3.0×10^{-6}/°C at 1000°C. It is more variable than in NC-350, probably due to the more hetergeneous nature of the KBI material. Note that KBI batches 2 and 3 do not exhibit the change at ~1350°C as do the other reaction sintered materials. The two KBI batches behave more like the hot pressed material in this respect. Since it has been previously shown that the KBI and NC-350 materials had similar low impurity contents with respect to the hot pressed material, this might be an indication of differences in oxidation rate or surface area exposed. Recall that the KBI material had more open porosity than NC-350. However, no visual evidence of oxidation was present on the KBI samples after testing (i.e., of a magnitude similar to that observed on the impure hot-pressed materials).

Figure 6.10 presents a composite curve of the thermal expansion coefficient of all materials tested. The three silicon nitride materials exhibit roughly similar behavior when compared to the silicon carbide material, which exhibits a considerably higher expansion coefficient. This high thermal expansion for silicon carbide is a detriment for thermal shock resistance (as is its high modulus), but is sometimes offset by high strength and especially high thermal conductivity (refer to Section 6.3, Thermal Shock). For thermal expansion, the data obtained show that an error band of $\pm 0.2 \times 10^{-6}$/°C encompasses the great majority of the within-and between-batch variability exhibited by NC-132 HPSN, NC-435 Si/SiC, NC-350 RSSN, and KBI RSSN.

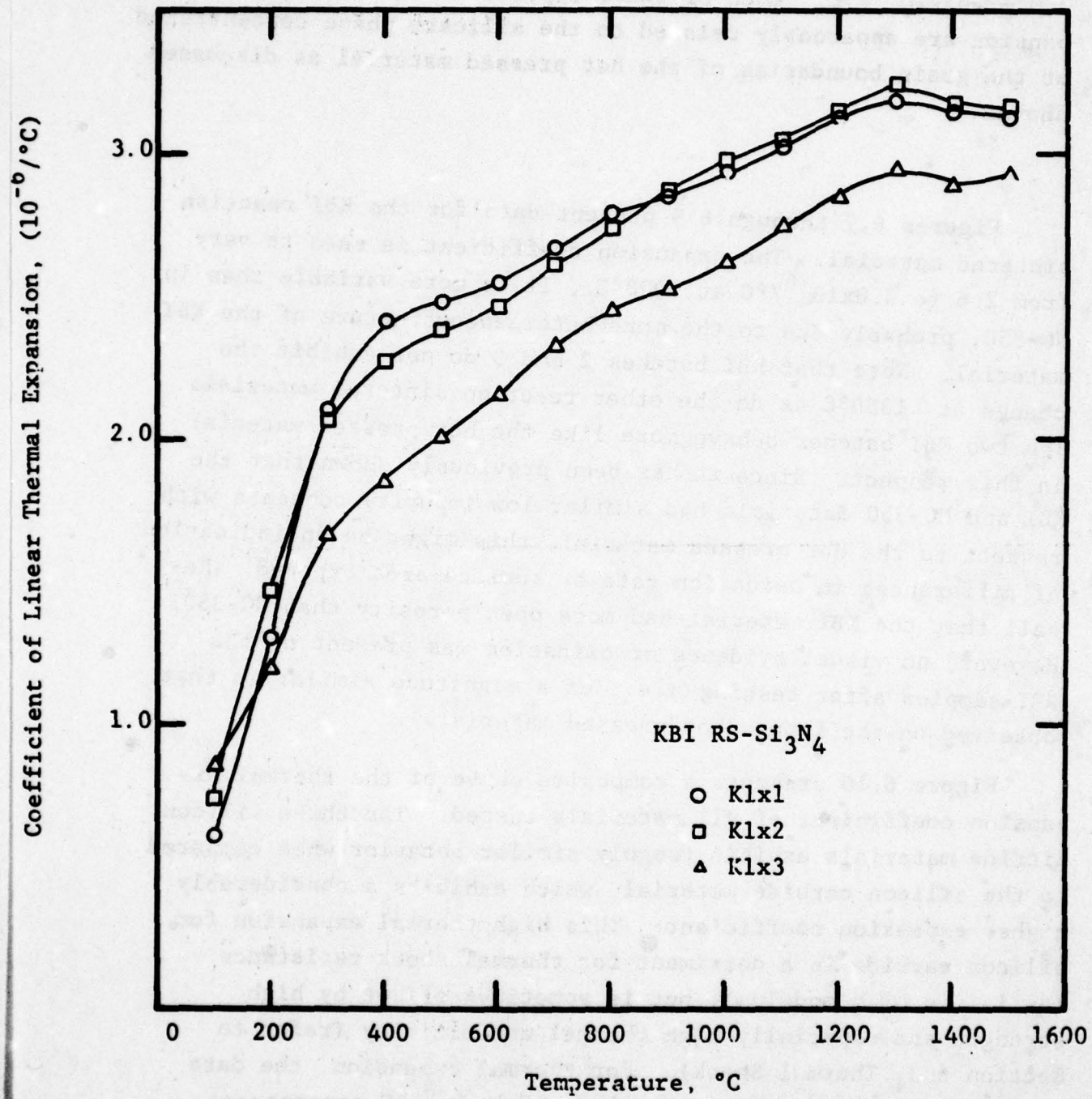

FIGURE 6.7 COEFFICIENT OF THERMAL EXPANSION FOR KBI RBSN, BATCH 1

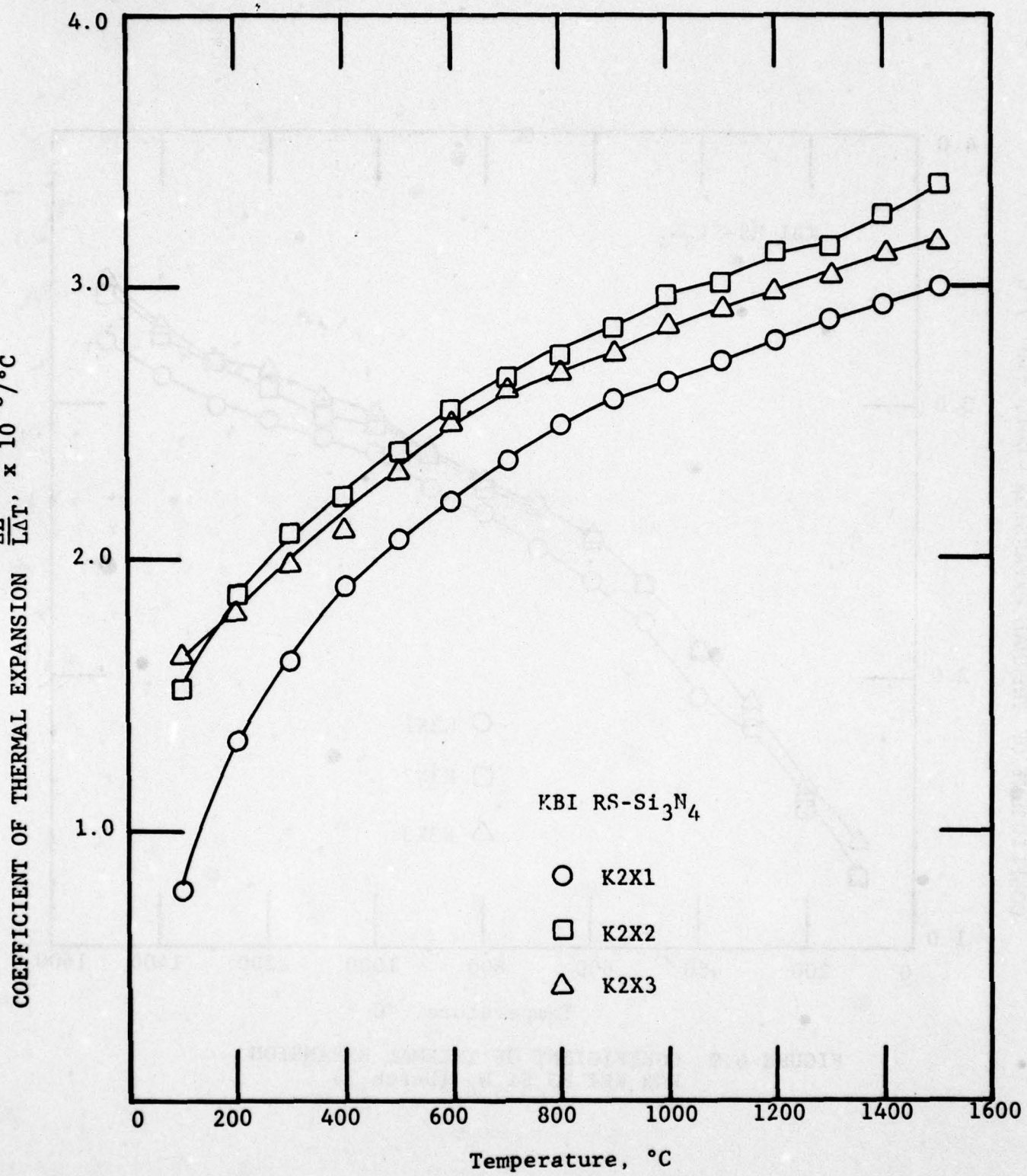

FIGURE 6.8 THERMAL EXPANSION COEFFICIENT OF KBI RS Si_3N_4, BATCH 2

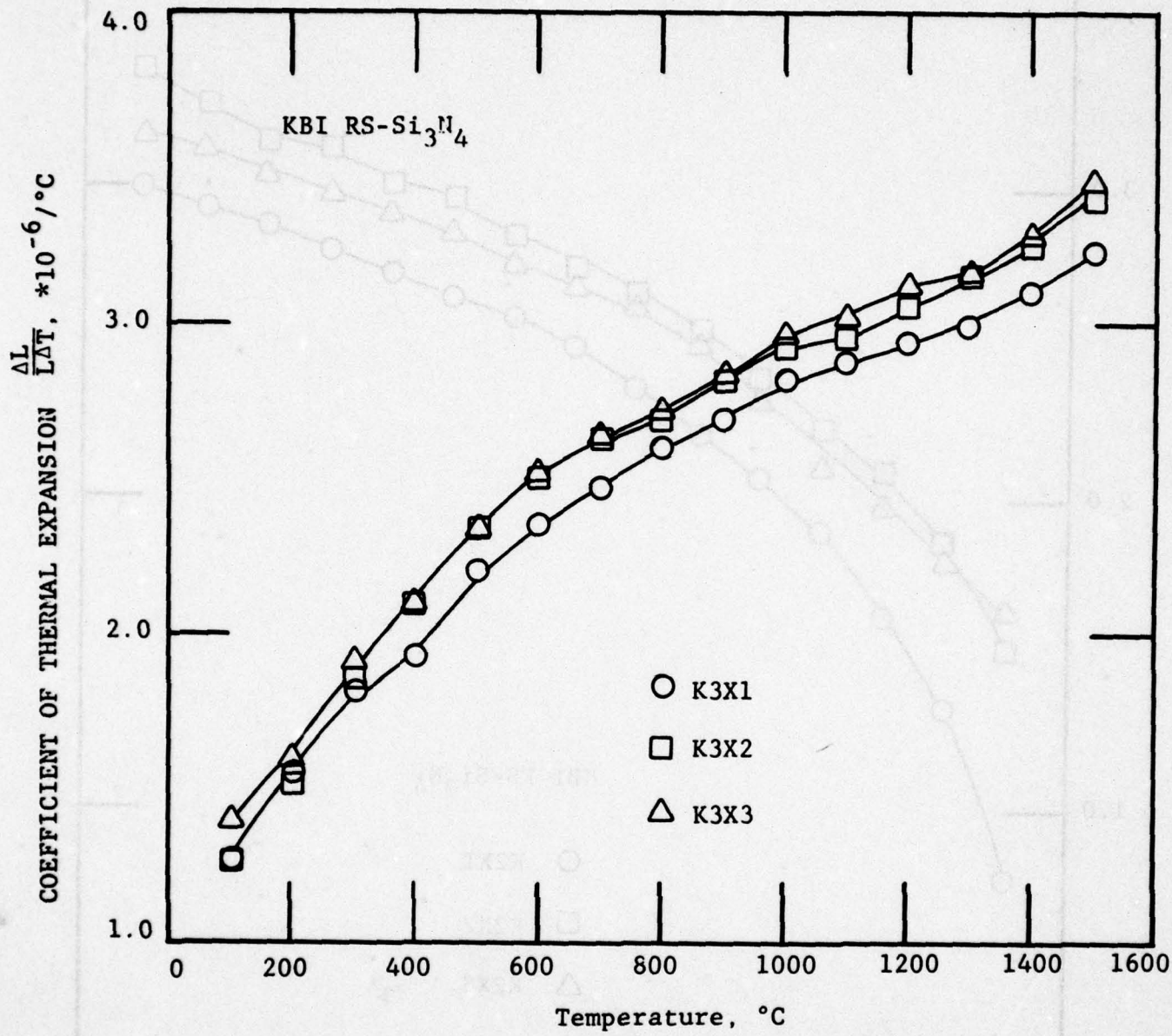

FIGURE 6.9 COEFFICIENT OF THERMAL EXPANSION FOR KBI RS Si_3N_4 (Batch 3)

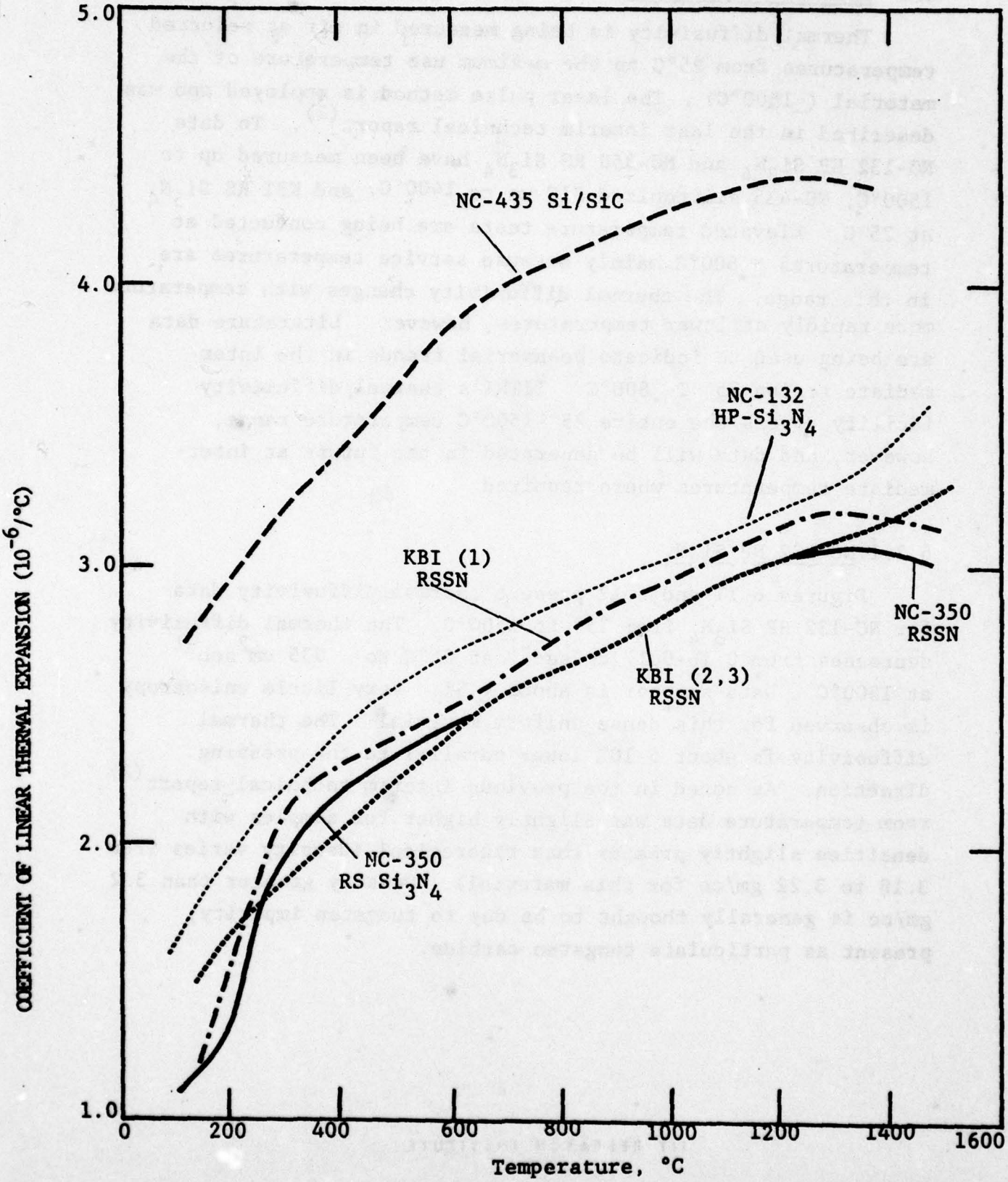

FIGURE 6.10 REPRESENTATIVE COMPOSITE THERMAL EXPANSION CURVES.

6.2 Thermal Diffusivity

Thermal diffusivity is being measured in air at selected temperatures from 25°C to the maximum use temperature of the material ($\leq$1500°C). The laser pulse method is employed and was described in the last interim technical report[2]. To date NC-132 HP Si_3N_4 and NC-350 RS Si_3N_4 have been measured up to 1500°C, NC-435 siliconized SiC up to 1400°C, and KBI RS Si_3N_4 at 25°C. Elevated temperature tests are being conducted at temperatures $\geq$ 800°C mainly because service temperatures are in this range. The thermal diffusivity changes with temperature more rapidly at lower temperatures, however. Literature data are being used to indicate behavorial trends in the intermediate region 25 <T< 800°C. IITRI's thermal diffusivity facility covers the entire 25°-1500°C temperature range, however, and data will be generated in the future at intermediate temperatures where required.

6.2.1 NC-132 HP Si_3N_4

Figures 6.11 and 6.12 present thermal diffusivity data for NC-132 HP Si_3N_4 from 25° to 1500°C. The thermal diffusivity decreases from 0.16-0.17 cm^2sec^{-1} at 25°C to ~.035 cm^2sec^{-1} at 1500°C. Data scatter is about $\pm$ 5%. Very little anisotropy is observed for this dense uniform material. The thermal diffusivity is about 5-10% lower parallel to the pressing direction. As noted in the previous interim technical report[2], room temperature data was slightly higher for samples with densities slightly greater than theoretical (density varies from 3.18 to 3.22 gm/cc for this material). Density greater than 3.2 gm/cc is generally thought to be due to tungsten impurity, present as particulate tungsten carbide.

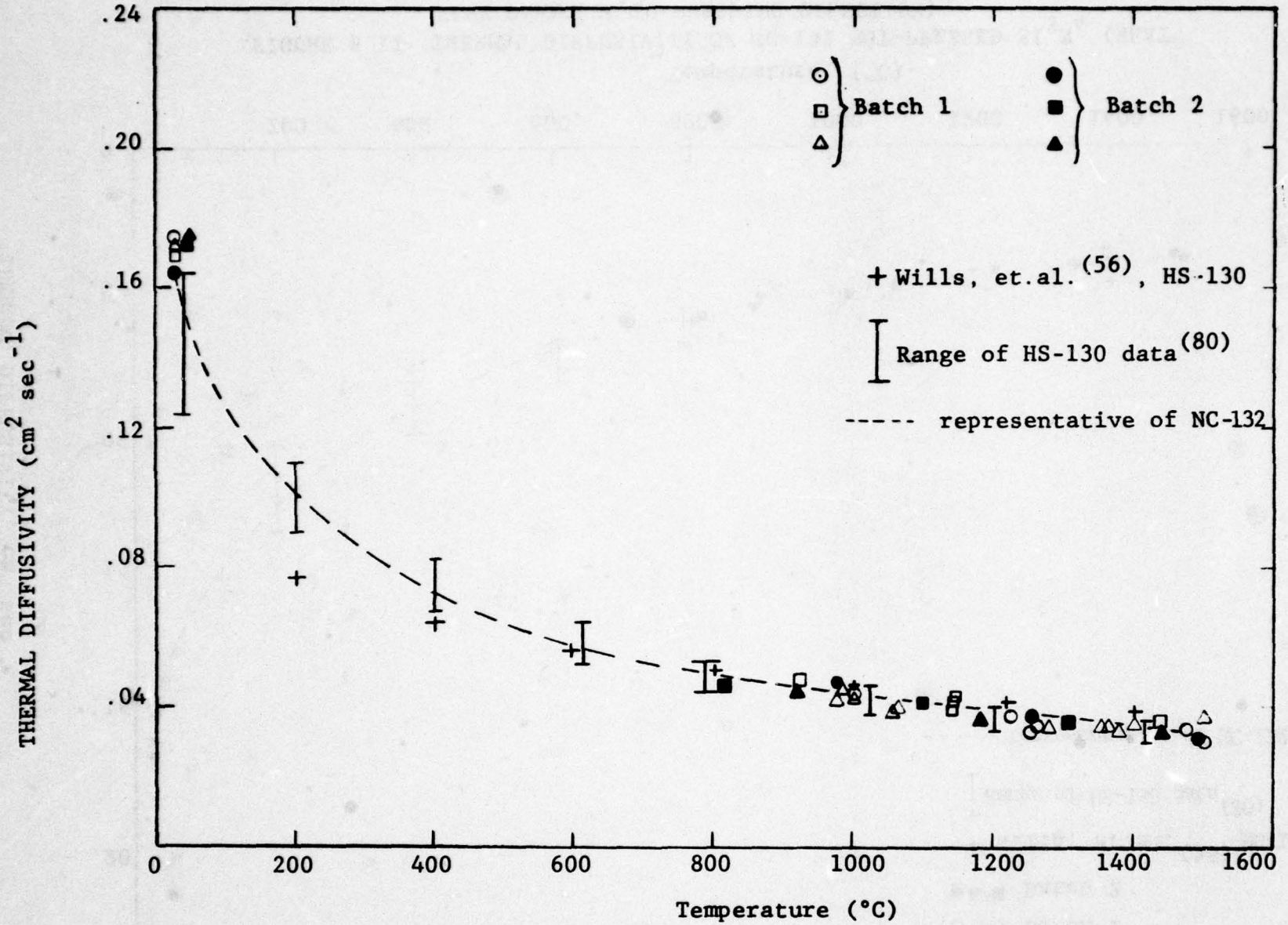

FIGURE 6.11 THERMAL DIFFUSIVITY OF NC-132 HOT PRESSED Si_3N_4
(HEAT FLUX PERPENDICULAR TO PRESSING DIRECTION)

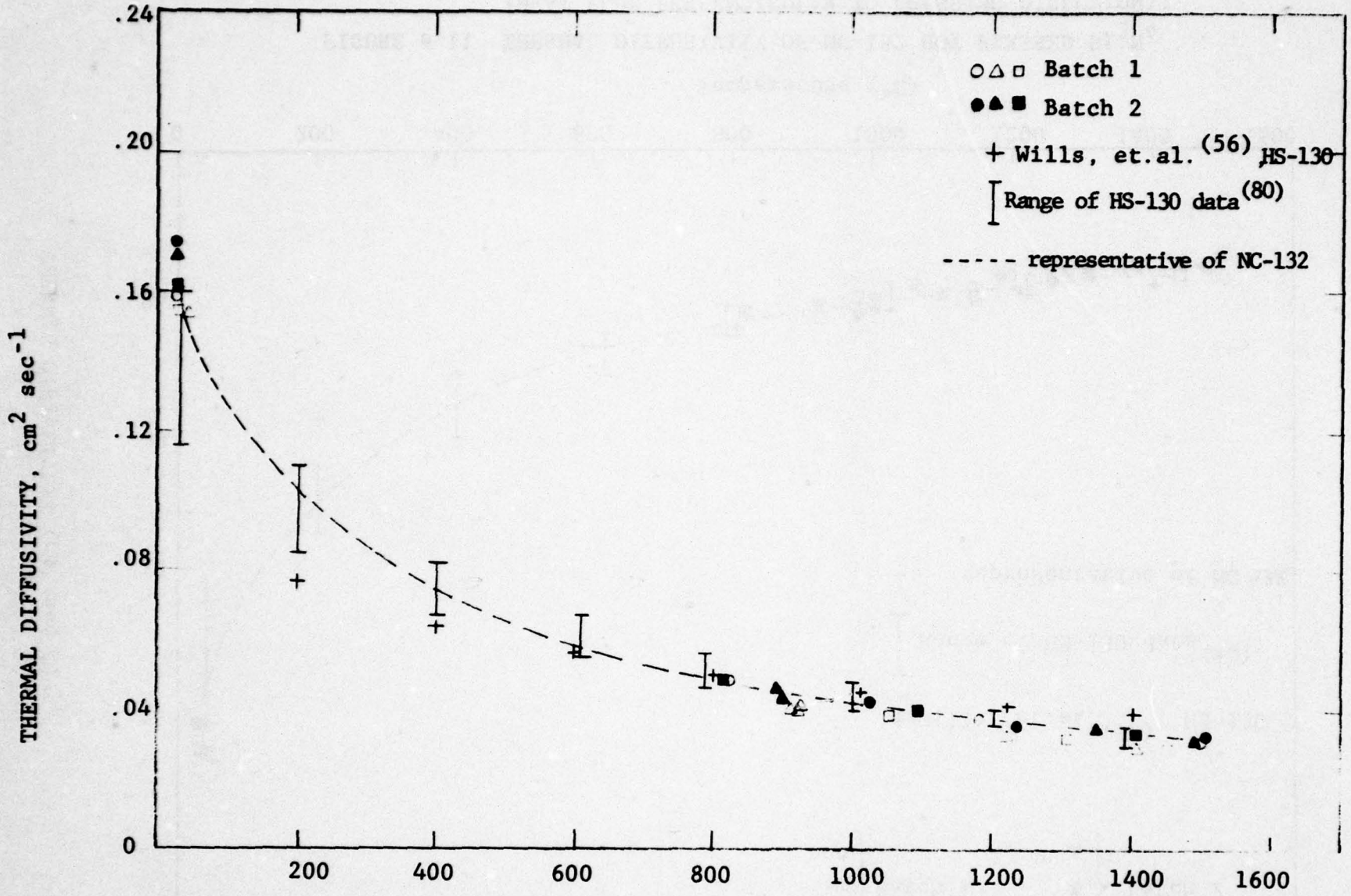

FIGURE 6.12 THERMAL DIFFUSIVITY OF NC-132 HOT-PRESSED Si_3N_4 (HEAT FLUX PARALLEL TO PRESSING DIRECTION)

The present room temperature data for NC-132 (~.16-.17 cm^2sec^{-1}) are higher than Norton data[32] (.13 cm^2sec^{-1}) for materials of density close to theoretical (3.2 gm/cc). However, Battelle data for Norton HS-130 HP Si_3N_4 (the predecessor to NC-132) generated on the AMMRC/Ford/Westinghouse program[80], showed a batch variability in room temperature thermal diffusivity equivalent to this discrepancy. At elevated temperatures the current NC-132 data (Figures 6.11 and 6.12) are in good agreement with Battelle data for HS-130 HP Si_3N_4[80,82]. The range of HS-130 data obtained on various samples and billets is illustrated in the figures, and was used to estimate behavior at intermidiate temperature for NC-132. Data on HS-130 obtained at AFML and reported by Wills, et.al[56] are shown in Figures 6.11 and 6.12 to be slightly higher than the Battelle (HS-130) and IITRI (NC-132) data at elevated temperatures, and lower than the Battelle and estimated NC-132 data at lower temperatures.

From the present thermal diffusivity data, it is concluded that NC-132 hot pressed Si_3N_4 exhibits 1) very uniform microstructure and composition, 2) very little anisotropy with respect to molding pressure, and 3) thermal diffusivity similar to its predecessor, HS-130.

6.2.2 NC-435 Siliconized SiC

The thermal diffusivity of NC-435 siliconized SiC is presented in Figure 6.13. Data were obtained in air at 25°C, and at various temperatures between 800°C and 1400°C. Good within batch and between batch variability was observed, the maximum variation for all samples being $\pm$ 5%. The thermal diffusivity is seen to decrease from ~0.7 cm^2sec^{-1} at 25°C to ~.07 cm^2sec^{-1} at 1400°C, being considerably higher, especially at room temperature, for this silicon carbide as compared to the high density silicon nitride.

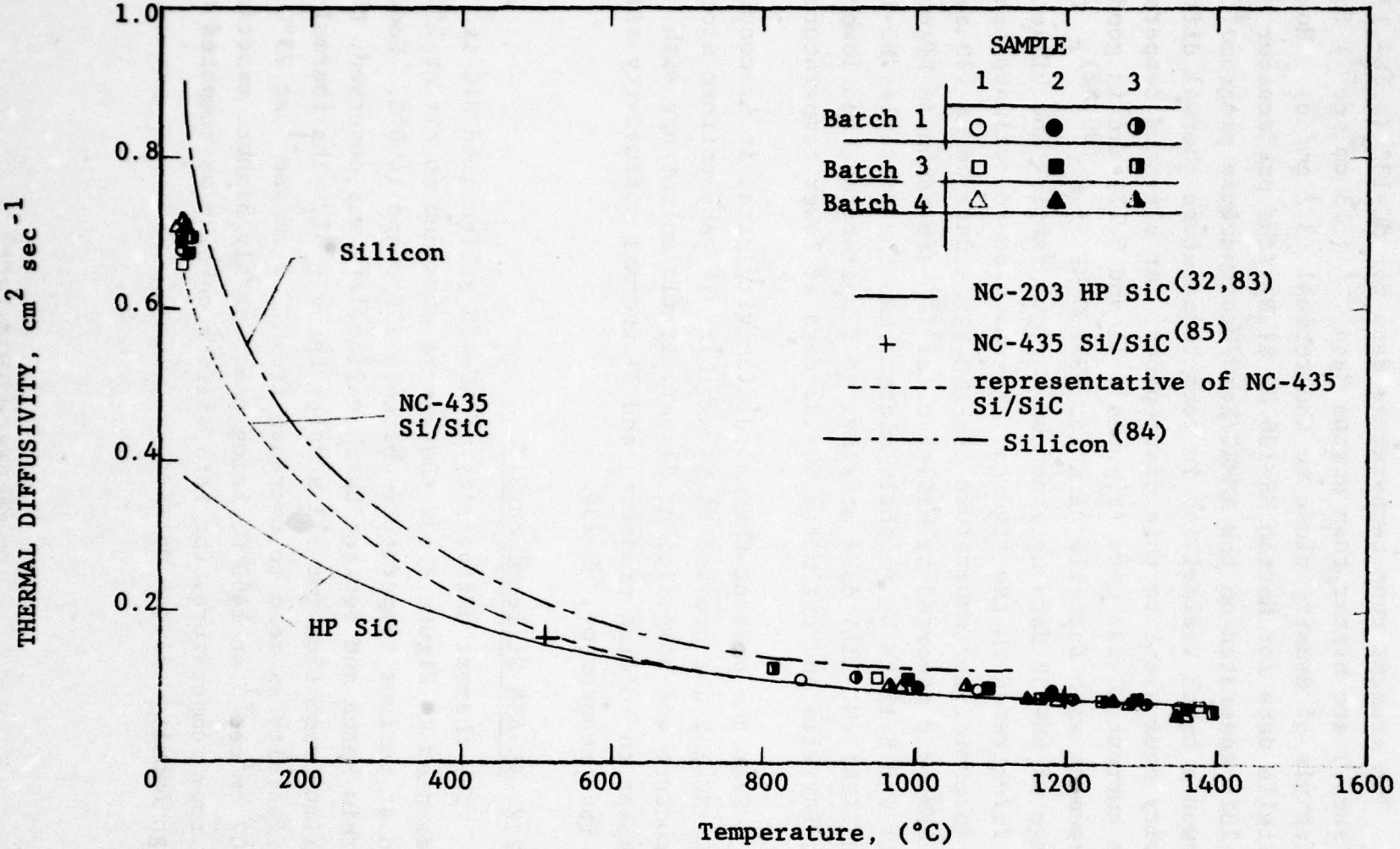

FIGURE 6.13 THERMAL DIFFUSIVITY OF NC-435 SILICONIZED SiC

High temperature data for this SiC-20 vol.% Si material is in good agreement with Norton product literature[85], as shown in Figure 6.13. Behavior at intermediate temperatures is estimated from the known behavior of silicon metal[84] and hot pressed silicon carbide[32,83], which would represent upper and lower bounds for the behavior of the Si/SiC composite. It is observed that the silicon phase, although present in a minor amount as a continuous grain boundary phase (v~.2), exerts a strong influence on the Si/SiC thermal diffusivity at low temperatures, particularly at 25°C where the thermal diffusivity of silicon is roughly a factor of three greater than hot pressed SiC. At elevated temperatures the thermal diffusivity of silicon decreases rapidly to a value only ~30% greater than that of hot pressed SiC. Thus, the thermal diffusivity of Si/SiC materials at high temperature would not deviate as much from HP SiC data.

The room temperature thermal diffusivity of the SiC-20vol.% Si material can be computed by application of the appropriate theoretical model for heterogeneous two-phase systems. Such models involve the thermal conductivity and volume fraction of each consitituent phase. Kingery[86] has applied the Eucken relation to Si/SiC materials with some degree of success. Application of this relation (for thermal conductivity) to the case of NC-435 (V_{Si} ~.2) results in a room temperature thermal diffusivity about 30% lower than measured. The high conductivity silicon phase has a greater influence on the thermal conductivity of the NC-435 Si/SiC material than predicted by the Eucken relation. Other theoretical relations for two-phase heterogeneous materials, such as models by Maxwell, Rayleigh, and Bruggeman, are discussed by Baxley[87], and will be applied to NC-435.

6.2.3 NC-350 RS Si_3N_4

The thermal diffusivity of NC-350 reaction sintered Si_3N_4 is presented in Figure 6.14. Measurements were made at 25°C, as discussed previously[2], and at elevated temperatures $\geq$ 900°C. At room temperature, the density variations between samples of NC-350 lead to $\pm$30% variations in thermal diffusivity, as shown in Figure 6.15. The high temperature results shown in Figure 6.14 exhibit the same $\pm$ 30% variation. The average density of the present NC-350 samples was $\bar{\rho}$ = 2.3 gm/cc. The curve shown dotted in Figure 6.14 is representative of the entire population of samples tested on this program (2.08 $\leq$ ρ $\leq$ 2.53 gm/cc). The behavior at intermediate temperatures (25 < T < 800°C) was estimated from the shape of the curve for NC-350 obtained at AFML and reported by Wills, et.al[56] for material with a density of 2.6 gm/cc. Data for the higher density material are substantially higher than the current data for NC-350. However, Norton data[32] for NC-350 at 25°C for a material with density ρ = 2.4 gm/cc (derived from thermal conductivity and specific heat) is in good agreement with the current data for materials of similar density.

Room temperature thermal conductivity for each sample of NC-350 was computed from the measured thermal diffusivity, known density, and literature values[83] for specific heat of injection molded reaction sintered silicon nitride ($\alpha = \lambda/\rho c_p$). Specific heat is a volumetric property and varies only slightly for a wide variety of silicon nitride materials. The results were used to determine the functional form of the porosity dependency of thermal conductivity for NC-350 reaction sintered Si_3N_4.

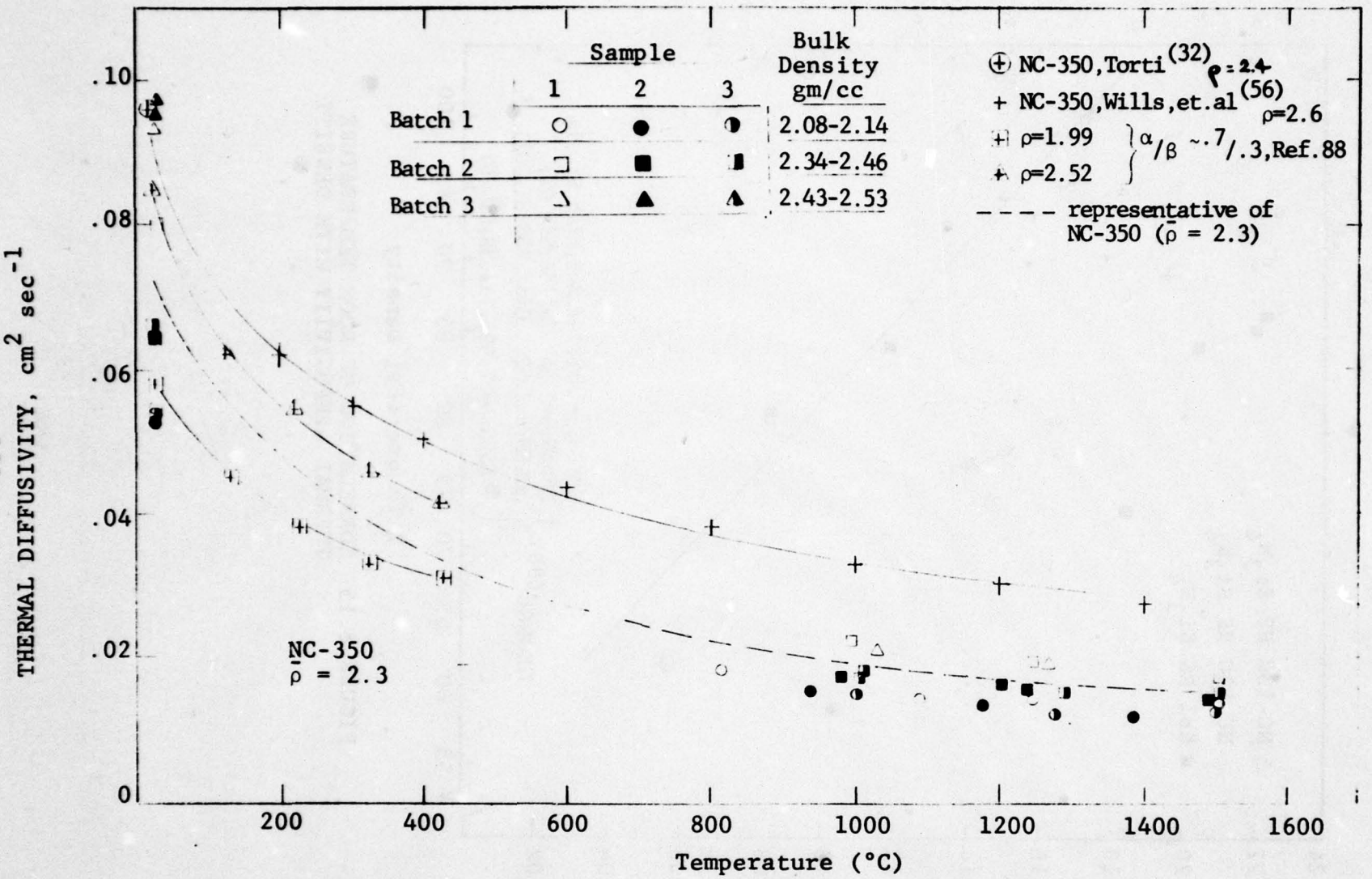

FIGURE 6.14 THERMAL DIFFUSIVITY OF NC-350 REACTION SINTERED Si_3N_4

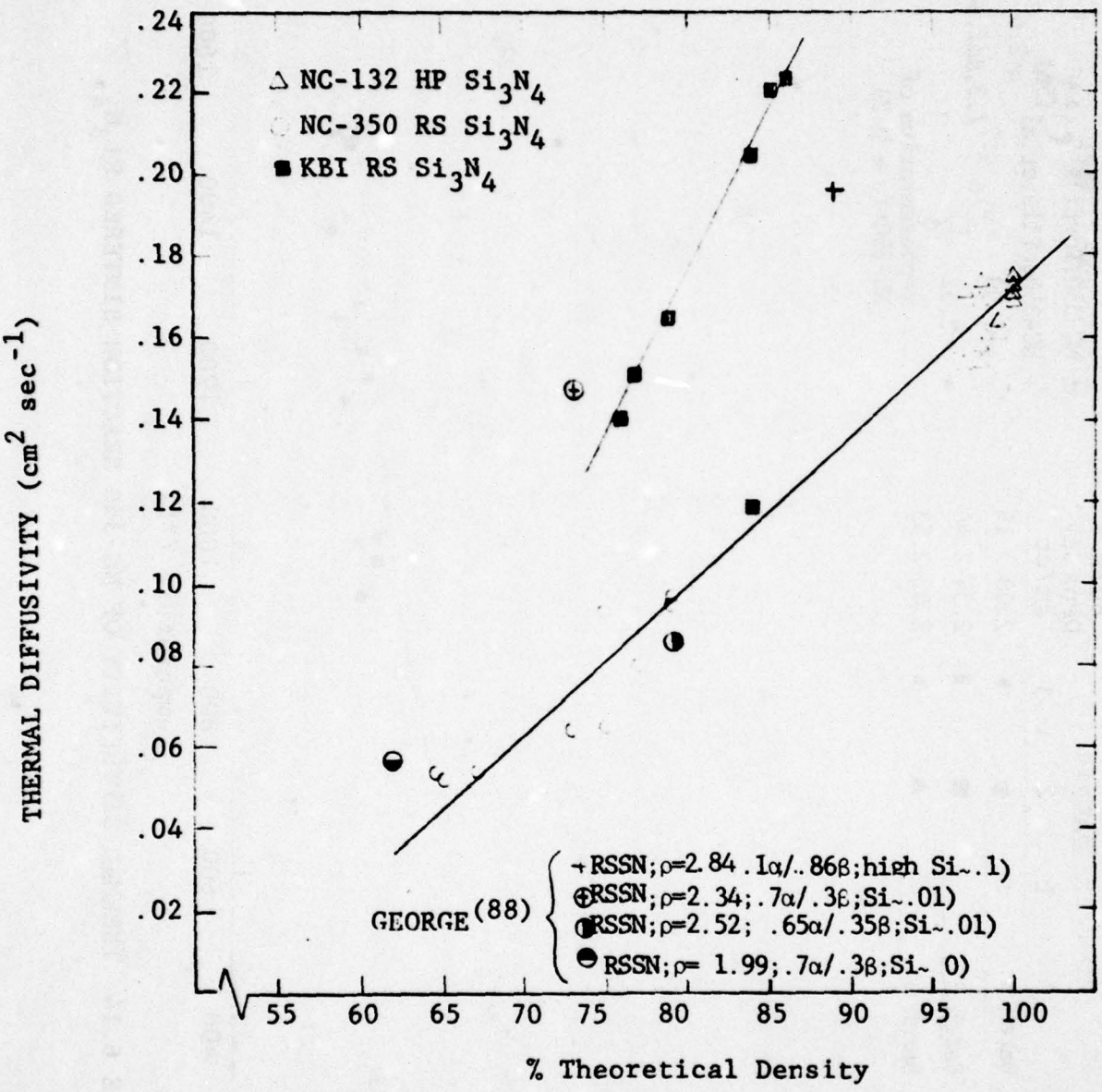

FIGURE 6.15 CORRELATION OF ROOM TEMPERATURE THERMAL DIFFUSIVITY WITH DENSITY

The relative thermal conductivity λ/λ_o for NC-350 is plotted as a function of volume fraction porosity in Figure 6.16. Fractional porosity is determined from the relation

$$P = 1 - \frac{\rho}{\rho_{theo.}}$$

A value of $\rho = 3.2$ gm/cc is used as the theoretical density. The term λ is the thermal conductivity at density ρ. The term λ_o is the thermal conductivity at zero porosity. The value of λ_o was determined from behavior of NC-132, the dense hot pressed material ($\alpha = .16$ cm^{2}sec^{-1}, $\rho = 3.18$ gm/cc, $c_p = .159$ cal gm^{-1} C^{-1}), to be $\lambda_o = .081$ cal cm^{-1} sec^{-1} C^{-1}.

Figure 6.16 illustrates the computed λ/λ_o vs P for NC-350 at room temperature, compared with various forms of the thermal conductivity-porosity dependency that have been applied to ceramic materials in the literature. Rhee[89] reviews most of these forms. The $(1-P)/(1+P)$ relationship was applied to silicon nitride by Godfrey and May[90]. Rhee found that for a wide variety of ceramic materials, including alumina and titanium nitride, that the porosity dependency took the form $(1-P)/(1+nP^2)$, where n is a constant ranging $0 \leq n \leq 14$.

The present data for porous NC-350 follows a similar relationship, but with $14 \leq n \leq 18$, as shown in Figure 6.16. It is important to note that for NC-350 RS Si_3N_4 that thermal conductivity is more strongly dependent on porosity than predicted by the Francl-Kingery-Loeb correlation ($\lambda/\lambda_o = 1-P$) or the Moore relation ($\lambda/\lambda_o = (1-P)/(1+P)$).

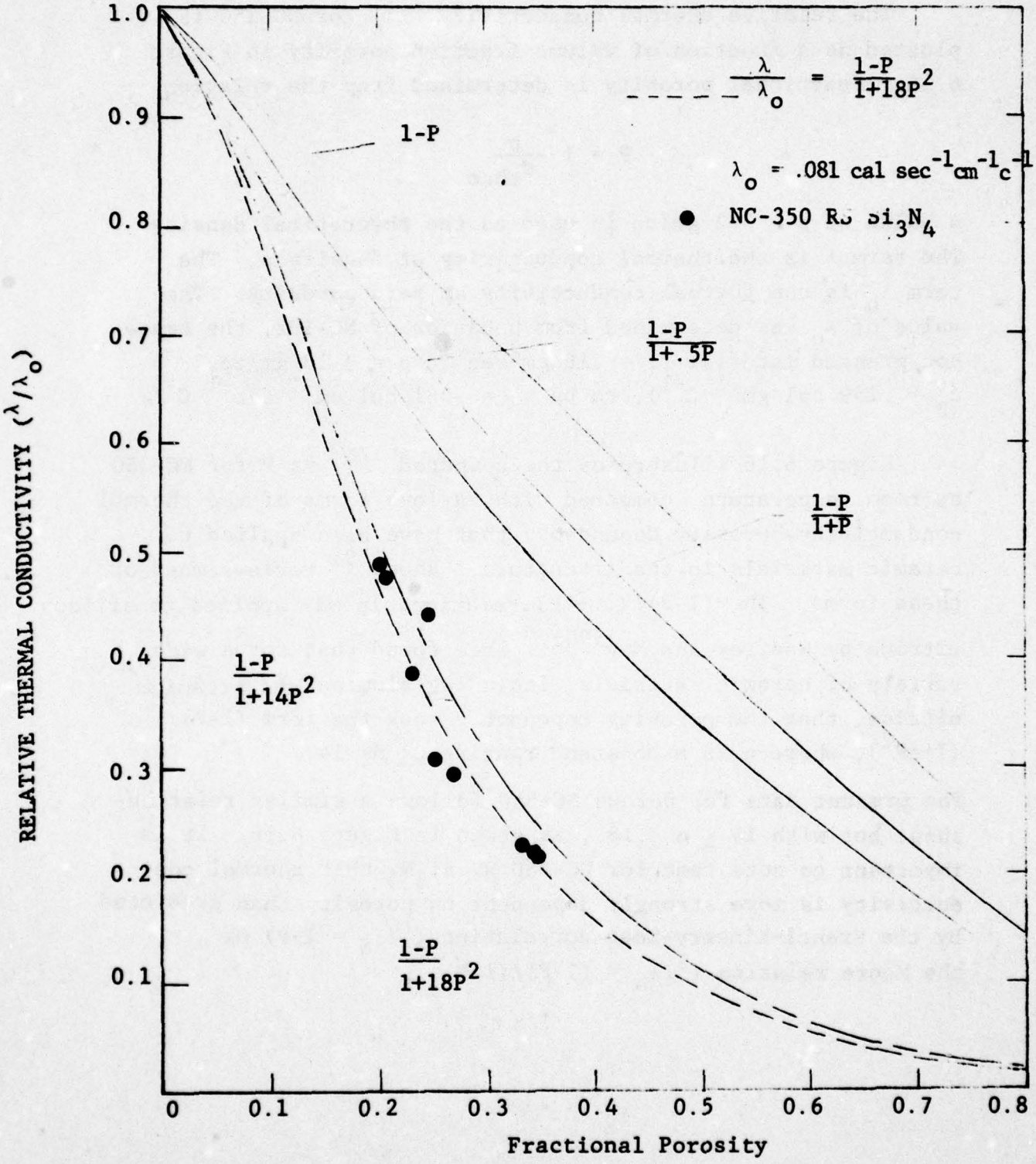

FIGURE 6.16 CORRELATION OF ROOM TEMPERATURE THERMAL CONDUCTIVITY OF NC-350 RS Si_3N_4 WITH POROSITY

George[88] has found a wide spread in thermal diffusivity behavior of silicon nitride ceramics. Heat flow mechanisms in silicon nitride are functions of porosity, high conductivity metal phases such as silicon, crystalline α/β form, grain morphology, defect structure, etc.. Figure 6.14 illustrates that two RS Si_3N_4 materials reported by George with similar density and phase composition to NC-350 give similar thermal diffusivity results. However, in general, the mechanisms of heat flow in nitrides (as well as carbides) are not well understood.

6.2.4 KBI RS Si_3N_4

The thermal diffusivity of the KBI reaction sintered material is currently being measured at elevated temperatures. At 25°C it was reported[2] that all except one of the KBI samples gave thermal diffusivity values much higher than expected. Roughly half the samples exhibited room temperature thermal diffusivity substantially greater than the hot pressed material, NC-132. This behavior is shown in Figure 6.15. The reaction sintered materials measured by George[88] provide insight into what may be the cause of this. Plotted with the KBI, NC-350 and NC-132 data in Figure 6.15 are data from four reaction sintered materials measured by George. These materials had a range of density, phase composition, and silicon content. Although there is not enough data with controlled variations of a single variable to be definitive it is noted that the two samples with high thermal diffusivity(similar to the KBI data) have high silicon content and/or high β-Si_3N_4 content. It was

determined in Section 4 that KBI RS Si_3N_4 contained substantially more β-Si_3N_4 than NC-350. It is not known at present whether α-or β-Si_3N_4 would be expected to exhibit the higher thermal diffusivity. However, NC-132 was shown in Section 4 to have a high β-Si_3N_4 content, whereas α-Si_3N_4 was shown to be the major phase of NC-350. This tends to rule out the possibility of a large difference in α/β-Si_3N_4 content between the KBI and Norton reaction sintered materials being the cause of the high thermal diffusivity of the KBI material, since the differences in NC-132 and NC-350 data are entirely explained by porosity.

However, it was noted in Section 6.2.2 that silicon has a very high thermal diffusivity at 25°C. Examination of the optical micrograph of the microstructure of KBI presented in Section 4, indicates the apparent presence of a substantial amount of unreacted silicon (light, highly reflecting phase in the micrograph). There presumably is enough "free" silicon metal in the structure to significantly affect the room temperature thermal diffusivity. This interpretation of the microstructure of the KBI RS Si_3N_4 materials is consistent with the interpretation of the fracture surfaces discussed in Section 5.1.4. It was concluded there that the KBI material was not as well sintered as the NC-350 material. For a reaction bonded material this would mean the presence of unreacted silicon in the structure would not be surprising.

6.2.5 Comparison of Materials

The thermal diffusivity of NC-132 HP Si_3N_4, NC-435 Si/SiC and NC-350 RS Si_3N_4 materials are compared in Figure 6.17. The lower thermal diffusivity of the reaction sintered Si_3N_4 compared to the hot pressed material is the result of lower density.

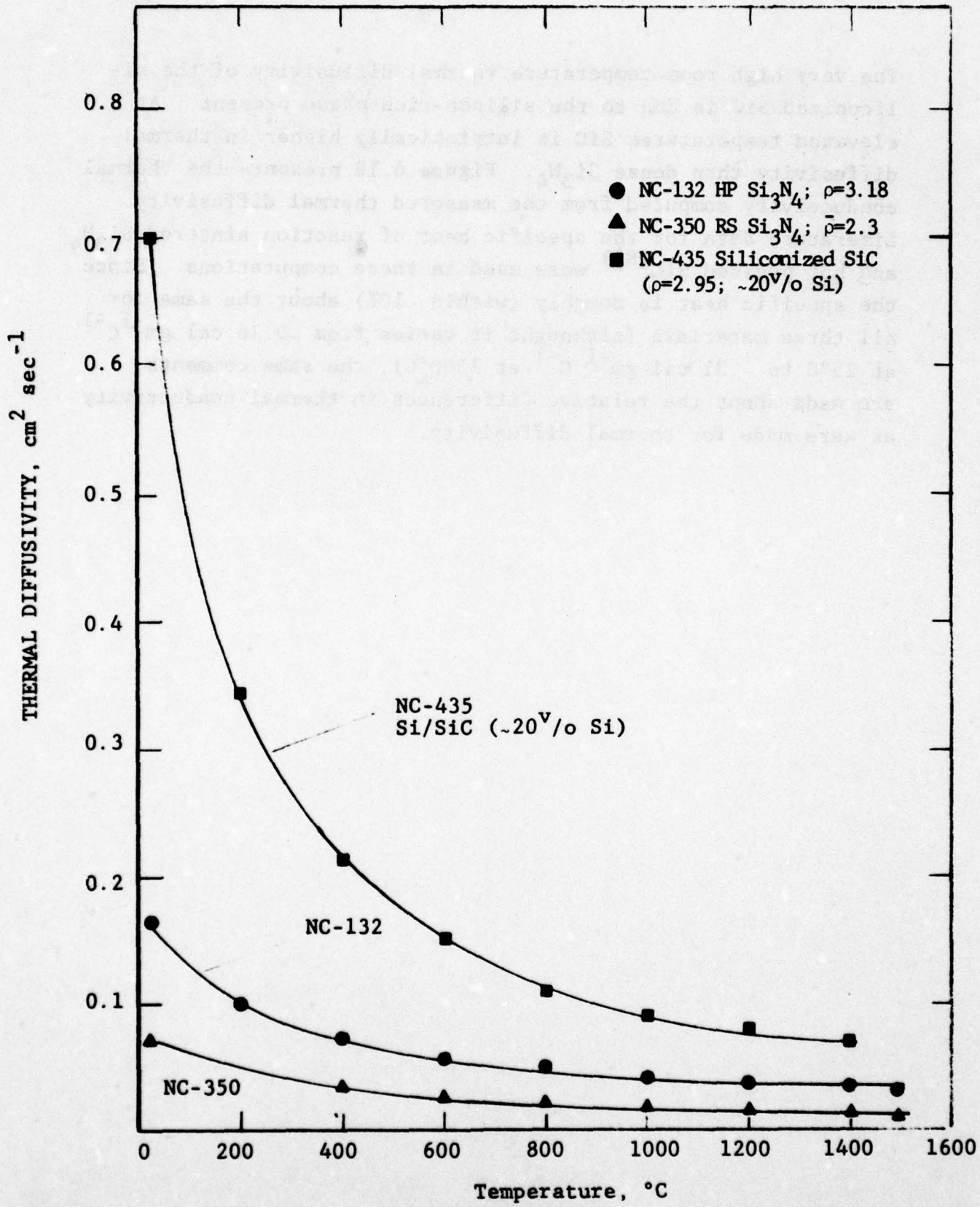

FIGURE 6.17 THERMAL DIFFUSIVITY OF NC-132, NC-435, and NC-350 MATERIALS.

The very high room temperature thermal diffusivity of the siliconized SiC is due to the silicon-rich phase present. At elevated temperatures SiC is intrinsically higher in thermal diffusivity than dense Si_3N_4. Figure 6.18 presents the thermal conductivity computed from the measured thermal diffusivity. Literature data for the specific heat of reaction sintered Si_3N_4 and hot pressed SiC[83] were used in these computations. Since the specific heat is roughly (within ~10%) about the same for all three materials (althought it varies from ~0.16 cal $gm^{-1}C^{-1}$ at 25°C to ~.31 cal gm^{-1} C^{-1} at 1500°C), the same comments are made about the relative differences in thermal conductivity as were made for thermal diffusivity.

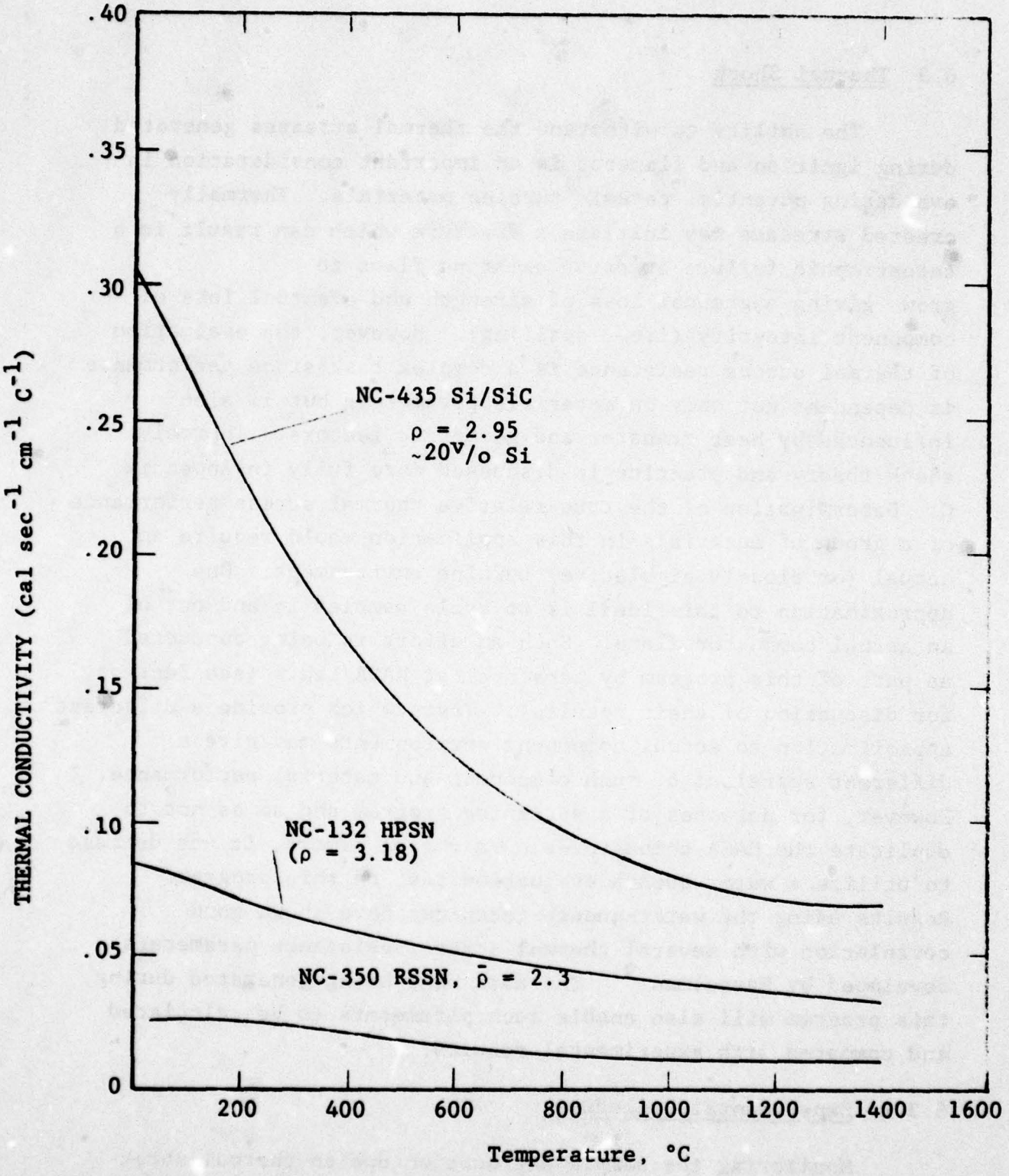

FIGURE 6.18 THERMAL CONDUCTIVITY OF NC-132, NC-435 and NC-350 MATERIALS.

6.3 Thermal Shock

The ability to withstand the thermal stresses generated during ignition and flameout is an important consideration in evaluating potential ceramic turbine materials. Thermally created stresses may initiate a fracture which can result in a catastrophic failure or cause existing flaws to grow giving a gradual loss of strength and eventual loss of component integrity (i.e., spalling). However, the evaluation of thermal stress resistance is a complex task since performance is dependent not only on materials parameters but is also influenced by heat transfer and geometric factors. Thermal shock theory and practice is discussed more fully in Appendix C. Determination of the true relative thermal stress performance of a group of materials in this application would require an actual (or closely simulative) turbine environment. One approximation to this ideal is to cycle samples in and out of an actual combustor flame. Such an effort is being conducted as part of this program by personnel at NASA/Lewis (see Section 7 for discussion of their results). Tests which provide a different approximation to actual component environments may give a different appraisal of such component and material performance. However, for purposes of a screening program and so as not to duplicate the NASA combustor-slow air cool effort, it was decided to utilize a water-quench evaluation test on this program. Results using the water-quench technique have shown good correlation with several thermal stress resistance parameters developed by Hasselman.[91] The data base being generated during this program will also enable such parameters to be calculated and compared with experimental results.

6.3.1 Experimental Procedure

Monitoring the sample degradation due to thermal shock is commonly done by measuring residual strength as a function

of quench temperature difference. However, the thermal stresses occurring during quenching may influence the total spectrum of cracks or flaws in the sample and not merely the critical flaw responsible for failure during mechanical strength evaluation. For this reason it was decided to evaluate the samples before and after quenching using internal friction as well as residual strength. Internal friction is discussed more fully in Appendix C. The Zener bandwidth technique[92] was selected for these evaluations due to its versatility. Figure 6.19 shows a schematic of the basic apparatus. The sample is vibrated at or near its flexural resonant frequency. The specimen is supported by two cotton threads which are attached to a piezoelectric driver and pickup, respectively. The threads transmit the signal to and from the sample and provide support with negligible friction and damping. This set-up is shown in Figure 6.20. Internal friction is then calculated from the expression:

$$Q^{-1} = \frac{\Delta f}{\sqrt{3}\, f}$$

Where Q^{-1} = internal friction
f = resonant frequency (flexural fundamental)
Δf = resonant peak width at half amplitude

A large increase in relative internal friction indicates a change in flaw structure due to thermal stresses.

The typical test sequence is to mark the nodal points for flexural vibration (0.224 times the length inward from each end) on the sample, place thread loops ~1mm towards the outer side of these nodal points, determine the appropriate resonant frequency manually, and then scan the neighboring frequency range (usually $\pm$ 25 Hz) at 6 Hz/min using a Hewlett-Packard spectrum analyzer while the pickup amplitude is recorded on the X-Y plotter. Figure 6.21 shows a typical example of such a curve

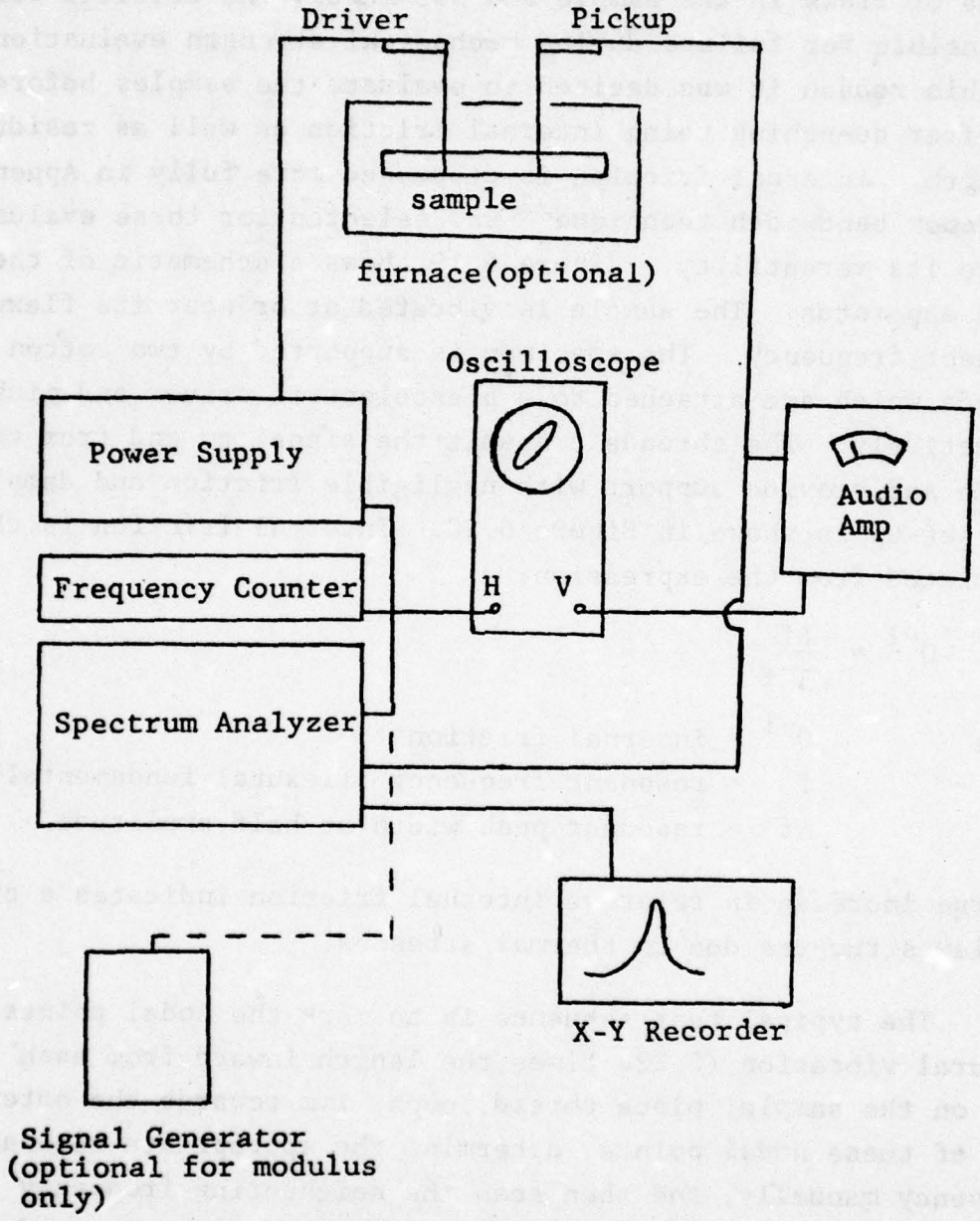

FIGURE 6.19 SONIC MODULUS AND INTERNAL FRICTION APPARATUS

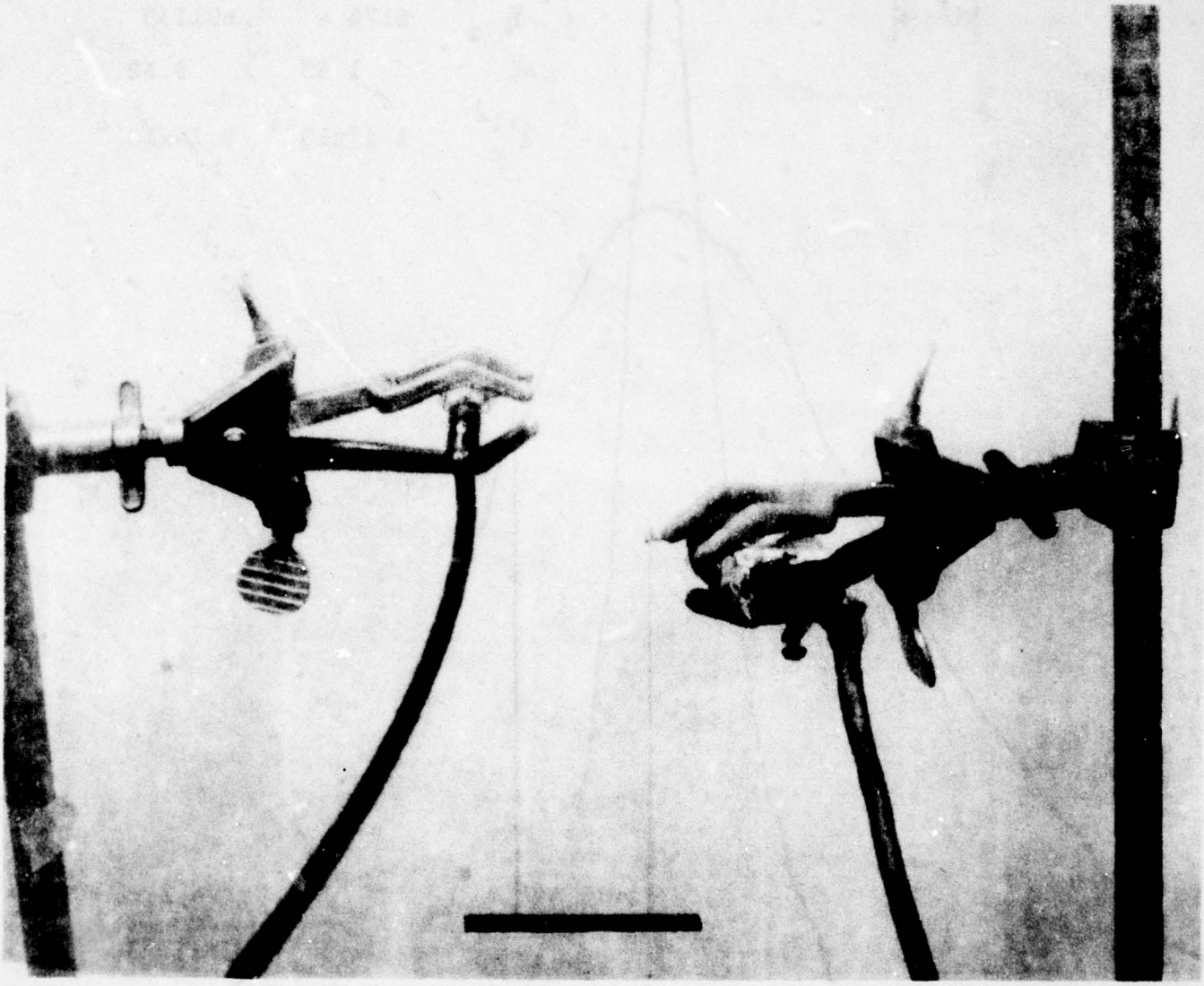

FIGURE 6.20 VIEW OF PIEZOELECTRIC PICKUP AND DRIVER WITH SAMPLE SUSPENDED ON COTTON THREAD.

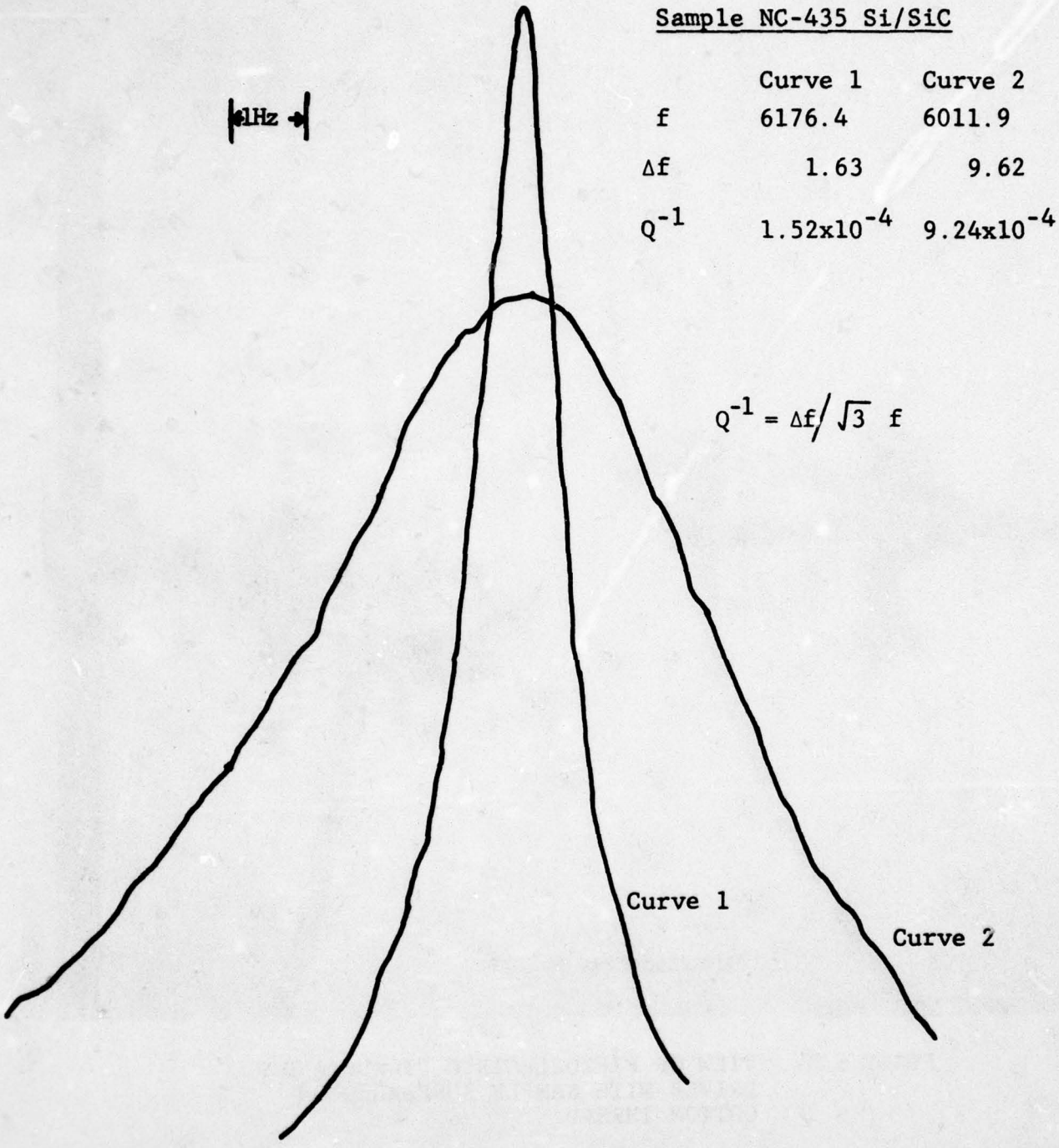

FIGURE 6.21 TYPICAL AMPLITUDE-FREQUENCY CURVES FOR INTERNAL FRICTION MEASUREMENTS. CURVE 2 WAS OBTAINED AFTER A $\Delta T = 450°C$ WATER QUENCH.

before and after shock. Half peak widths to ± 0.05 Hz can be readily measured. Slower frequency scanning rates are used for very low internal friction samples ($< 5 \times 10^{-5}$). Thread position with respect to the nodal points has been shown to influence internal friction values.[93] The 1 mm separation is an acceptable compromise that gives sufficient amplitude to be detected without distortion due to damping in the support.

The internal friction apparatus was checked against a Si_3N_4 sample supplied by Norton Company (courtesy of J.W. Lucek and G.Q. Weaver). They measured 1.27×10^{-4} for this sample while a value of 1.35×10^{-4} was obtained at IITRI. Their measurements were made using electromagnetic driver and pickup transducers; thus agreement is good considering the different transducers and probable small differences in support location. An NBS standard reference Al_2O_3 sample was also purchased to enable comparison of IITRI's setup with established high quality measurements.[94] The resonant frequency for standard Al_2O_3 reference bar D1 determined at NBS is 2043.27 Hz. The value measured at IITRI was 2042.8 Hz, or a difference of 0.023%. These measurements thus established the accuracy of the IITRI setup as compared to a calibrated standard material.

The thermal shock experiments were conducted in two stages. Initially one sample from each batch of the four materials under study was subjected to increasing increments of water quench thermal shock to bracket their thermal shock range. Approximately 50°C intervals were used. Sample size was approximately 70 mm x 6 mm x 3 mm. All samples were wired together, heated to a set temperature and allowed to reach thermal equilibrium, and then dropped into a room temperature water bath. After drying overnight, the samples' internal friction was measured using the apparatus and methods described above. Care was taken to retain the same sample orientation during all internal friction

determinations and for each subsequent quench. If no significant increase in Q^{-1} was observed this indicated the sample's flaw structure was unaffected by that quench.[95] Therefore the sample was quenched again at a larger temperature difference until a critical quench, ΔT_c, was found.

For the remaining samples quench conditions were selected based on the results obtained from the first stage. During the course of these experiments some samples fractured after a particular quench. In other cases many of these fractures were observed only after removal from the drying oven and during the unwrapping of the wire used to hold the samples together during a quench. Examination of only partially fractured pieces and preliminary observations by optical microscope on several fractured surfaces showed the cracks originating from the thin long edge of the samples (and corners in a few instances) and growing into the center, where their path was deflected lengthwise by internal compressive stresses. In some samples the cracks exited on the same edge as they entered and in others they continued to the end. These observations are in agreement with the stress states expected for such a water-bath quench.

The residual strength of all samples that survived the quenching experiments without fracturing was determined upon completion of internal friction measurements.

6.3.2 Experimental Results

Figures 6.22-6.32 show the results of the relative change in internal friction ($\Delta Q^{-1}/Q_o^{-1}$, where $\Delta Q^{-1} = Q^{-1} - Q_o^{-1}$) as a function of quench interval for the four materials examined to date. Q_o is the lowest Q^{-1} value measured, not necessarily the room temperature value, on the assumption that values higher than Q_o^{-1} at lower ΔT are spurious. These results showed relatively little change until a critical level of thermal quench was

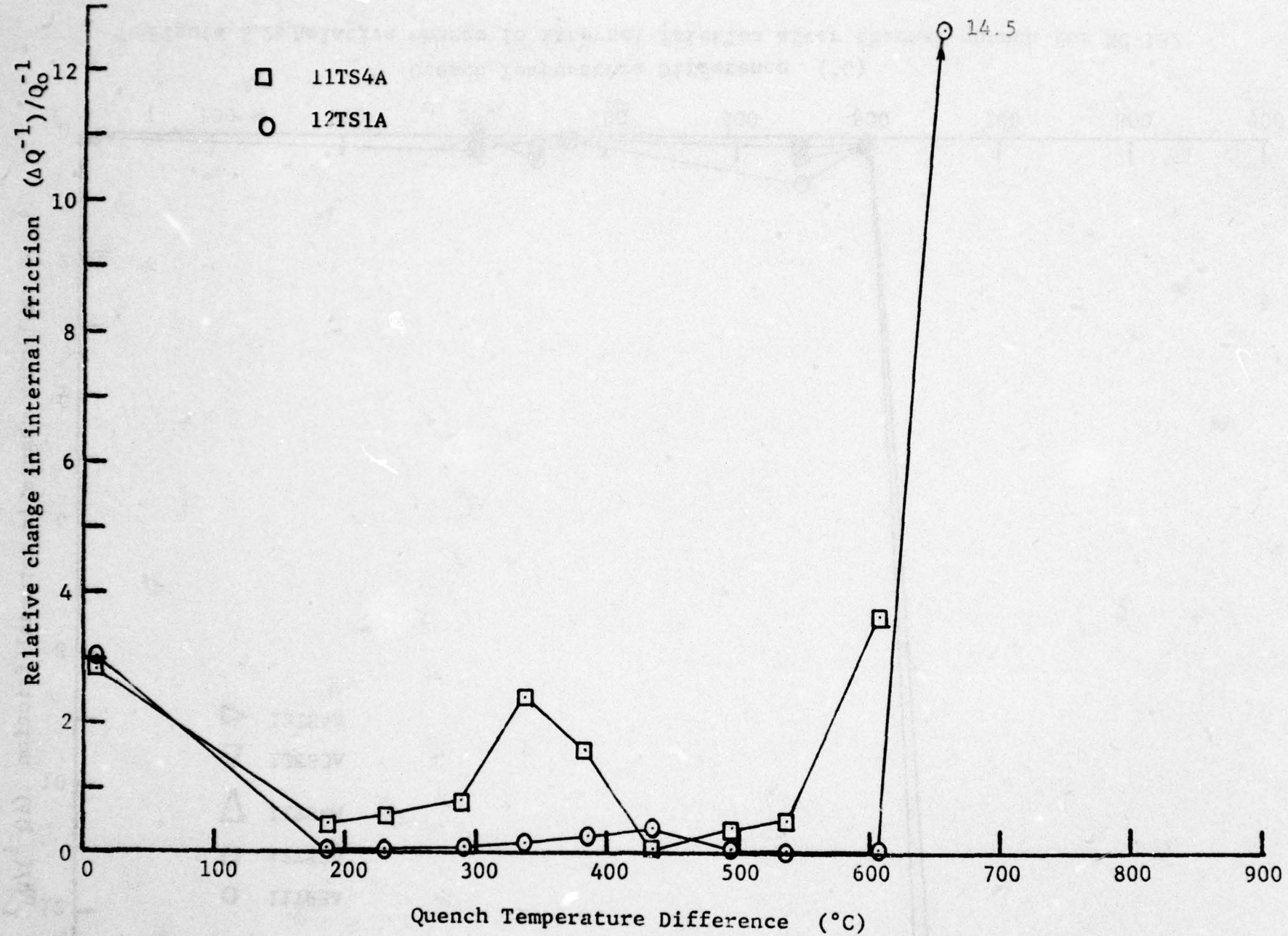

Figure 6.22 Relative change in internal friction after thermal quench for NC-132

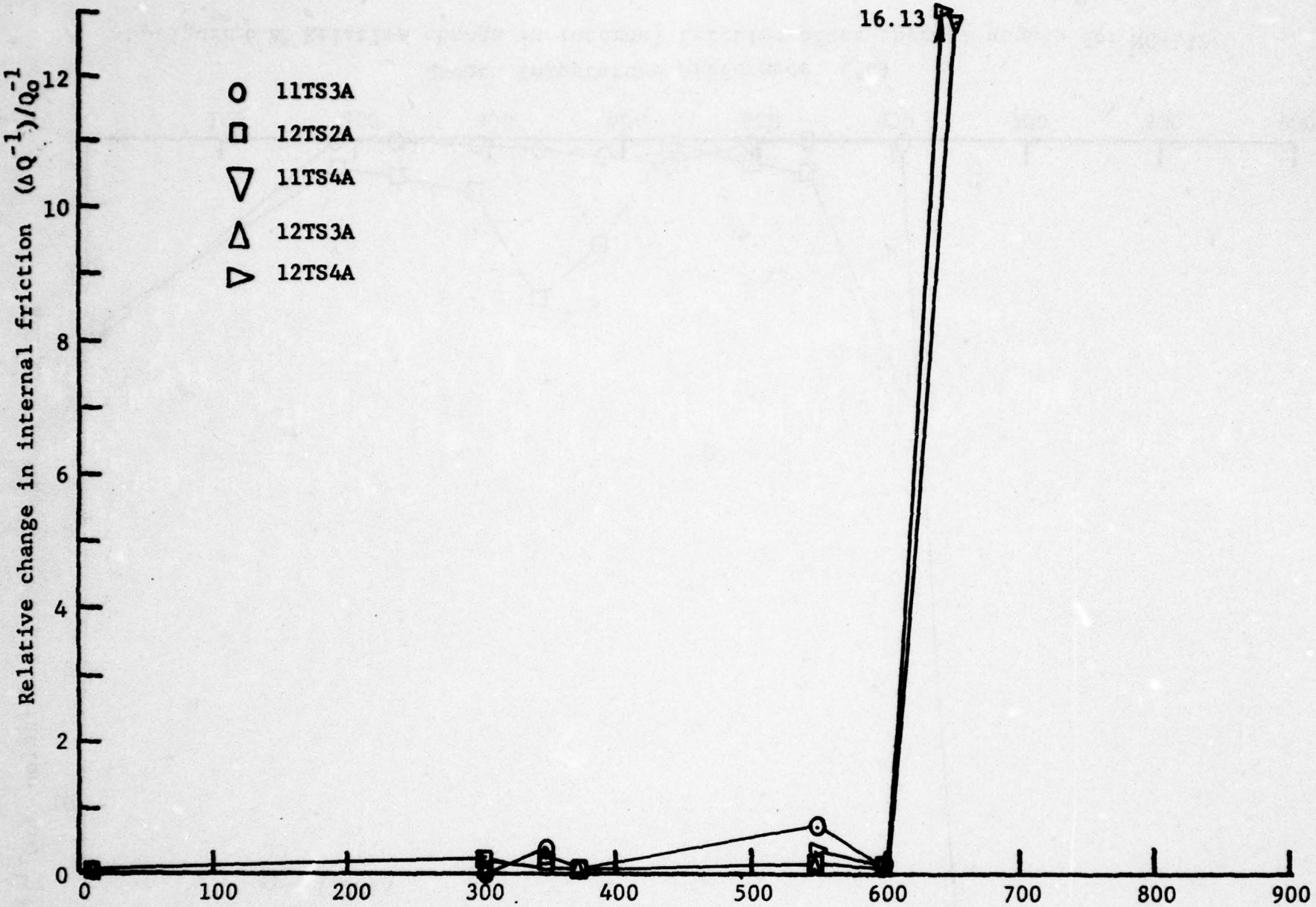

Figure 6.23 Relative change in internal friction after thermal quench for NC-132

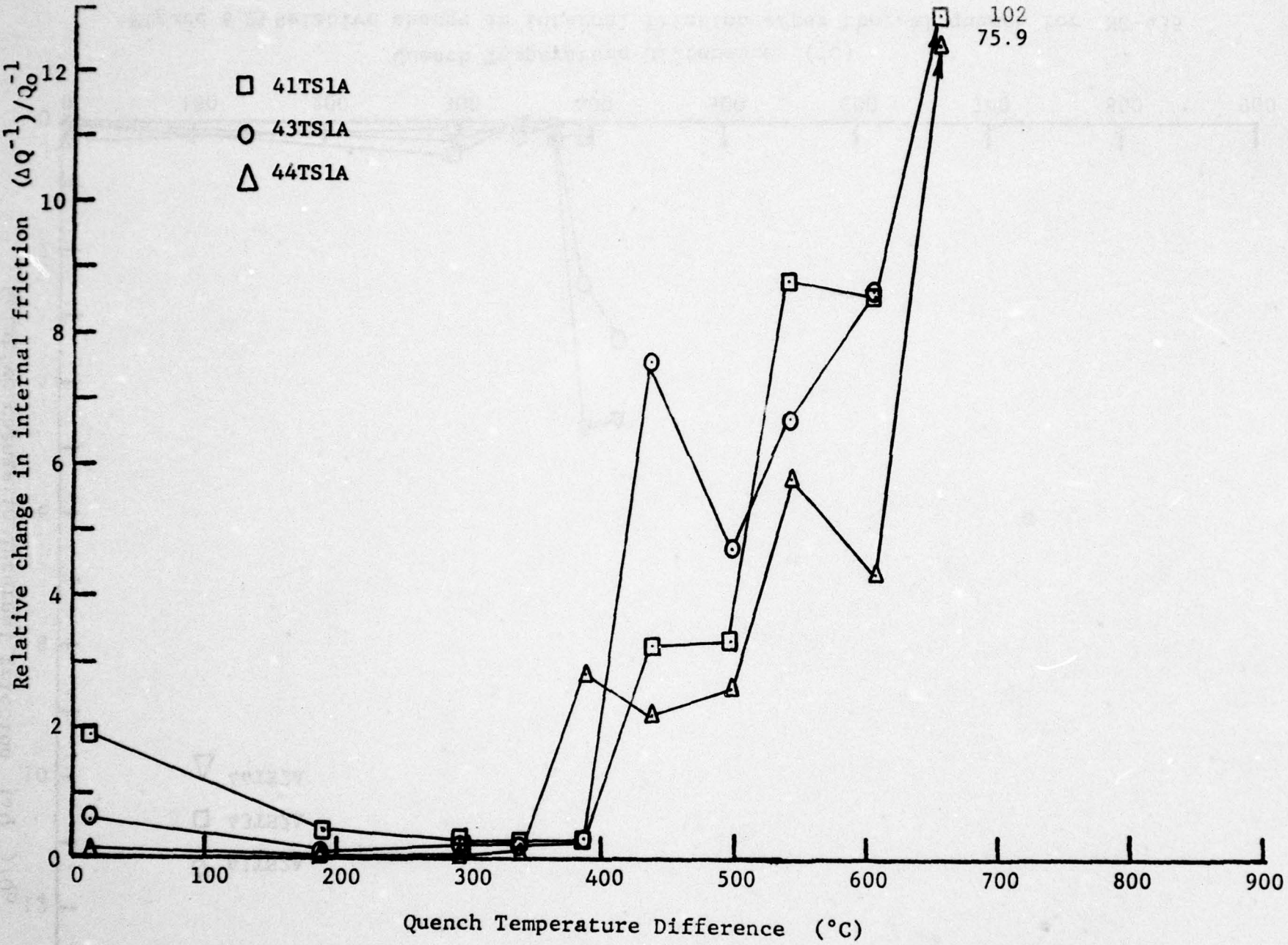

Figure 6.24 Relative change in internal friction after thermal quench for NC-435

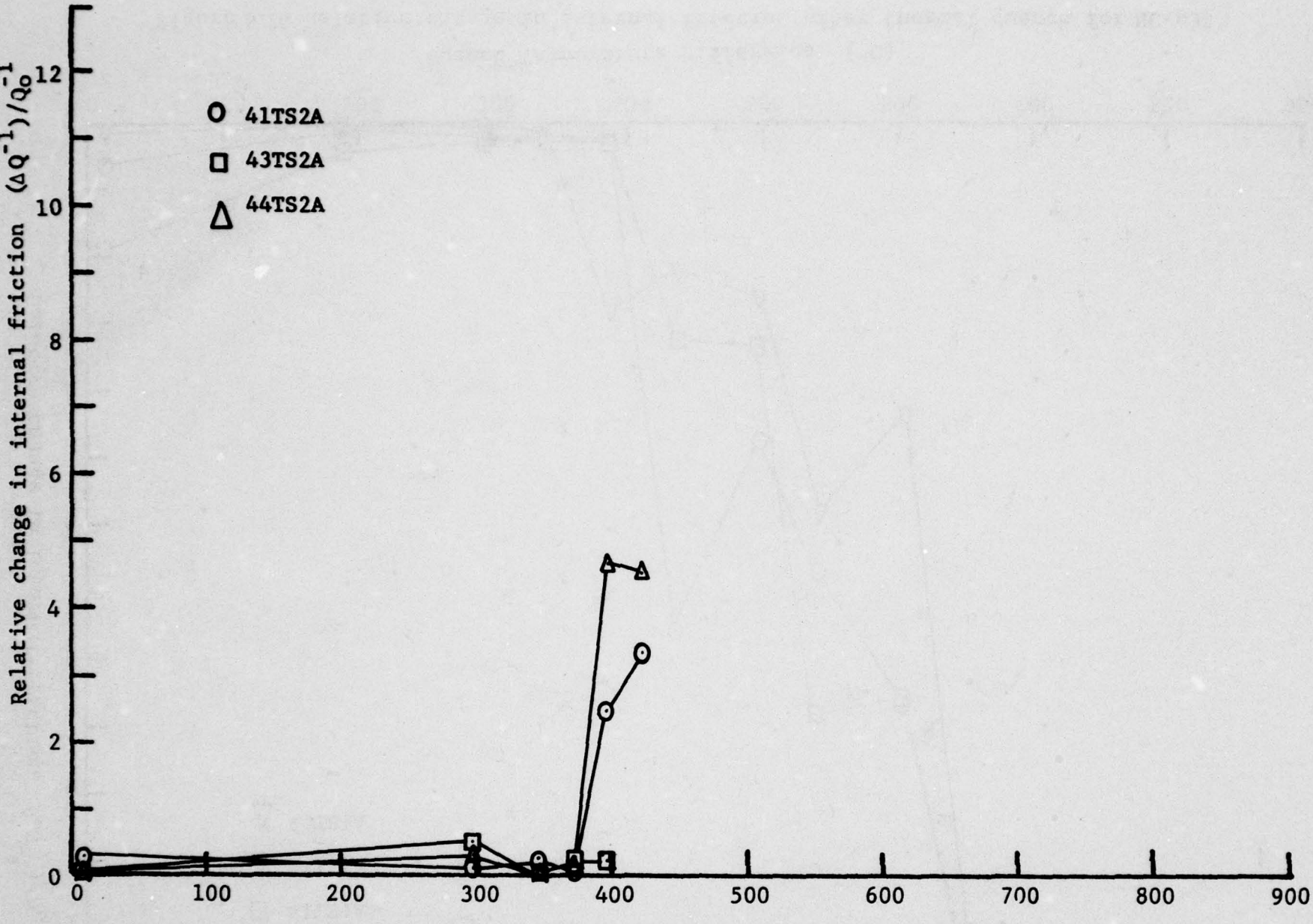

Figure 6.25 Relative change in internal friction after thermal quench for NC-435

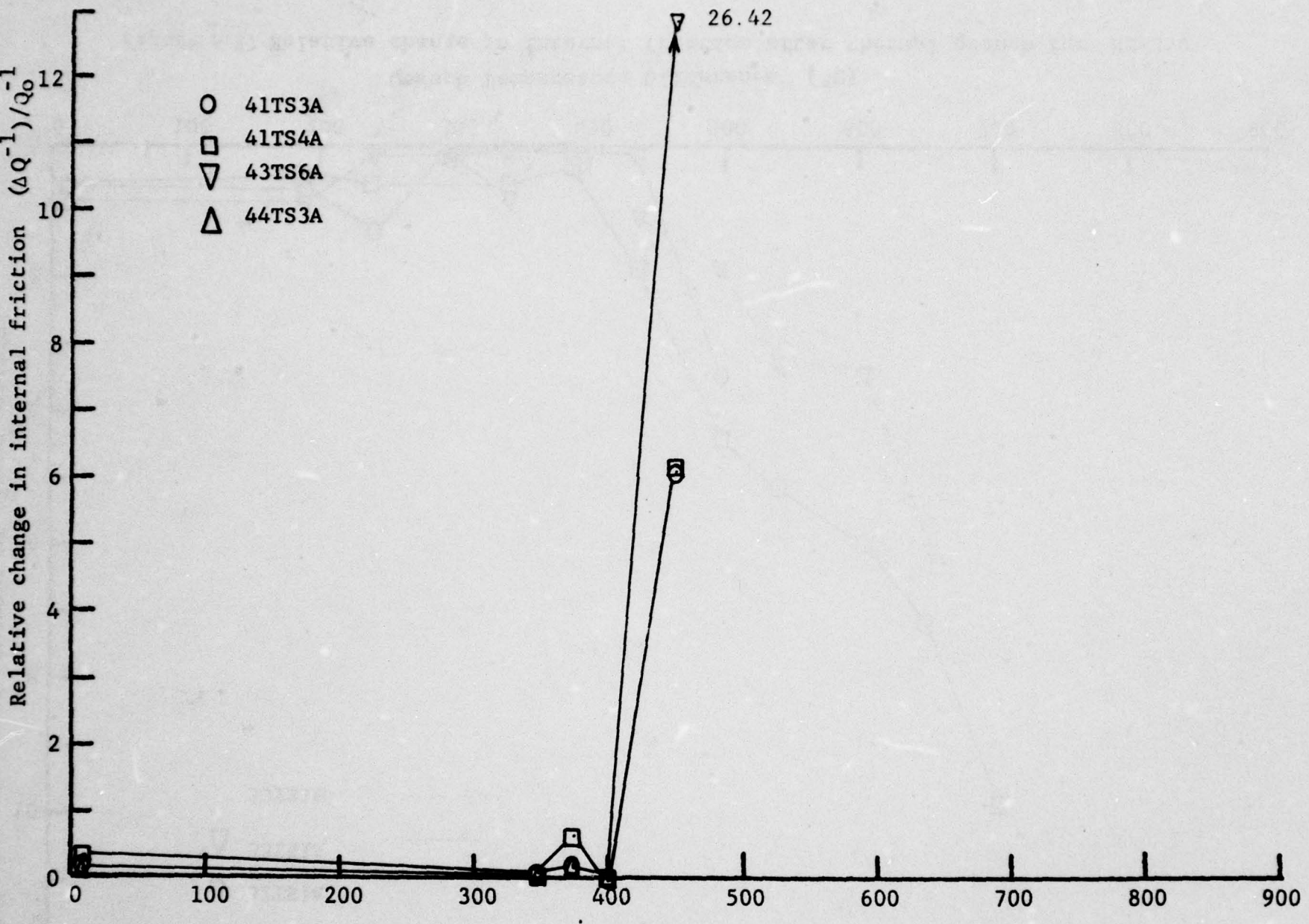

Figure 6.26 Relative change in internal friction after thermal quench for NC-435

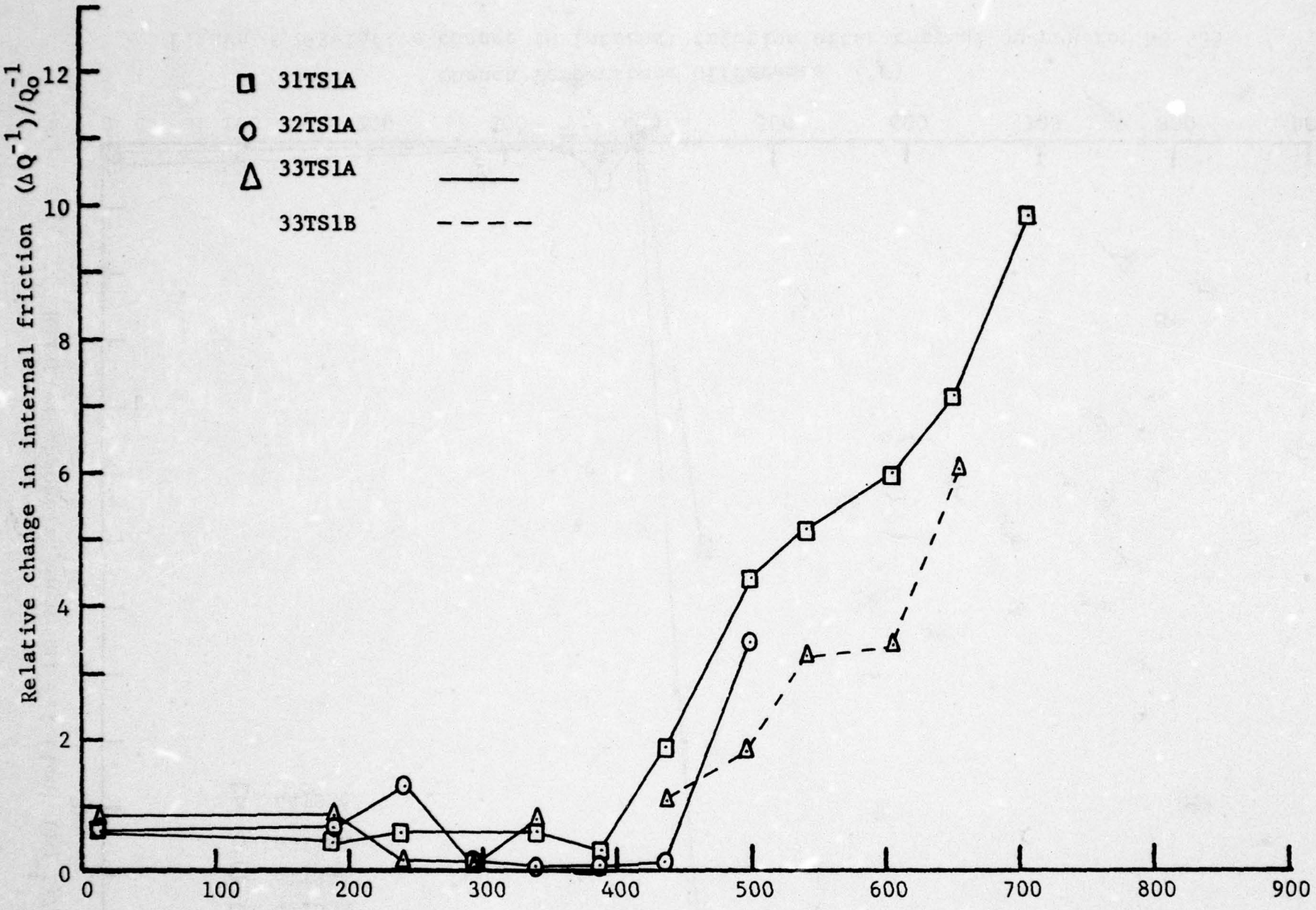

Figure 6.27 Relative change in internal friction after thermal quench for NC-350

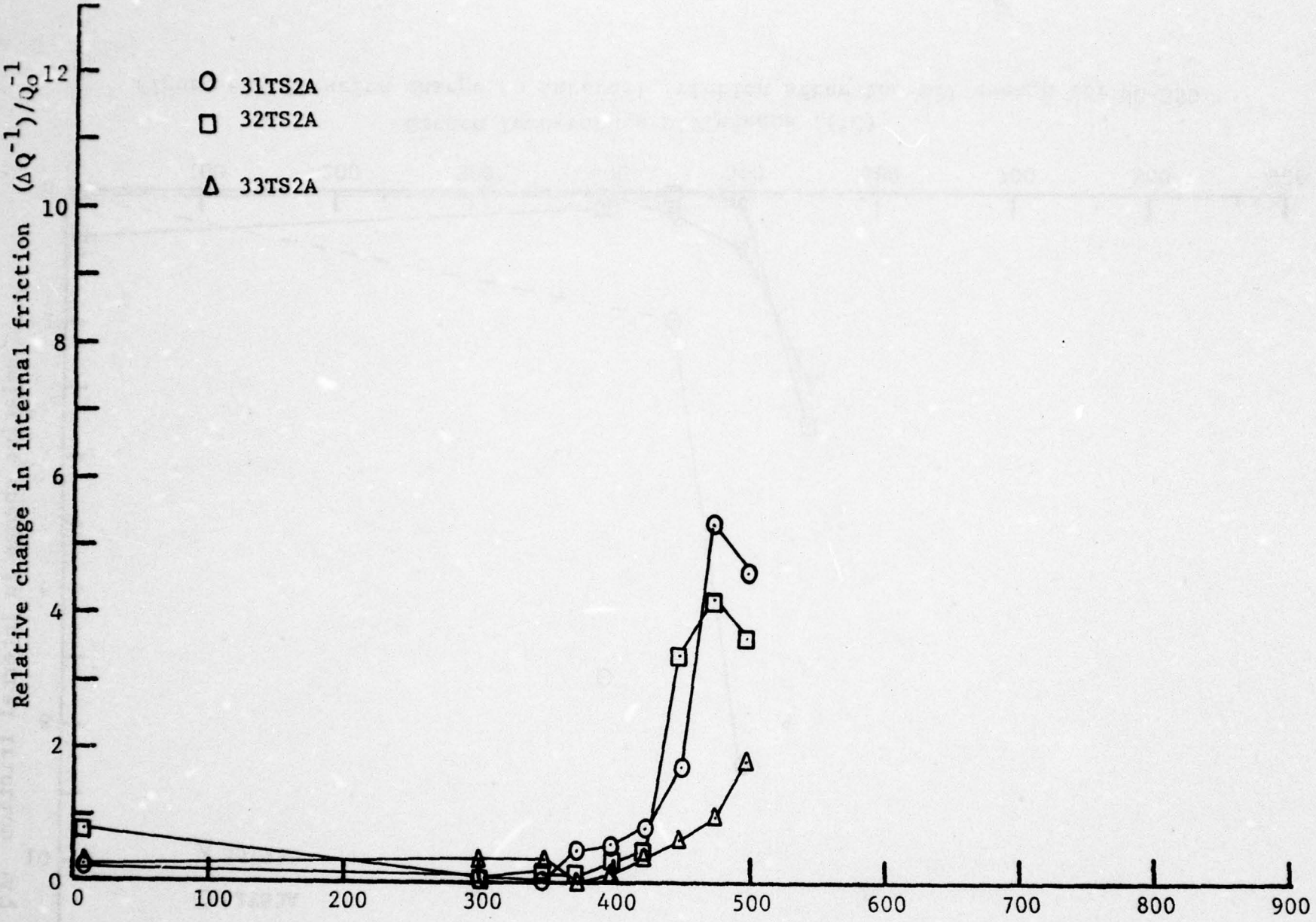

Figure 6.28 Relative change in internal friction after thermal quench for NC-350

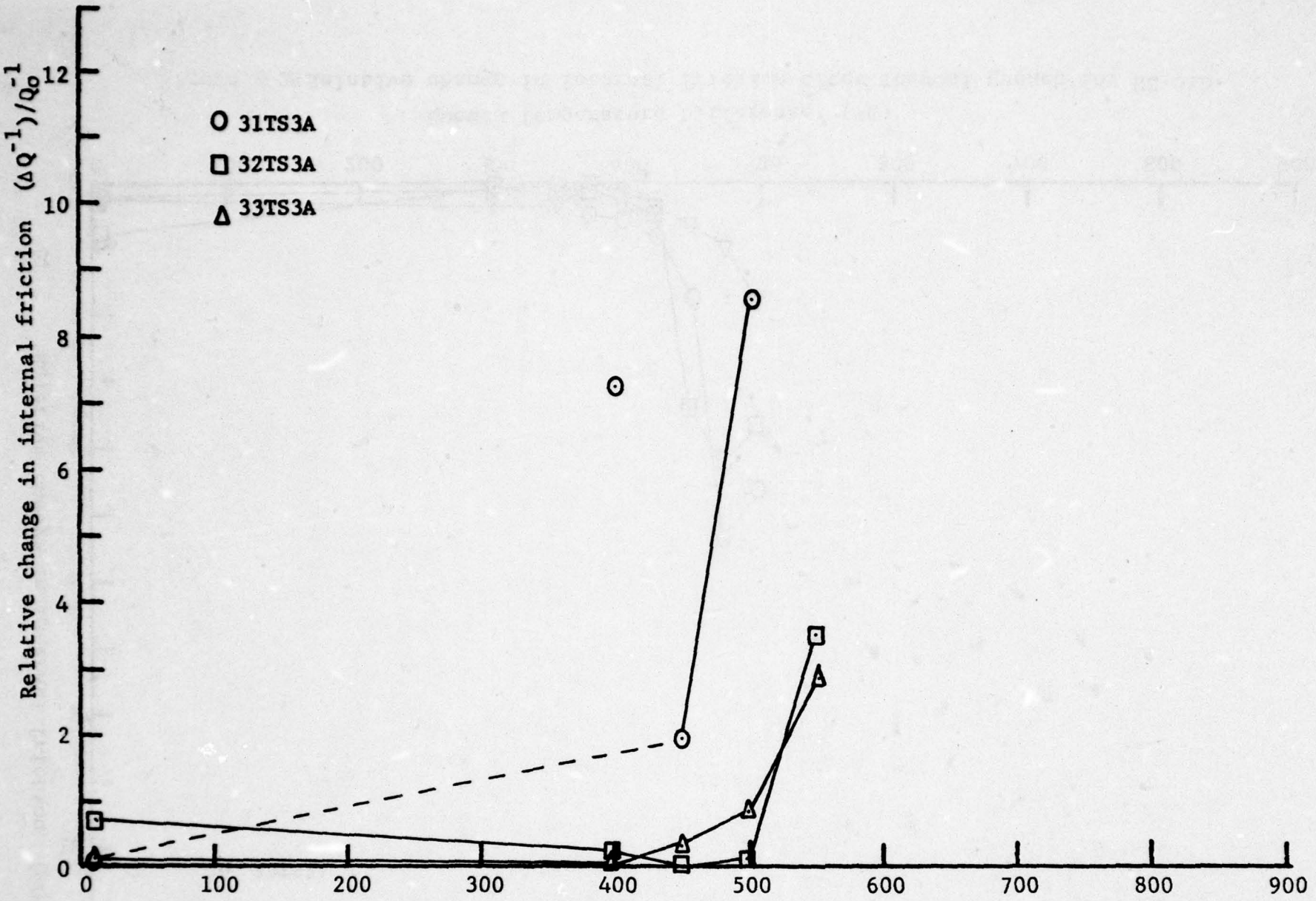

Figure 6.29 Relative change in internal friction after thermal quench for NC-350

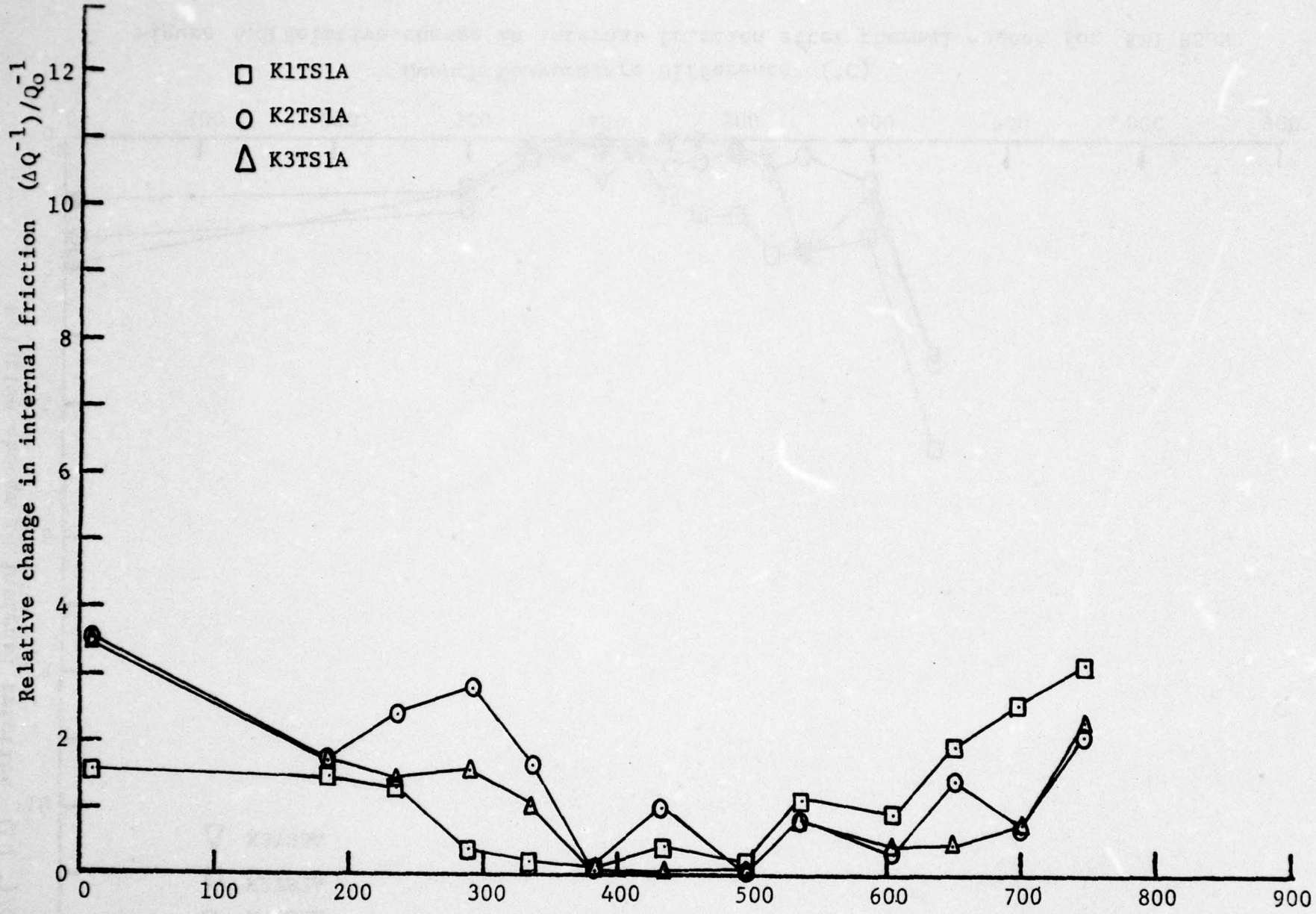

Figure 6.30 Relative change in internal friction after thermal quench for KBI RSSN

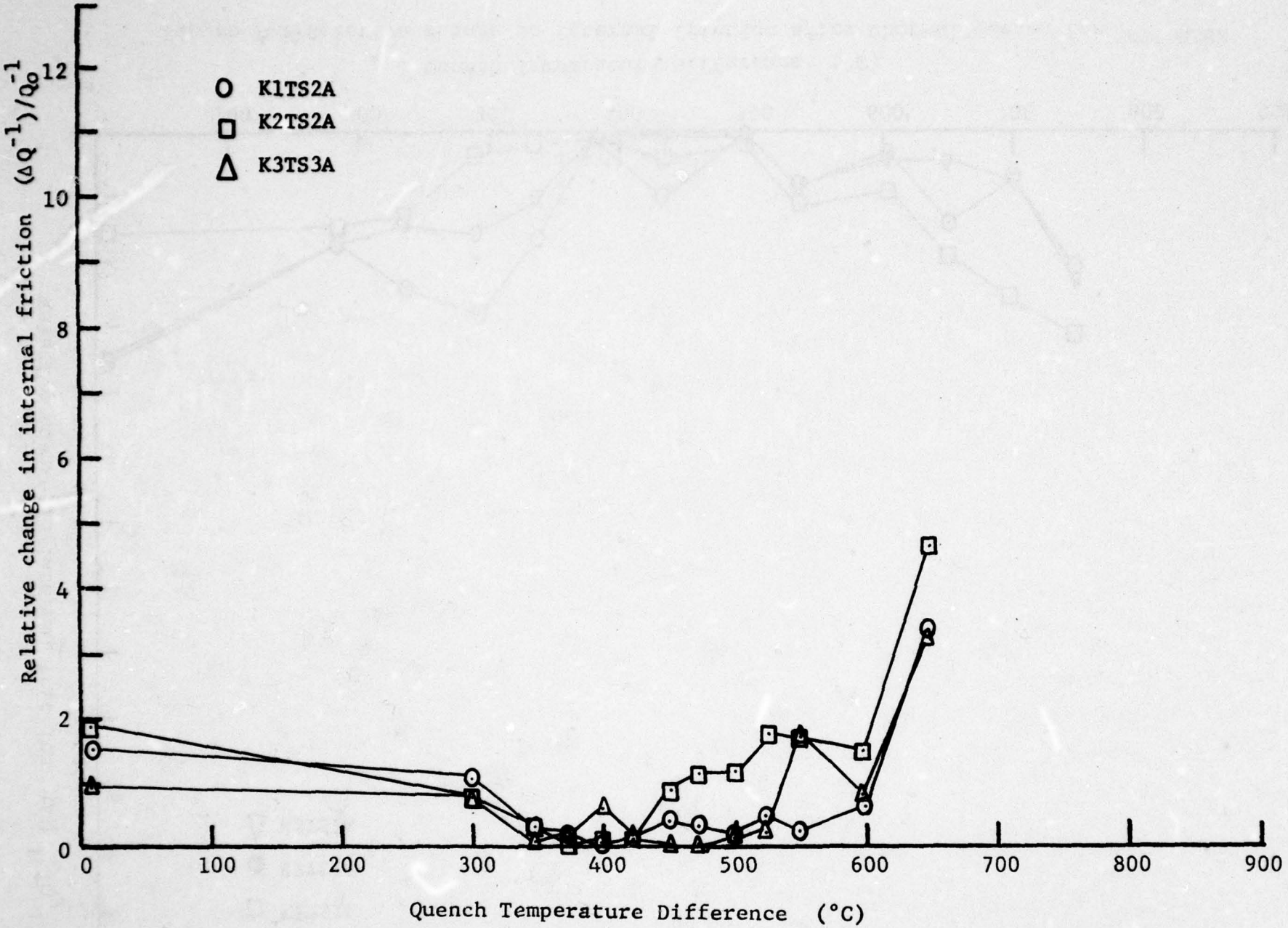

Figure 6.31 Relative change in internal friction after thermal quench for KBI RSSN

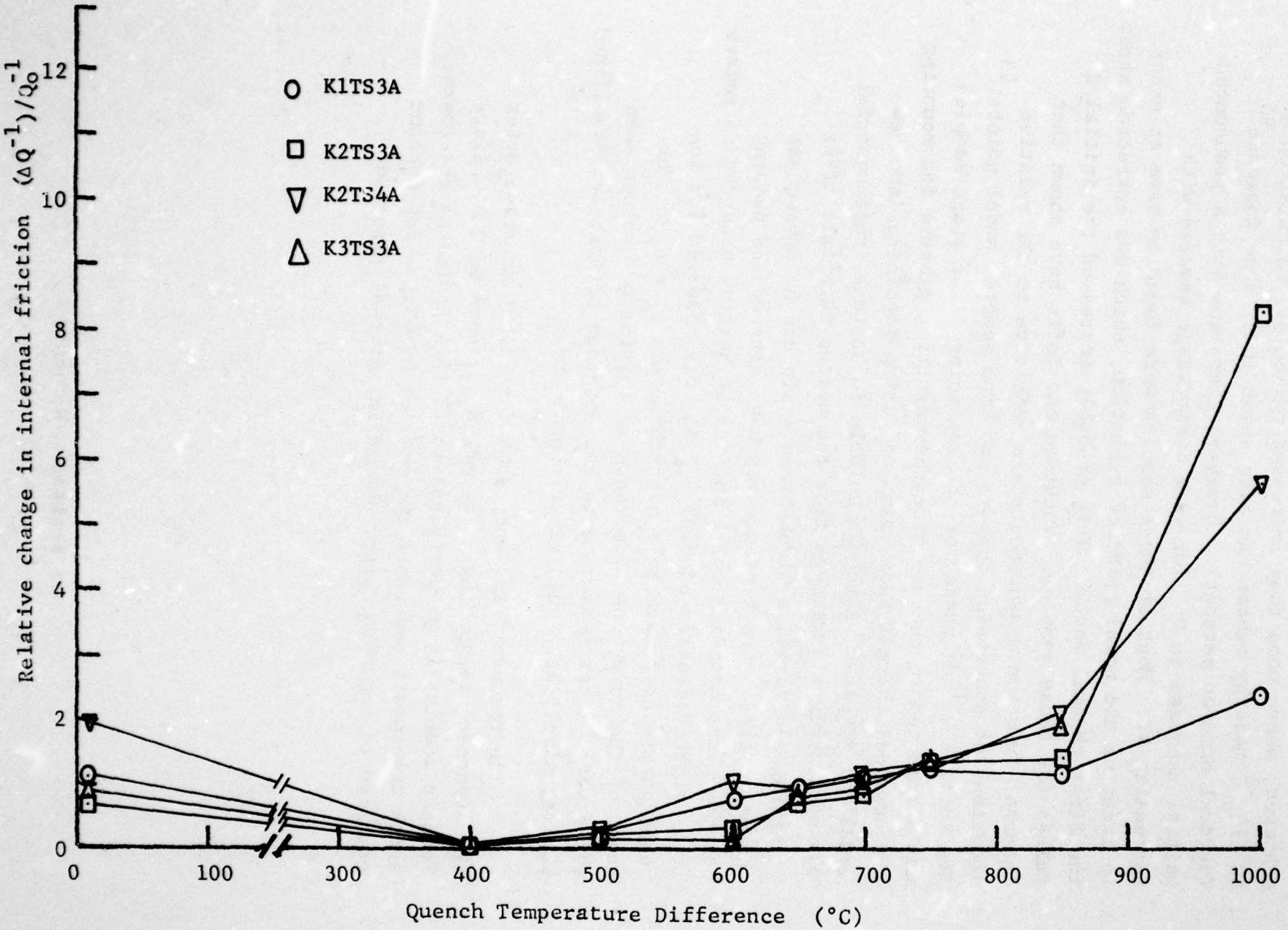

Figure 6.32 Relative change in internal friction after thermal quench for KBI RSSN

AD-A062 905 IIT RESEARCH INST CHICAGO ILL F/G 11/2
PROPERTY SCREENING AND EVALUATION OF CERAMIC VANE MATERIALS.(U)
OCT 77 D C LARSEN, G C WALTHER F33615-75-C-5196
UNCLASSIFIED IITRI-D6114-ITR-24 NL

3 OF 4
ADA
062905

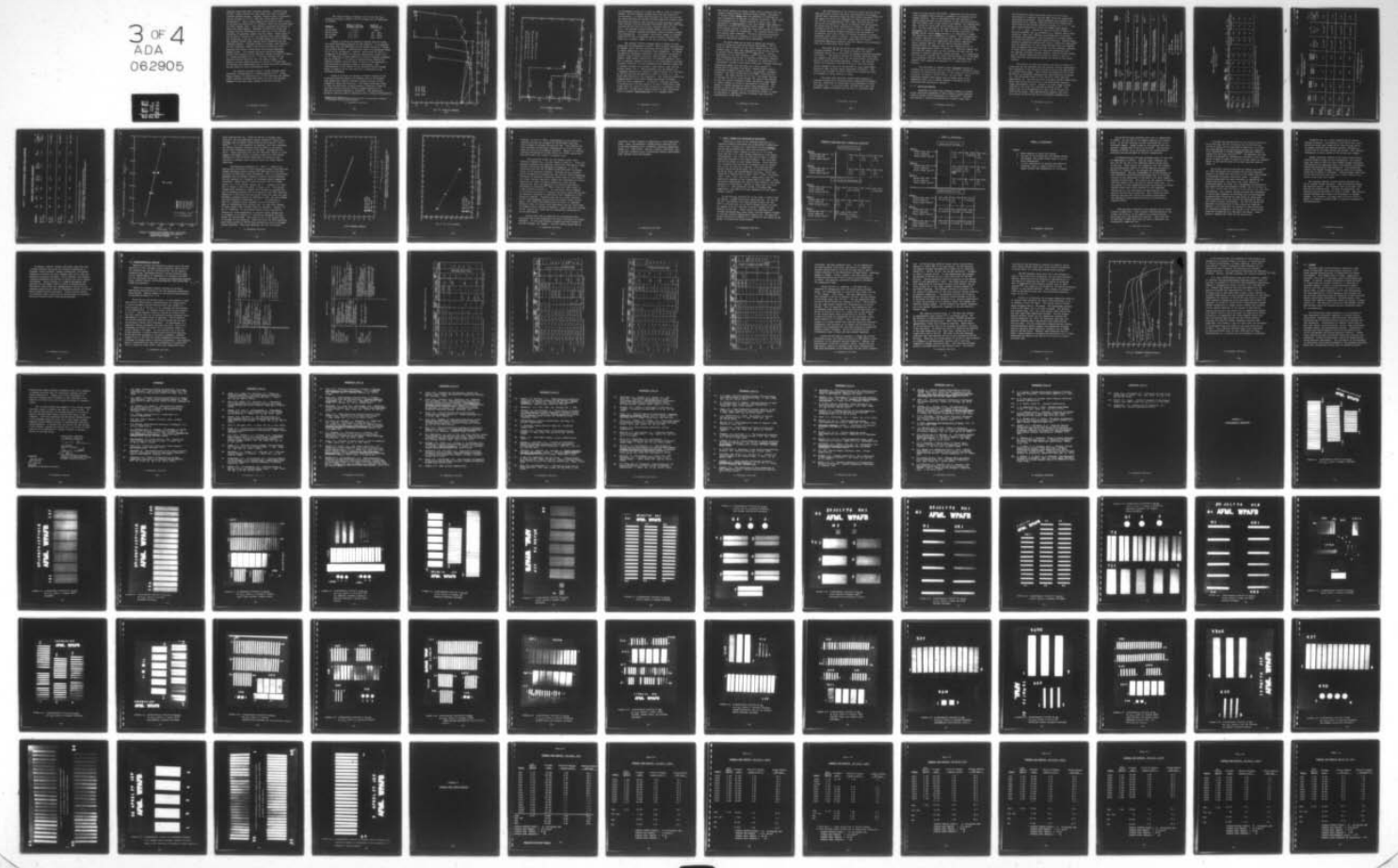

achieved, where upon they increased markedly. Calculation of $\Delta Q^{-1}/Q_o^{-1}$ made by others has also shown this large increase[95] (several hundred percent). However, there was also a pronounced initial decrease in Q^{-1} for some first stage samples with increasing ΔT. Most of these samples were found to have an error in locating the nodal point of vibration, which was corrected after the first thermal shock. This probably increased the initial Q^{-1} values for these samples. Wachtman and Tefft have shown that internal friction measurements are sensitive to the relative locations of suspension support and true sample nodal points.[93] The initial Q^{-1} decrease for the remaining first stage samples was attributed to the use of a thermosetting plastic for mounting the original thermal shock samples during machining into new (smaller) samples. Although soluble in acetone, this material was not completely removed from the porous materials after machining and formed a black-brown stain during subsequent thermal cycles. Its presence may have altered the damping nature of the material until sufficient heating occurred to remove it. Weight decreases of 0.05 - 0.5% were observed for the reaction sintered materials over this same ΔT range. The cause of the more modest decrease in initial Q^{-1} values seen for several later measurements has not been definitely established but may simply be within experimental error.

The resonant frequency showed a slight decrease after the quench corresponding to a marked increase in Q^{-1}. Since Young's modulus is proportional to f^2 this indicates the thermal shock treatments decreased the modulus by only a few percent compared to the much larger change in internal friction.

The results shown in Figures 6.22-6.32 for the four materials studied in Phase I of this program may be summarized as follows:

MATERIAL	RANGE OF INITIAL INTERNAL FRICTION	RANGE OF CRITICAL ΔT^*
NC-132 HPSN	1×10^{-4}	600°C
NC-435 Si/SiC	$1\text{-}2 \times 10^{-4}$	350 - 400°C
NC-350 RSSN	$2\text{-}3 \times 10^{-4}$	400 - 500°C
KBI RSSN	$2\text{-}5 \times 10^{-4}$	600 - 850°C

Figure 6.33 shows the measured internal friction values for better performing examples of each material. It is apparent from these that the RSSN materials had higher initial Q^{-1} values due to their porosity. Qualitatively there is a pronounced change in Q^{-1} at ΔT_c as expected. However, caution must be used in attempting to interpret the absolute quantitative values of Q^{-1} or ΔQ^{-1} measured. Values measured in vacuum or another atmosphere may be different.[93] No theory to quantitatively explain the measured internal friction values in terms of flaw spectrum or flaw structure is presently known to the authors. The interpretation of the results of the internal friction changes shown in Figure 6.33 for each material is developed in the following paragraphs.

Figure 6.34 shows the measured residual strength of the individual quenched samples and compares them to the average room temperature flexural strength obtained earlier in this program for these four materials. The dashed lines were drawn to show the qualitative strength behavior expected in light of this data and the internal friction changes measured as a function of quench temperature difference. The qualitative nature of this plot must be emphasized since strength determinations

*Temperature quench interval after which a pronounced increase in internal friction was observed.

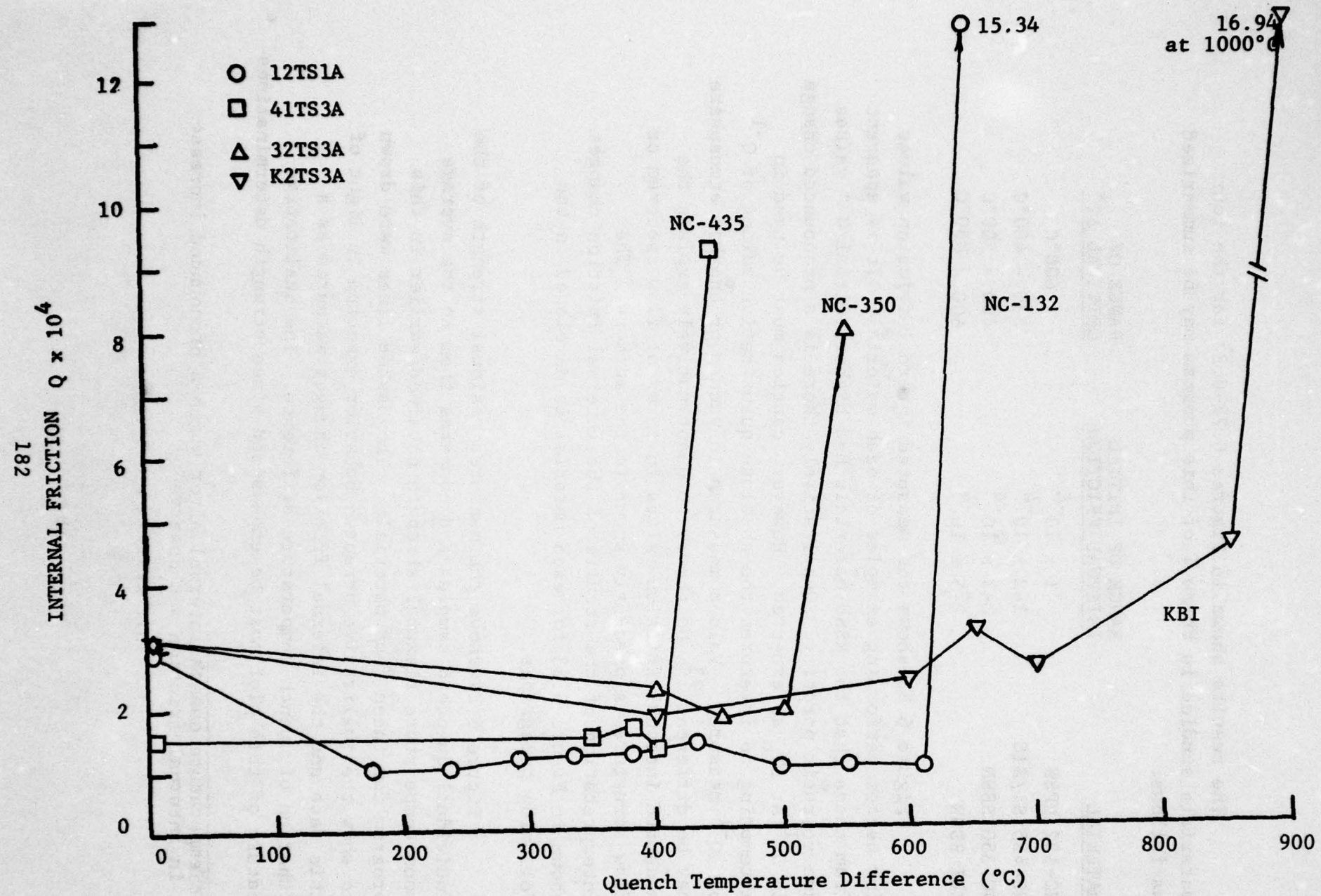

FIGURE 6.33 COMPARISON OF INTERNAL FRICTION AFTER THERMAL QUENCH FOR A BETTER PERFORMING SAMPLE OF EACH CANDIDATE MATERIAL.

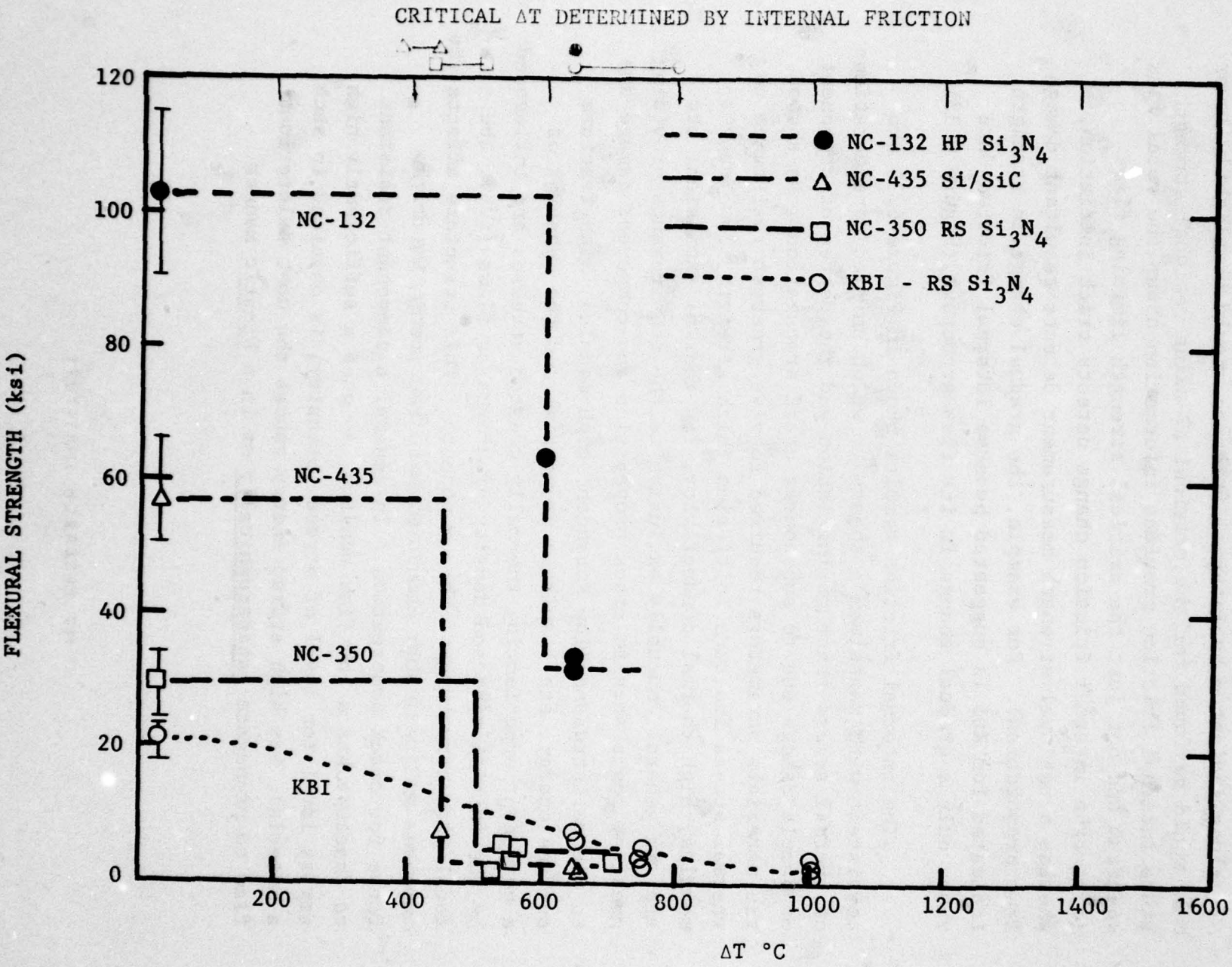

FIGURE 6.34 STRENGTH LOSS OF THERMALLY SHOCKED SAMPLES

at intermediate values of ΔT were not made in order to conserve samples, and the residual strength data that was obtained is not extensive. It should also be pointed out that the critical ΔT values indicated by internal friction should be slightly lower than would be found for the critical ΔT using residual strength since internal friction provides information about the total flaw spectrum and not just the critical strength limiting flaws (i.e., the internal friction change detects crack initiation, whereas a residual strength measurement detects resultant damage from propagation). For example, the gradual change in strength indicated for KBI is suggested because internal friction data shows only a gradual change in its flaw structure (Figure 6.33).

The internal friction results shown in Figure 6.34 are consistent with Hasselman's theory[95], which unified considerations of thermal stress fracture initiation and the degree of component or sample damage due to subsequent crack propagation. He showed the materials parameters required to give greatest resistance to thermal stress fracture initiation (high strength, low Young's modulus, high thermal conductivity, low thermal expansion, etc.) are, in general, mutually exclusive to the requirements providing greatest resistance to crack propagation and component damage due to thermal stresses (low strength, high modulus, high fracture surface energy, etc.). These properties and the behavior of a component experiencing thermally created stresses are influenced by the initial size and density of cracks or flaws (i.e., the total flaw structure of the component). This structure affects the components ability to store elastic thermal strain energy, the driving force for crack propagation. In general a component resistant to fracture has a low flaw density, so once a sufficiently high stress level (or level of stress intensity) is obtained in such a material, its high stored energy causes the most deleterious flaw to propagate catastrophically or in a kinetic manner.

This occurs because the energy release rate is greater than that needed to merely balance fracture surface energy. Resistance to thermal stress damage means the component is resistant to crack propagation, as opposed to fracture initiation. When cracks are propagated due to thermal stresses in such a case, the propagation is quasi-static in that only enough crack length is generated to absorb the available strain energy. The rate of strain energy release is lower and less strain energy is available as a driving force for propagation. This usually occurs in a more highly flawed component. The above discussion shows why internal friction, as a measure of total flaw structure, is useful in monitoring thermal shock performance.

The above ideas can be used to explain the observed behavior during the IITRI water-quench experiments. The ΔT_c value of ~600°C obtained for all seven samples of NC-132 hot pressed Si_3N_4 is lower than that reported for HS-130 or NC-132 by several other investigators[96-99] (800-1000°C). However, experiments at the Naval Research Labs[100] also show $\Delta T_c \simeq 600°C$. This discrepancy may be due to materials differences (impurity levels of HS-130 and NC-132 are different) or differences in experimental procedure which would affect heat transfer conditions (especially sample size and shape for a water quench[101]). Several NC-132 specimens from Batch I showed slightly poorer performance (complete fracture after a ΔT_c quench), presumably because of the lower average Batch I strength (discussed previously). The sharp increase in $\Delta Q^{-1}/Q_o^{-1}$ and larger decrease in strength for NC-132 occurs because its initial flaw density is low, its initial strength is high, and hence a large amount of elastic energy is stored in the material at failure. This energy is rapidly released by severe crack propagation. The ability to store this energy prior to failure accounts for NC-132 having the highest ΔT_c of the materials tested, in terms of resistance to thermal fracture initiation (see below for interpretation of KBI data).

The determination of ΔT_c for NC-435 Si/SiC and for NC-350 RSSN agree more closely with other investigations of relative thermal shock resistance using the water quench technique.[96,99,102] The values for NC-435 are comparable to other reaction sintered SiC,[102] but are approximately 50°C higher, possibly due to variations in quantity of free Si or particle size distribution. No strong batch to batch variability is evident. The rapid increase of $\Delta Q^{-1}/Q_o^{-1}$ at ΔT_c is evidence that the thermal strain and thermal expansion mismatch between Si and SiC phases is accomodated up to some critical ΔT without formation of energy absorbing cracks prior to failure. The high thermal conductivity of both phases could be partially responsible for this by miminizing temperature gradients and thus thermal stress gradients, even for a severe water batch quench.

The values of ΔT_c for NC-350 are comparable to those reported elsewhere.[96,99c] The range of results, 400-500°C, presumably occurs due to the porosity-strength variations discussed in Section 5. The gradual increase in internal friction around ΔT_c suggests some quasi-static (or non-catastrophic) crack propagation is occurring during quenching. However, the flaw and closed pore structure of NC-350 RS Si_3N_4 is such that enough elastic energy is stored in the material to cause catastrophic failure at some critical quench temperature difference. This level of ΔT_c is lower for NC-350 than NC-132 because its ratio of strength to elastic modulus is lower.

The above three materials showed sudden changes in internal friction with increasing quench temperature difference near ΔT_c, indicative of catastrophic crack propagation (shown in Figure 6.33). On the other hand, KBI RSSN had a much less dramatic change in internal friction until a relatively high

value of ΔT was reached (600-850°C), suggesting that quasi-static crack propagation was occuring in response to the quench-created thermal stresses. This is reasonable since this material is highly porous and much of this porosity is open and interconnected. Thus the samples have a high initial flaw density, are comparatively weak, and do not store much strain energy prior to crack propagation. On this basis KBI is the least resistant to thermal fracture initiation, but, for similar ΔT, KBI is the most resistant to further thermal stress damage because it is sufficiently flawed that additional crack propagation is limited. This interpretation is further supported by the available KBI residual strength data, the fairly constant room temperature and elevated temperature static strength behavior, and the similar fracture surface characteristics for samples broken at room temperature and at elevated temperatures (refer to Section 5). These all suggest that the IITRI KBI samples were not well sintered and could not be expected to support significant thermal stresses. It is emphasized that the static strength and overall microstructure of the KBI RSSN is so different from the other materials that different modes of thermal stress response are observed (i.e., quasi-static vs. kinetic).

The resistance to thermal stress initiated fracture is probably the best thermal shock criterion to use in evaluating these materials for turbine applications. On this basis NC-132 is the most promising, followed by NC-350, NC-435, and KBI RSSN. Direct comparison between water-quench and air-quench tests is not completely valid, but a similar ranking is indicated by the NASA/Lewis work described in Section 7.

6.3.3 Analytical Results

Hasselman and others have proposed a number of thermal stress resistance parameters or merit indices to help evaluate relative thermal shock performance of a material[91]. The model used assumes a uniform distribution of circular cracks with

non-interacting stress fields and so may not be strictly applicable to a material like KBI RSSN containing significant interconnected porosity. These parameters also depend on the appropriate heat transfer conditions and may be divided into those dealing with thermal failure initiation (R, R', R'') and with crack propagation or extent of thermal shock damage (R''', R'''', R_{st}). Several of these are given in Table 6.2. Strictly speaking, the R_{st} parameter is a "thermal stress crack stability" index that indicates the probability of fracture initiation and subsequent crack propagation of already flawed or porous materials for severe quench conditions. Several other analytical parameters dealing with creep or radiation conditions[91] were not appropriate for this study and hence were not computed. These parameters were calculated for the four materials examined by water-quench experiments by using room temperature data for flexural strength, flexural modulus, fracture surface energy, and the thermal properties data given in Table 6.3 and 6.4. These data have been obtained during the course of the current program.

The results of these calculations are shown in Table 6.5, along with the ΔT_c obtained from the internal friction measurements. The R parameter is the fracture initiation factor most applicable to a severe water quench. The R values calculated for NC-132 and NC-350 are in acceptable agreement with experimentally determined ΔT_c. The calculated value of R for NC-435 is lower than the experimental ΔT. This may be due to its higher thermal conductivity, which would reduce the severity of the water-quench and give higher experimental results. Figure 6.35 shows these R values compared to the trend line reported by Weaver *et al*[96]. The dashed line is an extrapolation of their line to include the IITRI NC-132 datum. This representation suggests that even the results for NC-435 are also in acceptable agreement with

Table 6.2

THERMAL STRESS RESISTANCE PARAMETERS

LITERATURE DESIGNATION	PARAMETER TYPE	PARAMETERS	PHYSICAL INTERPRETATION/ENVIRONMENT	TYPICAL UNITS
R	Resistance to Fracture Initiation	$\frac{\sigma_t (1-\mu)}{\alpha E}$	Maximum ΔT allowable for steady heat flow;	°C
R'	Resistance to Fracture Initiation	$\frac{\sigma_t (1-\mu) k}{\alpha E}$	Maximum heat flux for steady flow;	cal cm^{-1} sec^{-1}
R''	Resistance to Fracture Initiation	$\frac{\sigma_t (1-\mu) \alpha_{TH}}{\alpha E}$	Maximum allowable rate of surface heating;	cm^2 °C sec^{-1}
R'''	Resistance to Propagation Damage	$\frac{E}{\sigma^2 (1-\mu)}$	Minimum in elastic energy at fracture available for crack propagation	$(psi)^{-1}$
R''''	Resistance to Propagation Damage	$\frac{\gamma E}{\sigma^2 (1-\mu)}$	Minimum in extent of crack propagation on initiation of thermal stress fracture	cm
R_{st}	Resistance to further crack propagation	$\left[\frac{\gamma}{\alpha^2 E}\right]^{1/2}$	Minimum ΔT allowed for propagation long cracks	°$Cm^{-1/2}$

σ_t = Tensile Strength
μ = Poisson's ratio
α = Coefficient of Thermal Expansion
E = Young's Modulus of Elasticity
ρ = Density
C_p = Specific Heat
k = Thermal Conductivity
α_{TH} = Thermal Diffusivity
γ = Fracture Surface Energy

Table 6.3

THERMAL STRESS RESISTANCE PARAMETERS

(CRACK INITIATION)*

MATERIAL	FLEXURAL** STRENGTH (ksi)	POISSON'S RATIO***	THERMAL EXPANSION (10^{-6}/°C)	YOUNG'S MODULUS (10^6psi)	$R = \frac{\sigma(1-\mu)}{\alpha E}$	ρ gm/cc	c_p cal $gm^{-1}C^{-1}$	$k = \alpha_{th}\rho c_p$	α_{th} $cm^2 sec^{-1}$	$R' = Rk$	$R'' = R\alpha_{th}$
			(500C)		(°C)			(cal/cmsecC)		(cal/cmsec)	(cm^2 °C sec^{-1})
NC-132 (HP Si_3N_4)	103	.27	2.5	47.1	638	3.18	.16	.084	.166	54	106
NC-435 (Si/SiC)	57.2	.17	3.8	50.7	246	2.95	.16	.326	.690	80	170
NC-350 (RS Si_3N_4)	29.5	.22	2.2	25.6	409	2.48	.16	.032	.081	13	33
KBI (RS Si_3N_4)	21.1	.24	2.3	20.9	334	2.42	.16	.068	.175	23	58

* All properties at 25°C, unless otherwise indicated computed as averages of all materials tested.

** Flexural strength being used instead of tensile strength.

*** Determined at AFML by resonant sphere technique.

Table 6.4

THERMAL STRESS RESISTANCE PARAMETERS*

(CRACK PROPAGATION)

MATERIAL	YOUNG'S MODULUS (10^6 psi)	FLEXURAL STRENGTH (ksi)	POISSON'S RATIO	FRACTURE SURFACE ENERGY γ, Jm^{-2}	$R''' = E/\sigma^2(1-\mu)$ $(psi)^{-1}$	$R'''' = \gamma R'''$ (cm)	$R_{st} = \left[\frac{\gamma}{\alpha^2 E}\right]^{1/2}$ $^\circ Cm^{+1/2}$
NC-132 (HP Si_3N_4)	47.1	103	.27	37.1	6.1×10^{-3}	3.3×10^{-3}	4.27
NC-435 (Si/SiC)	50.7	57.2	.17	19.3	18.7×10^{-3}	5.2×10^{-3}	1.96
NC-350 (RS Si_3N_4)	25.6	29.5	.22	11.3	37.7×10^{-3}	6.2×10^{-3}	3.64
KBI (RS Si_3N_4)	20.9	21.1	.24	15.8	61.8×10^{-3}	14.2×10^{-3}	4.55

* Room Temperature Properties used

** $R''' \gamma = (psi)\frac{J}{m^2}(.0145) = R'''' cm$

TABLE 6.5 ANALYTICAL/EXPERIMENTAL THERMAL SHOCK PARAMETERS

MATERIAL	THERMAL STRESS RESISTANCE PARAMETERS*						
	R	R'	R''	R''' (10^{-3})	R'''' (10^{-3})	R_{st}	$\Delta T_{crit.}$ ** (ΔQ^{-1})
NC-132 HP Si_3N_4	638	54	106	6.1	3.3	4.27	600°C
NC-435 Si/SiC	246	80	170	18.7	5.2	1.96	375-400°C
NC-350 RS Si_3N_4	409	13	33	37.7	6.2	3.64	400-500°C
KBI RS Si_3N_4	334	23	58	61.8	14.2	4.55	600-750°C

* Using room temperature property values

** Critical ΔT measured by change in internal friction due to 25°C water quench from various elevated temperatures.

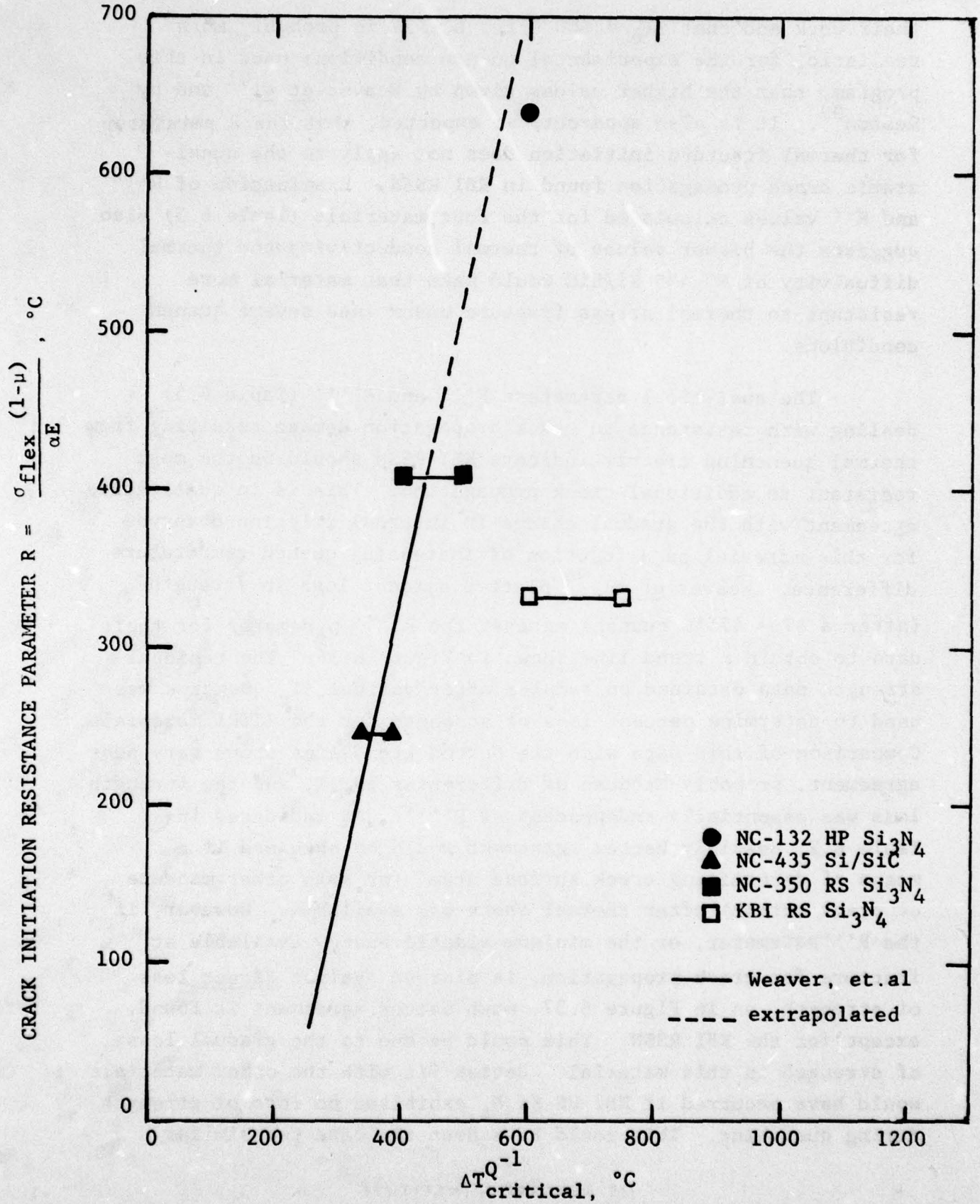

FIGURE 6.35 CORRELATION BETWEEN CRACK INITIATION RESISTANCE PARAMETER AND ONSET OF THERMAL SHOCK DAMAGE

their work and that ΔT_c = 600°C for NC-132 is probably more realistic, for the experimental quench conditions used in this program, than the higher values given by Weaver et al[91] and by Seaton[99]. It is also apparent, as expected, that the R parameter for thermal fracture initiation does not apply to the quasi-static crack propagation found in KBI RSSN. Examination of R' and R'' values calculated for the four materials (Table 6.5) also suggests the higher values of thermal conductivity and thermal diffusivity of NC-435 Si/SiC would make that material more resistant to thermal stress fracture under less severe quench conditions.

The analytical parameters R''' and R'''' (Table 6.5) dealing with resistance to crack propagation damage resulting from thermal quenching clearly indicate KBI RSSN should be the most resistant to additional crack propagation. This is in qualitative agreement with the gradual change in internal friction observed for this material as a function of increasing quench temperature difference. Weaver et al.[96] plotted percent loss in strength (after a ΔT = 475°C quench) against the R'''' parameter for their data to obtain a trend line shown in Figure 6.36. The residual strength data obtained on samples after various ΔT_c quenches was used to determine percent loss of strength for the IITRI materials. Comparison of this data with the Norton trend line shows very poor agreement, probably because of differences in ΔT, and the strength loss was essentially independent of R''''. As indicated in Table 6.2, possibly better agreement would be obtained if a means of determining crack surface area (or some other measure of crack extent) after thermal shock was available. However, if the R'''parameter, or the minimum elastic energy available at fracture for crack propagation, is plotted against direct loss of strength, as in Figure 6.37, much better agreement is found, except for the KBI RSSN. This could be due to the gradual loss of strength in this material. Better fit with the other materials would have occurred if KBI RS Si_3N_4 exhibited no loss of strength during quenching. This could have been the case for similar

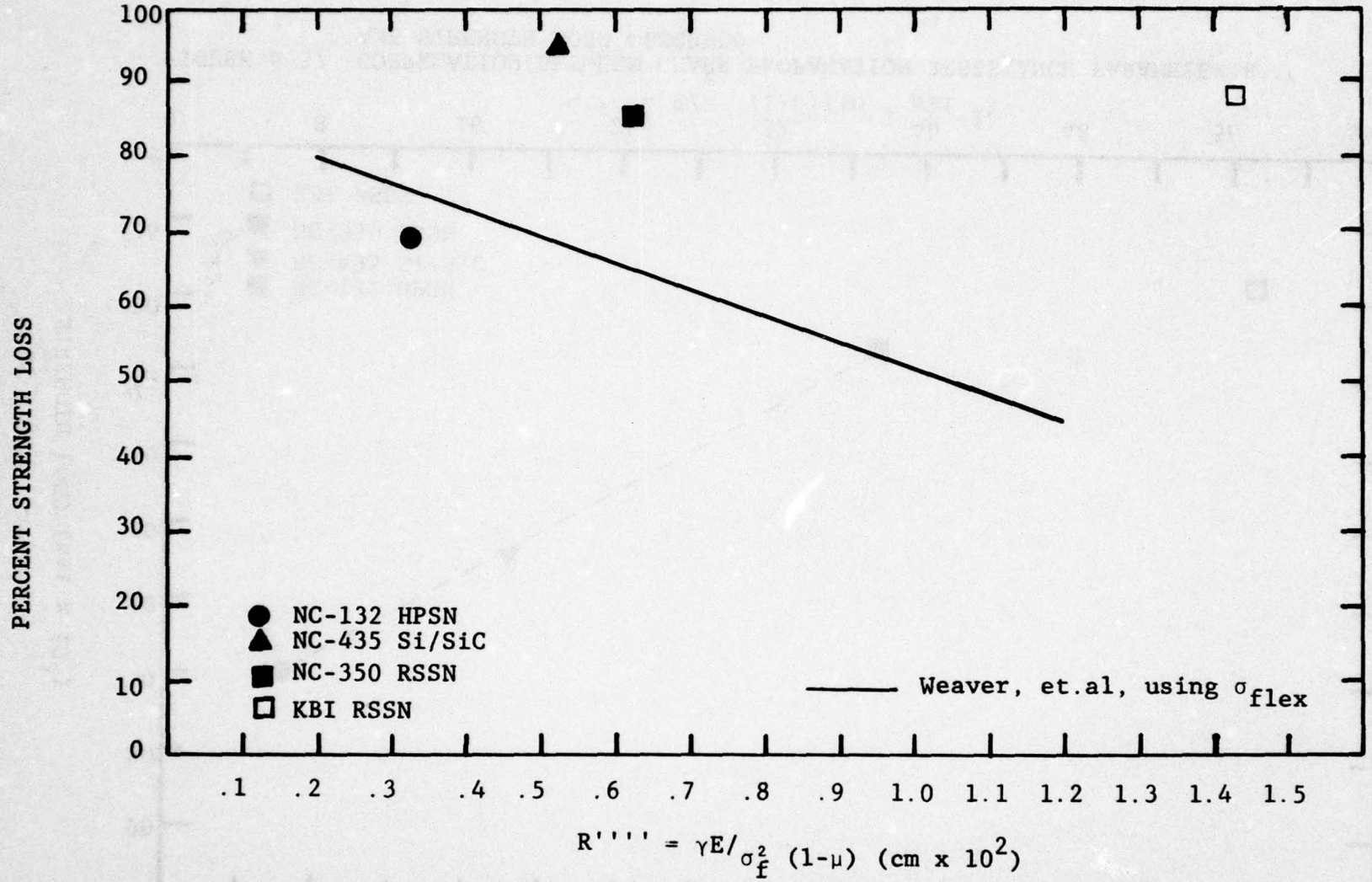

FIGURE 6.36 CORRELATION BETWEEN CRACK PROPAGATION RESISTANCE PARAMETER AND THERMAL SHOCK DAMAGE OBSERVED

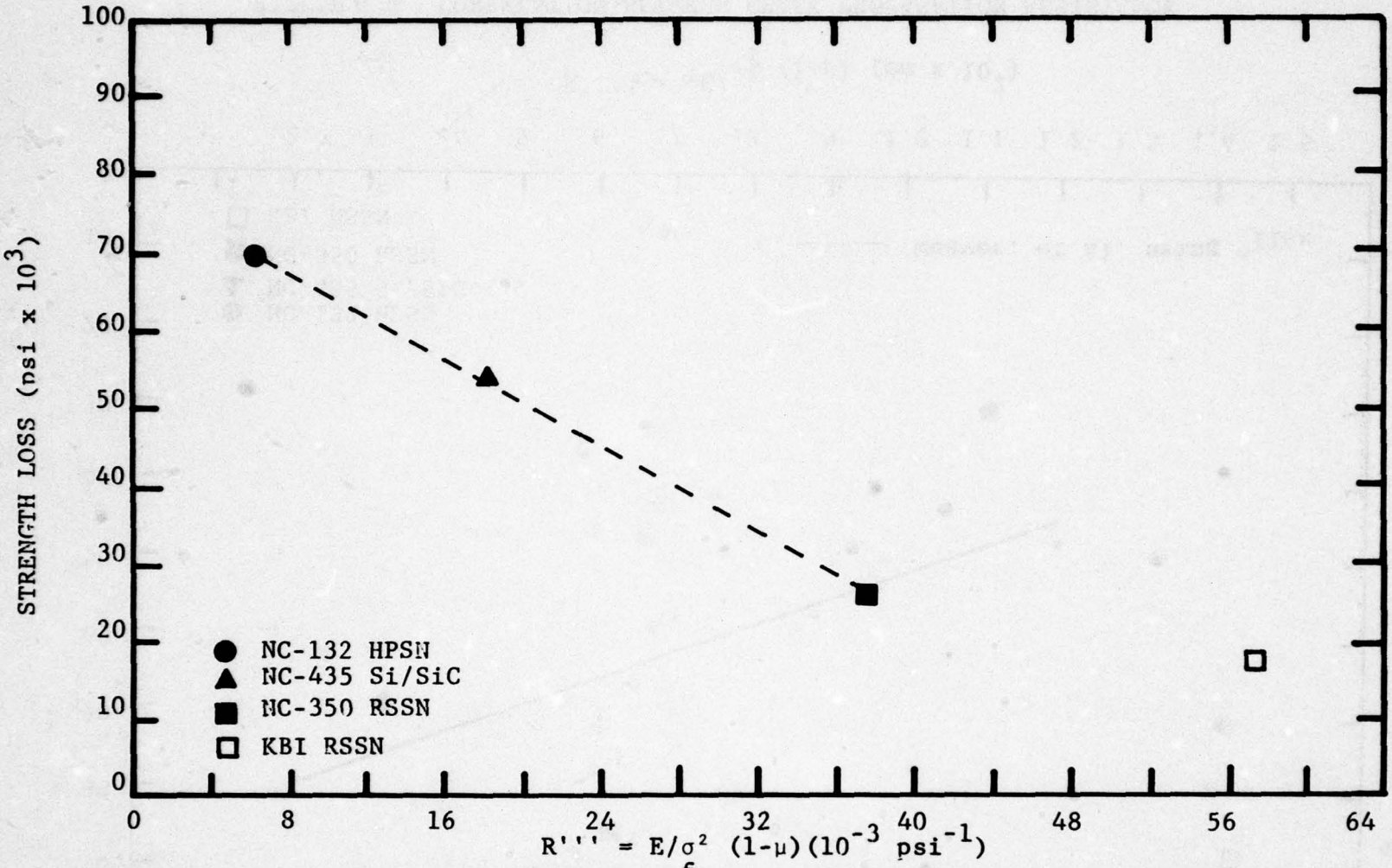

FIGURE 6.37 CORRELATION BETWEEN CRACK PROPAGATION RESISTANCE PARAMETER R''' AND STRENGTH LOSS OBSERVED

quenches: at the $\Delta T = 500°C$, corresponding to the changes in internal friction and strength for NC-350 RSSN, there was little change in internal friction for KBI. This implies the flaw structure was basically unchanged and so it may be that there was also little change in strength. However, no residual strength determinations on KBI after a $\Delta T = 500°C$ quench were made that would help confirm or disprove this.

The calculated values for the thermal stress crack stability parameter R_{st}, are also shown in Table 6.5. Since this parameter combines the properties desired for resistance to both fracture initiation and subsequent propagation, it is not surprising that both NC-132 HPSN and KBI RSSN show the highest values of the materials examined. Although the R_{st} parameter may be obtained from relations for the relative crack propagation resistance of materials containing either short or long cracks,[95] it is most usefully applied to compare the performance of various materials in a spall resistant application, such as some refractories, where the components are already purposefully precracked or pre-flawed.[91] Thus it does not really apply to a dense material like NC-132. As noted above, NC-132 appears to be the most resistant to fracture initiation while KBI provides the greatest resistance to additional crack propagation of the materials examined. Therefore each may be a useful material, but for much different applications and thermal stress environments. This result also demonstrates the merit of examining different types of thermal shock experiments and the total range of thermal stress resistance parameters, rather than just focusing on one, such as R_{st}, which may give misleading indications of actual performance.

Caution must also be exercised in interpreting these parameters since data appropriate for their calculation is seldom available. In this case flexural strength was used instead of tensile strength, for example. Fracture surface energy may be

sensitive to small changes in temperature at some temperature level. Also, the materials' thermal stress resistance may be entirely different over a different quenching temperature range, e.g., 1300-1100°C. However, properly considered, they do provide a helpful guide to evaluating relative performance under thermal stress environments.

7.0 MACH I BURNER RIG EVALUATION AT NASA-LEWIS

Evaluation of four of the candidate materials in a simulated turbine environment was accomplished by NASA-Lewis using a Mach I burner rig. Description of this equipment and testing procedures have been given previously[103,104]. In the current study, samples of size 1/4 x 1 x 4 inch, which had the 1/4 x 4 inch surface machined to a 45° wedge, were employed. Jet A fuel was used and the Mach 1 velocity gases were directed at the wedge surfaces. The tests were run for 250 cycles or until sample failure. Cycle duration was 15 minutes with the burner in operation for 12 minutes and a still air cool for 3 minutes. Four materials were tested, Norton NC-132 HP Si_3N_4, NC-435 siliconized SiC, NC-350 RS Si_3N_4, and Kawecki-Berylco RS Si_3N_4. Tests were conducted at temperatures of 2200°, 2300° , 2400°, and 2500°F, (1204°, 1260°, 1316°, and 1371°C, respectively) with the temperature measured at the leading edge of the wedge. Three successive temperatures were used for each material, the values depending on performance. Results of these tests are given in Table 7.1. Data presented include the leading edge temperature, the number of cycles completed, and the weight change in mg/cm^2.

NC-132 HP Si_3N_4 survived all of the tests to 2500°F without failure. Weight losses were relatively low. For the NC-435 SiC, considerable variations between batches was seen. Batch 3 survived tests up to 2400°F without failure but only one sample of batch 1 and none of batch 4 samples ran the duration of the test. These results are consistent with strength determinations, since batch 3 had the highest strength at room and elevated temperatures (Figure 5.6). We have previously discussed in Section 5.1.2 how this is the result of the amount of silicon-rich phase present.

TABLE 7.1

SUMMARY OF NASA-LEWIS MACH I BURNER RIG EVALUATION*

Norton NC-132 HP Si_3N_4

Batch 1				
Leading Edge Temp. °F, (°C)		2300 (1260)	2400 (1316)	2500 (1371)
Cycles Completed		250	250	250
Weight Change (mg/cm^2)		-0.9	-0.28	-0.53
Batch 2				
Leading Edge Temp. °F, (°C)		2300 (1260)	2400 (1316)	2500 (1371)
Cycles Completed		250	250	250
Weight Change (mg/cm^2)		+0.04	-0.18	-0.23

Norton NC-435 SILICONIZED SiC

Batch 1				
Leading Edge Temp. °F (°C)	2200 (1204)	2300 (1260)	2400 (1316)	2500 (1371)
Cycles Completed	250	134 (failed)		19 (failed)
Weight Change (mg/cm^2)				
Batch 3				
Leading Edge Temp. °F, (°C)	2200 (1204)	2300 (1260)	2400 (1316)	
Cycles Completed	250	250	250	
Weight Change (mg/cm^2)	+0.35	+0.27	+0.15	
Batch 4				
Leading Edge Temp. °F, (°C)	2200 (1204)	2300 (1260)		
Cycles Completed	126 (failed)	1 (failed)		
Weight Change (mg/cm^2)		125 (failed)		
		2.94		

TABLE 7.1 (Continued)

Norton NC-350 RS Si_3N_4

Batch 1				
Leading Edge Temp. °F, (°C)		2300 (1260)	2400 (1316)	2500 (1371)
Cycles Completed		250	76 (failed)	250
Weight Change (mg/cm^2)		-0.96		-0.26
Batch 2				
Leading Edge Temp. °F, (°C)		2300 (1260)	2400 (1316)	2500 (1371)
Cycles Completed		20 (failed)	250	250
Weight Change (mg/cm^2)		Installation Damage	+2.99	+2.51
Batch 3				
Leading Edge Temp. °F, (°C)		2300 (1260)	2400 (1316)	2500 (1371)
Cycles Completed		250	250	250
Weight Change (mg/cm^2)		+2.94	+1.53	+0.73

KAWECKI-BERYLCO RS Si_3N_4

Batch 1				
Leading Edge Temp. °F (°C)	2200 (1204)	2300 (1260)	2400 (1316)	
Cycles Completed	98 (failed)	250	1 (failed)	
Weight Change (mg/cm^2)		+5.56		
Batch 2				
Leading Edge Temp. °F, (°C)	2200 (1204)	2300 (1260)	2400 (1316)	
Cycles Completed	20 (failed)	5 (failed)	1 (failed)	
Weight Change (mg/cm^2)				
Batch 3				
Leading Edge Temp. °F, (°C)	2200 (1204)	2300 (1260)	2400 (1316)	
Cycles Completed	5 (failed)	5 (failed)	1 (failed)	
Weight Change (mg/cm^2)				

TABLE 7.1 (Continued)

* NOTES:

1. Three samples per batch were tested.
2. The goal of the testing was 250 exposure cycles per sample, each sample being tested at one of three temperatures.
3. A cycle consisted of 12 minutes with burner in operation, then a 3 minute still-air cool. Sample reaches test temperature in ~10 seconds.

The NC-350 RS Si_3N_4 performed quite well at temperatures to 2500°F. All but two of the samples completed the testing cycle. Of the two failures, one was considered due to installation damage. Weight change on this material was quite variable, ranging from -0.96 to +2.99 mg/cm^2. The good performance of NC-350 can be attributed to its uniform microstructure and high strength at elevated temperatures.

The Kawecki-Berylco RS Si_3N_4 performed poorly in this test at temperatures to 2400°F. Only one sample completed the test and all but one of the remaining samples failed early in the test. These results are consistent with the strength and microstructural aspects of the KBI material discussed in Section 5.1.4 above (i.e. low strength and inhomogeneous microstructure). The poor performance of the KBI material in this simulative shock/fatigue/environment test is in marked contrast to the performance of KBI RSSN in the water quench/internal friction test. This points out the dangers of ranking materials based on only one type of thermal shock test. It also points out that comparing materials performance in various thermal stress tests often involves not only comparing results per se, but considering the applicability of each material for the test in question. Thus, results for each material and each test must be interpreted individually and individual failure mechanisms must be established to compare results.

More detailed evaluation of the samples will be accomplished by NASA-Lewis. This includes characterization of the surface and interior of the samples by scanning electron microscopy and x-ray diffraction analysis. These data will be published by NASA-Lewis when the work is completed, and subsequently summarized here.

Although the interpretation of the results obtained on NC-132 HP Si_3N_4, NC-435 siliconized SiC, NC-350 RS Si_3N_4 and KBI RS Si_3N_4 will be published by NASA-Lewis at a later date when SEM and x-ray diffraction analyses are complete, it is informative to review previously published results on similar SiC and Si_3N_4 materials[105]. We emphasize that this review is presented for informational purposes at this time, and by no means is meant to apply in any way except in a general manner to the specific data on the four materials shown in Table 7.1.

The results reported previously by Sanders and Probst[105] for other hot pressed and sintered SiC and Si_3N_4 materials tested on the NASA-Lewis Mach 1/Jet A Fuel Burner Rig provides an indication of general behavioral trends. In general, features associated with good resistance to degradation included high density, fine grain size, small amounts of microconstituents and flaws, and a homogeneous microstructure. Hot pressed SiC was particularily thermal fatigue resistant in this test, mainly being attributed to its duplex fine grain size distribution. Most thermal fatigue failures were attributed to second phase remnants of sintering aids and heterogeneous microstructures consisting of large grains or large pores. Starting powder purity was found to be important as well as the overall porosity distribution. For the siliconized SiC materials the distribution of free silicon was important. However, it was found that the presence of free silicon was not inherently detrimental, as long as it was finely distributed and accompained by a fine grain SiC matrix. Such a material compared well with the hot pressed SiC.

Oxidation rate is a prime consideration in thermal fatigue resistance. For instance it was found that a more protective oxide layer formed on SiC than on Si_3N_4 due to its higher viscosity and therefore greater resistance to viscous flow in the high velocity gas stream. This reflects differences in purity levels of the various test samples.

Sanders and Probst results on hot pressed and reaction sintered forms of Si_3N_4 are also informative. Hot pressed Si_3N_4 was found to have very good thermal fatigue resistance. Such materials are generally dense, fine grained, and possess uniform microstructural characteristics. The controlling property for thermal fatigue in HPSN was found to be purity level and its effect on oxidation. Starting powder impurities and the densification aids used have a great effect on the nature of the SiO_2 layer formed.

The reaction sintered silicon nitride materials were not as thermal fatigue resistant. They are generally weaker and much more porous. The oxidation rate can be much lower than for hot pressed Si_3N_4. Porosity non-uniformity, and unreacted silicon particles are often a problem. Many process-related variables were found to be detrimental to thermal fatigue. For instance: α/β Si_3N_4 ratio variations within a sample, or excessive oxidation due to localized variations in nitriding process.

In general, however, Sanders and Probst found that once a ceramic material possessed the necessary combination of strength, elastic modulus, thermal conductivity, and thermal expansion to survive the first thermal shock cycle, then the mechanical properties strength, elastic modulus, and fracture toughness determined the ability to survive the cyclic thermal environment. Thermal fatigue is a complex phenomenon that involves the environment and its effect on microstructure. Subcritical crack growth and chemomechanical effects in the candidate materials are thus the determining factors in environmental thermal fatigue resistance. Failure can not easily be predicted, since a multitude of failure modes are possible, and often involve several interacting phenomena.

8.0 SUMMARY/MATERIALS OVERVIEW

Extensive thermal and mechanical property data have been generated on four candidate turbine materials, Norton NC-132 hot pressed Si_3N_4, NC-435 siliconized SiC, NC-350 reaction sintered Si_3N_4, and Kawecki-Berylco reaction sintered Si_3N_4. A more limited amount of information is currently available for six additional materials. Kyocera hot pressed and sintered Si_3N_4, General Electric and Carborundum SiC, and various NRL Si_3N_4-ZrO_2 materials.

Table 8.1 provides a general overview of the major descriptive characteristics of the four materials extensively characterized. Tabular summary of the data for each material is provided in Tables 8.2 - 8.5.

Norton NC-132 hot-pressed Si_3N_4 is a fine-grained (1-2μm) high density (99%) material composed mainly of β-Si_3N_4 grains. It has an extremely uniform microstructure that results in high strength (up to 120 ksi in 4 pt. bending) and high modulus at low temperatures. It exhibits linear stress-strain behavior to 1200°C. Some apparent oxidative healing of surface flaws has been observed (but not for extended oxidative exposure where degradation of strength would be expected). NC-132 exhibits low thermal expansion typical of silicon nitride and has good severe-quench thermal shock resistance. Its performance in a simulated turbine environment has been very good. NC-132 disadvantages are mainly the result of its relatively high impurity content (~3% oxygen, ~3% total metals) due to the use of MgO additions to promote densification during hot-pressing. These impurities segregate at the grain boundaries, commonly thought to be in the form of a glassy magnesium silicate phase (although not always found by electron microscopy). This impurity phase is responsible for the rapid degradation of strength and loss of elasticity above 1200°C, poor high temperature creep

TABLE 8.1 GENERAL SUMMARY OF RESULTS TO DATE

MATERIAL SYSTEM	ADVANTAGES	DISADVANTAGES
Norton NC-132 Hot Pressed Silicon Nitride 99% Dense 3.3 w/o Oxygen 3.1 w/o Metal. β-Si_3N_4 (MAJOR)	• Uniform microstructure (1-2μm grain size), minimal processing flaws • High Density • High Strength • Intermediate Modulus at 25°C • Good properties to 1200°C • Apparent "healing" of flaws at elevated temperature by oxidative exposure. • Low thermal expansion typical of Si_3N_4. • Linear elastic behavior to 1200°C, plastic component at 1350°C • Good thermal shock and hot gas exposure resistance. • Predictable properties.	• Apparent machining damage (since processing flaws are minimal) • Grain boundary impurity presumably magnesium silicate that controls high temperature properties • Rapidly decreasing strength and modulus @ T ≥ 1200°C. • Poor creep resistance at elevated temperature (T > 1200°C)
Norton NC-435 Sintered SiC, Densified by Silicon Impregnation 93% Dense 80 v/o (α)SiC/20 v/o Si 0.3 w/o Oxygen, 0.6 w/o Metal	• High Density • Medium strength, High Modulus system. • Retains RT strength to 1275°C. • High thermal conductivity (can be a disadvantage also)	• Silicon phase melts at 1410°C • Temperature limitation T < 1350°C. for structural applications. • Plastic component to deformation at 1200°C • Variation in amount and distribution of Si phase causes property variation. • More silicon than expected (~20% vs. 5-10%) • Intermediate creep strength. • High Thermal Expansion

TABLE 8.1 (Continued)

MATERIAL SYSTEM	ADVANTAGES	DISADVANTAGES
Norton NC-350 Reaction Sintered Silicon Nitride α-Si_3N_4 (Major) 0.8 w/o Oxygen, 0.5% Metal ~78% Dense.	• High purity • Uniform microstructure • Highest creep resistance of all materials tested. • Possible materials improvement through density-open porosity relationship • Significant strength increase with temperature to 1200°C (oxidative porosity modification for short-term exposure) • Linear elastic to failure at 1500°C. • Modulus increase to 1200°C related density. • Highest strength and modulus at T>1400°C • Low thermal expansion. • Good hot gas exposure endurance.	• High porosity typical of reaction sintered materials. • 3/16" thickness limitation imposed by production process. • Density variable, slightly. • Low strength and modulus at low temperatures controlled by porosity. • Low thermal conductivity (can be an advantage also) • Large pores and pore agglomerates (10μm) control properties. - thus, processing improvements are required to improve mechanical properties.
KBI-RBSN Kawecki-Berylco Reaction Bonded Si_3N_4 ~75% Dense .7 w/o Metal; β-Si_3N_4 + α-Si_3N_4	• Potential for higher density seen. • Apparently no 3/16" thickness limitation in production.	• Variable properties • Non-uniform microstructure. • Large pores and pore agglomerates (~50μm) • Low strength, modulus, creep resistance. • No beneficial effect of oxidation at elevated temperature seen under conditions of test • Apparently not as well reaction sintered as NC-350. • Apparently large free silicon content (~20%) • Poor performance in hot gas exposure tests. • Low Weibull modulus. • Flaw structure of such an extent to result in quasi-static behavior in water quench thermal shock.

TABLE 8.2 SUMMARY OF PROPERTIES FOR NORTON NC-132 HP Si_3N_4

TEMPERATURE / BATCH		AVERAGE BULK DENSITY (gm/cc)*	FLEXURAL STRENGTH (psi)	STRAIN-TO-FAILURE (in/in$\times 10^{-3}$)	SECANT MODULUS (10^6 psi)	WEIBULL MODULUS, STRENGTH	K_{I_C} ($MNm^{-3/2}$)	FRACTURE SURFACE ENERGY (Jm^{-2})	CREEP** STRENGTH (hr^{-1}/ksi)	THERMAL EXPANSION (10^{-6}/°C)	THERMAL DIFFUSIVITY ($cm^2 sec^{-1}$)	THERMAL COND. $\frac{cal}{sec\ cm\ C}$	ΔT^{Q-1}_{crit}	HOT GAS EXPOSURE
25°C	1	3.177	90,910	1.83	48.4	5.13	4.48	37.1	-	3.0 (25-1000°)	.16 (25°C)	.085	Onset of Thermal Shock Damage at 600°C in Water Quench Test	-
	2	3.186	115,210	2.49	45.7	7.60	5.04		-	3.0 (25-1000°)				-
1200°C	1	3.179	88,190	2.05	42.8	11.58	-	-	-	3.2	.065 (500°C)	.055		Good
	2	3.180	79,240	2.11	39.2	17.21	-	-	-	3.2				Good
1350°C	1	3.178	58,620	3.31	30.8	11.44	8.55	233.5	3.3×10^{-4}/10	3.3	.045 (1000°C)	.04		Good
	2	3.184	48,800	4.22	22.7	26.61	10.4		5.1×10^{-4}/15	3.3				Good
1500°C	1	3.178	27,770	6.18	7.7	8.26	-	-	1.6×10^{-4}/2	3.6	.035 (1500°C)	.03		-
	2	3.186	25,210	6.32	6.5	30.63	-	-	1.9×10^{-4}/2	3.6				-

** Steady State Creep Rate/Applied Stress

* Average Bulk Density of Flexural Strength Samples.

TABLE 8.3 SUMMARY OF PROPERTIES FOR NORTON NC-435 Si/SiC

TEMPERATURE / BATCH		Average BULK DENSITY (gm/cc)*	FLEXURAL STRENGTH (psi)	STRAIN-TO-FAILURE ($in/in \times 10^{-3}$)	SECANT MODULUS (10^6 psi)	WEIBULL MODULUS (STRENGTH)	K_{I_C} ($MNm^{-3/2}$)	FRACTURE SURFACE ENERGY (Jm^{-2})	CREEP** STRENGTH (hr^{-1}/ksi)	THERMAL EXPANSION (10^{-6}/ °C)	THERMAL DIFFUSIVITY ($cm^2 sec^{-1}$)	THERMAL COND. cal / sec cm C	$\Delta T^{Q-1}_{crit.}$	HOT GAS EXPOSURE
25°C	1	2.936	50,460	0.95	53.9	3.20	3.93	19.3	-	4.3 (25-1000°)	0.7 (25°C)	.3	Onset of Thermal Shock Damage at 350-400°C in Water Quench Test	-
	3	2.997	65,980	1.33	49.5	5.93	3.92		-	4.35 (25-1000°)				-
	4	2.962	55,150	1.13	48.8	10.67	3.40		-	4.4 (25-1000°)				-
1200°C	1	2.938	57,400	1.49	46.4	6.22	-	-	2.1×10^{-5}/35	4.4	.17 (500°C)	.14		Good
	3	2.996	79,660	2.06	43.4	16.41	-	-	8.4×10^{-6}/30	4.5				Good
	4	2.975	62,390	2.09	39.7	13.55	-	-	6.2×10^{-6}/30	4.5				Fair
1275°C	1	2.922	57,820	1.88	40.6	5.53	-	-	-	4.35	.09 (1000°C)	.08		Fair
	3	2.989	59,010	1.65	42.8	5.51	-	-	-	4.45				Good
	4	2.959	60,200	1.95	39.1	13.99	-	-	-	4.5				Fair/ Poor
1350°C	1	2.929	44,120	1.39	36.1	5.38	7.30	88.6	4.4×10^{-5}/30	4.3	.07 (1400°C)	.07		Poor
	3	3.000	48,310	1.41	37.7	7.40	7.20		--	4.4				Good
	4	2.965	41,410	1.43	34.9	19.73	6.30		2.6×10^{-5}/20	4.5				---

** Steady State Creep Rate/Applied Stress

* Average Bulk Density of Flexural Strength Samples

TABLE 8.4 SUMMARY OF PROPERTIES FOR NOTRON NC-350 RB Si_3N_4

TEMPERATURE / BATCH		AVERAGE BULK DENSITY (gm/cc)*	FLEXURAL STRENGTH (psi)	STRAIN-TO FAILURE (in/in$\times 10^{-3}$)	SECANT MODULUS (10^6psi)	WEIBULL MODULUS (Strength)	K_{I_C} (MNm$^{-3/2}$)	FRACTURE SURFACE ENERGY (Jm^{-2})	CREEP** STRENGTH (hr^{-1}/ ksi)	THERMAL EXPANSION (10^{-6}/ °C)	THERMAL DIFFUSIVITY (cm^2 sec^{-1})	THERMAL COND. $\frac{cal}{sec\ cm\ C}$	$\Delta T_{crit.}$	HOT GAS EXPOSURE
25°C	1	2.52	30,870	1.20	25.5	3.35	1.88	11.3	-	2.8 (25-1000°)	($\bar{\rho}$ ~ 2.3) .07 (25°C)	.026	Onset of Thermal Shock Damage at 400°C-500°C in Water Quench Test	-
	2	2.40	23,530	0.99	23.5	3.34	2.16		-	2 8 (25-1000°)				-
	3	2.54	33,960	1.21	27.7	4.65	2.08		-	2.7 (25-1000°)				-
1200°C	1	2.52	59,970	1.92	32.5	5.65	-	-	-	3.0	.03 (500°C)	.018		Fair /Good
	2	2.40	58,620	2.47	23.1	8.12	-	-	-	3.0				Good
	3	2.53	56,320	1.88	29.7	4.28	-	-	-	2.9				Good
1350°C	1	2.50	54,480	1.99	26.9	7.52	3.10	19.2	~0/40	3.05	.02 (1000°C)	.012		Good
	2	2.40	62,130	2.63	23.5	11.12	2.73		~0/40	3.1				Good
	3	2.55	57,140	2.20	25.5	5.23	2.54		~0/40	3.0				Good
1500°C	1	2.52	46,150	2.00	23.7	7.37	-	-	1.5×10^{-5}/25	2.95	.015 (1500°C)	.01		-
	2	2.41	45,430	2.23	20.5	4.49	-	-	0.9×10^{-5}/25	3.0				-
	3	2.53	53,060	1.98	28.8	12.51	-	-	0.9×10^{-5}/25	3.1				-

** Steady State Creep Rate/Applied Stress

* Average Bilk Density of Flexural Strength Samples

TABLE 8.5 SUMMARY OF PROPERTIES FOR KBI RB Si_3N_4

TEMPERATURE / BATCH		AVERAGE BULK DENSITY* (gm/cc)	FLEXURAL STRENGTH (psi)	STRAIN-TO FAILURE ($in/in \times 10^{-3}$)	SECANT MODULUS (10^6 psi)	WEIBULL MODULUS (STRENGTH)	K_{I_C} ($ft^{1/2}lbm^{-3/2}$)	FRACTURE SURFACE ENERGY (Jm^{-2})	CREEP** STRENGTH (hr^{-1}/ksi)	THERMAL EXPANSION ($10^{-6}/°C$)	THERMAL DIFFUSIVITY ($cm^2\ sec^{-1}$)	THERMAL COND. $\frac{cal.}{sec\ cm\ C}$	$\Delta T_{crit.}^{Q^{-1}}$	HOT GAS EXPOSURE
25°C	1	2.51	23,270	1.08	21.5	3.51	2.35	15.8	-	2.8 (25-1000°)	.14-.22 (25°C)		Onset of Thermal Shock Damage at T > 750°C in Water Quench Test (Quasi-Static Hasselman Region).	-
	2	2.45	21,800	1.03	21.1	3.89	2.08		-	2.8 (25-1000°)				-
	3	2.35	18,080	0.91	20.0	3.52	2.21		-	2.9 (25-1000°)				-
1200°C	1	2.35	20,500	.91	23.2	7.29	-	-	-	3.0				Good/ Fair
	2	2.43	23,020	.74	32.5	2.68	-	-	-	3.0				Poor
	3	2.36	22,040	.84	26.9	4.33	-	-	-	3.0				Poor
1350°C	1	2.52	27,350	.97	29.2	2.51	2.16	12.7	$1.2 \times 10^{-5}/4.5$	3.1				Poor
	2	2.46	24,030	.88	30.0	3.16	2.22		$1.5 \times 10^{-5}/4.5$	3.1				Poor
	3	2.35	20,190	.69	30.1	2.12	2.41		$1.8 \times 10^{-5}/4.5$	3.2				Poor
1500°C	1	2.45	24,190	1.02	23.9	3.24	-	-	$1 \times 10^{-5}/1.2$	3.0				-
	2	2.40	16,460	.78	23.0	2.99	-	-	$1.7 \times 10^{-5}/1.5$	3.2				-
	3	2.33	18,760	.93	22.4	2.78	-	-	$1.6 \times 10^{-5}/1.3$	3.4				-

** Steady State Creep Rate/Applied Stress

* Average Bulk Density of Flexural Strength Samples

resistance, and high oxidation rates. At low temperatures the high strength, elasticity, and absence of significant process-related defects in NC-132 HP Si_3N_4 make it particularly sensitive to the distribution of small flaws - machining damage is common. Overall, however, the high density and uniform microstructure of NC-132 result in good properties to 1200°C, and generally predictable properties throughout the temperature range.

Norton NC-435 is a sintered α - SiC body that is densified by impregnation with ~20 volume percent silicon metal. The resulting body is relatively dense (93%) and pure (~.3^{w}/o oxygen, ~.6^{w}/o metal). The room temperature 4 pt. bend strength of NC-435 is moderate (55 ksi), and the modulus is relatively high (50 x 10^6 psi). The low temperature properties of NC-435 Si/SiC are retained to 1275°C. This material has the high thermal conductivity characteristic of silicon carbide. This is especially true at room temperature due to extremely high conductivity of the silicon phase near 25°C. NC-435 is limited to use to $T \leq 1350$°C, due to the presence of the silicon phase (pure silicon melts at 1410°C). This silicon-rich phase is responsible for the non-linear stress-strain behavior at $T \geq 1200$°C. This secondary phase was present to a greater extent than expected (based on literature information) and variation in its amount and distribution is thought to be responsible for the wide variation in properties observed (mainly strength). NC-435 siliconized SiC has intermediate creep strength and high thermal expansion.

Norton NC-350 reaction sintered α —Si_3N_4 can be characterized as pure, but relatively porous (ρ~78%) which is characteristic of all reaction sintered materials. However, the microstructure of NC-350 is uniform, which, coupled with the high purity, results in extremely high creep resistance and very good performance in the NASA-Lewis hot gas cyclic exposure

test. NC-350 RS Si_3N_4 exhibits linear elastic stress-strain behavior at 1500°C due to its high purity. NC-350 exhibited the highest strength and modulus at T>1400°C of all materials tested (i.e., NC-132, NC-435, and the KBI materials). Strength at 1500°C is almost 50 ksi. At low temperatures the strength and modulus of NC-350 are low, being controlled by the high porosity. Failure generally occurs by extension of the largest pores or pore agglomerate (~10μm). The slight modulus increase with temperature is correlated inversely with density, and results in part due to the large strength increase between 25° and 1200°C observed. The strength increase is believed to be the result of modification of the pore structure during oxidation at elevated temperature. Fractographic analysis and fracture mechanics calculations are currently being performed on NC-350 to determine the effect of oxidation (e.g., porosity modification by crack tip blunting or by a chemical effect that changes the fracture surface energy). NC-350 exhibits low thermal expansion, and a low thermal conductivity compared to the more dense hot pressed Si_3N_4.

KBI reaction sintered Si_3N_4 is ~75% dense and consists of approximately equal amounts of α- and β-Si_3N_4 grains. The KBI material is characterized by extremely variable properties and a nonuniform microstructure. Many large pores and pore agglomerates (~50μm) were frequently observed. These aspects of the microstructure lead to low strength and modulus, and poor creep resistance. No beneficial effect of oxidation was observed in the high temperature 4-pt. bend tests, perhaps due to the larger pores than in NC-350. SEM views of fracture features indicated that this material was not as well sintered as NC-350 RS Si_3N_4. There may be a large amount of silicon in the structure, as evidenced in microstructural analysis and in the room temperature thermal diffusivity data. This material performed poorly in the NASA-Lewis hot gas exposure tests. The overall

structure of the KBI material resulted in behavior during water quench thermal shock tests that would be interpreted as quasi-static in a Hasselman thermal shock analysis.

The KBI material tested thus far in the program is seen to have much poorer properties than the other materials. However, these data are not necessarily representative of the quality of materials that KBI is capable of producing. This is supported by KBI-obtained property data on their product[111] and indicates the probability of atypical processing defects in the current material. More testing is planned by IITRI on the KBI RS Si_3N_4 when KBI processing operations begin in the U.S.

Figure 8.1 illustrates the strength-temperature behavior of several other materials for which characterization is not as complete or has just begin. The General Electric boron-doped sintered β-SiC is ~95% dense. The Carborundum sintered α-SiC is 98% dense, but is of lower strength. The Kyocera hot pressed Si_3N_4, SN-3, has lower density (96%) than NC-132, and also lower room temperature strength. The hot pressed Kyocera material losses its low temperature strength and elastic properties at ~750°C, an indication that less pure precursor powders and/or significant oxide densification aids are used. The two pressureless sintered Kyocera silicon nitride materials exhibit higher room temperature strength than the reaction bonded materials, primarily due to higher density (88-94% dense). However, these materials also exhibit a rapid decrease in strength and elasiticity at T > 750°C, indicating the affect of the use of large amounts of oxide sintering aids.

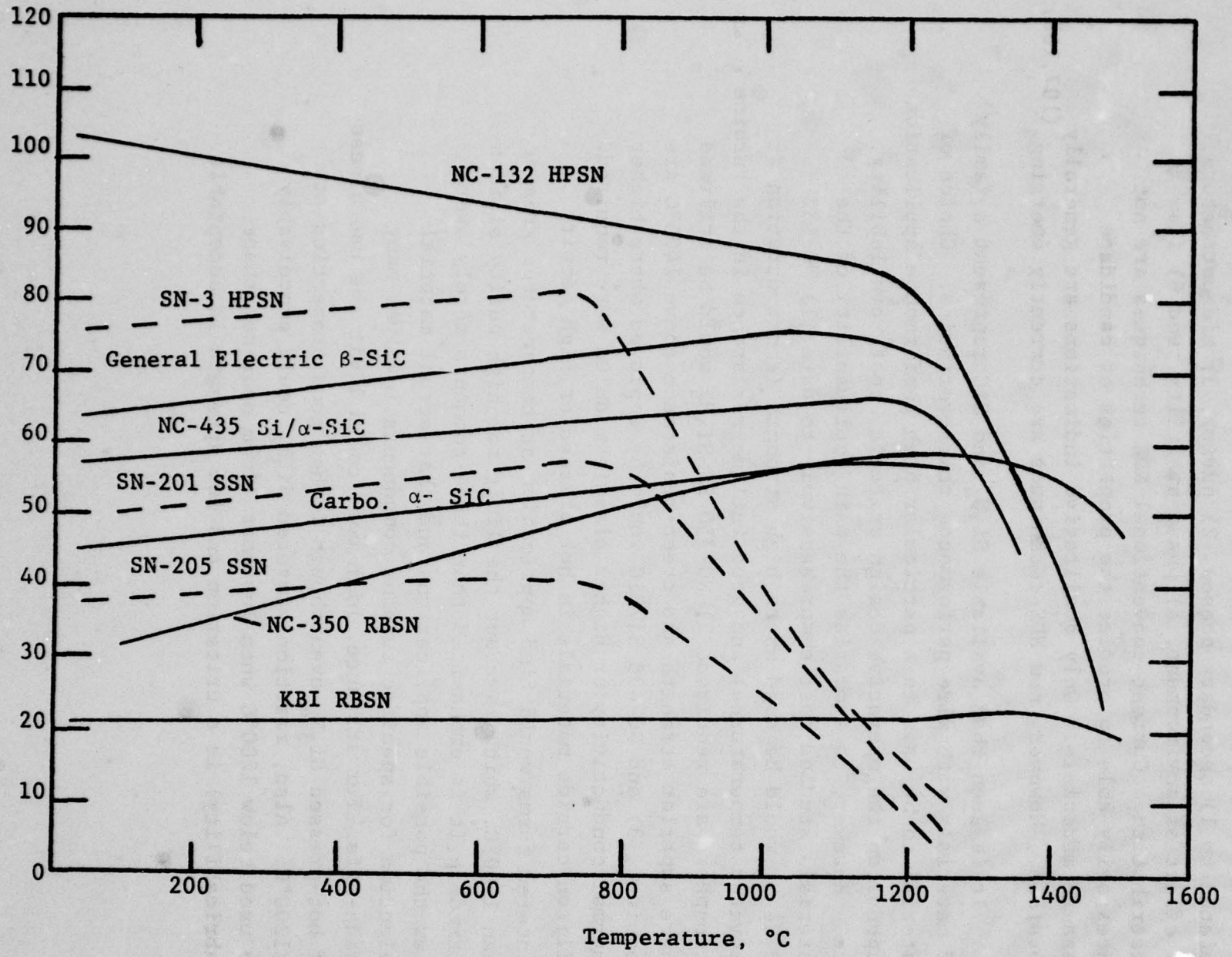

FIGURE 8.1 REPRESENTATIVE 4-POINT FLEXURAL STRENGTH OF Si_3N_4 AND SiC MATERIALS

It is observed that the properties of each material are related to 1) secondary phases, 2) purity, 3) microstructure, 4) effect of environment, 5) phase stability, and 6) flaw distribution. Current conventional NDE techniques are not necessarily able to predict the properties of candidate ceramic materials. Only qualitative indications are generally possible. However, new NDE techniques are currently emerging.[107,108]

It is seen that available Si_3N_4 and SiC represent a family of materials with wide performance characteristics. Choice of material to be used in a particular high performance application depends on the operative design criteria, cost, availability, etc. However, to summarize the main applicability of the materials studied most comprehensively to date: 1) NC-132 HP Si_3N_4 would be used where high strength (short duration at elevated temperatures) and good fatigue resistance in the turbine atmosphere are required, 2) NC-350 RS Si_3N_4 would be utilized where superior strength and creep resistance above 1400°C are required, 3) and NC-435 Si/SiC would be employed where higher thermal conductivity or higher elastic modulus were required. Silicon carbide materials in hot pressed or high density sintered forms would find application at temperatures greater than 1500°C, which is about the limit for high purity silicon nitride. It is emphasized that these comments merely overview the possible applications and that actual material selection for specific turbine components involves many trade-offs. For instance, high cost could limit the usefulness of hot-pressed Si_3N_4 even though it has good properties at T<1200°C. Also, reaction sintered Si_3N_4 could conceivably be used below 1200°C when low cost (from near-net shape fabricability) is a criterion and low strength is acceptable.

9.0 CLOSURE

Available Si_3N_4 and SiC materials represent a large family of materials with wide property variation and broad response characteristics to interaction with severe environments. Even though some are termed commercially available they are in a continual state of development and change. In general, property differences between materials of a given type are directly related to: 1) existence of secondary phases; 2) purity; 3) microstructural aspects such as pore size and distribution, etc., 4) relative oxidation rates, 5) phase stability, and 6) flaw distribution. For such materials it is thus imperative that adequate pre- and post-test characterization be conducted for microstructure, density and porosity distribution, secondary phases, crystalline form, impurity (especially metals and oxygen), surface finish, etc. The necessity of post-test fractographic failure mode analysis using the scanning electron microscope cannot be over-emphasized.

For silicon-base ceramic materials to be successful as high temperature structural components in advanced engine applications, comprehensive characterization and properties evaluation must be conducted using controlled techniques and test parameters. Interpretation of behavior should then be made with respect to microstructure, purity, flaw distribution, secondary phases, and environmental exposure. Mechanisms of fracture and crack propagation should be determined by the use of fractography and fracture mechanics analysis. Statistical analysis and data correlation permit more accurate life prediction. Process-related effects should be documented for future materials improvement. The realization of the existence of subcritical crack growth phenomena in the candidate materials means that environmental effects must be studied in detail.

Simulated gas turbine exposure through hot gas cyclic exposure is perhaps the final test of a materials candidacy for gas turbine application. Finally all of this information on materials behavior must ultimately be made available to designers in a format that can be readily utilized in component design.

All of these aspects are elements of our current program with AFML, some to a greater and some to a lesser extent. In gas turbine applications, the optimum material to be used depends on the particular design criteria that apply to each component. Since the properties and behavioral characteristics of the candidate materials cover such a wide range, optimum component design depends strongly on comprehensive materials characterization. A program like the current one thus becomes a major element, perhaps the initial one, in a series of tasks that must be accomplished for ceramic turbines to become a reality in the near future.

Respectfully submitted,
IIT RESEARCH INSTITUTE

D.C. Larsen
Research Engineer

G.C. Walther
Associate Research Engineer
Mechanics of Materials Division
Ceramics Research Section

APPROVED:

S.A. Bortz
Director
Mechanics of Materials Division

REFERENCES

1. T.B. Wade, "Property Screening and Evaluation of Ceramic Vane Materials," IITRI Interim Technical Report No. IITRI-D6114-ITR-12 on AFML Contract F33615-75-C-5196, (July 15, 1976).

2. D.C. Larsen, "Property Screening and Evaluation of Ceramic Vane Materials," IITRI Interim Technical Report No. IITRI-D6114-ITR-18 on AFML Contract F33615-75-C-5196, (February 26, 1977).

3. J.A. Coppola, C.H. McMurtry, "Substitution of Ceramics for Ductile Materials in Design," paper presented at National Symposium on Ceramics in the Service of Man, Washington, D.C., June 7, 1976.

4. C.A. Johnson, General Electric, Schenectady, N.Y., private communication.

5. R.K. Bart, Norton Company, Worcester, Mass., private communication.

6. S.W. Freiman, Naval Research Laboratory, Washington, D.C., private communication.

7. J.J. Petrovic and L.A. Jacobson, "The Strength of Silicon Nitride After Exposure to Different Environments," in J.J. Burke, A.E. Gorum and R.N. Katz, editors, Ceramics for High-Performance Applications-I, Brook-Hill Publ., Chestnut Hill, MA, pp. 397-414, (1974).

8. Ram Kossowsky, D.C. Miller and E.S. Diaz, "Tensile and Creep Strength of Hot Pressed Si_3N_4," J. Mater. Sci. 10 (6) pp. 983-97, (1975).

9. Hauck, E.W., "Future for Ceramic Gas Turbine Design," Gas Turbine World, September, 1974.

10. Kossowsky, R., "The Microstructure of Hot Pressed Silicon-Nitride," Westinghouse Research Laboratories Scientific Paper 73-9D4-Foram-P2, (February 22, 1973).

11. Richerson, D.W., "Effect of Impurities on the High Temperature Properties of Hot Pressed Silicon Nitride," Bull. Am. Ceram. Soc. 52 (7) pp. 560-9, (1973).

REFERENCES (Cont'd)

12. Iskoe, J.L., Lange, F.F. and Diaz, E.S., "Effect of Selected Impurities on the High Temperature Mechanical Properties of Hot-Pressed Silicon Nitride," J. Mater. Sci. 11, pp. 908-12, (1976).

13. Bart, R.K., Hauck, E.W., and Torti, M.L., "Experience in the Manufacture of Gas Turbine Vanes of Hot Pressed Silicon Nitride and Silicon Carbide," ASME Paper 75-GT-99, (1975).

14. Mosher, D.R., Raj, R., and Kossowsky, R., "Measurement of Viscosity of the Grain-Boundary Phase in Hot-Pressed Silicon Nitride," J. Mater. Sci. 11, pp. 49-53, (1976).

15. Powell, B.D., and Drew, P., "The Identification of a Grain-Boundary Phase in Hot-Pressed Silicon Nitride by Auger Electron Spectroscopy," J. Mater. Sci. 9, pp. 1867-70, (1974).

16. Drew, P. and Lewis, M.H., J. Mater. Sci. 9, p. 261, (1974).

17. Tighe, N.J., "Microstructural Aspects of Deformation and Oxidation of Magnesia-Doped Silicon Nitride," NBSIR 76-1153, September 1976.

18. Lou, L.K.V., Mitchell, T.E. and Heuer, A.H., "Continuous Grain Boundary Film in Hot-Pressed Si_3N_4," Ceramographic Contest Winner (Transmission Electron Micrographs), American Ceramic Society, Bull. Am. Ceram. Soc. 56, (8), p. 748, (1977).

19. Lange, F.F., "Relation Between Strength, Fracture Energy, and Microstructure of Hot-Pressed Si_3N_4," J. Amer. Ceram. Soc., 56, (10), pp. 518-22, (1973).

20. Mecholsky, J.J., Freiman, S.W., and Rice, R.W., "Fracture Surface Analysis of Ceramics," J. Mater. Sci., 11, pp. 1310-19, (1976).

21. Baumgartner, H.R., and Richerson, D.W., "Inclusion Effects on the Strength of Hot Pressed Si_3N_4," Pennsylvania State University Symposium on Fracture Mechanics of Ceramics, July 11-13, 1973.

22. Bansal, G.K., and Duckworth, W.H., "Fracture Stress as Related to Flaw and Fracture Mirror Sizes," J. Amer. Ceram. Soc. 60, (7-8), pp. 304-10, (1977).

REFERENCES (Cont'd)

23. Rice, R.W., "Fracture Topography of Ceramics," Surfaces and Interfaces of Glass and Ceramics, W.D. Frechette, W.C. LaCourse, and V.L. Burdick, Editors, pp. 439-72, Plenum.

24. Rice, R.W., "Fractographic Identification of Strength-Controlling Flaws and Microstructure," Fracture Mechanics of Ceramics, Vol. I, Bradt, R.C., Hasselman, D.P.H., and Lange, F.F., Editors, pp. 323-45, Plenum (1974).

25. Mecholsky, J.J., Rice, R.W., and Freiman, S.W., "Prediction of Fracture Energy and Flaw Size in Glasses from Measurements of Mirror Size," J. Amer. Ceram. Soc., 57(10), pp. 440-443, (1974).

26. Lange, F.F., "High-Temperature Strength Behavior of Hot-Pressed Si_3N_4: Evidence for Subcritical Crack Growth," J. Amer. Ceram. Soc., 57, (2), pp. 84-87, (1974).

27. R.W. Rice, S.W. Freiman, J.J. Mecholsky, Jr., Robert Ruh and Y. Harada, "Fractography of Si_3N_4 and SiC," in J.J. Burke, R.N. Katz, E.M. Lenoe and A. Tarpean, editors, Ceramics for High-Performance Applications-II, Proceedings, Fifth Army Materials Technology Conference, Newport, RI, 21-25 March 1977.

28. J.W. Edington, D.J. Rowcliffe and J.L. Henshall, "The Mechanical Properties of Silicon Nitride and Silicon Carbide-Part I: Materials and Strength," Powder Metallurgy International 7 (2), pp. 82-96, (1975).

29. Lange, F.F., "Healing of Surface Cracks in SiC by Oxidation," J. Amer. Ceram. Soc., 53 (5), p. 290, (1970).

30. Larsen, D.C., Bortz, S.A., Ruh, Robert and Tallan, N.M., "Evaluation of Four Commercial Si_3N_4 and SiC Materials for Turbine Applications," in J.J. Burke, R.N. Katz, E.M. Lenoe and H. Tarpean, Editors, Ceramics for High Performance Applications-II, Proceedings Fifth Army Materials Technology Conference, Newport, Rhode Island, 21-25 March 1977.

31. Washburn, M.E., and Baumgartner, H.R., "High Temperature Properties of Reaction-Bonded Silicon Nitride," Proceedings of Second Army Materials Technology Conference, Hyannis, Mass. (13-16 November 1973), in J.J. Burke, A.E. Gorum and R.N. Katz, Editors, Ceramics for High Performance Applications, (Brook Hill), pp. 479-91, (1974).

32. Torti, M.L., "Ceramics for Gas Turbines, Present and Future," Paper 740242, SAE Automotive Engineering Congress, Feb. 25-March 1, 1974.

33. Torti, M.L., Alliegro, R.A., Richerson, D.W., Washburn, M.E. and Weaver, G.Q., "High-Temperature Properties of Silicon Carbide and Silicon Nitride," High-Temperature Materials in Gas Turbines, Proceedings of a Symposium held at Brown Boveri Central Research Laboratories, Baden, Switzerland, 12-13 March, 1973, published by Elsevier Scientific Publishing Company, Amsterdam, 1974.

34. Torti, M.L., "Silicon Nitride and Silicon Carbide--Properties and Shape Capability," Powder Metallurgy Int'l 6 (4) pp. 186-9, (1974).

35. Rice, R.W., "Comment on 'Additional Observations on the Strength/Nitrided Density Relationship for a Reaction Sintered Silicon Nitride'," Journal of Materials Science 12, pp. 627-30 (1977)-Letters.

36. Rice, R.W., "The Microstructural Dependence of Mechanical Behavior of Ceramics," in "Properties and Microstructure," edited by R.K. MacCrone, (Academic Press) in press.

37. M.G. Mendiratta, P.L. Land, R. Ruh, R.W. Rice, and D.C. Larsen, "Fractography of Reaction Sintered Si_3N_4," paper 66-BN-77F, presented at American Ceramic Society Basic Science Division Fall Meeting, Hyannis, Mass. (Sept. 25-28, 1977).

38. Davidge, R.W., Evans, A.G., Gilling, D., and Wilyman, P.R., "Oxidation of Reaction-Sintered Silicon Nitride and Effects on Strength," Special Ceramics 5, P. Popper, ed., British Ceramic Research Association, pp. 329-43 (1972)

39. Wiederhorn, S.M. and Tighe, N.J., "Application of Proof Testing to Silicon Nitride," ERDA/Proceedings of Workshop on Ceramics for Advanced Heat Engines, Orlando, Florida; January 24-26 (1977).

40. Evans, A.G., and Davidge, R.W., "The Strength and Oxidation of Reaction-Sintered Silicon Nitride," Journal of Materials Science 5 pp. 314-25 (1970.

41. Graham, H.C., AFML, private communication.

REFERENCES (Cont'd)

42. Noakes, P.B. and Pratt, P.L., "High-Temperature Mechanical Properties of Reaction-Sintered Silicon Nitride," Special Ceramics 5, P. Popper, Ed., British Ceramic Research Association, Stoke-on-Trent (1972) pp. 299-310.

43. Mackenzie , J.K., Proc. Phys. Soc. (London) 63B, 2, 1949.

44. Johnson, C.A. and Prochazka, S., "Investigation of Ceramics for High Temperature Turbine Components," General Electric Report SRD-76-143, (Quarterly Progress Report #2) on Naval Air Development Center Contract No. N62269-76-C-0245 (September, 1976).

45. William Everitt, Kyocera International, San Diego, CA, private communciation.

46. S. Prochazka, General Electric Report No. 74-CRD-186 (August 1974).

47. Coblenz, W.S., "Elastic Moduli of Boron-Doped Silicon Carbide," J. Amer. Ceram. Soc. 58 (11-12) pp. 530-531, (1975).

48. Kraft, E.H., Carborundum Company, private communications (1977).

49. Spinner, S. and Tefft, W.E., "A Method for Determining Mechanical Resonance Frequencies and for Calculating Elastic Moduli from these Frequencies," ASTM Proc., Vol. 61 pp. 1221-38 (1961).

50. Schreiber, E., Anderson, O.L. and Soga, N., Elastic Constants and Their Measurement, Chapter 5: "Resonant-Sphere Methods for Measuring the Velocity of Sound," McGraw-Hill (1973).

51. R. Ruh, K.S. Mazdiyasni, and Tai-Il Mah, "Elastic Moduli of Si_3N_4 and SiC," Paper (43-BN-77F), American Ceramic Society Basic Science Division Fall Meeting, Hyannis, Ma., (Sept., 25-28, 1977).

52. Rice, R.W. and McDonough, W.J., "Hot-Pressed Si_3N_4 with Zr-Based Additions," Jour. Amer. Ceram. Soc. 58 (5-6), p. 264 (1975).

REFERENCES (Cont'd)

53. McDonough, W.J., Freiman, S.W., Becher, P.F., and Rice, R.W., "Fabrication and Evaluation of Si_3N_4 Hot-Pressed with ZrO_2," ARPA/NAVSEA-Garrett/Airesearch Ceramic Gas Turbine Engine Program Review, Maine Maritime Academy, Castine, Maine, August 1-4, 1977.

54. Freiman, S.W., "Effect of Environment on Fracture of Ceramics," Ceramurgia International, 2 (3) pp. 111-118 (1976).

55. Evans, A.G., "Fracture Mechanics Determination," Fracture Mechanics of Ceramics, Vol. 1, Ed, R.C. Bradt, D.P.H. Hasselman and F.F. Lange, Plenum Press, New York 1974.

56. Wills, R.R., Stewart, R.W. Wimmer, J.M., "Instrinsic Thermal and Mechanical Properties of Reaction-Sintered $Si_4Al_2N_6O_2$ Sialon," Bull. Amer. Ceram. Soc. 55 (11) 1976.

57. Freiman, S.W., Naval Research Laboratory, private communication.

58. Petrovic, J.J. and Jacobson, L.A., "Controlled Surface Flaws in Hot-Pressed SiC," J. Amer. Ceram. Soc. 59 (1-2) pp. 34-37, (1976).

59. Wills, R.R., Mendiratta, M.G. and Petrovic, J.J., "Controlled Surface-Flaw-Initiated Fracture in Reaction Bonded Si_3N_4," J. Mater. Sci. 11, pp. 1330-4 (1976).

60. Petrovic, J.J. and Jacobson, L.A., "The Strength of Silicon Nitride After Exposure to Different Environments," Ceramics for High-Performance Applications, Proceedings of Second Army Materials Technology Conference, J.J. Burke, et al, Eds, Brook Hill Publishing Co. (1974).

61. Petrovic, J.J. and Jacobson, L.A., Talty, P.K., and Vasudevan, A.K., "Controlled Surface Flaws in Hot-Pressed Si_3N_4," J. Amer. Ceram. Soc., 58, pp. 113-16 (1975).

62. A.E. Evans and S.M. Weiderhorn, "Crack Propagation and Failure Prediction in Silicon Nitride at Elevated Temperatures," J. Mater. Sci., 9, pp. 270-78, (1974).

REFERENCES (Cont'd)

63. F.F. Lange, "Relation Between Strength, Fracture Energy and Microstructure of Hot-Pressed Si_3N_4," J. Amer. Ceram. Soc., 56, pp. 518-22 (1973).

64. N. Claussen and C.P. Lahmann, "Fracture Behavior of Some Hot-Pressed Si_3N_4 Ceramics at High Temperatures," Powder Met. Intl., 7 (3) (1975).

65. Lange, F.F., "High Temperature Strength Behavior of Hot-Pressed Si_3N_4: Evidence for Subcritical Crack Growth," J. Amer. Ceram. Soc., 57, pp. 84-87 (1974).

66. J.A. Coppola and R.C. Bradt, "Measurement of Fracture Surface Energy of SiC," J. Amer. Ceram. Soc., 55, pp. 455-60 (1972).

67. Seltzer, M.S., "High Temperature Creep of Ceramics," AFML-TR12-76-97, June, 1976.

68. Seltzer, M.S., "High Temperature Creep of Silicon-Base Compounds," Bull. Am. Ceram. Soc. 56 (4) pp. 418-423 (1977).

69. Thompson, D.S. and Pratt, P.L., "The Mechanical Properties of Reaction-Sintered Silicon Nitride," Proc. Brit. Ceram. Soc., (6) 37-47 (June 1966).

70. Langdon, T.G. et al. "Creep Mechanisms in Ceramic Materials at Elevated Temperatures," pp. 297-313, Ceramics in Severe Environments, W. Kriegel and H. Palmour III, Eds., Plenum Press (1971).

71. S. Ud Din and P.S. Nicholson, "Creep of Hot-Pressed Silicon Nitride," Jour. Material Science 10, 1375-80, (1975).

72. Kossowsky, Ram, Miller, D.G. and Diaz, E.S., "Tensile and Creep Strengths of Hot-Pressed Si_3N_4," J. Mater. Sci 10 983-97, 1975.

73. Langdon, T.G., "Grain Boundary Deformation Processes," Deformation of Ceramic Materials, pp. 101-126, R.C. Bradt and R.E. Tressler, Eds., Plenum Press.

74. Langdon, T.G., "The Significance of Grain Boundaries in High Temperature Creep," Canadian Metallurgical Quarterly 13 (1) 223-8, (1974).

REFERENCES (Cont'd)

75. Kossowsky, R., "The Microstructure of Hot Pressed Silicon-Nitride," Westinghouse Research Laboratories Scientific Paper 73-9D4-Foram-P2, (February 22, 1973).

76. Mangels, J.A., "Development of a Creep-Resistant Reaction Sintered Si_3N_4," pp. 195-206, Ceramics for High-Performance Applications, J.J. Burke, et al., Brookhill (1974).

77. S. Ud Din, and P.S. Nicholson, "Creep Deformation of Reaction-Sintered Silicon Nitrides," Jour. Amer. Ceram. Soc. 58 (11-12), 500-503 (1975).

78. Singhal. S.C., "Thermal Analysis of the High-Temperature Stability of Silicon Nitride and Silicon Carbide", Ceramurgia Intnl. 2 (3) 123-30 (1976).

79. Evans, A.G. and Davidge, R.W., J. Mater. Sci. 5 314 (1970).

80. McLean, A.F. et. al., "Brittle Materials Design, High Temperature Gas Turbine" AMMRC-CTR-73-9 (March 1973).

81. ASM Metals Handbook, Volume 1, " Properties and Selection of Metals," 8th Edition, Lyman Taylor Editor, pp. 1222.

82. McLean, A.F. et. al., "Brittle Materials Design, High Temperature Gas Turbine", AMMRC-CTR-72-19 (September 1972).

83. McLean, A.F., et. al., "Brittle Materials Design, High Temperature Gas Turbine", AMMRC-CTR-73-32, (September 1973).

84. Touloukian, Y.S., Powell, R.W., Ho, C.Y., and Nicolaou, M.C., Thermophysical Properties of Matter, Vol. 10-Thermal Diffusivity, IFI/Plenum (1973).

85. R.K. Bart, Norton Company, Worcester, Mass., Private Communication.

86. Kingery, W.D., "Thermal Conductivity: XIV, Conductivity of Multicomponent Systems", J. Am. Ceram. Soc. 42 (12) 617-27 (1959).

87. Baxley, A.L. Jr., "Thermal Conductivity of Suspensions", Doctoral Dissertation., Chemical Engineering, University of Arkansas, 1967.

REFERENCES (Cont'd)

88. George, W., "Thermal Property Measurements on Silicon Nitride and Silicon Carbide Ceramics Between 290° and 700°K", Proc. Brit. Ceram. Soc., Ceramics for Turbines and Other High-Temperature Engineering Applications, Proceedings 22, pp. 147-167, June, 1973.

89. Rhee, S.K., "Porosity-Thermal Conductivity Correlations for Ceramic Materials," Mater. Sci and Engr. 20, 89-93 (1975).

90. Godfrey, D.J., and May, E.R.W., "The Resistance of Silicon-Nitride Ceramics to Thermal Shock and Other Hostile Environments", in Ceramics in Severe Environments, Materials Science Research, Volume 5, W.W. Kriegel and H. Palmour III, Editors, Plenum Press (1971), pp. 149-62.

91. D.P.H. Hasselman, "Thermal Stress Resistance Parameters for Brittle Refractory Ceramics: A Compendium," Bull. Amer. Ceramic Soc., 49 1033-37 (1970).

92. C. Zener, Elasticity and Anelasticity of Metals, Univ. of Chicago Press, 1948.

93. J.B. Wachtman and W.E. Teft, "Effect of Suspension Position on Apparent Values of Internal Friction Determined by Forester's Method," Rev. Sci. Inst. 29 517-20 (1958).

94. R.W. Dickson and J.B. Wachtman, Jr., "An Alumina Standard Reference Material for Resonance Frequency and Dynamic Moduli Measurement I. For Use at 25°C," J. Res. Natl. Bur. Stds., 75A (3) 155-62 (1971).

95. D.P.H. Hasselman, "Unified Theory of Thermal Shock Fracture Initiation and Crack Propagation in Brittle Ceramics," J. Am. Cer. Soc., 52 600-4 (1969).

96. G.Q. Weaver, H.R. Baumgartner and M.L. Torti, "Thermal Shock Behavior of Sintered Silicon Carbide and Reaction Bonded Silicon Nitride," Special Ceramics 6, Ed. P. Popper, 1975.

97. G.Q. Weaver and M.L. Torti, "Thermal Shock Resistance of Hot Pressed Si_3N_4, SiC, and Si_3N_4-SiC Composites," Bull. Amer. Ceram. Soc., 53 395 (1974).

98. J.W. Edington, D.J. Rowcliff, and J.L. Henshall, "The Mechanical Properties of Silicon Nitride and Silicon Carbide. Part 1: Materials and Strength," Powder Met. Intl.., 7 (2) 82-96 (1975).

REFERENCES (Cont'd)

99. C. C. Seaton, "Thermal and Acoustic Fatigue of Ceramics and Their Evaluation," Final Report AMMRC MS 74-7, June, 1974.

100. R. W. Rice and S. W. Freiman, Naval Research Laboratory, personal communication.

101. G. Q. Weaver, Norton Co., personal communication.

102. J. A. Coppola and R. C. Bradt, "Thermal Shock Damage in SiC," J. Amer. Ceram. Soc., 56 214-18 (1973).

103. J. R. Johnston and R. L. Ashbrook, "Oxidation and Thermal Fatigue Cracking of Nickel and Cobalt Base Alloys in a High Velocity Gas Stream," NASA TN D-5376, 1969.

104. W. A. Sanders and H. B. Probst, "Evaluation of Oxidation Resistant Non-metallic Materials at 1204°C (2200°F) in a Mach I Burner," NASA TN D-6890, 1972.

105. Sanders, W. A. and Probst, H. B., "High Gas Velocity Burner Tests on Silicon Carbide and Silicon Nitride at 1200°C," NASA TM X-71479, Presented at Army Materials Technology Conference on Ceramics for High-Performance Applications, Hyannis, Massachusetts, November 13-16, 1973.

106. F. Thümmler and G. Grathwohl, "Creep of Ceramic Materials for Gas turbine Application," in "Mechanical Properties of Ceramics for High Temperature Applications," AGARD-R-651, 1976.

107. A. G. Evans, B. R. Tittmann, and L. A. Ahlberg, "Failure Prediction in Ceramics Using Ultrasonic," Rockwell International Science Center Report SC-5064, ITR on Project No. 471(NR-039-129). Submitted to Office of Naval Research on contract No. N00014-76-C-0624 (Nov. 17, 1976).

108. T. Derkacs, I. M. Matay, W. D. Brentnall, "Non-destructive Evaluation of Ceramics," TRW, Inc. Final Report ER-7798-F on Naval Air Systems Command Contract No. N00019-75-C-0238. (July, 1976).

REFERENCES (Cont'd)

109. Tripp, W.C., and Graham, H.C., "Oxidation of Si_3N_4 in the Range 1300° to 1500°C," Jour. Amer. Ceram. Soc. 59 (9-10) pp. 399-403 (1976).

110. Kiehle, A.J., et.al., "Oxidation Behavior of Hot-Pressed Si_3N_4," Jour. Amer. Ceram. Soc. 58 (1-2) p. 17-20 (1975).

111. Longenecker, R.J., Kawecki Berylco Industries, Inc., Reading, Pa., private communication (1977).

APPENDIX A

X-RADIOGRAPHIC INSPECTION

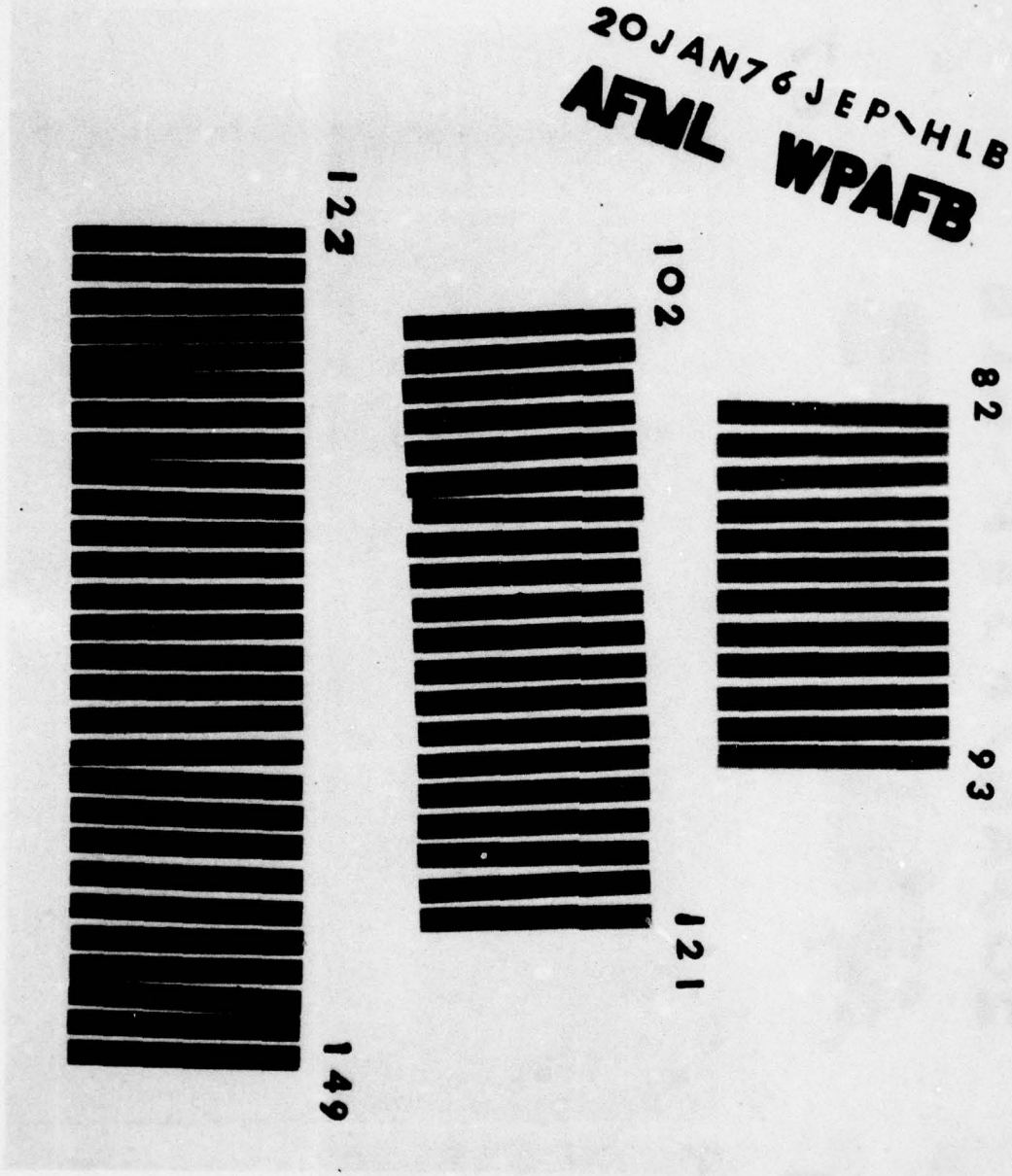

FIGURE A-1 X-RADIOGRAPHIC POSITIVE OF NC-132
HP-Si_3N_4, BATCH 1 FLEXURAL SPECIMENS.

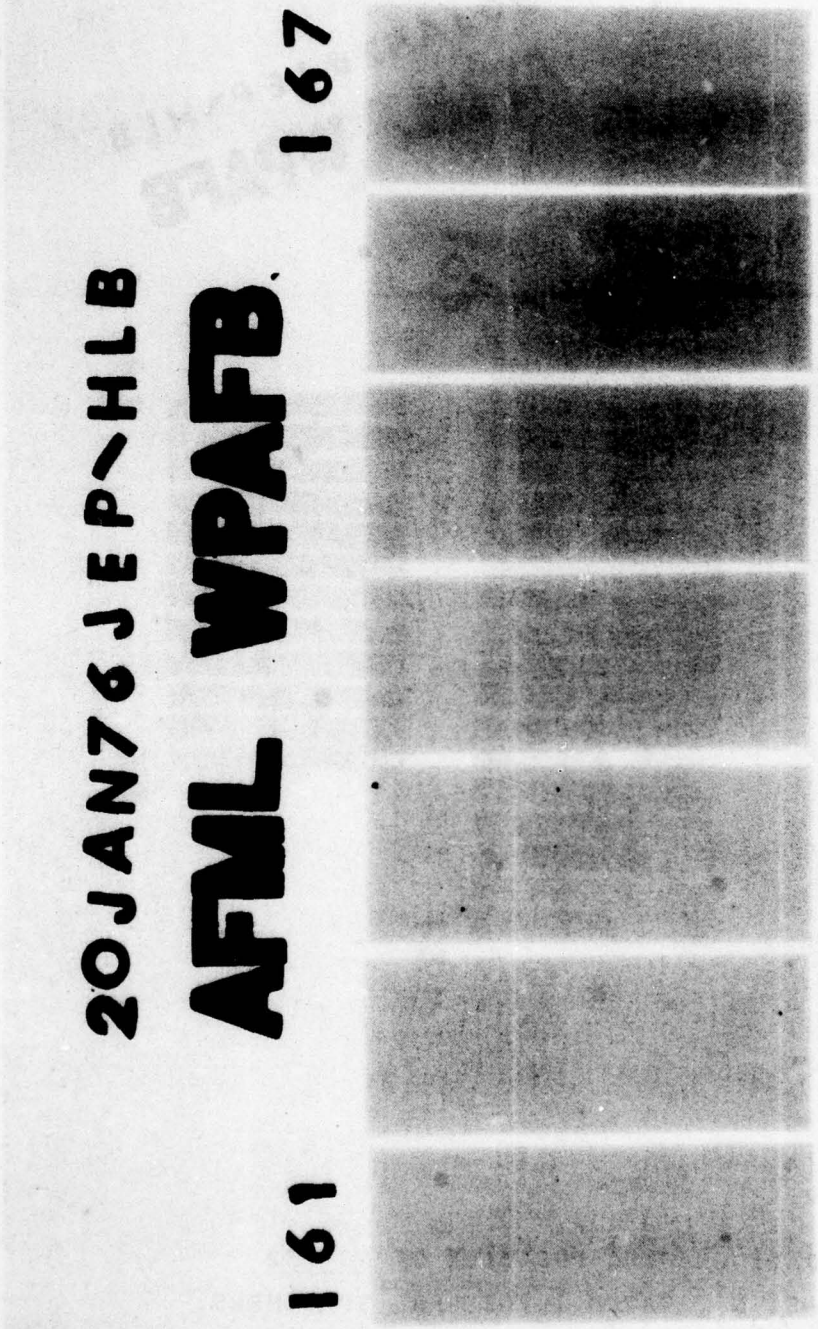

FIGURE A-2 X-RADIOGRAPHIC POSITIVE OF NC-132 HP-Si_3N_4 (BATCH 1) THERMAL SHOCK SPECIMENS.

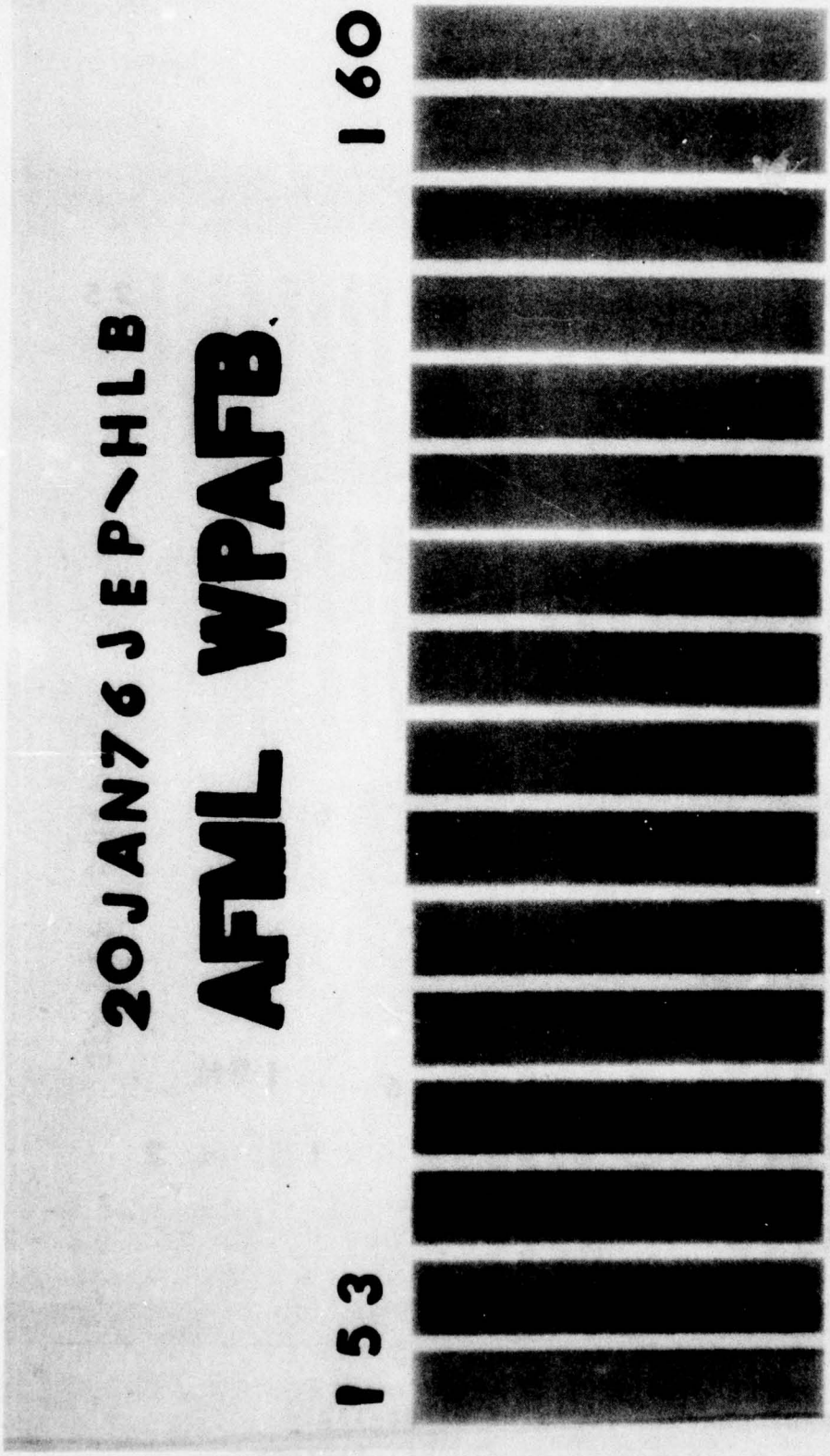

FIGURE A-3 X-RADIOGRAPHIC POSITIVE OF NC-132 HP Si_3N_4 (BATCH 1) FRACTURE TOUGHNESS SPECIMENS.

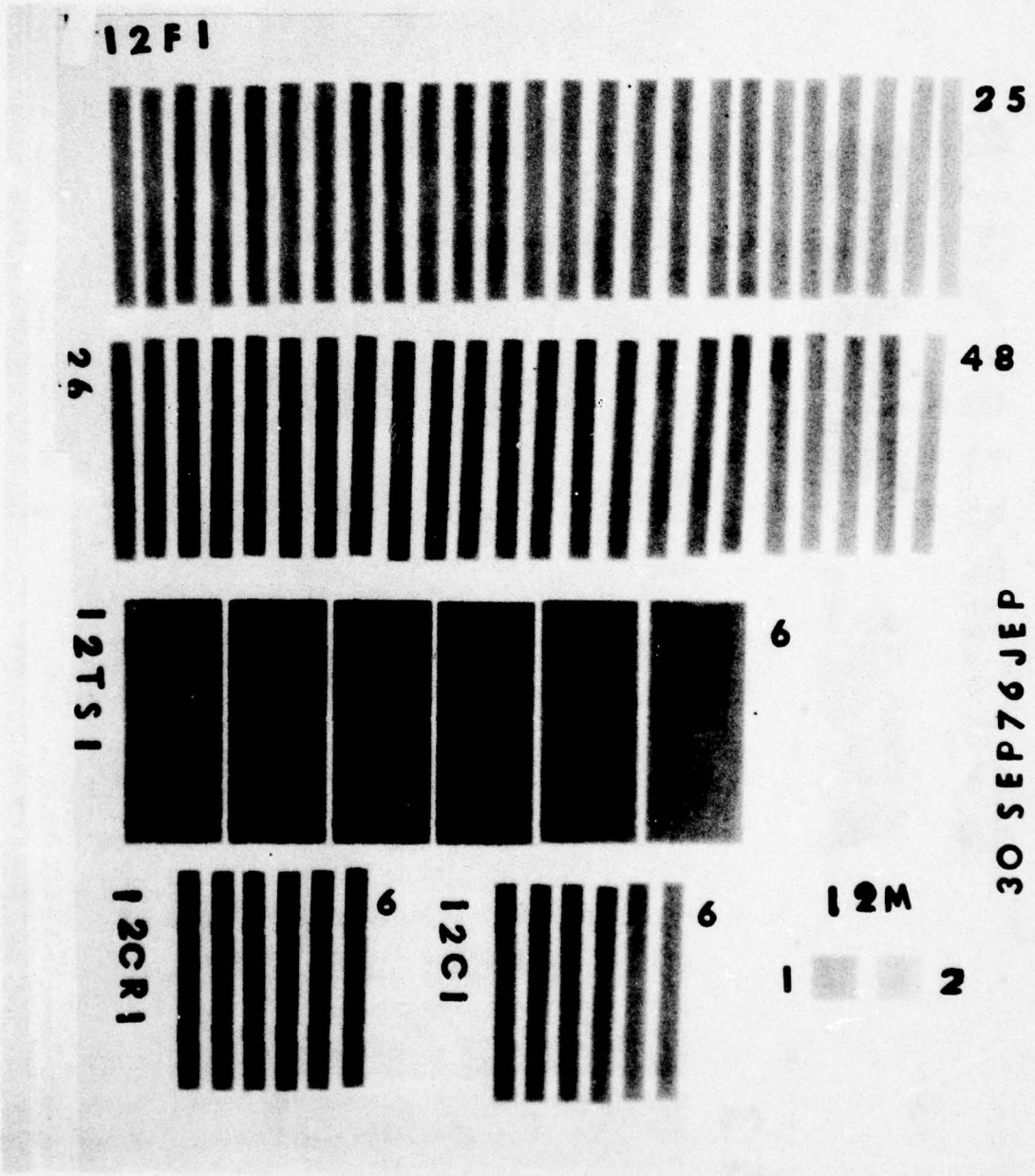

FIGURE A-4 X-RADIOGRAPHIC POSITIVE OF NC-132 HP Si_3N_4 (BATCH 2) SPECIMENS: FLEXURE, CREEP, CREEP RUPTURE, THERMAL SHOCK.

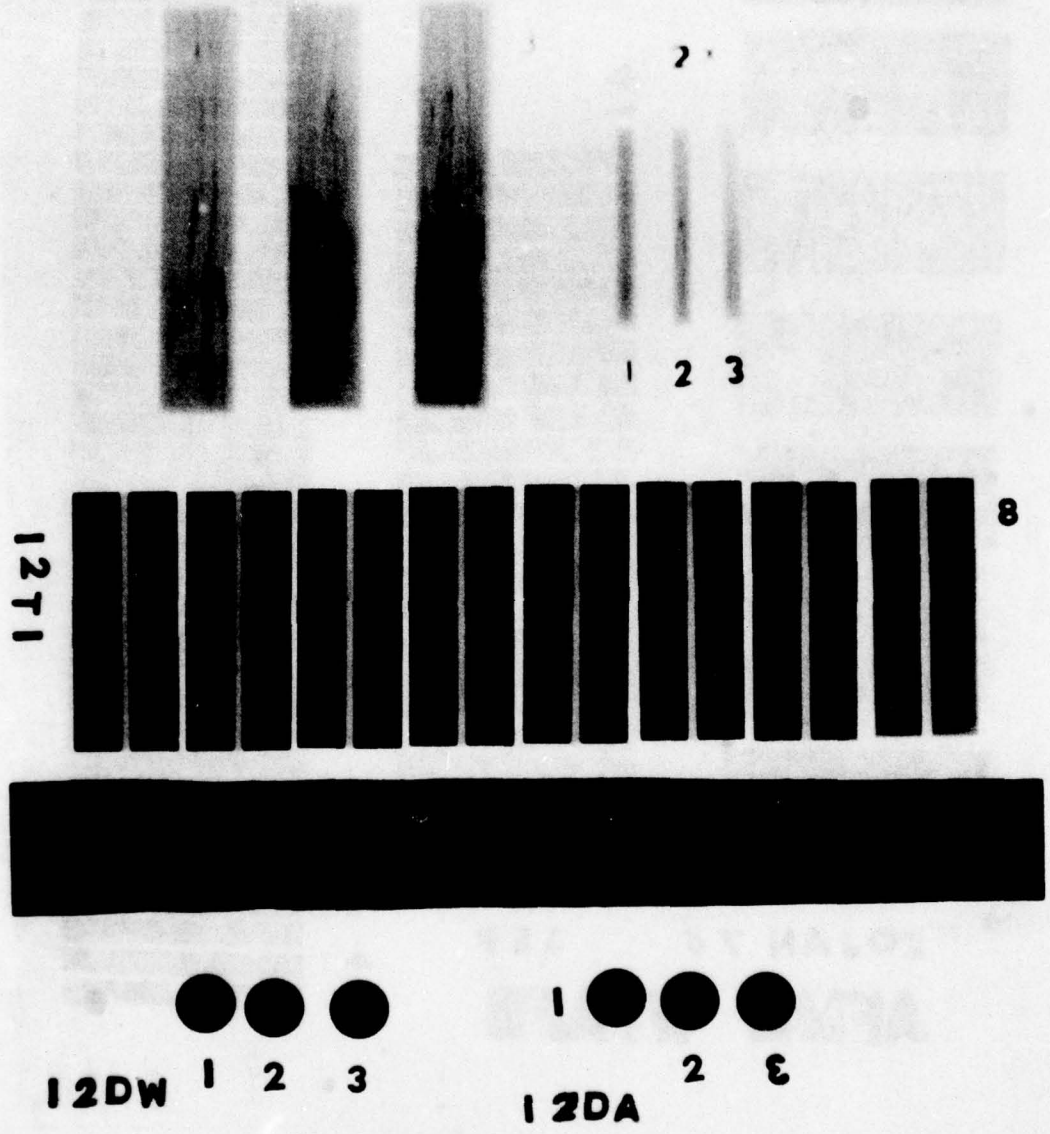

FIGURE A-5 X-RADIOGRAPHIC POSITIVE OF NC-132 HP Si_3N_4 (BATCH 2) SPECIMENS: HOT GAS EXPOSURE, THERMAL EXPANSION, FRACTURE TOUGHNESS, THERMAL DIFFUSIVITY.

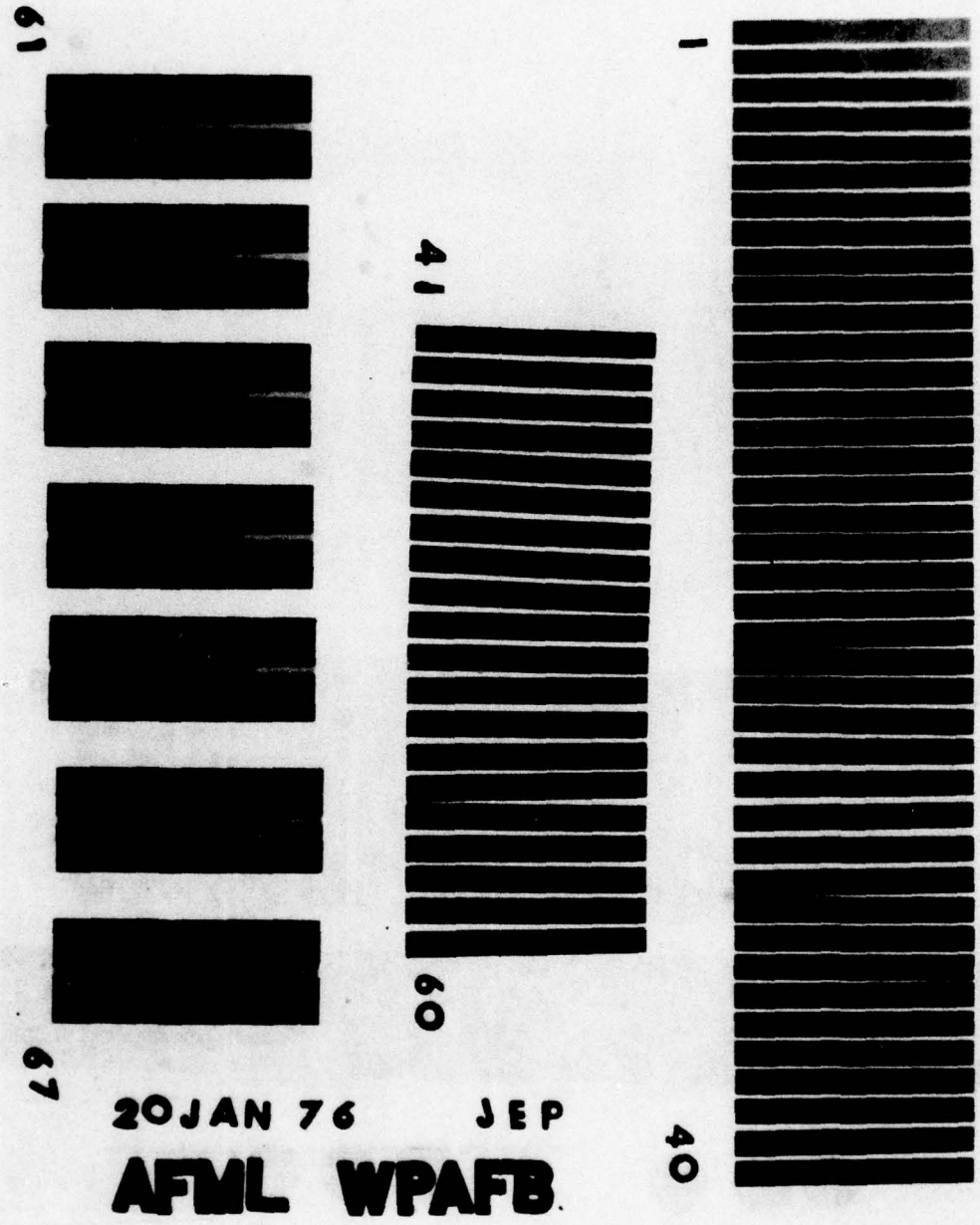

FIGURE A-6 X-RADIOGRAPHIC POSITIVE OF NC-435 Si/SiC (BATCH 1) FLEXURE AND FRACTURE TOUGHNESS SPECIMENS.

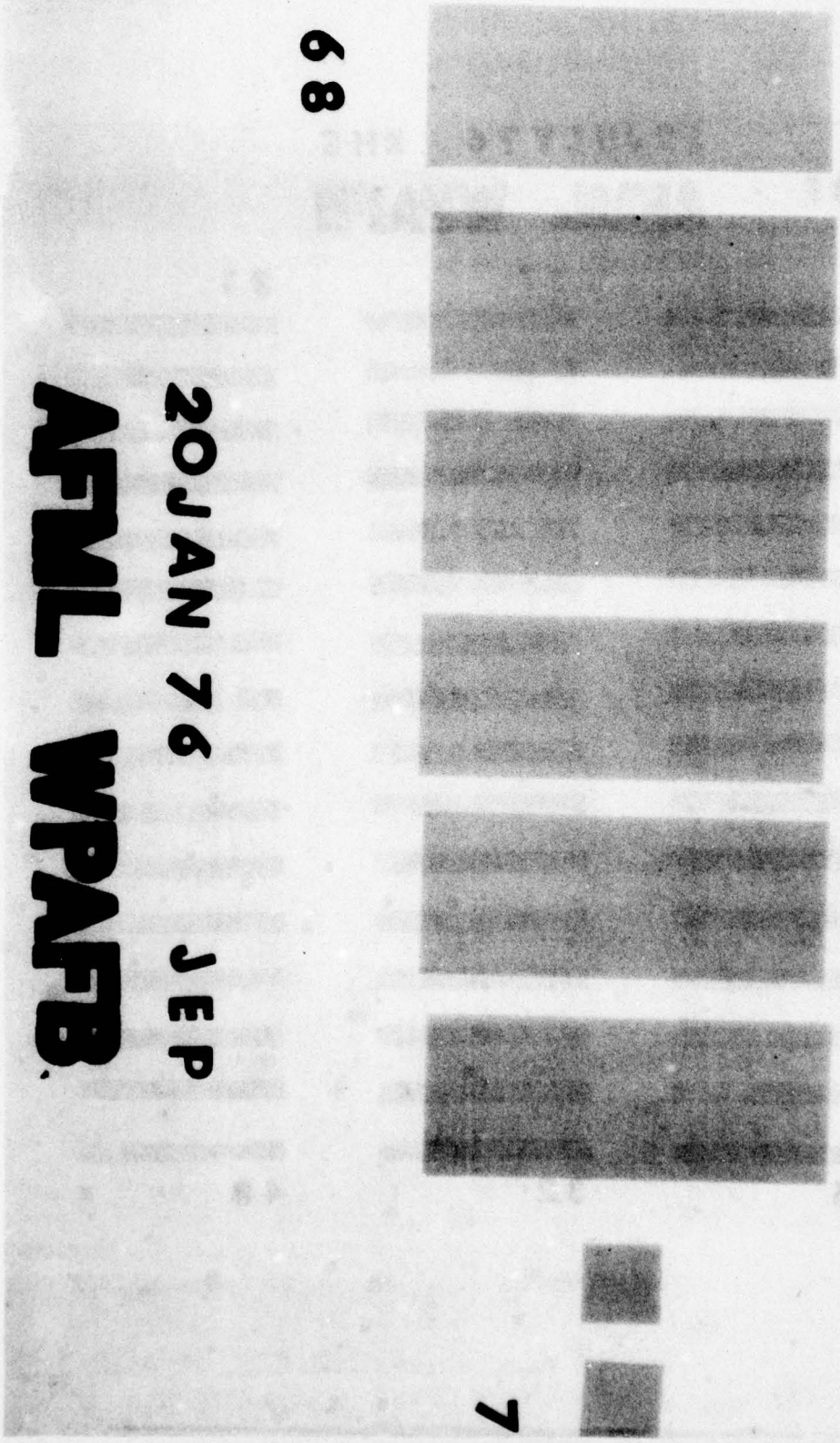

FIGURE A-7 X-RADIOGRAPHIC POSITIVE OF NC-435 Si/SiC (BATCH 1) THERMAL SHOCK SPECIMENS.

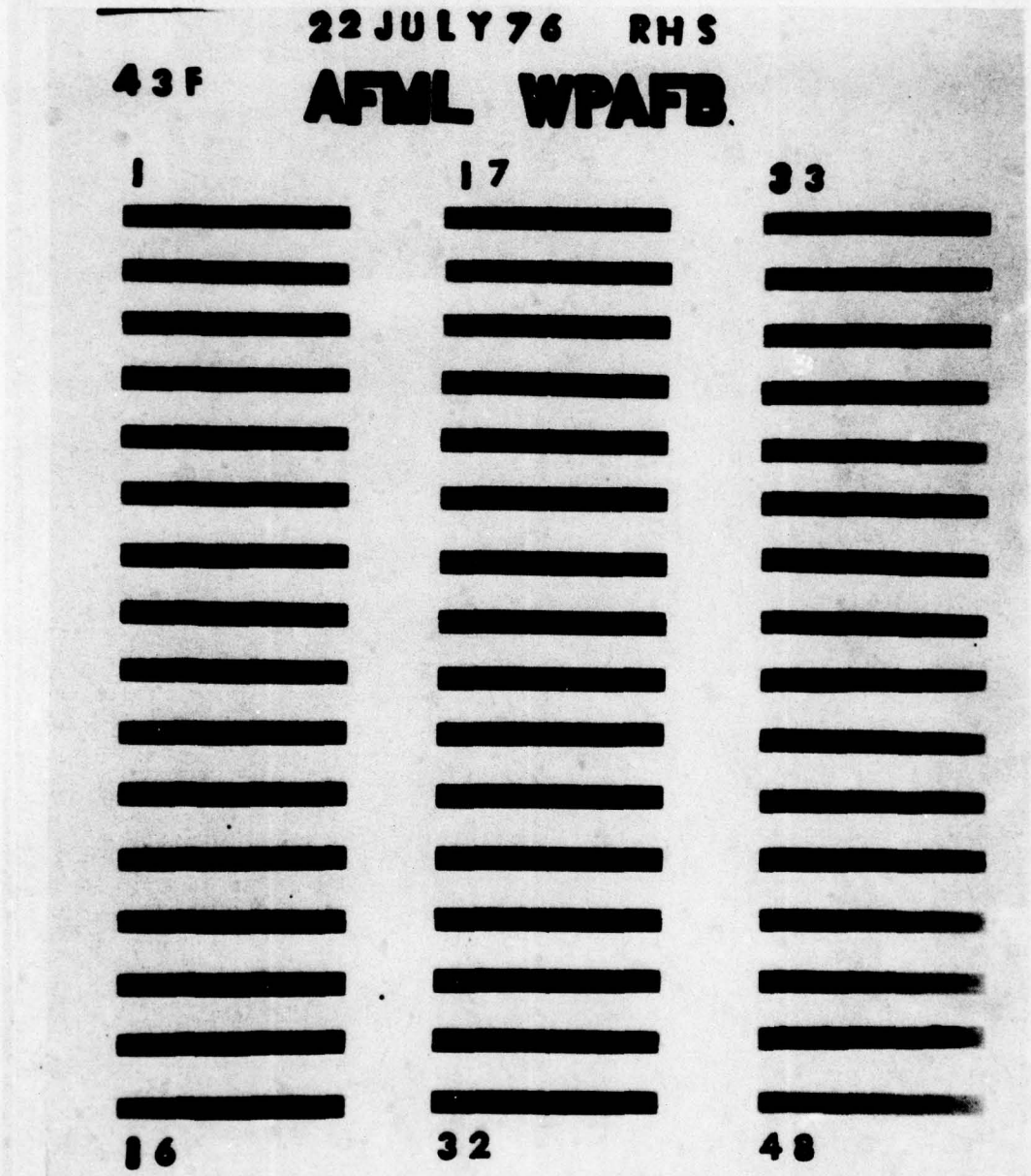

FIGURE A-8 X-RADIOGRAPHIC POSITIVE OF NC-435 Si/SiC (BATCH 3) FLEXURE SPECIMENS.

FIGURE A-9 X-RADIOGRAPHIC POSITIVE OF NC-435 Si/SiC (BATCH 3) FRACTURE TOUGHNESS AND THERMAL DIFFUSIVITY SPECIMENS.

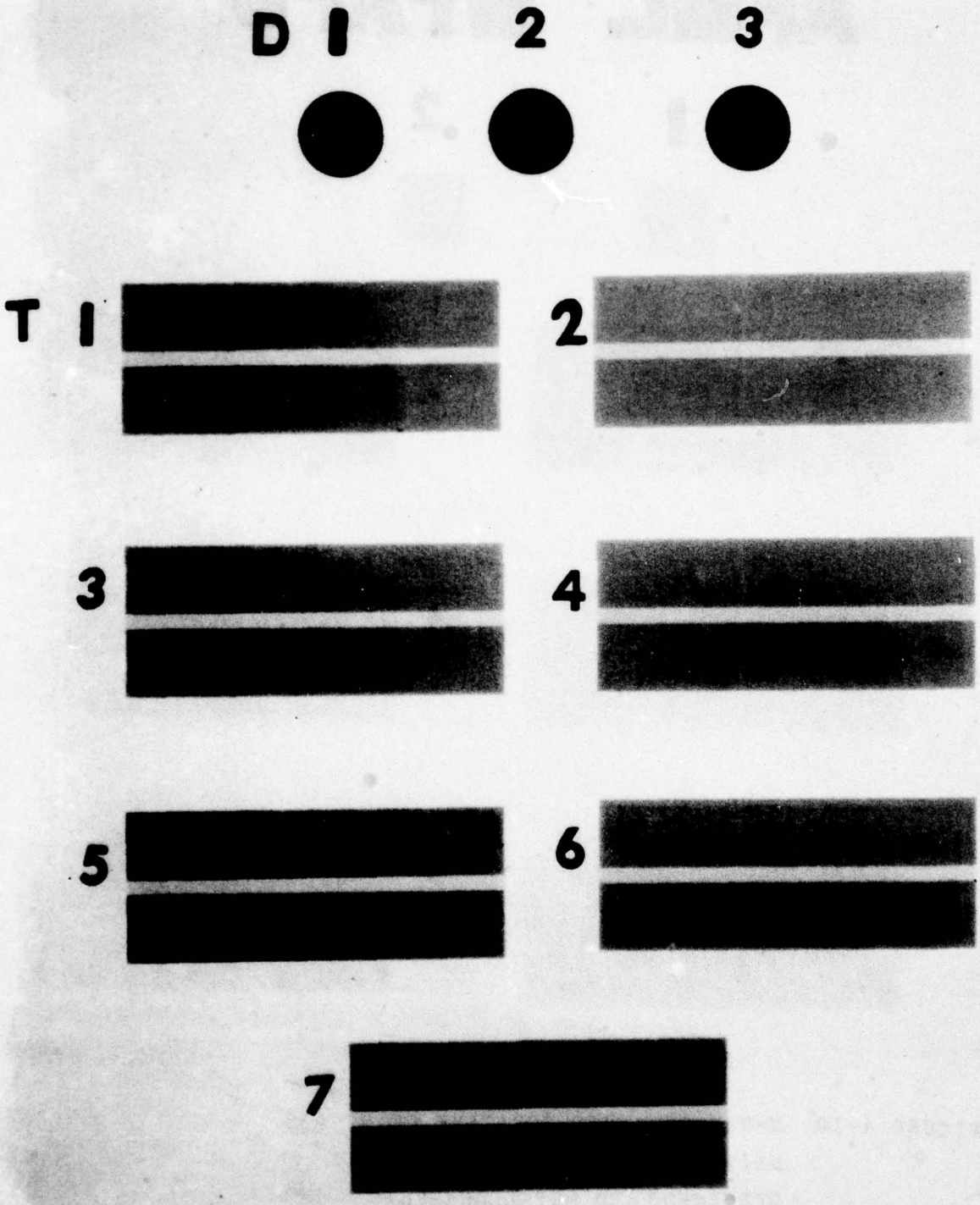

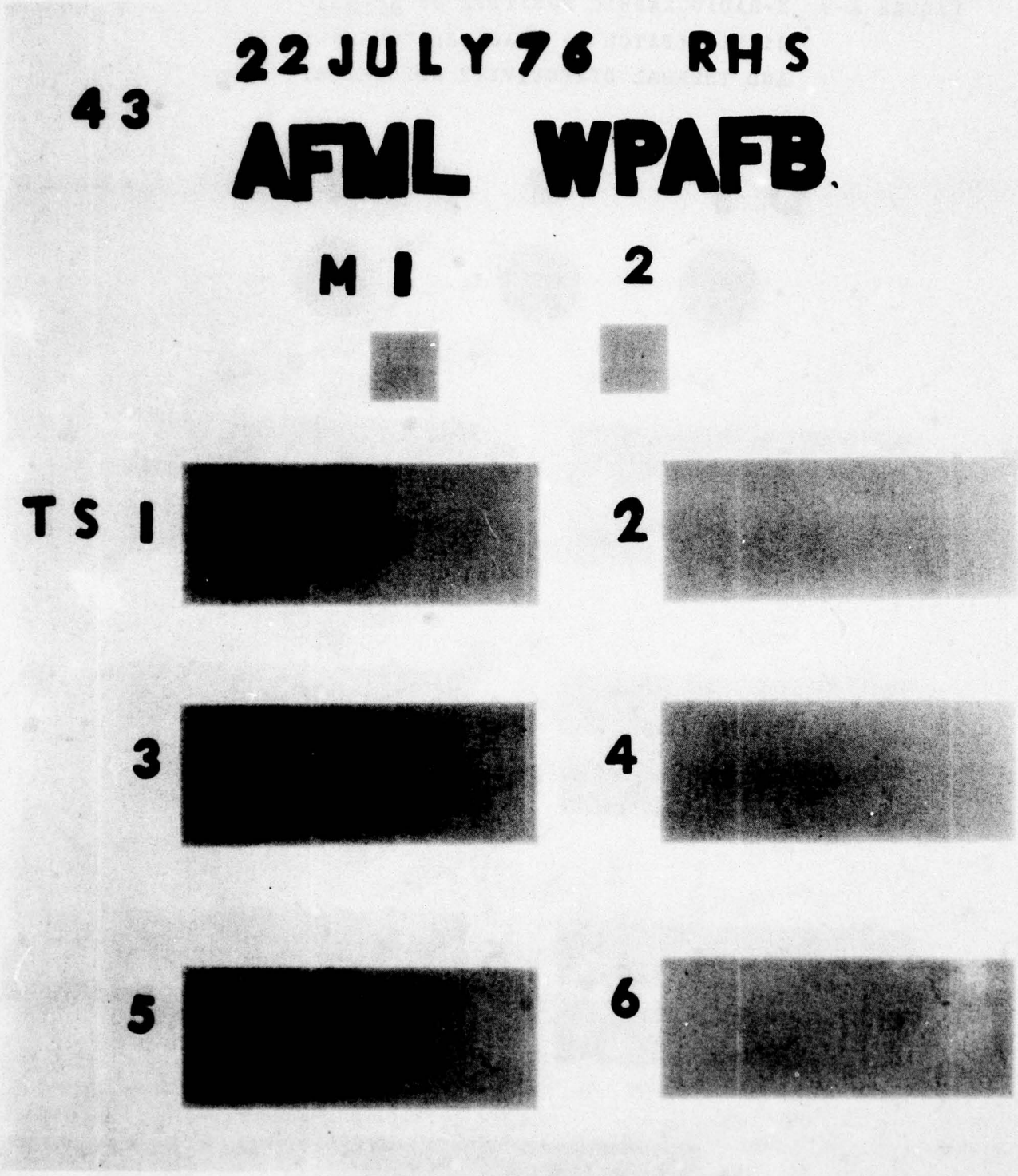

FIGURE A-10 X-RADIOGRAPHIC POSITIVE OF NC-435 Si/SiC (BATCH 3) THERMAL SHOCK SPECIMENS AND METALLOGRAPHIC SAMPLES.

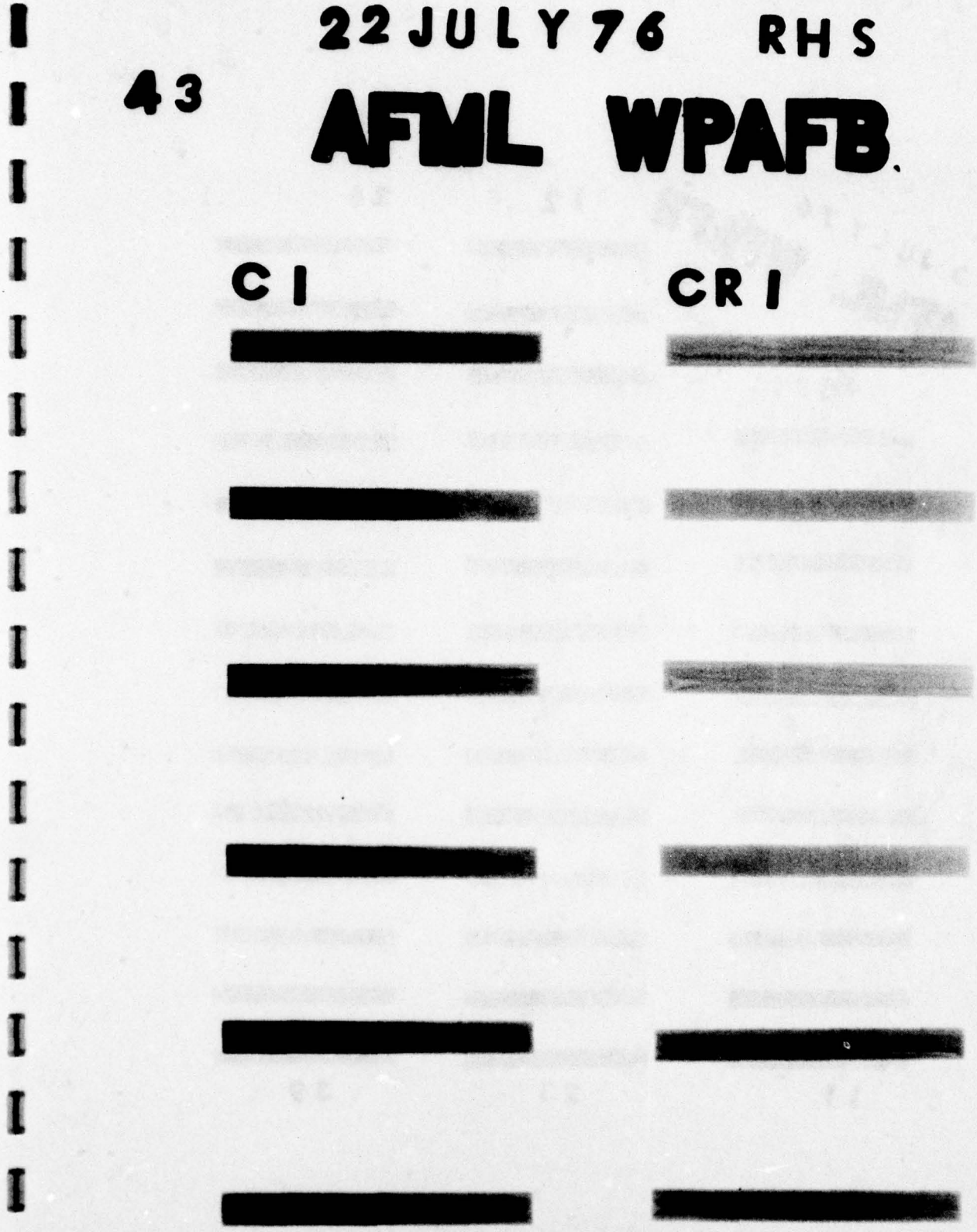

FIGURE A-11 X-RADIOGRAPHIC POSITIVE OF NC-435 S1/S1C (BATCH 3) CREEP AND CREEP RUPTURE SPECIMENS.

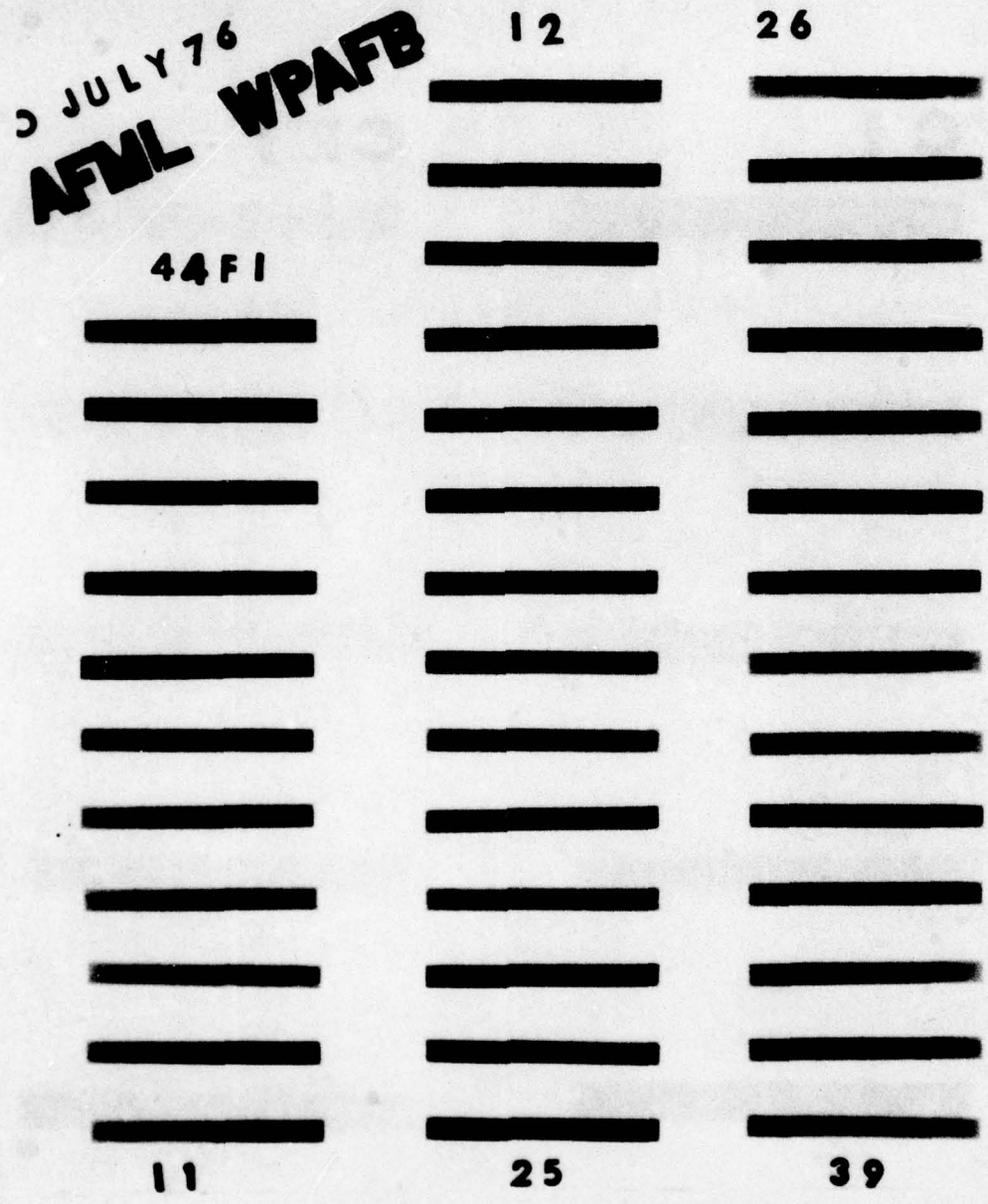

FIGURE A-12 X-RADIOGRAPHIC POSITIVE OF NC-435 Si/SiC (BATCH 4) FLEXURAL SPECIMENS.

FIGURE A-13 X-RADIOGRAPHIC POSITIVE OF NC-435 Si/SiC (BATCH 4) THERMAL DIFFUSIVITY, FRACTURE TOUGHNESS, AND THERMAL SHOCK SPECIMENS.

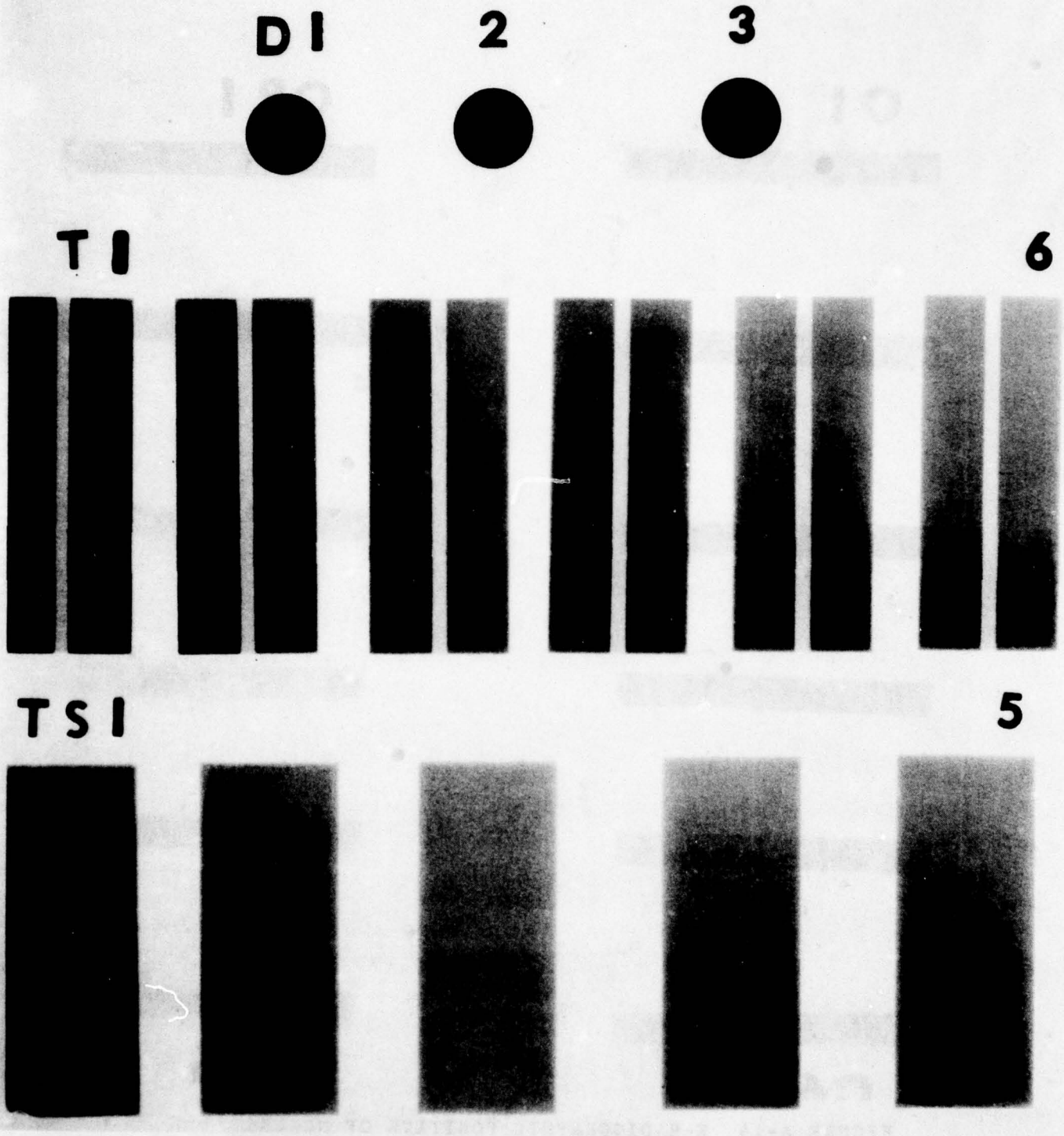

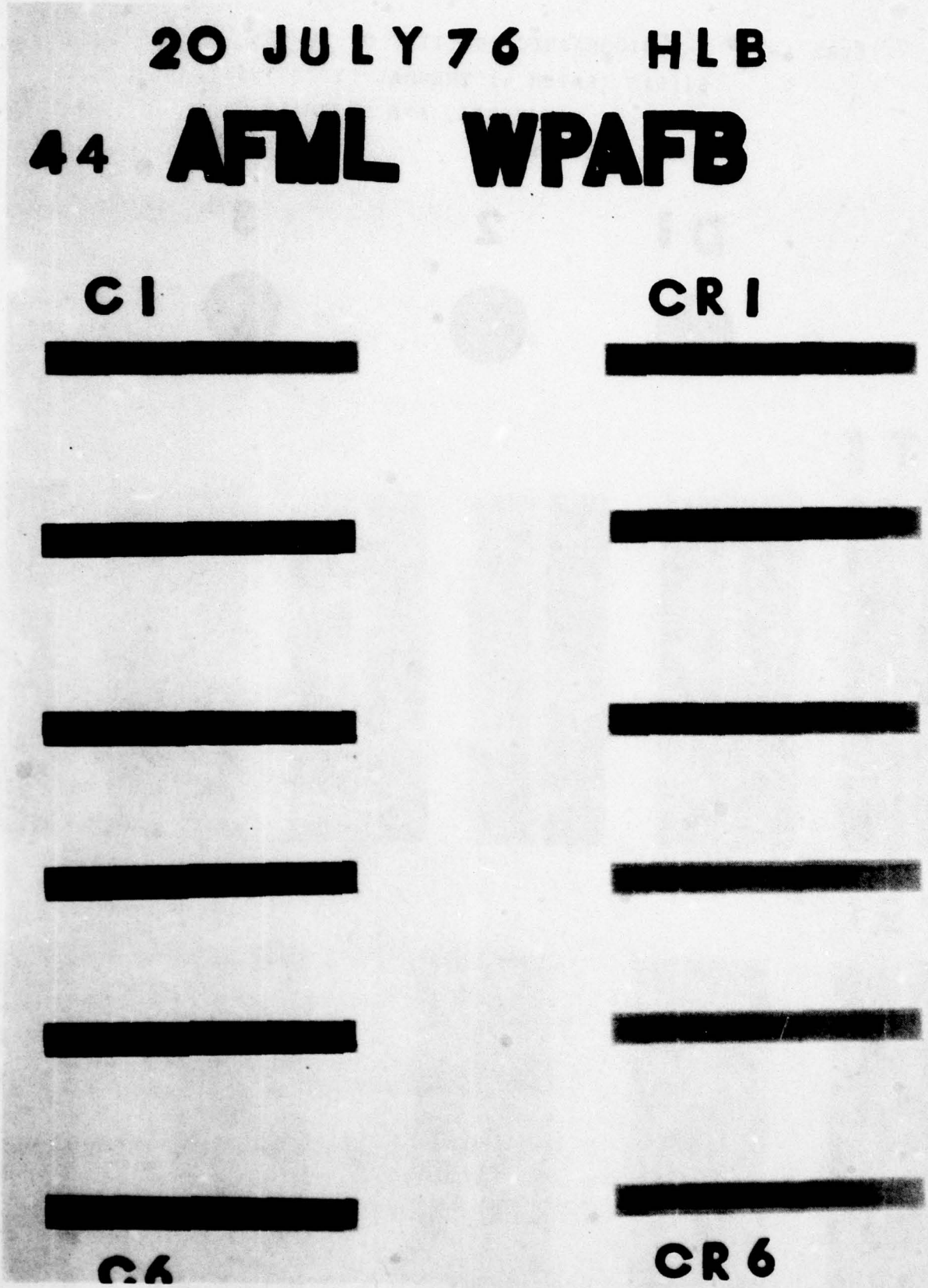

FIGURE A-14 X-RADIOGRAPHIC POSITIVE OF NC-435 Si/SiC (BATCH 4) CREEP AND CREEP RUPTURE SPECIMENS.

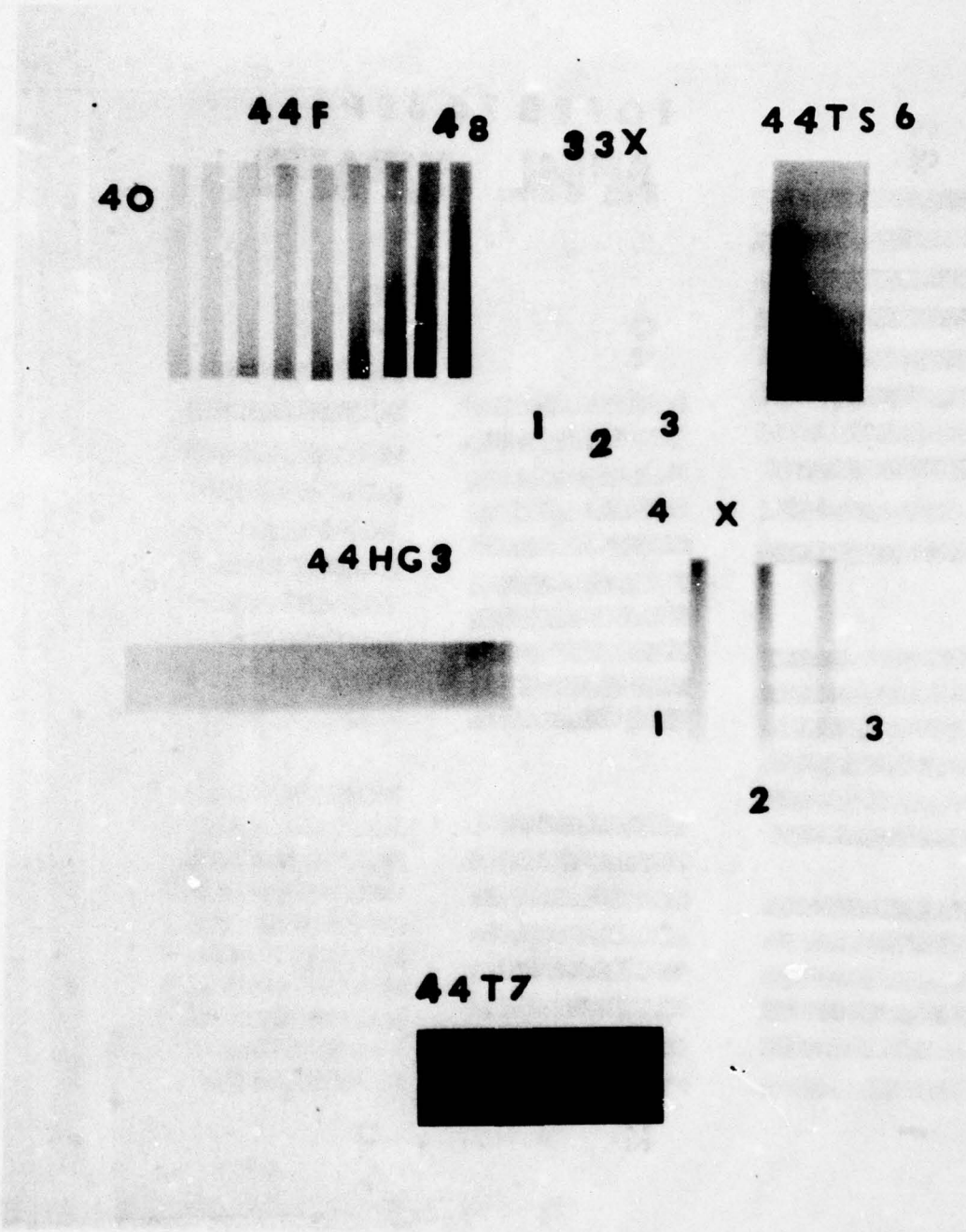

FIGURE A-15 X-RADIOGRAPHIC POSITIVE OF NC-435 Si/SiC BATCH 4, VARIOUS SPECIMENS.

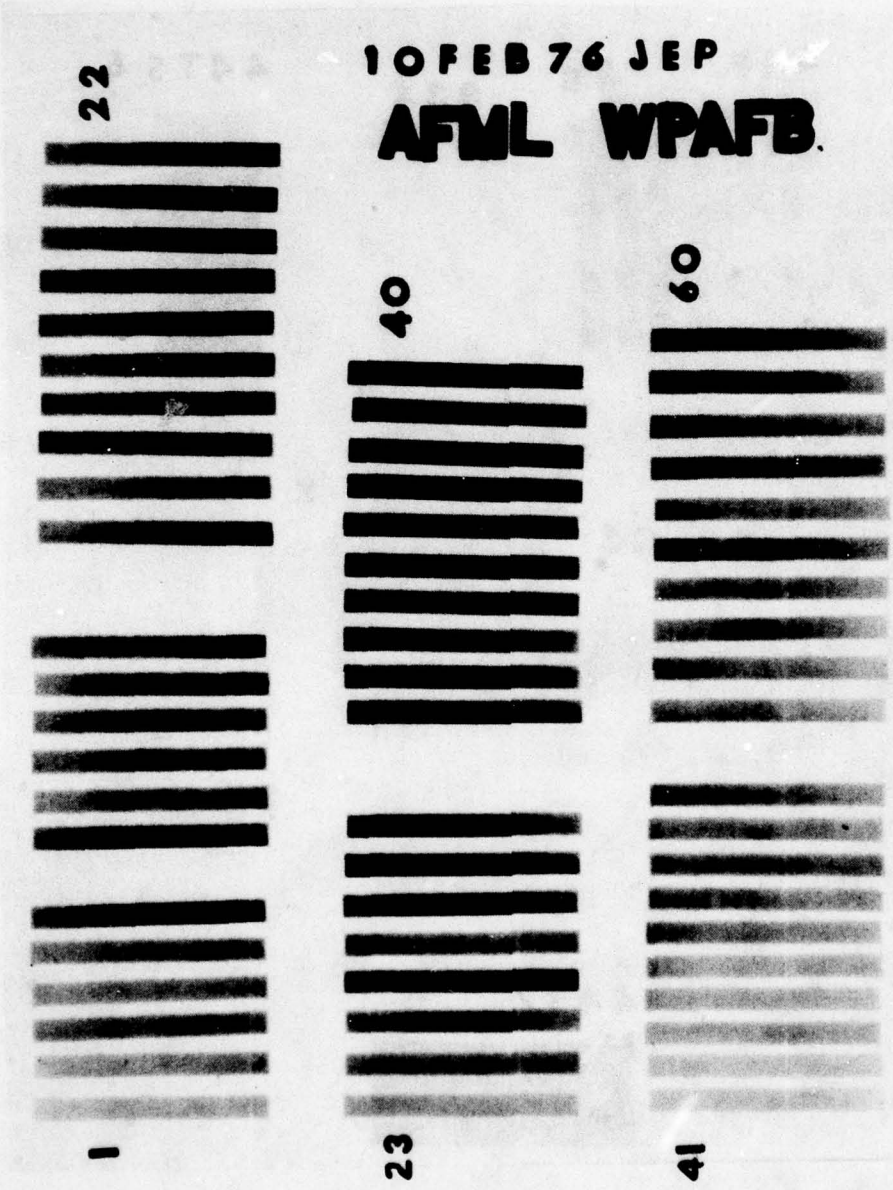

FIGURE A-16 X-RADIOGRAPHIC POSITIVE OF NC-350 RS Si_3N_4 (BATCH 1) FLEXURAL SPECIMENS.

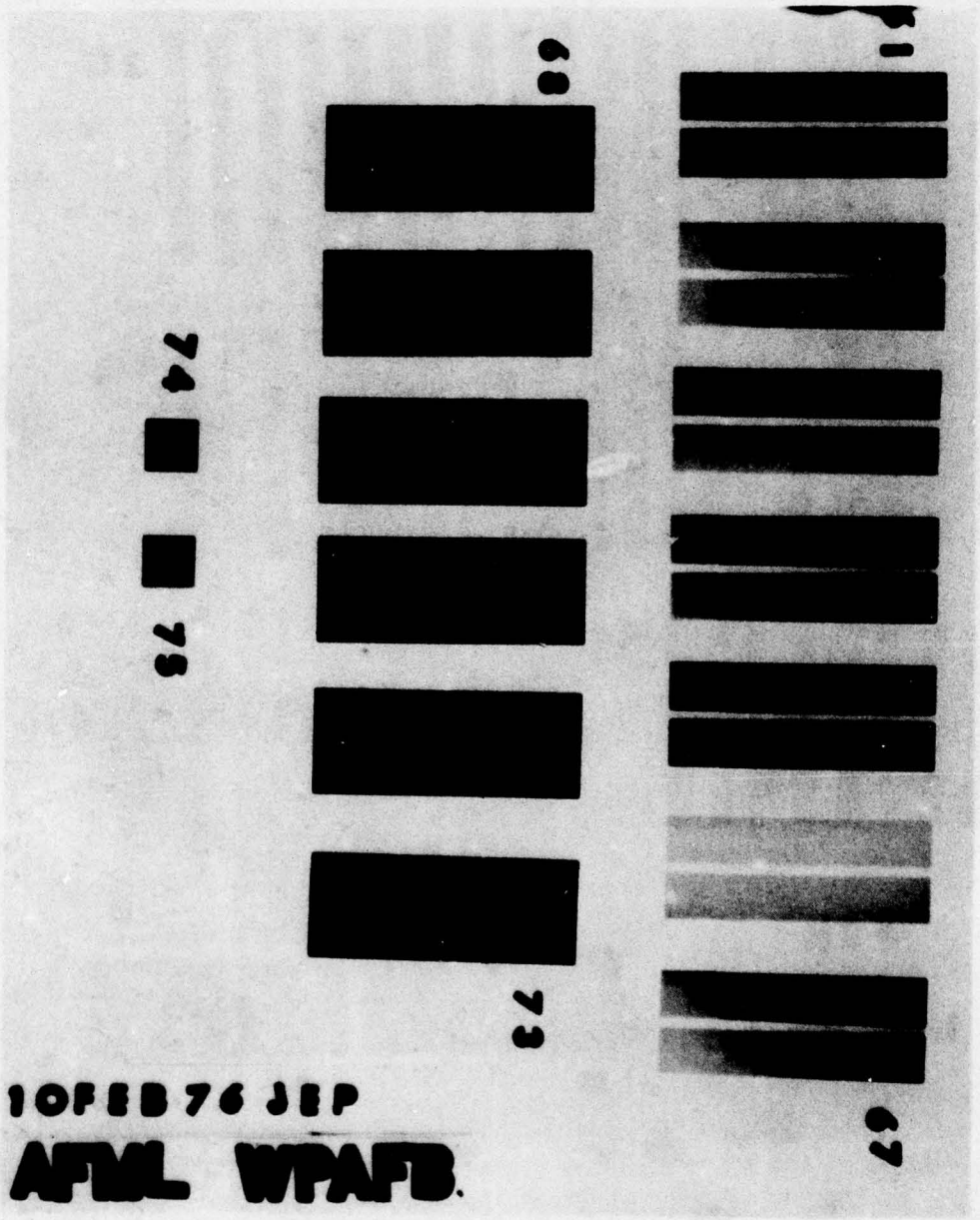

FIGURE A-17 X-RADIOGRAPHIC POSITIVE OF NC-350 RS Si_3N_4 (BATCH 1) THERMAL SHOCK AND FRACTURE TOUGHNESS SPECIMENS.

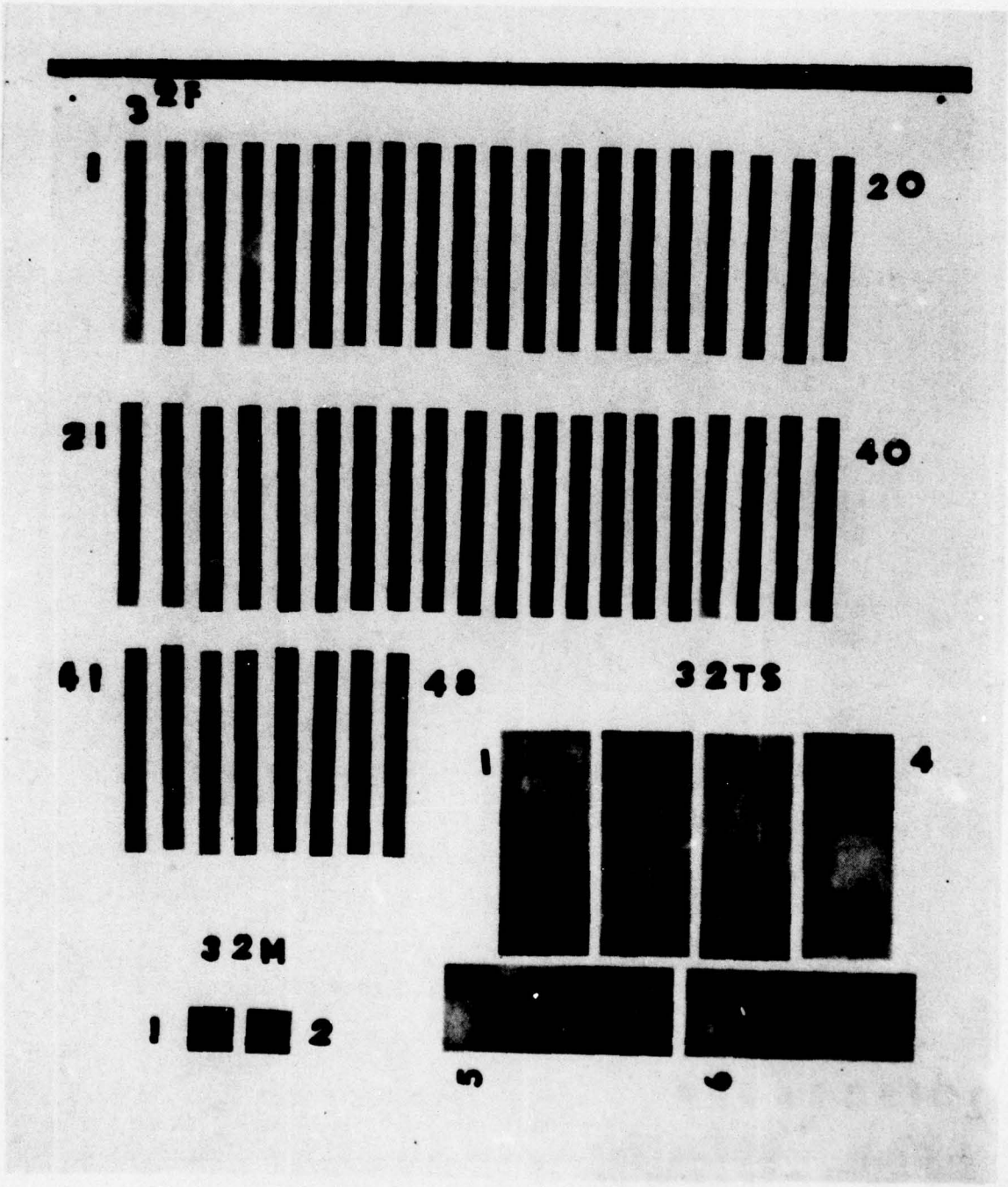

FIGURE A-18 X-RADIOGRAPHIC POSITIVE OF NC-350 RS Si_3N_4 (BATCH 2) FLEXURAL THERMAL SHOCK SPECIMENS, AND METALLOGRAPHIC SAMPLES.

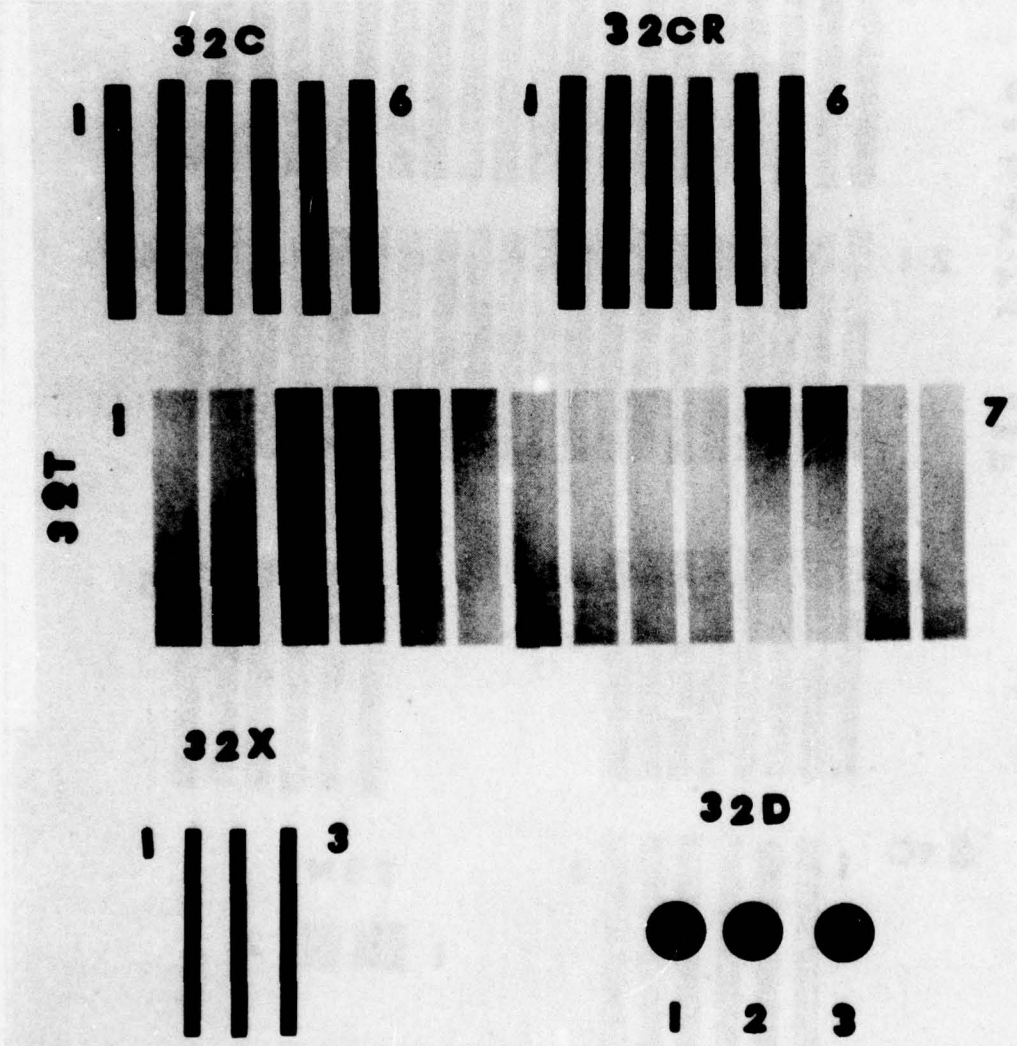

FIGURE A-19 X-RADIOGRAPHIC POSITIVE OF NC-350 RS Si_3N_4 (BATCH 2) VARIOUS SPECIMENS.

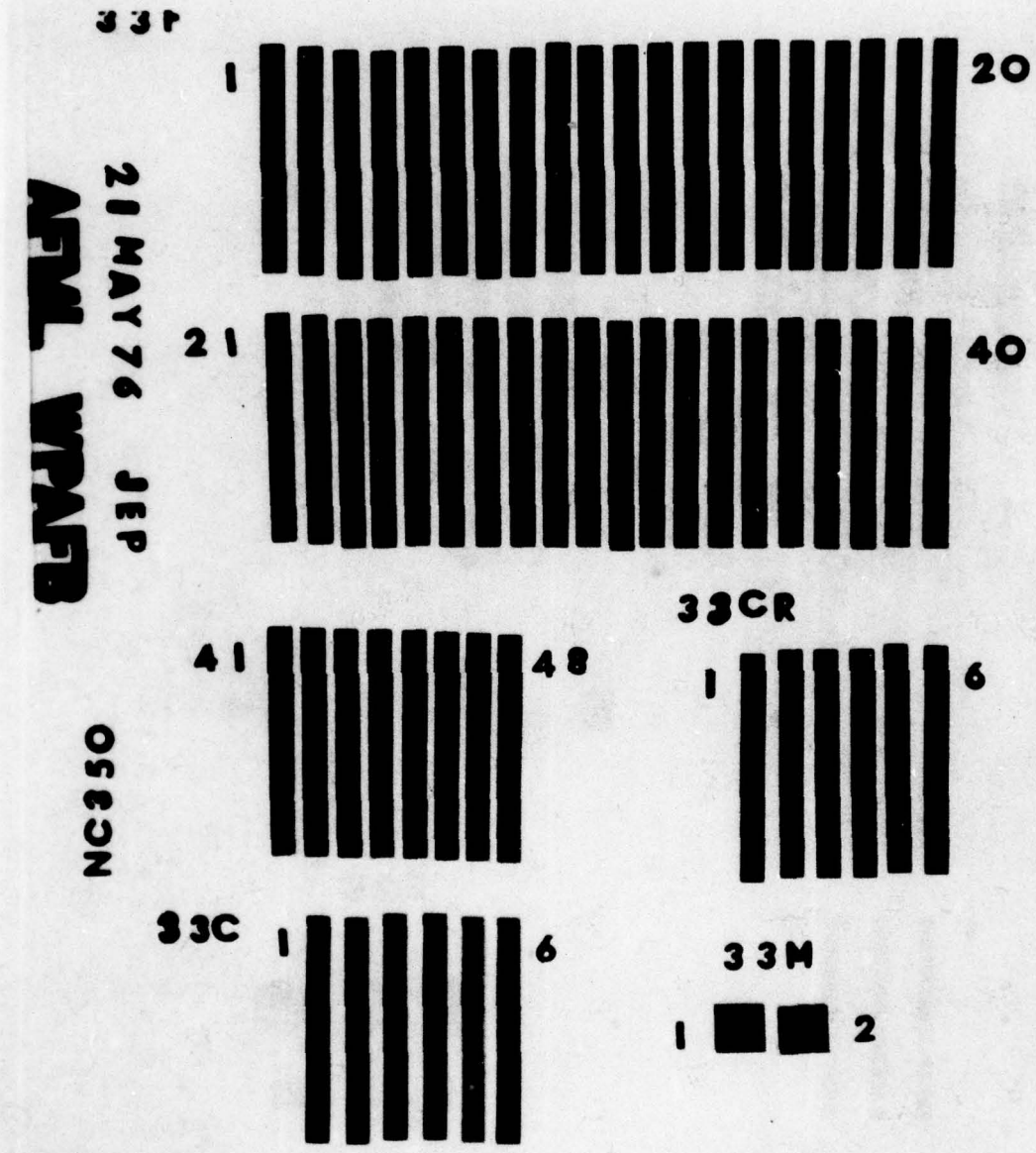

FIGURE A-20 X-RADIOGRAPHIC POSITIVE OF NC-350 RS Si_3N_4 (BATCH 3) FLEXURAL, CREEP, CREEP RUPTURE SPECIMENS AND METALLOGRAPHIC SAMPLES.

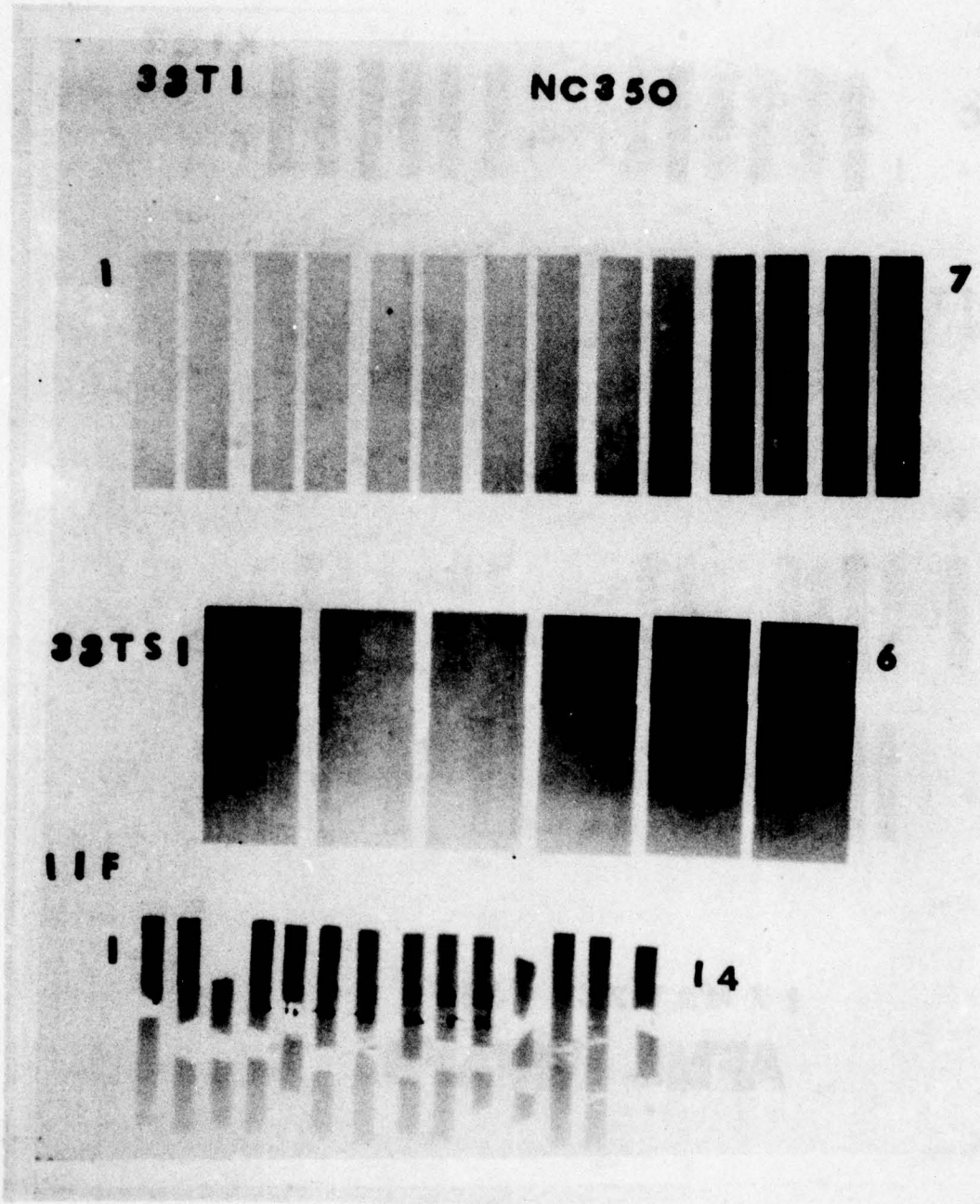

FIGURE A-21 X-RADIOGRAPHIC POSITIVE OF NC-350 RS Si_3N_4 (BATCH 3) FRACTURE TOUGHNESS, THERMAL SHOCK AND FLEXURAL SPECIMENS.

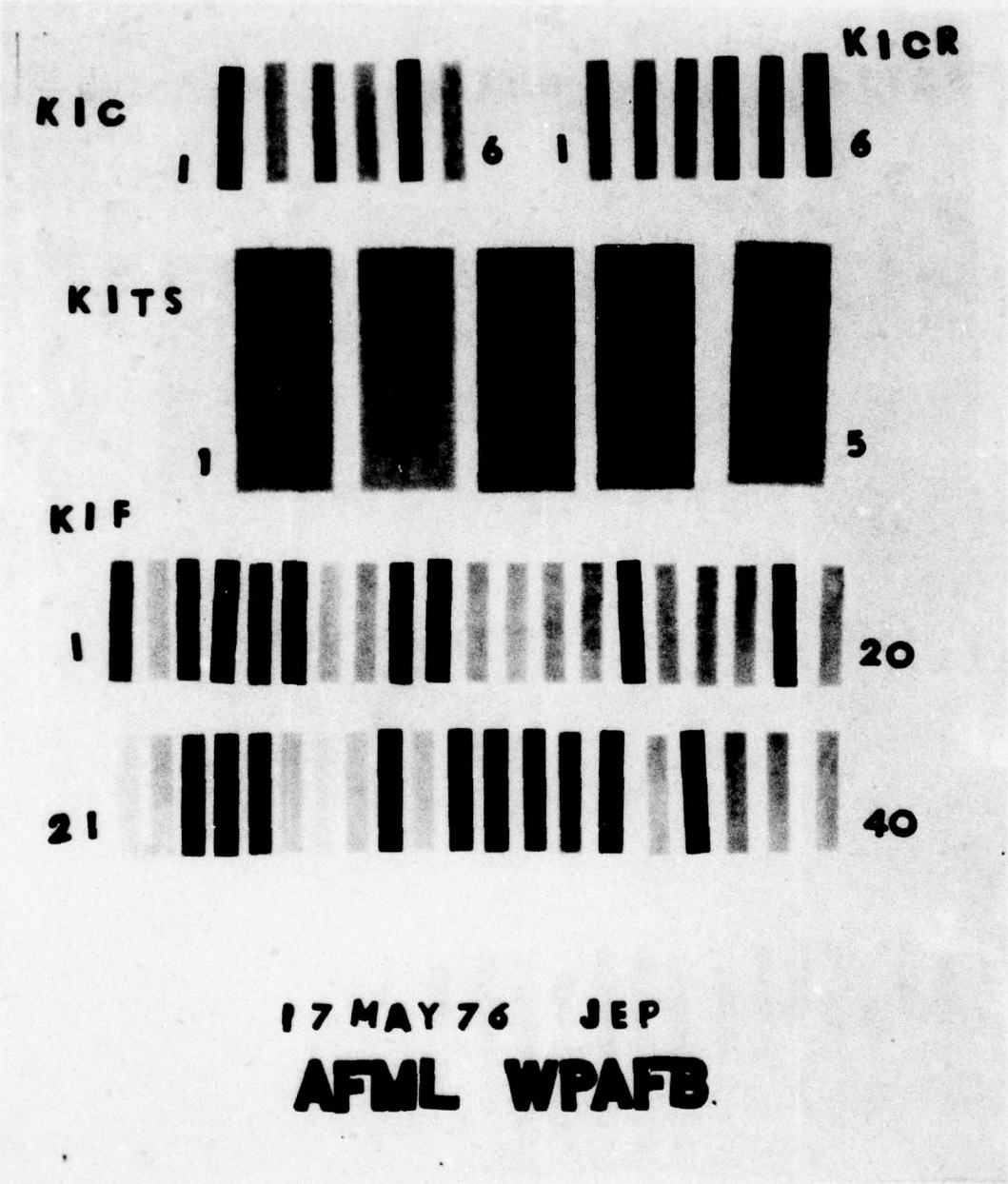

FIGURE A-22 X-RADIOGRAPHIC POSITIVE OF KBI RS Si_3N_4 (BATCH 1) CREEP, CREEP RUPTURE, THERMAL SHOCK, AND FLEXURAL SPECIMENS.

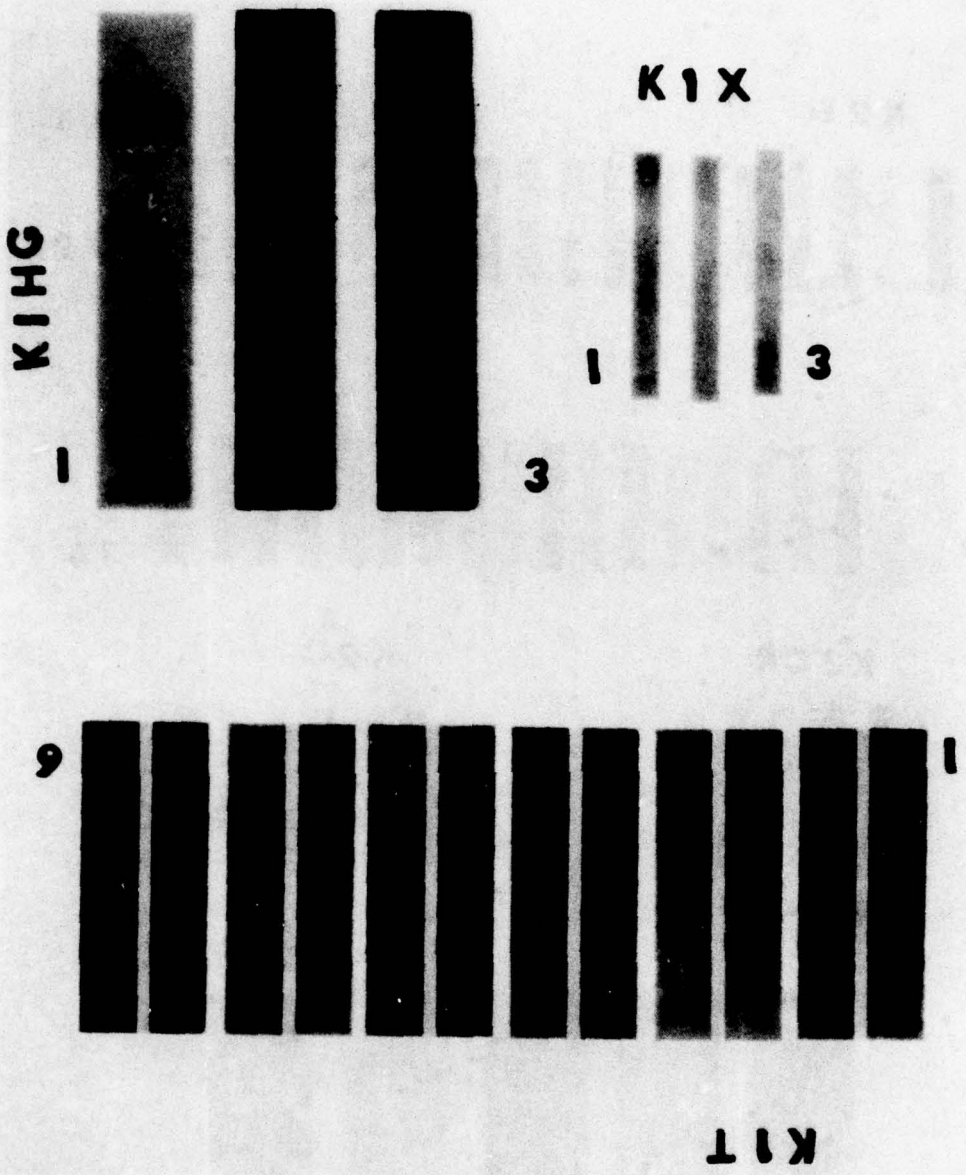

FIGURE A-23 X-RADIOGRAPHIC POSITIVE OF KBI RS Si_3N_4 (BATCH 1) FRACTURE TOUGHNESS, THERMAL EXPANSION, AND HOT GAS ENVIRONMENTAL EXPOSURE SPECIMENS.

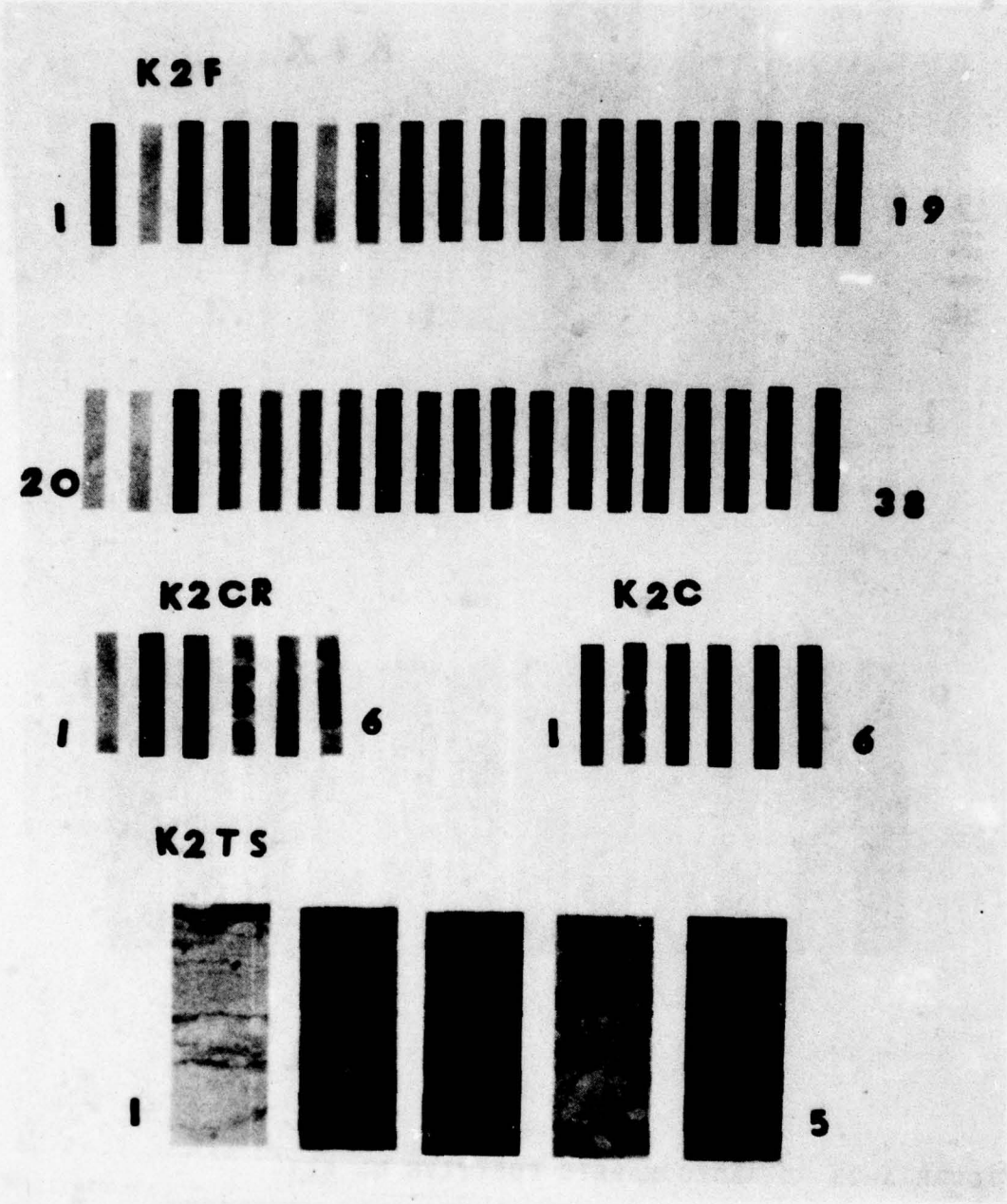

FIGURE A-24 X-RADIOGRAPHIC POSITIVE OF KB1 RS Si_3N_4 (BATCH 2) FLEXURE, CREEP RUPTURE, CREEP, AND THERMAL SHOCK SPECIMENS.

FIGURE A-25 X-RADIOGRAPHIC POSITIVE OF KBI RS Si_3N_4 (BATCH 2) FRACTURE TOUGHNESS SPECIMENS AND METALLOGRAPHIC SAMPLES.

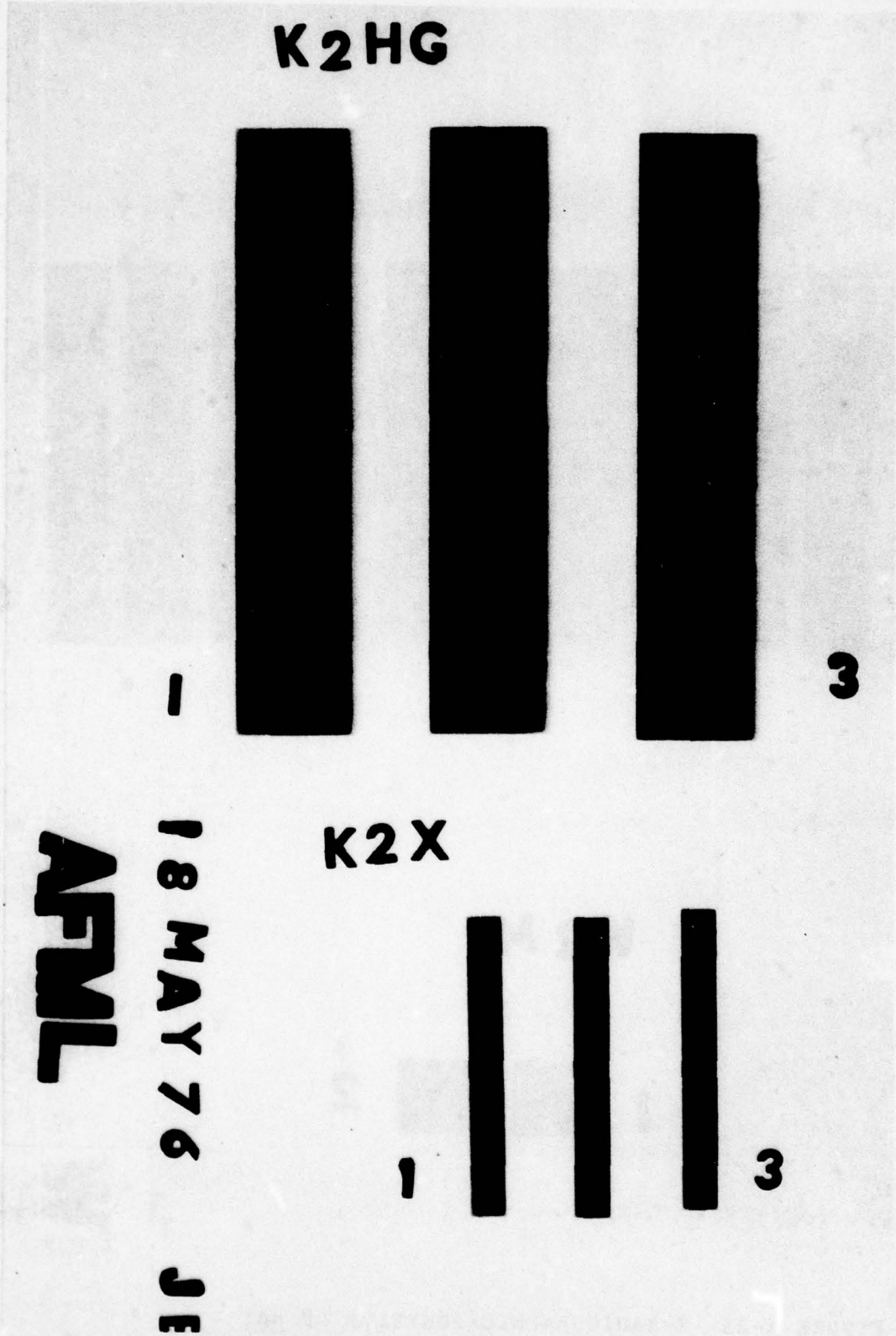

FIGURE A-26 X-RADIOGRAPHIC POSITIVE OF KBI RS Si_3N_4 (BATCH 2) HOT GAS EXPOSURE AND THERMAL EXPANSION SPECIMENS.

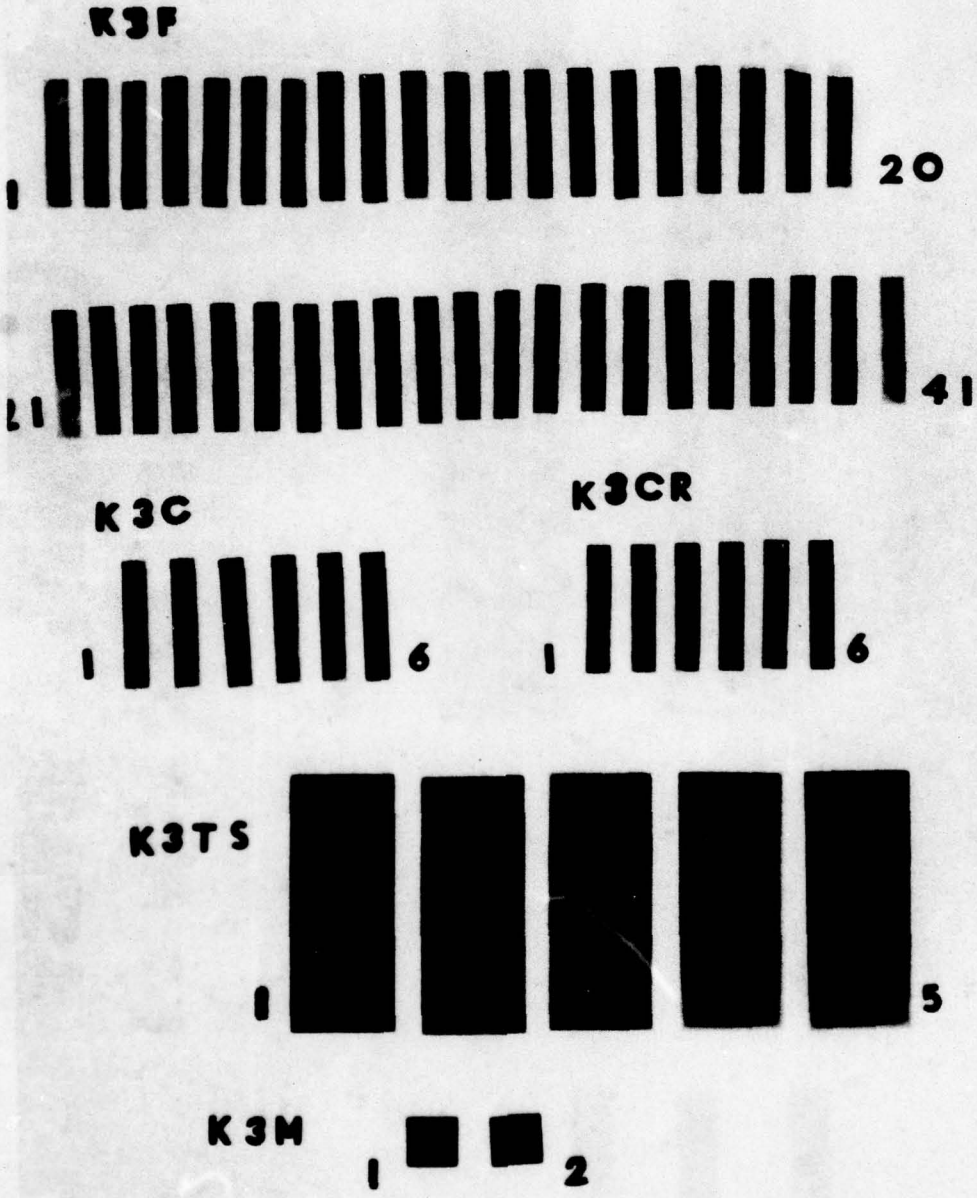

FIGURE A-27 X-RADIOGRAPHIC POSITIVE OF KBI RS Si_3N_4 (BATCH 3) FLEXURE CREEP, CREEP RUPTURE, AND THERMAL SHOCK SPECIMENS. THERMAL SHOCK, AND METALOGRAPHIC SAMPLES.

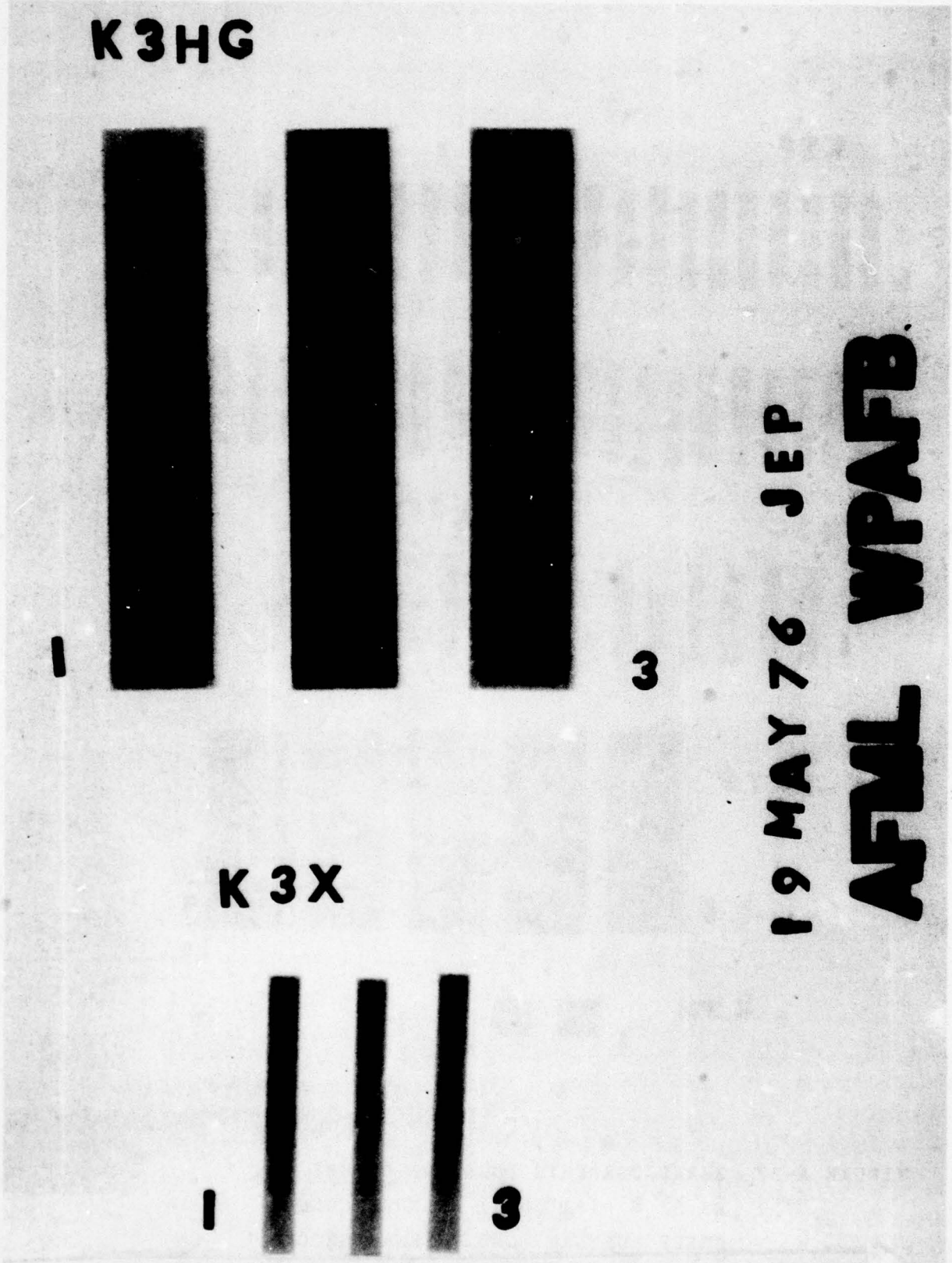

FIGURE A-28 X-RADIOGRAPHIC POSITIVE OF KBI RS Si_3N_4 (BATCH 3) HOT GAS EXPOSURE AND THERMAL EXPANSION SAMPLES.

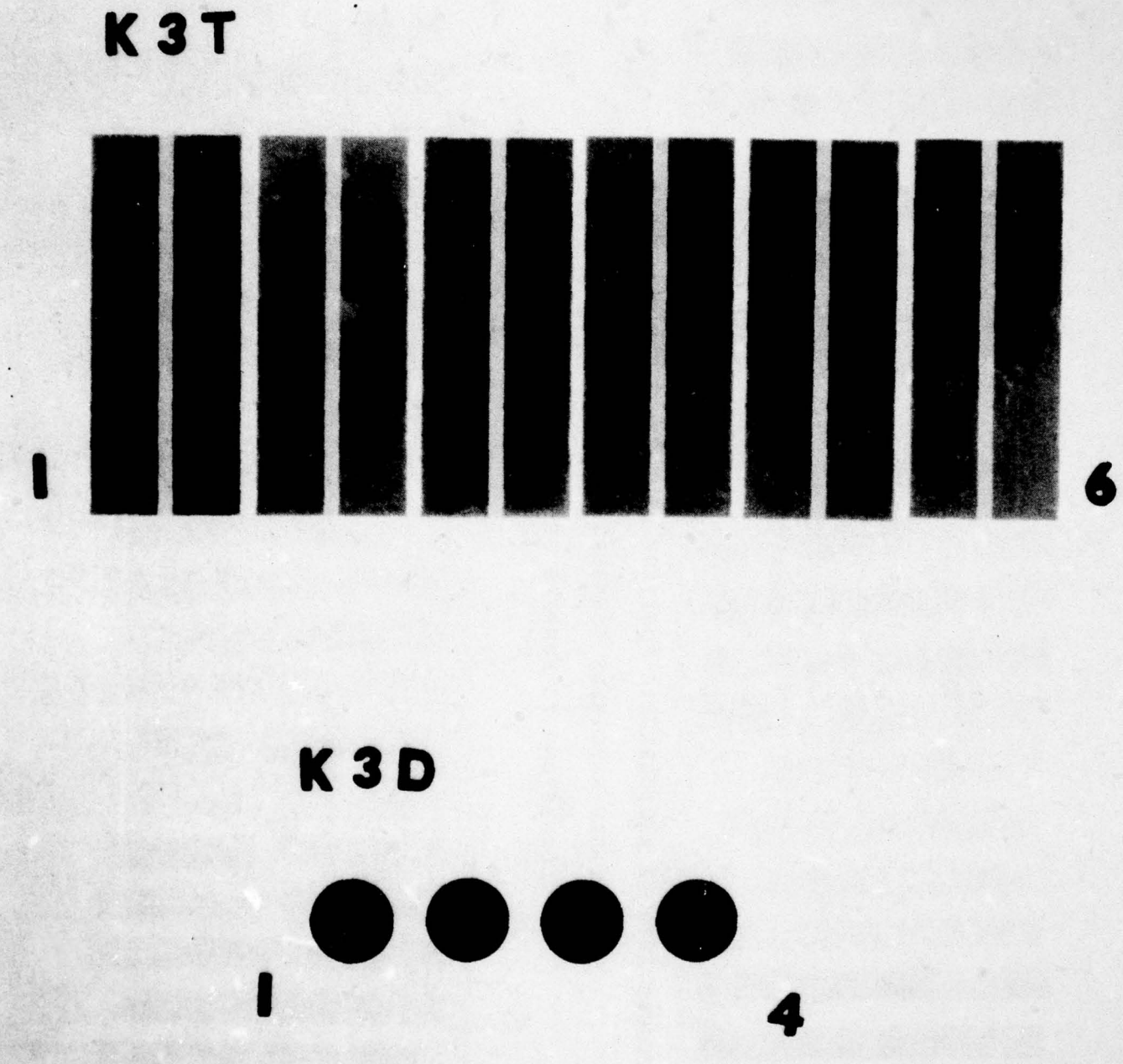

FIGURE A-29 X-RADIOGRAPHIC POSITIVE OF KBI RS Si_3N_4 (BATCH 3) FRACTURE TOUGHNESS AND THERMAL DIFFUSIVITY SPECIMENS.

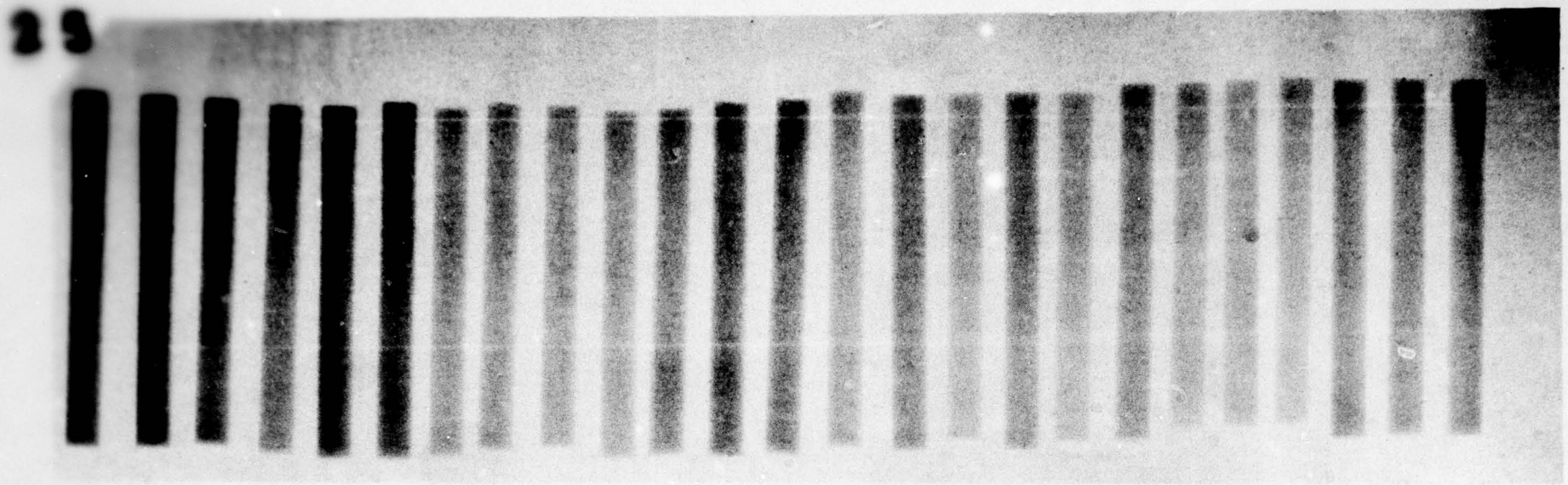

FIGURE A-30 X-RADIOGRAPHIC POSITIVE OF CARBORUNDUM SINTERED α-SiC SPECIMENS (NUMBERS IN PHOTOGRAPH DO NOT CORRESPOND TO NUMBERS OF TESTED SAMPLES).

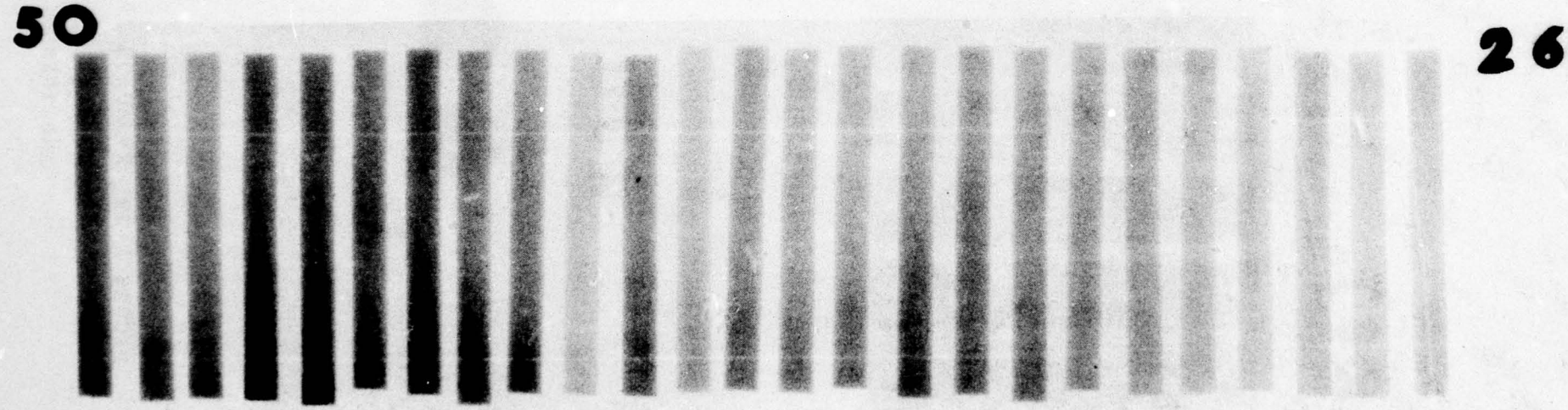

FIGURE A-31 X-RADIOGRAPHIC POSITIVE OF CARBORUMDUM SINTERED α-SiC THERMAL SHOCK SPECIMENS (NUMBERS IN PHOTOGRAPH DO NOT CORRESPOND TO NUMBERS OF TESTED SAMLPLES).

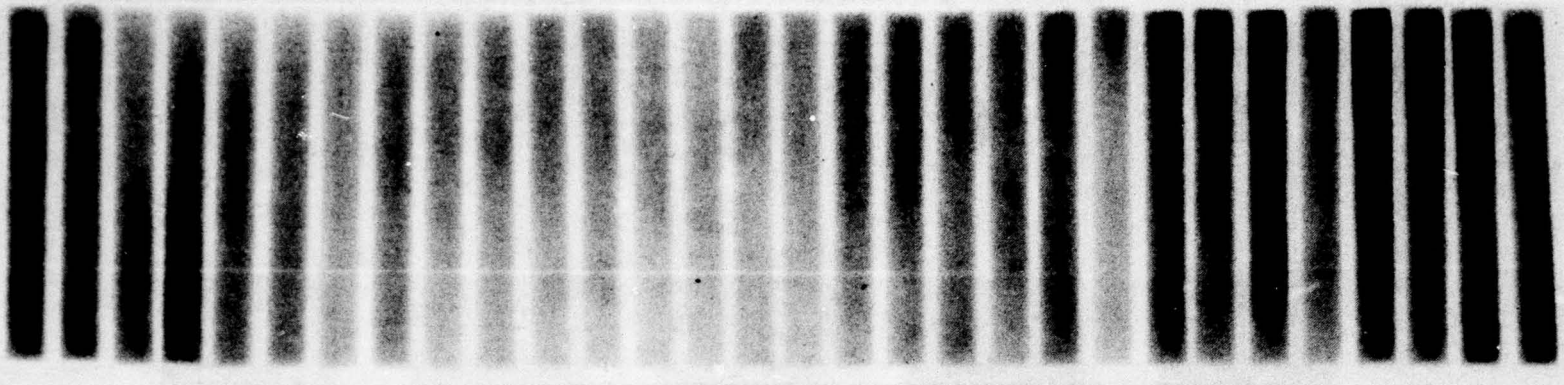

FIGURE A-32 X-RADIOGRAPHIC POSITIVE OF GENERAL ELECECTRIC SINTERED β-SiC SPECIMENS (NUMBERS IN PHOTOGRAPH DO NOT CORRESPOND TO NUMBERS OF TESTED SAMPLES).

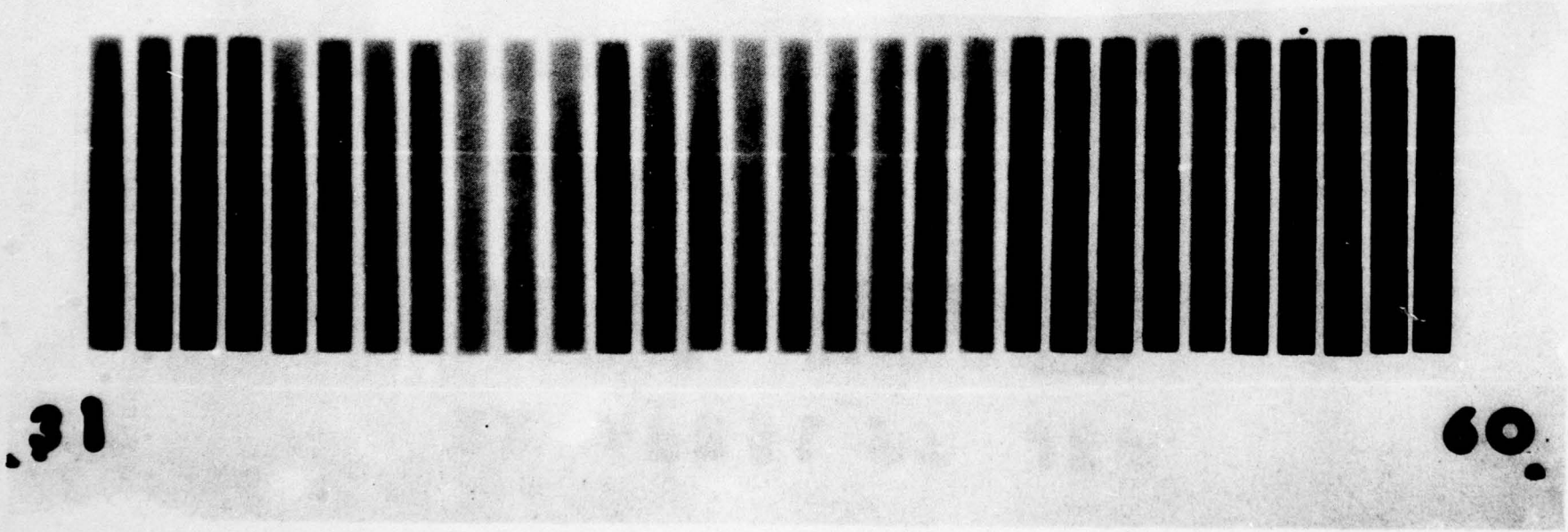

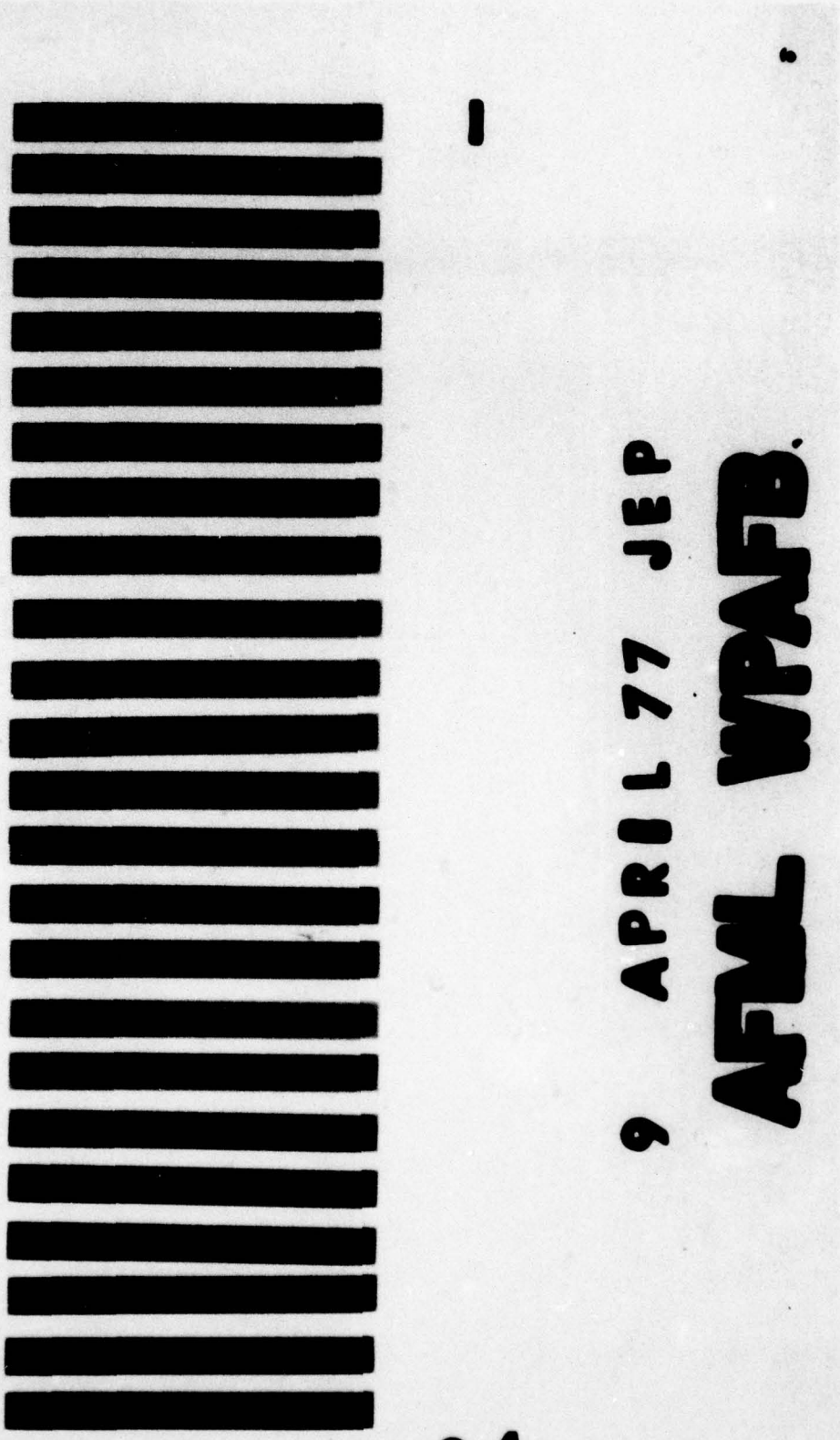

FIGURE A-33 X-RADIOGRAPHIC POSITIVE OF KYOCERA SN-201 SINTERED Si_3N_4 SPECIMENS (NUMBERS IN PHOTOGRAPH DO NOT CORRESPOND TO NUMBERS OF TESTED SAMPLES)

APPENDIX B

FLEXURAL TEST TABULAR RESULTS

Table B-1

FLEXURAL TEST RESULTS: NC-132(1), 25°C

Sample	Bulk Density (gm/cc)	Strength (psi)	Strain-To-Failure (in/in x 10^{-3})	Elastic Modulus (10^6 psi)
11F1	3.175	75,840	1.66	48.2
11F2	3.177	102,900	2.17	49.7
11F3	3.177	71,720	1.49	48.3
11F4	3.178	88,700	1.77	49.4
11F5	3.179	103,900	2.06	49.1
11F6	3.170	88,040	2.03	43.0
11F7	3.172	92,330	1.90	49.7
11F8	3.180	68,250	1.51	48.1
11F9	3.172	99,580	2.02	49.4
11F10	3.177	85,010	1.70	49.1
11F11	3.179	127,100	----	-----
11F12	3.180	75,840	----	-----
11F13	3.174	90,680	----	-----
11F14	3.180	56,050	----	-----
11F15*	3.176	118,700	----	-----
11F16*	3.184	97,100	----	-----
11F17*	3.179	103,700	----	-----
Mean	3.177	90,908	1.83	48.4
Std. Dev.		18,153	0.24	2.0
Max.		127,100	2.17	49.7
Min.		56,050	1.49	43.0

AVERAGE SURFACE FINISH = 12 microinches RMS
AVERAGE BULK DENSITY = 3.18 gm/cm^3
AVERAGE THEO. DENSITY = 99.3%
AVERAGE TOTAL POROSITY = .7%

*Measured at Norton Company

Table B-2

FLEXURAL TEST RESULTS: NC-132(1), 1200°C

Sample	Bulk Density (gm/cc)	Strength (psi)	Strain-To-Failure (in/in x 10^{-3})	Secant Modulus (10^6 psi)
11F18	3.180	80,350	1.87	39.4
11F19	3.173	81,330	1.87	43.0
11F20	3.176	89,300	2.17	42.9
11F21	3.176	97,820	2.23	44.0
11F22	3.185	89,170	2.10	42.2
11F23	3.185	96,870	2.25	42.8
11F24	3.176	94,270	2.16	43.6
11F25	3.182	92,330	2.08	44.7
11F26	3.175	75,840	1.83	41.2
11F27	3.179	84,630	1.92	44.1
Mean	3.179	88,190	2.05	42.8
Std. Dev.		7,439	0.16	1.6
Max.		97,820	2.25	44.7
Min.		75,840	1.83	39.4

AVERAGE SURFACE FINISH = 11.6 microinches RMS
AVERAGE BULK DENSITY = 3.18 gm/cm^3
AVERAGE THEO. DENSITY = 99.3%
AVERAGE TOTAL POROSITY = .7%

Table B-3

FLEXURAL TEST RESULTS: NC-132(1), 1350°C

Sample	Bulk Density (gm/cc)	Strength (psi)	Strain-To-Failure (in/in x 10^{-3})	Secant Modulus (10^6 psi)
11F28	3.168	57,060	3.13	32.8
11F29	3.175	61,650	3.69	31.5
11F30	3.176	61,000	3.32	31.4
11F31	3.180	68,250	3.48	34.5
11F32	3.172	64,300	3.00	40.7
11F33	3.180	54,400	3.50	23.5
11F34	3.178	60,450	4.03	26.5
11F35	3.185	53,860	3.01	30.7
11F36	3.182	53,940	3.00	28.7
11F37	3.179	53,310	3.20	28.0
11F38	3.182	56,600	3.01	31.1
Mean	3.178	58,620	3.31	30.8
Std. Dev.		4,900	.34	4.7
Max.		68,250	4.03	40.7
Min.		53,310	3.00	23.5

AVERAGE SURFACE FINISH = 12 microinches RMS
AVERAGE BULK DENSITY = 3.18 gm/cm^3
AVERAGE THEO. DENSITY = 99.3%
AVERAGE TOTAL POROSITY = .7%

Table B-4

FLEXURAL TEST RESULTS: NC-132(1), 1500C°

Sample	Bulk Density (gm/cc)	Strength (psi)	Strain-To-Failure (in/in x 10^{-3})	Secant Modulus (10^6 psi)
11F39	3.177	25,280	6.18	5.3
11F40*	3.174			
11F41**	3.171			
11F42	3.181	24,730	6.94	6.5
11F43	3.178	30,820	6.74	11.0
11F44	3.179	30,780	6.16	7.9
11F45	3.184	31,370	6.27	9.0
11F46	3.172	25,280	5.66	7.3
11F47	3.183	28,620	6.05	7.7
11F48	3.185	25,280	5.43	6.8
Mean	3.178	27,770	6.18	7.7
Std. Dev.		2,920	.50	1.7
Max.		31,370	6.94	11.0
Min.		24,730	5.43	5.3

* Data obtained judged invalid due to fixture jamming

** Data obtained judged invalid due to temperature instability.

AVERAGE SURFACE FINISH = 12 microinches RMS

AVERAGE BULK DENSITY = 3.18 gm/cm^3

AVERAGE THEO. DENSITY = 99.4%

AVERAGE TOTAL POROSITY = .6%

Table B-5

FLEXURAL TEST RESULTS: NC-132(2), 25°C

Sample	Bulk Density (gm/cc)	Strength (psi)	Strain-To-Failure (in/in x 10^{-3})	Elastic Modulus (10^6 psi)
12F11	3.189	129,300	2.78	46.0
12F12	3.191	114,700	2.45	45.9
12F13	3.189	115,900	2.49	46.3
12F14	3.183	130,700	2.82	46.4
12F15	3.178	120,600	2.65	44.1
12F16	3.187	110,000	2.38	45.7
12F17	3.184	93,830	2.02	45.9
12F18	3.191	132,500	2.88	45.4
12F19	3.179	113,000	2.46	45.3
12F20	3.193	91,540	1.98	46.2
Mean	3.186	115,210	2.49	45.7
Std. Dev.		14,210	0.31	0.7
Max.		132,500	2.88	46.4
Min.		91,540	1.98	44.1

AVERAGE SURFACE FINISH = 11 microinches RMS
AVERAGE BULK DENSITY = 3.19 gm/cm^3
AVERAGE THEO. DENSITY = 99.6%
AVERAGE TOTAL POROSITY = .4%

Table B-6

FLEXURAL TEST RESULTS: NC-132(2), 1200°C

Sample	Bulk Density (gm/cc)	Strength (psi)	Strain-To-Failure (in/in x 10^{-3})	Secant Modulus (10^6 psi)
12F1	3.180	78,840	2.10	40.2
12F2	3.179	76,680	2.14	34.8
12F3	3.172	79,410	2.13	38.0
12F4	3.187	73,460	2.07	36.8
12F5	3.175	85,470	2.62	31.9
12F6	3.185	77,620	2.03	40.5
12F7	3.174	77,520	1.93	43.5
12F8	3.184	75,200	1.79	41.7
12F9	3.185	87,510	2.28	40.5
12F10	3.181	80,680	2.01	43.8
Mean	3.180	79,240	2.11	39.2
Std. Dev.		4,360	0.22	3.8
Max.		87,510	2.62	43.8
Min.		73,460	1.79	31.9

AVERAGE SURFACE FINISH = 11 microinches RMS
AVERAGE BULK DENSITY = 3.18 gm/cm^3
AVERAGE THEO. DENSITY = 99.4%
AVERAGE TOTAL POROSITY = .6%

Table B-7

FLEXURAL TEST RESULTS: NC-132(2), 1350°C

Sample	Bulk Density (gm/cc)	Strength (psi)	Strain-To-Failure (in/in x 10^{-3})	Secant Modulus (10^6 psi)
12F21	3.177	45,500	4.58	21.3
12F22	3.185	48,670	2.96	27.3
12F23	3.177	50,360	4.06	25.1
12F24	3.187	46,970	3.20	25.4
12F25	3.179	49,260	4.05	20.6
12F26	3.184	50,670	5.25	20.0
12F27	3.196	48,980	4.75	23.0
12F28	3.190	46,970	4.22	21.3
12F29	3.186	50,500	4.92	21.2
12F30	3.180	50,080	4.23	22.0
Mean	3.184	48,800	4.22	22.7
Std. Dev.		770	.72	2.4
Max.		50,670	5.25	27.3
Min.		45,500	2.96	20.0

AVERAGE SURFACE FINISH = 11 microinches RMS
AVERAGE BULK DENSITY = 3.18 gm/cm^3
AVERAGE THEO. DENSITY = 99.5%
AVERAGE TOTAL POROSITY = .5%

Table B-8

FLEXURAL TEST RESULTS: NC-132(2), 1500°C

Sample	Bulk Density (gm/cc)	Strength (psi)	Strain-To-Failure (in/in x 10^{-3})	Secant Modulus (10^6 psi)
12F31	3.193	26,000	5.92	7.0
12F32	3.196	24,980	6.19	6.6
12F33	3.186	24,670	5.88	7.3
12F34	3.189	24,670	5.12	7.5
12F35	3.185	25,300	6.10	6.5
12F36	3.190	26,040	7.08	6.0
12F37	3.184	24,670	6.19	6.5
12F38	3.180	23,890	6.30	6.2
12F39	3.179	25,340	7.21	5.8
12F40	3.182	26,500	7.19	5.6
Mean	3.186	25,210	6.32	6.5
Std. Dev.		790	.67	0.6
Max.		26,500	7.21	7.5
Min.		23,890	5.12	5.6

AVERAGE SURFACE FINISH = 10 microinches RMS
AVERAGE BULK DENSITY = 3.19 gm/cm^3
AVERAGE THEO. DENSITY = 99.6%
AVERAGE TOTAL POROSITY = .4%

TABLE B-9

FLEXURAL TEST RESULTS: NC-435 (1), 25°C

Sample	Bulk Density (gm/cc)	Strength (psi)	Elastic Modulus (10^6 psi)	Strain-To-Failure (in/inx10^{-3})
41F1	2.916	58,340	51.2	1.15
41F2	2.929	54,600	55.1	.99
41F3	2.931	37,800	47.8	.77
41F4	2.918	62,900	53.4	1.21
41F5	2.985	50,080	54.6	.93
41F41	2.913	56,350	50.5	1.11
41F42	2.945	60,810	54.2	1.15
41F43	2.929	31,450	59.2	.53
41F44	2.951	28,310	54.9	.52
41F45	2.947	63,950	57.8	1.13
Mean	2.936	50,460	53.9	.95
Std. Dev.		13,210	3.4	.26
Max.		63,950	59.2	1.21
Min.		28,310	47.8	.52

AVERAGE SURFACE FINISH = 14 microinches RMS
AVERAGE BULK DENSITY = 2.93 gm/cm^3
AVERAGE THEO. DENSITY = 91.1%
AVERAGE TOTAL POROSITY = 8.9%
AVERAGE OPEN POROSITY (meas.) = 1.5%
AVERAGE CLOSED POROSITY (by difference) = 7.4%

AD-A062 905 IIT RESEARCH INST CHICAGO ILL F/G 11/2
PROPERTY SCREENING AND EVALUATION OF CERAMIC VANE MATERIALS.(U)
OCT 77 D C LARSEN, G C WALTHER F33615-75-C-5196
UNCLASSIFIED IITRI-D6114-ITR-24 NL

4 OF 4
ADA
062905

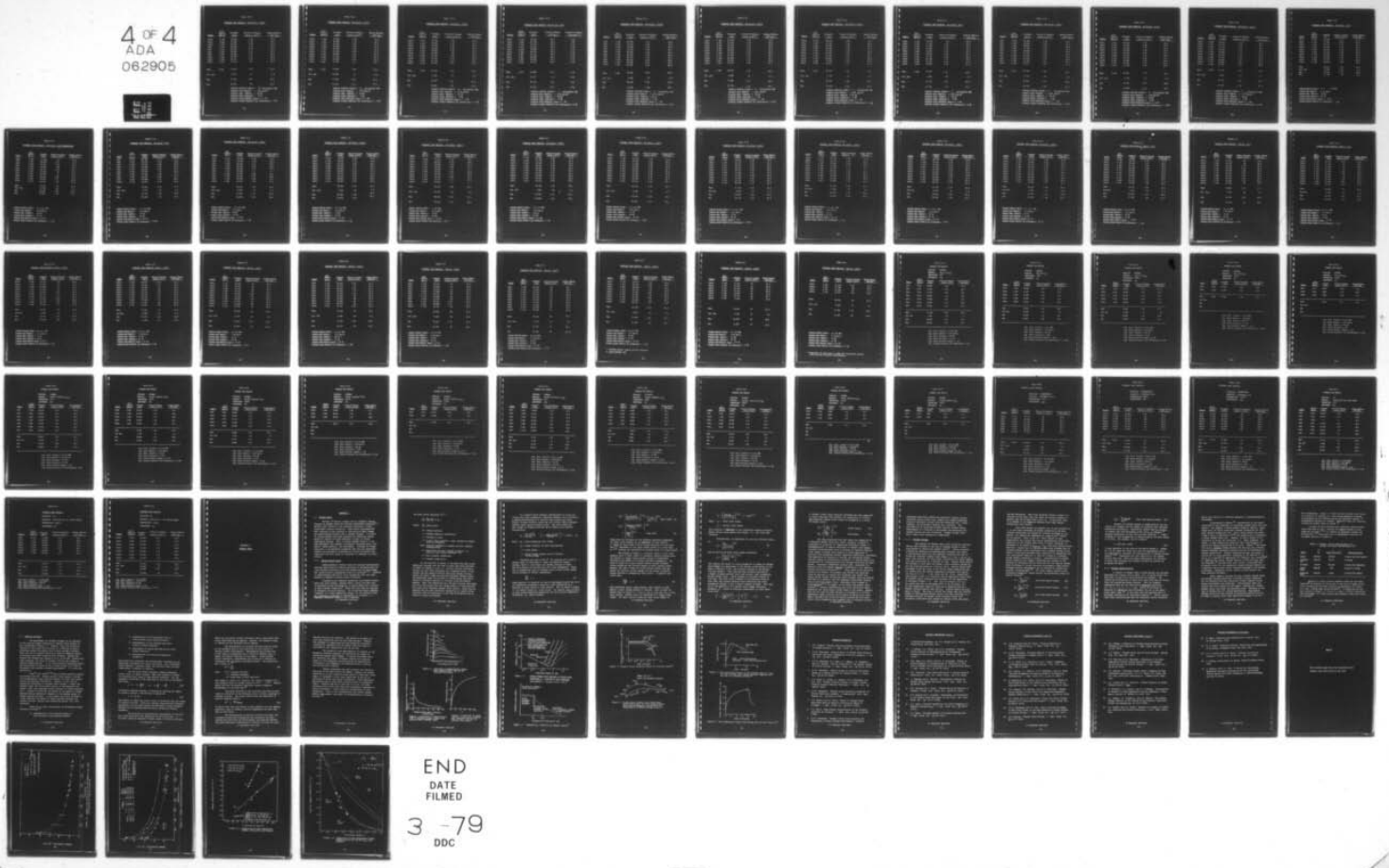

END
DATE
FILMED
3 -79
DDC

Table B-10

FLEXURAL TEST RESULTS: NC-435(1), 1200°C

Sample	Bulk Density (gm/cc)	Strength (psi)	Strain-To-Failure (in/in x 10^{-3})	Secant Modulus (10^6 psi)
41F46	2.939	52,640	1.34	45.0
41F47	2.956	70,560	1.93	50.4
41F48	2.928	40,320	0.98	40.3
41F6	2.945	60,480	1.55	45.8
41F7	2.917	64,000	1.96	45.1
41F8	2.935	58,340	1.40	49.4
41F9	2.937	49,280	1.13	46.5
41F10	2.938	56,380	1.43	49.5
41F11	2.948	64,120	1.63	45.8
41F12	2.933	57,920	1.51	46.0
Mean	2.938	57,400	1.49	46.4
Std. Dev.		8,520	.31	2.9
Max.		70,560	1.96	50.4
Min.		40,320	.98	40.3

AVERAGE SURFACE FINISH = 16 microinches RMS
AVERAGE BULK DENSITY = 2.94 gm/cm^3
AVERAGE THEO. DENSITY = 91.3%
AVERAGE TOTAL POROSITY = 8.7%
AVERAGE OPEN POROSITY (meas.) = 1.2%
AVERAGE CLOSED POROSITY (by difference) = 7.5%

Table B-11

FLEXURAL TEST RESULTS: NC-435(1), 1275°C

Sample	Bulk Density (gm/cc)	Strength (psi)	Strain-To-Failure (in/in x 10^{-3})	Secant Modulus (10^6 psi)
41F23	2.928	51,040	1.40	43.3
41F24	2.915	58,900	1.74	41.5
41F25	2.922	63,340	1.85	42.8
41F26	2.938	46,480	1.35	37.5
41F27	2.915	54,880	1.85	41.6
41F28	2.917	70,560	2.90	37.9
41F29	2.923	65,980	2.34	39.8
41F30	2.911	73,250	3.10	39.4
41F31	2.936	49,280	1.14	42.5
41F32	2.917	44,450	1.15	39.7
Mean	2.922	57,820	1.88	40.6
Std. Dev.		10,180	.70	2.0
Max.		73,250	3.10	43.3
Min.		44,450	1.14	37.5

AVERAGE SURFACE FINISH = 13 microinches RMS
AVERAGE BULK DENSITY = 2.92 gm/cm^3
AVERAGE THEO. DENSITY = 90.8%
AVERAGE TOTAL POROSITY = 9.2%
AVERAGE OPEN POROSITY (meas.) = 1.3%
AVERAGE CLOSED POROSITY (by difference) = 7.9%

Table B-12

FLEXURAL TEST RESULTS: NC-435(1), 1350°C

Sample	Bulk Density (gm/cc)	Strength (psi)	Strain-To-Failure (in/in x 10^{-3})	Secant Modulus (10^6 psi)
41F13	2.951	46,750	1.15	34.4
41F14	2.914	42,290	1.32	34.1
41F15	2.943	49,420	1.57	36.3
41F16	2.908	45,840	1.64	31.4
41F17	2.931	38,680	1.16	35.2
41F18	2.920	28,380	.81	75.5
41F19	2.919	45,780	1.48	38.2
41F20	2.952	51,920	1.68	40.6
41F21	2.928	41,740	1.23	40.1
41F22	2.926	50,360	1.85	35.0
Mean	2.929	44,120	1.39	36.1
Std. Dev.		6,890	.31	2.8
Max.		51,920	1.85	40.6
Min.		28,380	.81	31.4

AVERAGE SURFACE FINISH = 13 microinches RMS
AVERAGE BULK DENSITY = 2.93 gm/cm^3
AVERAGE THEO. DENSITY = 91.1%
AVERAGE TOTAL POROSITY = 9.0%
AVERAGE OPEN POROSITY (meas.) = 1.7%
AVERAGE CLOSED POROSITY (by difference) = 7.3%

TABLE B-13

FLEXURAL TEST RESULTS: NC-435 (3), 25°C

Sample	Bulk Density (gm/cc)	Strength (psi)	Elastic Modulus (10^6 psi)	Strain-To-Failure (in/inx10^{-3})
43F11	2.995	78,230	50.7	1.51
43F12	2.994	82,320	48.4	1.66
43F13	3.012	61,490	50.5	1.19
43F14	2.972	55,100	50.1	1.10
43F15	2.999	59,900	51.6	1.16
43F16	2.989	80,130	48.2	1.60
43F17	3.007	62,750	48.4	1.48
43F18	3.005	68,490	49.4	1.35
43F19	3.005	58,930	48.7	1.19
43F20	2.992	52,410	48.9	1.06
Mean	2.997	65,980	49.5	1.33
Std. Dev.		10,770	1.2	0.22
Max.		82,320	51.6	1.66
Min.		52,410	48.2	1.06

AVERAGE SURFACE FINISH = 3 microinches RMS
AVERAGE BULK DENSITY = 3.00 gm/cm^3
AVERAGE THEO. DENSITY = 93.2%
AVERAGE TOTAL POROSITY = 6.8%
AVERAGE OPEN POROSITY (meas.) = .6%
AVERAGE CLOSED POROSITY (by difference) = 6.3%

Table B-14

FLEXURAL TEST RESULTS: NC-435(3), 1200°C

Sample	Bulk Density (gm/cc)	Strength (psi)	Strain-To-Failure (in/in x 10^{-3})	Secant Modulus (10^6 psi)
43F1	2.996	81,440	1.97	45.4
43F2	3.008	75,130	1.86	43.6
43F3	2.980	73,250	1.94	41.3
43F4	2.992	75,940	1.95	43.7
43F5	3.018	78,200	1.89	46.2
43F6	2.976	81,310	2.36	40.8
43F7	2.998	89,520	1.95	55.9
43F8	3.009	81,630	2.12	42.0
43F9	2.993	78,200	2.26	36.4
43F10	2.993	81,990	2.32	38.8
Mean	2.996	79,660	2.06	43.4
Std. Dev.		4,620	.19	5.3
Max.		89,520	2.36	55.9
Min.		73,250	1.86	36.4

AVERAGE SURFACE FINISH = 3 microinches RMS
AVERAGE BULK DENSITY = 3.00 gm/cm^3
AVERAGE THEO. DENSITY = 93.1%
AVERAGE TOTAL POROSITY = 6.9%
AVERAGE OPEN POROSITY (meas.) = .5%
AVERAGE CLOSED POROSITY (by difference) = 6.4%

Table B-15

FLEXURAL TEST RESULTS: NC-435(3), 1275°C

Sample	Bulk Density (gm/cc)	Strength (psi)	Strain-To-Failure (in/in x 10^{-3})	Secant Modulus (10^6 psi)
43F21	2.986	63,840	1.76	43.9
43F22	2.994	64,350	1.72	39.6
43F23	2.970	41,780	1.02	50.6
43F24	2.998	62,030	1.83	41.9
43F25	3.003	46,870	1.16	43.1
43F26	2.968	55,830	1.78	38.2
43F27	2.972	71,900	2.13	46.1
43F28	2.998	66,380	1.75	43.7
43F29	3.004	50,070	1.45	39.0
43F30	3.001	67,060	1.88	42.0
Mean	2.989	59,010	1.65	42.8
Std. Dev.		9,890	.34	3.7
Max.		71,900	2.13	50.6
Min.		41,780	1.02	38.2

AVERAGE SURFACE FINISH = 3 microinches RMS
AVERAGE BULK DENSITY = 2.99 gm/cm^3
AVERAGE THEO. DENSITY = 92.9%
AVERAGE TOTAL POROSITY = 7.1%
AVERAGE OPEN POROSITY (meas.) = .9%
AVERAGE CLOSED POROSITY (by difference) = 6.2%

Table B-16

FLEXURAL TEST RESULTS: NC-435(3), 1350°C

Sample	Bulk Density (gm/cc)	Strength (psi)	Strain-To-Failure (in/in x 10^{-3})	Secant Modulus (10^6 psi)
43F31	2.979	58,560	1.90	37.2
43F32	2.987	49,130	1.38	40.6
43F33	3.007	48,100	1.48	35.0
43F34	3.009	54,280	1.48	42.9
43F35	3.014	46,420	1.30	36.1
43F36	2.995	49,080	1.48	38.7
43F37	3.016	49,160	1.34	38.1
43F38	2.993	50,800	1.47	36.8
43F39	2.992	37,550	1.04	33.4
43F40	3.008	40,040	1.21	37.9
Mean	3.000	48,310	1.41	37.7
Std. Dev.		6,120	.22	2.7
Max.		58,550	1.90	42.9
Min.		37,550	1.04	33.4

AVERAGE SURFACE FINISH = 4 microinches RMS
AVERAGE BULK DENSITY = 3.00 gm/cm^3
AVERAGE THEO. DENSITY = 93.3%
AVERAGE TOTAL POROSITY = 6.8%
AVERAGE OPEN POROSITY (meas.) = .8%
AVERAGE CLOSED POROSITY (by difference) = 6.0%

Table B-17

FLEXURAL TEST RESULTS: NC-435(4), 25°C

Sample	Bulk Density (gm/cc)	Strength (psi)	Strain-To-Failure (in/in x 10^{-3})	Elastic Modulus (10^6 psi)
44F21	2.952	45,720	.92	49.2
44F22	2.976	57,760	1.14	50.3
44F23	2.953	57,970	1.18	49.2
44F24	2.953	54,660	1.12	48.6
44F25	2.966	53,670	1.10	48.7
44F26	2.952	49,870	1.05	47.7
44F27	2.955	55,740	1.20	48.0
44F28	2.981	62,390	1.25	48.5
44F29	2.949	52,670	1.10	47.5
44F30	2.982	61,000	1.20	50.3
Mean	2.962	55,150	1.13	48.8
Std. Dev.		5,020	.09	1.0
Max.		62,390	1.25	50.3
Min.		45,720	.92	47.5

AVERAGE SURFACE FINISH = 3 microinches RMS
AVERAGE BULK DENSITY = 2.96 gm/cm^3
AVERAGE THEO. DENSITY = 92.1%
AVERAGE TOTAL POROSITY = 7.9%
AVERAGE OPEN POROSITY (meas.) = 1.3%
AVERAGE CLOSED POROSITY (by difference) = 6.6%

Table B-18

FLEXURAL TEST RESULTS: NC-435(4), 1200°C

Sample	Bulk Density (gm/cc)	Strength (psi)	Strain-To-Failure (in/in x 10^{-3})	Secant Modulus (10^6 psi)
44F1	2.958	56,760	2.18	33.3
44F2	2.981	59,490	1.92	41.3
44F3	2.981	68,820	1.82	46.8
44F4	2.983	67,700	2.37	39.2
44F5	2.986	56,800	1.90	36.9
44F6	2.981	61,940	2.00	43.2
44F7	2.978	67,450	2.42	39.2
44F8	2.962	61,550	1.97	38.9
44F9	2.968	63,720	2.41	38.3
44F10	2.968	59,630	1.89	40.7
Mean	2.975	62,390	2.09	39.7
Std. Dev.		4,430	.24	3.7
Max.		68,820	2.42	46.8
Min.		56,760	1.82	33.3

AVERAGE SURFACE FINISH = 5 microinches RMS
AVERAGE BULK DENSITY = 2.98 gm/cm^3
AVERAGE THEO. DENSITY = 92.5%
AVERAGE TOTAL POROSITY = 7.5%
AVERAGE OPEN POROSITY (meas.) = 1.2%
AVERAGE CLOSED POROSITY (by difference) = 6.3%

Table B-19

FLEXURAL TEST RESULTS: NC-435(4), 1275°C

Sample	Bulk Density (gm/cc)	Strength (psi)	Strain-To-Failure (in/in x 10^{-3})	Secant Modulus (10^6 psi)
44F11	2.956	60,960	2.20	34.8
44F12	2.959	54,990	1.88	37.0
44F13	2.956	59,490	1.76	41.3
44F14	2.952	55,660	1.86	38.9
44F15	2.946	59,120	2.40	34.3
44F16	2.963	56,070	1.76	44.2
44F17	2.961	61,620	2.02	33.3
44F18	2.970	65,480	1.65	48.0
44F19	2.953	60,960	1.80	42.7
44F20	2.975	67,700	2.16	36.4
Mean	2.959	60,200	1.95	39.1
Std. Dev.		4,130	.24	4.8
Max.		67,700	2.40	48.0
Min.		54,990	1.65	33.3

AVERAGE SURFACE FINISH = 4 microinches RMS
AVERAGE BULK DENSITY = 2.96 gm/cm^3
AVERAGE THEO. DENSITY = 92.0%
AVERAGE TOTAL POROSITY = 8.0%
AVERAGE OPEN POROSITY (meas.) = 1.4%
AVERAGE CLOSED POROSITY (by difference) = 6.6%

Table B-20

FLEXURAL TEST RESULTS: NC-435(4), 1350°C

Sample	Bulk Density (gm/cc)	Strength (psi)	Strain-To-Failure (in/in x 10^{-3})	Secant Modulus (10^6 psi)
44F31	2.966	42,670	1.53	35.3
44F32	2.971	43,770	1.48	36.7
44F33	2.969	43,770	1.55	35.6
44F34	2.957	42,400	1.62	31.3
44F35	2.948	40,000	1.37	34.6
44F36	2.960	42,000	1.48	36.4
44F37	2.963	43,770	1.48	35.0
44F38	2.956	38,000	1.30	33.9
44F39	2.970	42,400	1.35	36.5
44F40	2.990	35,340	1.16	33.3
Mean	2.965	41,410	1.44	34.9
Std. Dev.		2,810	.14	1.7
Max.		43,770	1.62	36.7
Min.		35,340	1.16	31.3

AVERAGE SURFACE FINISH = 4 microinches RMS
AVERAGE BULK DENSITY = 2.97 gm/cm^3
AVERAGE THEO. DENSITY = 92.2%
AVERAGE TOTAL POROSITY = 7.8%
AVERAGE OPEN POROSITY (meas.) = 1.2%
AVERAGE CLOSED POROSITY (by difference) = 6.7%

TABLE B-21

FLEXURAL TEST RESULTS: NC-350(1), 25°C

SAMPLE	BULK DENSITY gm/cc	STRENGTH (psi)	STRAIN-TO-FAILURE (in/in x 10^{-3})	ELASTIC MODULUS (10^6 psi)
31F11	2.534	38,760	1.70	21.5
31F12	2.544	17,390	0.65	26.2
31F13	2.527	37,270	1.45	25.5
31F14	2.535	25,550	1.10	22.5
31F15	2.539	39,940	1.58	24.5
31F16	2.503	31,470	1.28	24.2
31F17	2.520	19,850	0.68	29.8
31F18	2.518	32,250	1.16	27.1
31F19	2.484	27,250	1.01	26.6
31F20	2.529	38,930	1.40	26.6
Mean		30,870	1.20	25.5
Std. Dev.		8,150	0.35	2.4
Max.		39,940	1.70	29.8
Min.		17,390	.65	21.5

AVERAGE SURFACE FINISH = 5.5 μin RMS
AVERAGE BULK DENSITY = 2.52 gm/cc
AVERAGE THEO. DENSITY = 78.9%
AVERAGE TOTAL POROSITY = 21.1%
AVERAGE OPEN POROSITY (meas) = 13.6%
AVERAGE CLOSED POROSITY (by difference) = 7.5%

TABLE B-22

FLEXURAL TEST RESULTS: NC-350(2), ROOM TEMPERATURE

SAMPLE	BULK DENSITY gm/cc	STRENGTH (psi)	STRAIN-TO-FAILURE (in/in x 10^{-3})	ELASTIC MODULUS (10^6 psi)
32F1	2.383	16,280	.74	21.7
32F2	2.412	28,580	1.21	23.3
32F3	2.385	29,610	1.26	23.5
32F4	2.329	19,610	.88	22.1
32F5	2.399	26,250	1.10	23.7
32F6	2.415	17,810	.70	25.1
32F7	2.426	18,420	.74	25.0
32F8	2.428	36,540	1.50	24.1
32F9	2.404	25,420	1.11	22.6
32F10	2.378	16,750	.70	23.8
Mean		23,530	.99	23.5
Std. Dev.		6,790	.28	1.1
Max.		36,540	1.50	25.1
Min.		16,280	.70	21.7

AVERAGE SURFACE FINISH = 6.4 µin RMS
AVERAGE BULK DENSITY = 2.40 gm/cc
AVERAGE THEO. DENSITY = 74.9%
AVERAGE TOTAL POROSITY = 25.1%
AVERAGE OPEN POROSITY (meas) = 17.4%
AVERAGE CLOSED POROSITY (by difference) = 7.7%

TABLE B-23

FLEXURAL TEST RESULTS: NC-350(3), 25°C

SAMPLE	BULK DENSITY gm/cc	STRENGTH (psi)	STRAIN-TO-FAILURE (in/in x 10^{-3})	ELASTIC MODULUS (10^6 psi)
33F1	2.547	45,460	1.55	28.6
33F2	2.561	30,340	1.04	28.1
33F3	2.569	45,720	1.56	29.2
33F4	2.510	33,900	1.28	25.8
33F5	2.513	26,540	1.02	25.7
33F6	2.539	25,760	.91	28.3
33F7	2.536	37,980	1.38	27.5
33F8	2.547	30,190	1.08	27.7
33F9	2.533	29,080	1.03	28.2
33F10	2.532	34,620	1.26	27.5
Mean		33,960	1.21	27.7
Std. Dev.		7,154	.23	1.1
Max.		45,720	1.56	29.2
Min.		25,760	.91	25.7

AVERAGE SURFACE FINISH = 4.5 µin RMS
AVERAGE BULK DENSITY = 2.54 gm/cc
AVERAGE THEO. DENSITY = 79.3%
AVERAGE TOTAL POROSITY = 20.7%
AVERAGE OPEN POROSITY (meas) = 10.3%
AVERAGE CLOSED POROSITY (by difference) = 10.4%

TABLE B-24

FLEXURAL TEST RESULTS: NC-350(1), 1200°C

SAMPLE	BULK DENSITY gm/cc	STRENGTH (psi)	STRAIN-TO-FAILURE (in/in x 10^{-3})	ELASTIC MODULUS (10^6 psi)
31F1	2.537	63,240	1.82	34.1
31F2	2.511	64,450	1.76	40.9
31F3	2.502	63,500	2.17	28.9
31F4	2.523	46,670	1.62	28.4
31F5	2.518	62,000	1.97	32.9
31F6	2.517	42,030	----	----
31F7	2.530	67,790	2.00	33.4
31F8	2.530	64,450	2.04	30.6
31F9	2.536	65,560	1.99	32.1
31F10	2.520	60,010	1.93	31.5
Mean		59,970	1.92	32.5
Std. Dev.		8,550	.16	3.7
Max.		67,790	2.17	40.9
Min.		42,030	1.62	28.4

AVERAGE SURFACE FINISH = 5.0 µin RMS
AVERAGE BULK DENSITY = 2.52 gm/cc
AVERAGE THEO. DENSITY = 78.8%
AVERAGE TOTAL POROSITY = 21.2%
AVERAGE OPEN POROSITY (meas) = 13.9%
AVERAGE CLOSED POROSITY (by difference) = 7.3%

TABLE B-25

FLEXURAL TEST RESULTS: NC-350(2), 1200°C

SAMPLE	BULK DENSITY gm/cc	STRENGTH (psi)	STRAIN-TO-FAILURE (in/in x 10^{-3})	ELASTIC MODULUS (10^6 psi)
32F11	2.410	51,500	1.98	24.4
32F12	2.408	48,220	2.14	21.8
32F13	2.389	55,100	2.66	20.1
32F14	2.383	61,810	2.75	22.3
32F15	2.385	68,350	2.72	21.5
32F16	2.418	58,950	2.41	24.7
32F17	2.373	63,310	2.88	21.6
32F18	2.374	51,570	2.30	22.0
32F19	2.419	58,950	2.23	26.1
32F20	2.413	68,460	2.59	26.3
Mean		58,620	2.47	23.1
Std. Dev.		7,030	.30	2.1
Max.		68,460	2.88	26.3
Min.		48,220	1.98	20.1

AVERAGE SURFACE FINISH = 8.4 µin RMS
AVERAGE BULK DENSITY = 2.40 gm/cc
AVERAGE THEO. DENSITY = 74.9%
AVERAGE TOTAL POROSITY = 25.1%
AVERAGE OPEN POROSITY (meas) = 17.5%
AVERAGE CLOSED POROSITY (by difference) = 7.6%

TABLE B-26

FLEXURAL TEST RESULTS: NC-350(3), 1200°C

SAMPLE	BULK DENSITY gm/cc	STRENGTH (psi)	STRAIN-TO-FAILURE (in/in x 10^{-3})	ELASTIC MODULUS (10^6 psi)
33F11	2.508	64,110	2.30	28.0
33F12	2.541	68,910	2.29	30.1
33F13	2.541	50,830	1.63	32.0
33F14	2.515	58,100	2.06	27.7
33F15	2.551	49,850	1.77	27.7
33F16	2.500	60,200	2.30	26.2
33F17	2.529	32,050	1.14	26.8
33F18	2.531	61,810	1.64	37.2
33F19	2.546	55,170	1.77	31.4
33F20	2.542	62,200	----	----
Mean		56,320	1.88	29.7
Std. Dev.		10,350	.39	3.5
Max.		68,910	2.30	37.2
Min.		32,050	1.14	26.2

AVERAGE SURFACE FINISH = 4 μin RMS
AVERAGE BULK DENSITY = 2.53 gm/cc
AVERAGE THEO. DENSITY = 79.1%
AVERAGE TOTAL POROSITY = 20.9%
AVERAGE OPEN POROSITY (meas) = 10.9%
AVERAGE CLOSED POROSITY (by difference) = 10%

TABLE B-27

FLEXURAL TEST RESULTS: NC-350(1), 1350°C

SAMPLE	BULK DENSITY gm/cc	STRENGTH (psi)	STRAIN-TO-FAILURE (in/in x 10^{-3})	ELASTIC MODULUS (10^6 psi)
31F21	2.503	50,800	1.84	25.4
31F22	2.496	47,780	1.90	24.3
31F23	2.516	63,340	2.24	26.6
31F24	2.484	60,010	1.95	31.2
31F25	2.476	55,650	1.86	29.2
31F26	2.496	43,890	1.43	30.7
31F27	2.494	64,050	2.25	28.1
31F28	2.515	49,690	1.82	26.6
31F40	2.547	50,025	2.52	18.5
31F41	2.510	59,540	2.09	28.5
Mean		54,480	1.99	26.9
Std. Dev.		7,000	.30	3.7
Max.		64,050	2.52	31.2
Min.		43,890	1.43	18.5

AVERAGE SURFACE FINISH = 5.5 µin RMS
AVERAGE BULK DENSITY = 2.50 gm/cc
AVERAGE THEO. DENSITY = 78.1%
AVERAGE TOTAL POROSITY = 21.9%
AVERAGE OPEN POROSITY (meas) = 14.8%
AVERAGE CLOSED POROSITY (by difference) = 7.1%

TABLE B-28

FLEXURAL TEST RESULTS: NC-350(2), 1350°C

SAMPLE	BULK DENSITY gm/cc	STRENGTH (psi)	STRAIN-TO-FAILURE (in/in x 10^{-3})	ELASTIC MODULUS (10^6 psi)
32F21	2.395	61,330	2.53	24.4
32F22	2.392	61,920	2.50	24.9
32F23	2.413	67,790	2.82	23.6
32F24	2.403	73,480	2.96	24.9
32F25	2.395	60,000	2.38	26.7
32F26	2.406	54,520	2.56	20.8
32F27	2.416	57,160	2.68	21.2
32F28	2.383	59,820	2.27	27.9
32F29	2.375	61,240	2.72	18.1
32F30	2.452	64,040	2.86	22.1
Mean		62,130	2.63	23.5
Std. Dev.		5,360	.22	2.9
Max.		73,480	2.96	27.9
Min.		54,520	2.27	18.1

AVERAGE SURFACE FINISH = 6.1 µin RMS
AVERAGE BULK DENSITY = 2.40 gm/cc
AVERAGE THEO. DENSITY = 75.1%
AVERAGE TOTAL POROSITY = 24.9%
AVERAGE OPEN POROSITY (meas) = 16.9%
AVERAGE CLOSED POROSITY (by difference) = 8.0%

Table B-29

FLEXURAL TEST RESULTS: NC-350(3), 1350°C

SAMPLE	BULK DENSITY gm/cc	STRENGTH (psi)	STRAIN-TO-FAILURE (in/in x 10^{-3})	SECANT MODULUS (10^6 psi)
33F21	2.559	58,100	2.30	25.0
33F22	2.562	64,470	2.29	27.6
33F23	2.547	58,120	2.04	26.3
33F24	2.552	66,220	2.58	25.4
33F25	2.554	36,120	1.42	25.0
33F26	2.528	51,180	1.95	24.8
33F27	2.539	61,440	2.58	23.8
33F28	2.552	54,400	2.20	24.8
33F29	2.545	60,770	2.33	26.1
33F30	2.525	60,480	2.34	26.2
Mean		57,140	2.20	25.5
Std.Dev.		8,600	.34	1.1
Max.		66,220	2.58	27.6
Min.		36,120	1.42	23.8

AVERAGE SURFACE FINISH = 4.3 µin. RMS
AVERAGE BULK DENSITY = 2.55 gm/cc
AVERAGE THEO. DENSITY = 79.6%
AVERAGE TOTAL POROSITY = 20.4%
AVERAGE OPEN POROSITY (meas) = 9.8%
AVERAGE CLOSED POROSITY (by difference) = 10.6%

Table B-30

FLEXURAL TEST RESULTS: NC-350(1), 1500°C

SAMPLE	BULK DENSITY gm/cc	STRENGTH (psi)	STRAIN-TO-FAILURE (in/in x 10^{-3})	SECANT MODULUS (10^6 psi)
31F29	2.478	34,780	1.85	18.9
31F30	2.515	44,720	1.94	23.6
31F31	2.492	50,000	2.55	21.4
31F32	2.498	47,480	2.16	21.8
31F33	2.545	43,000	----	----
31F34	2.528	49,525	2.19	22.1
31F35	2.559	51,010	1.91	26.7
31F36	2.506	47,930	1.97	24.3
31F37	2.532	54,010	1.92	28.5
31F38	2.514	39,090	1.50	26.2
Mean		46,150	2.00	23.7
Std.Dev.		5,850	.29	3.0
Max.		54,010	2.55	28.5
Min.		34,780	1.50	18.9

AVERAGE SURFACE FINISH = 5.2 µin. RMS
AVERAGE BULK DENSITY = 2.52 gm/cc
AVERAGE THEO. DENSITY = 78.6%
AVERAGE TOTAL POROSITY = 21.4%
AVERAGE OPEN POROSITY (meas) = 14.1%
AVERAGE CLOSED POROSITY (by difference) = 7.3%

Table B-31

FLEXURAL TEST RESULTS: NC-350(2), 1500°C

SAMPLE	BULK DENSITY gm/cc	STRENGTH (psi)	STRAIN-TO-FAILURE (in/in x 10^{-3})	SECANT MODULUS (10^6 psi)
32F31	2.347	39,460	2.06	19.8
32F32	2.488	48,440	2.30	21.3
32F33	2.358	37,460	2.26	16.9
32F34	2.407	47,780	2.50	19.1
32F35	2.501	55,430	2.49	22.1
32F36	2.465	54,840	2.32	23.8
32F37	2.360	36,790	1.89	19.8
32F38	2.403	56,850	2.65	21.2
32F39	2.386	48,080	2.44	19.3
32F40	2.378	29,150	1.39	22.1
Mean		45,430	2.23	20.5
Std.Dev.		9,130	.37	2.0
Max.		56,850	2.65	23.8
Min.		29,150	1.39	16.9

AVERAGE SURFACE FINISH = 6.3 µin. RMS
AVERAGE BULK DENSITY = 2.41 gm/cc
AVERAGE THEO. DENSITY = 75.3%
AVERAGE TOTAL POROSITY = 24.7%
AVERAGE OPEN POROSITY (meas) = 18.3%
AVERAGE CLOSED POROSITY (by difference) = 6.4%

Table B-32

FLEXURAL TEST RESULTS: NC-350(3), 1500°C

SAMPLE	BULK DENSITY gm/cc	STRENGTH (psi)	STRAIN-TO-FAILURE (in/in x 10^{-3})	SECANT MODULUS (10^6 psi)
33F31	2.566	55,430	1.90	26.8
33F32	2.550	52,840	1.94	27.8
33F33	2.506	55,170	1.98	28.1
33F34	2.466	45,200	1.91	23.7
33F35	2.560	57,730	2.13	27.4
33F36	2.522	55,170	2.07	26.1
33F37	2.522	47,490	1.67	32.7
33F38	2.548	56,180	1.60	34.9
33F39	2.534	53,500	1.83	29.5
33F40	2.535	51,840	1.71	31.3
Mean		53,060	1.88	28.8
Std.Dev.		3,950	.17	3.3
Max.		57,730	2.13	34.9
Min.		45,200	1.60	23.7

AVERAGE SURFACE FINISH = 4.7 µin. RMS
AVERAGE BULK DENSITY = 2.53 gm/cc
AVERAGE THEO. DENSITY = 79.1%
AVERAGE TOTAL POROSITY = 20.9%
AVERAGE OPEN POROSITY (meas) = 10.8%
AVERAGE CLOSED POROSITY (by difference) = 10.1%

Table B-33

FLEXURAL TEST RESULTS: KBI(1), 25°C

SAMPLE	BULK DENSITY gm/cc	STRENGTH (psi)	STRAIN-TO-FAILURE (in/in x 10^{-3})	ELASTIC MODULUS (10^6 psi)
K1F31	2.700	28,130	1.02	27.2
K1F32	2.708	28,830	1.02	28.5
K1F33	2.560	27,760	1.23	22.6
K1F34	2.480	18,060	1.08	16.8
K1F35	2.713	29,190	1.08	26.5
K1F36	2.265	16,490	1.12	14.5
K1F37	2.717	29,390	1.12	26.6
K1F38	2.355	21,330	1.15	18.7
K1F39	2.308	19,210	1.10	17.4
K1F40	2.287	14,290	.88	16.1
Mean		23,270	1.08	21.5
Std.Dev.		5,970	.09	5.4
Max.		29,390	1.23	28.5
Min.		14,290	.88	14.5

AVERAGE SURFACE FINISH = 58 μin RMS
AVERAGE BULK DENSITY = 2.51 gm/cc
AVERAGE THEO. DENSITY = 78.4%
AVERAGE TOTAL POROSITY = 21.6%
AVERAGE OPEN POROSITY (meas) = 19.8%
AVERAGE CLOSED POROSITY (by difference) = 1.8%

TABLE B-34

FLEXURAL TEST RESULTS: KBI(2), 25°C

SAMPLE	BULK DENSITY gm/cc	STRENGTH (psi)	STRAIN-TO-FAILURE (in/in x 10^{-3})	ELASTIC MODULUS (10^6 psi)
K2F21	2.329	15,550	.96	16.5
K2F22	2.669	27,570	.96	28.8
K2F23	2.365	20,220	1.10	18.5
K2F24	2.351	19,550	1.10	18.0
K2F25	2.351	20,040	1.06	18.8
K2F26	2.357	19,520	1.05	18.1
K2F27	2.689	30,530	1.06	28.7
K2F28	2.368	19,840	1.10	18.2
K2F29	2.718	29,200	1.00	28.9
K2F30	2.342	16,000	.95	17.0
Mean		21,800	1.03	21.1
Std. Dev.		5,340	.06	5.3
Max.		30,530	1.10	28.9
Min.		15,550	.95	16.5

AVERAGE SURFACE FINISH = 34 µin RMS
AVERAGE BULK DENSITY = 2.45 gm/cc
AVERAGE THEO. DENSITY = 76.7%
AVERAGE TOTAL POROSITY = 23.3%
AVERAGE OPEN POROSITY (meas) = 21.1%
AVERAGE CLOSED POROSITY (by difference) = 2.2%

Table B-35

FLEXURAL TEST RESULTS: KBI(3), 25°C

SAMPLE	BULK DENSITY gm/cc	STRENGTH (psi)	STRAIN-TO-FAILURE (in/in x 10^{-3})	ELASTIC MODULUS (10^6 psi)
K3F21	2.339	24,770	1.23	20.0
K3F22	2.371	17,470	.85	20.6
K3F23	2.371	11,320	.55	20.7
K3F24	2.366	13.080	.62	21.2
K3F25	2.336	21,360	1.06	19.9
K3F26	2.384	19,590	.96	20.7
K3F27	2.320	18,930	.98	19.1
K3F28	2.335	11,960	.63	19.3
K3F29	2.384	23,250	1.09	21.3
K3F30	2.284	19,160	1.10	17.5
Mean		18,080	.91	20.0
Std.Dev.		4,650	.23	1.2
Max.		24,770	1.23	21.3
Min.		11,320	.55	17.5

AVERAGE SURFACE FINISH = 22 µin. RMS
AVERAGE BULK DENSITY = 2.35 gm/cc
AVERAGE THEO. DENSITY = 73.4%
AVERAGE TOTAL POROSITY = 26.6%
AVERAGE OPEN POROSITY (meas) = 23.9%
AVERAGE CLOSED POROSITY (by difference) = 2.7%

Table B-36

FLEXURAL TEST RESULTS: KBI(1), 1200°C

SAMPLE	BULK DENSITY gm/cc	STRENGTH (psi)	STRAIN-TO-FAILURE (in/in x 10^{-3})	ELASTIC MODULUS (10^6 psi)
K1F11	2.289	20,320	.68	30.6
K1F12	2.245	17,500	.71	25.4
K1F13	2.290	20,630	.91	21.4
K1F14	2.299	17,930	.75	23.6
K1F15	2.704	23,510	1.01	25.5
K1F16	2.269	18,770	.87	22.0
K1F17	2.278	20,190	1.10	18.4
K1F18	2.279	20,100	1.09	18.3
K1F19	2.508	26,470	1.22	21.8
K1F20	2.289	19,560	.79	25.0
Mean		20,500	.91	23.2
Std.Dev.		2,680	.18	3.7
Max.		26,470	1.22	30.6
Min.		17,500	.68	18.3

AVERAGE SURFACE FINISH = 56 µin. RMS
AVERAGE BULK DENSITY = 2.35 gm/cc
AVERAGE THEO. DENSITY = 73.4%
AVERAGE TOTAL POROSITY = 26.6%
AVERAGE OPEN POROSITY (meas) = 25.4%
AVERAGE CLOSED POROSITY (by difference) = 1.2%

Table B-37

FLEXURAL TEST RESULTS: KBI(2), 1200°C

SAMPLE	BULK DENSITY gm/cc	STRENGTH (psi)	STRAIN-TO-FAILURE (in/in x 10^{-3})	ELASTIC MODULUS (10^6 psi)
K2F11	2.548	31,620	1.36	22.4
K2F12	2.356	16,260	.53	30.3
K2F13	2.341	21,660	.73	29.1
K2F14	2.351	23,970	.69	34.5
K2F15	2.348	20,700	.59	35.2
K2F16	2.565	32,710	.93	34.5
K2F17	2.376	22,050	.79	27.1
K2F18	2.687	27,190	.71	39.5
K2F19	2.351	9,480	.22	42.6
K2F20	2.354	24,540	.82	29.5
Mean		23,020	.74	32.5
Std.Dev.		6,880	.29	6.0
Max.		32,710	1.36	42.8
Min.		9,480	.22	22.4

AVERAGE SURFACE FINISH = 35 µin. RMS
AVERAGE BULK DENSITY = 2.43 gm/cc
AVERAGE THEO. DENSITY = 75.9%
AVERAGE TOTAL POROSITY = 24.1%
AVERAGE OPEN POROSITY (meas) = 22.5%
AVERAGE CLOSED POROSITY (by difference) = 1.6%

TABLE B-38

FLEXURAL TEST RESULTS: KBI(3), 1200°C

SAMPLE	BULK DENSITY gm/cc	STRENGTH (psi)	STRAIN-TO-FAILURE (in/in x 10^{-3})	ELASTIC MODULUS (10^6 psi)
K3F11	2.377	26,480	.75	35.2
K3F12	2.321	24,170	.87	27.7
K3F13	2.383	25,030	.94	32.7
K3F14	2.362	21,510	.82	27.7
K3F15	2.341	23,560	1.01	23.1
K3F16	2.384	27,220	.91	30.1
K3F17	2.326	16,520	.84	20.3
K3F18	2.348	19,970	.72	27.6
K3F19	2.375	22,680	.94	22.4
K3F20	2.356	13,250	.57	22.6
Mean		22,040	.84	26.9
Std. Dev.		4,410	.13	4.9
Max.		27,220	1.01	35.2
Min.		13,250	.57	20.3

AVERAGE SURFACE FINISH = 22 µin RMS
AVERAGE BULK DENSITY = 2.36 gm/cc
AVERAGE THEO. DENSITY = 73.7%
AVERAGE TOTAL POROSITY = 26.3%
AVERAGE OPEN POROSITY (meas) = 23.6%
AVERAGE CLOSED POROSITY (by difference) = 2.7%

TABLE B-39

FLEXURAL TEST RESULTS: KBI(1), 1350°C

SAMPLE	BULK DENSITY gm/cc	STRENGTH (psi)	STRAIN-TO-FAILURE (in/in x 10^{-3})	SECANT MODULUS (10^6 psi)
K1F1	2.673	31,690	1.52	21.1
K1F2	2.307	15,170	.55	27.5
K1F3	2.549	29,910	1.25	23.7
K1F4	2.691	32,510	.72	45.4
K1F5	2.518	27,270	1.12	24.8
K1F6	2.679	34,050	.80	43.2
K1F7	2.232	22,660	.89	24.6
K1F8	2.314	22,480	.95	22.7
K1F9	2.545	20,570	.92	22.1
K1F10	2.673	37,160	1.00	36.9
Mean		27,350	.97	29.2
Std. Dev.		6,940	.28	9.1
Max.		37,160	1.52	45.4
Min.		15,170	.55	21.1

AVERAGE SURFACE FINISH = 47 μin RMS
AVERAGE BULK DENSITY = 2.52 gm/cc
AVERAGE THEO. DENSITY = 78.7%
AVERAGE TOTAL POROSITY = 21.3%
AVERAGE OPEN POROSITY (meas) = 18.5%
AVERAGE CLOSED POROSITY (by difference) = 2.8%

TABLE B-40

FLEXURAL TEST RESULTS: KBI(2), 1350°C

SAMPLE	BULK DENSITY gm/cc	STRENGTH (psi)	STRAIN-TO-FAILURE (in/in x 10^{-3})	SECANT MODULUS (10^6 psi)
K2F1	2.670	29,110	.79	36.3
K2F2	2.354	18,640	.44	42.8
K2F3	2.565	34,240	.75	44.8
K2F4	2.669	32,880	.80	40.2
K2F5	2.718	32,770	.75	45.1
K2F6	2.279	13,890	.68	20.4
K2F7	2.343	14,610	.86	16.7
K2F8	2.345	20,610	1.27	16.5
K2F9	2.341	30,380	1.77	17.1
K2F10	2.335	13,210	.68	19.4
Mean		24,030	.88	30.0
Std. Dev.		8,660	.38	12.8
Max.		34,240	1.77	45.1
Min.		13,210	.44	16.5

AVERAGE SURFACE FINISH = 34 µin RMS
AVERAGE BULK DENSITY = 2.46 gm/cc
AVERAGE THEO. DENSITY = 76.9%
AVERAGE TOTAL POROSITY = 23.1%
AVERAGE OPEN POROSITY (meas) = 20.3%
AVERAGE CLOSED POROSITY (by difference) = 2.8%

TABLE B-41

FLEXURAL TEST RESULTS: KBI(3), 1350°C

SAMPLE	BULK DENSITY gm/cc	STRENGTH (psi)	STRAIN-TO-FAILURE (in/in x 10^{-3})	SECANT MODULUS (10^6 psi)
K3F1	2.380	19,530	.43	50.7
K3F2	2.378	10,260	.34	29.3
K3F3	2.321	25,750	.95	26.5
K3F4	2.375	27,970	.77	36.0
K3F5	2.347	21,960	.73	30.0
K3F6	2.304	19,570	.97	20.1
K3F7	2.315	15,100	.63	23.3
K3F8	2.374	17,940	.56	31.8
K3F9	2.357	23,360	.77	30.7
K3F10	2.343	20,480	.74	22.6
Mean		20,190	.69	30.1
Std. Dev.		5,110	.20	8.7
Max.		27,970	.97	50.7
Min.		10,260	.34	20.12

AVERAGE SURFACE FINISH = 24 μin RMS
AVERAGE BULK DENSITY = 2.35 gm/cc
AVERAGE THEO. DENSITY = 73.4%
AVERAGE TOTAL POROSITY = 26.6%
AVERAGE OPEN POROSITY (meas) = 23.9%
AVERAGE CLOSED POROSITY (by difference) = 2.7%

TABLE B-42

FLEXURAL TEST RESULTS: KBI(1), 1500°C

SAMPLE	BULK DENSITY gm/cc	STRENGTH (psi)	STRAIN-TO-FAILURE (in/in x 10^{-3})	SECANT MODULUS (10^6 psi)
K1F21	2.237	18,170	.86	20.9
K1F22	2.313	20,570	1.32	15.7
K1F23	2.696	28,100*	.93	24.0
K1F24	2.743	32,210	.91	35.4
K1F25	2.539	34,290	1.66	22.1
K1F26	2.275	19,360	.86	22.6
K1F27	2.262	21,530	1.05	23.9
K1F28	2.273	14,140	.53	26.4
K1F29	2.724	29,300	--**	--**
Mean		24,190	1.02	23.9
Std. Dev.		6,970	.34	5.6
Max.		34,290	1.66	35.4
Min.		14,140	.53	15.7

AVERAGE SURFACE FINISH = 64 μin RMS
AVERAGE BULK DENSITY = 2.45 gm/cc
AVERAGE THEO. DENSITY = 76.6%
AVERAGE TOTAL POROSITY = 23.4%
AVERAGE OPEN POROSITY (meas) = 22.1%
AVERAGE CLOSED POROSITY (by difference) = 1.3%

* FIXTURE FAILED, sample did not fracture
** DEFLECTOMETER JAM

TABLE B-43

FLEXURAL TEST RESULTS: KBI(2), 1500°C

SAMPLE	BULK DENSITY gm/cc	STRENGTH (psi)	STRAIN-TO-FAILURE (in/in x 10^{-3})	SECANT MODULUS (10^6 psi)
K2F31	2.340	17,150	.73	27.2
K2F32	2.348	14,520	.81	20.3
K2F33	2.367	18,710	.88	21.5
K2F35	2.653	20,930	.54	38.2
K2F36	2.356	15,520	.99	15.8
K2F37	2.369	19,750	.88	22.7
K2F38	2.355	8,630	.64	15.6
Mean		16,460	.78	23.0
Std. Dev.		4,130	.16	7.8
Max.		20,930	.99	38.2
Min.		8,630	.54	15.6

AVERAGE SURFACE FINISH = 41 µin RMS
AVERAGE BULK DENSITY = 2.40 gm/cc
AVERAGE THEO. DENSITY = 74.9%
AVERAGE TOTAL POROSITY = 25.1%
AVERAGE OPEN POROSITY (meas) = 22.3%
AVERAGE CLOSED POROSITY (by difference) = 2.8%

TABLE B-44

FLEXURAL TEST RESULTS: KBI(3), 1500°C

SAMPLE	BULK DENSITY gm/cc	STRENGTH (psi)	STRAIN-TO-FAILURE (in/in x 10^{-3})	SECANT MODULUS (10^6 psi)
K3F31	2.301	21,140	1.18	19.7
K3F32	2.331	12,380	.68	18.3
K3F33	2.347	21,100	.97	21.7
K3F34	2.320	20,410	.88	29.7
Mean		18,760	.93	22.4
Std. Dev.		4,260	.21	5.1
Max.		21,140	1.18	29.7
Min.		12,380	.68	18.3

AVERAGE SURFACE FINISH = 19 µin RMS
AVERAGE BULK DENSITY = 2.33 gm/cc
AVERAGE THEO. DENSITY = 72.7%
AVERAGE TOTAL POROSITY = 27.3%
AVERAGE OPEN POROSITY (meas) = 24.9%
AVERAGE CLOSED POROSITY (by difference) = 2.4%

* Remainder of batch sent to AFML for controlled surface flaw fracture mechanics measurements.

Table B-45

FLEXURAL TEST RESULTS

SUPPLIER: KYOCERA
MATERIAL: SN-3, HPSi_3N_4
TEMPERATURE: 25°C
ATMOSPHERE: Air

Sample	Bulk Density (gm/cc)	Strength (psi)	Strain-To-Failure (in/in x 10^{-3})	Secant Modulus (10^6 psi)
A1F1	3.072	68,280	1.90	35.8
A1F2	3.071	79,350	2.20	35.7
A1F3	3.077	71,450	1.92	37.1
A1F4	3.072	64,660	1.75	36.9
A1F5	3.072	79,000	2.10	37.1
A1F6	3.070	76,560	2.15	36.6
A1F7	3.073	84,700	2.22	37.1
Mean		74,860	2.03	36.6
Std. Dev.		7,020	.18	.6
Max.		84,700	2.22	37.1
Min.		64,660	1.75	35.7

Avg. Surf. Finish = 8 µin RMS
Avg. Bulk Density = 3.07 gm/cc
Avg. Theo. Density = 95.9%
Avg. Total Porosity = 4.1%
Avg. Open Porosity (meas) = .1%
Avg. Closed Porosity (by Difference) = 4%

Table B-46

FLEXURAL TEST RESULTS

SUPPLIER: KYOCERA
MATERIAL: SN-3 HP Si_3N_4
TEMPERATURE: 750°C
ATMOSPHERE: Air

Sample	Bulk Density (gm/cc)	Strength (psi)	Strain-To-Failure (in/in x 10^{-3})	Secant Modulus (10^6 psi)
A1F14	3.056	91,090	2.37	37.6
A1F15	3.058	85,540	2.32	37.3
A1F16	3.055	76,280	2.21	34.5
A1F17	3.039	63,800	1.86	34.5
A1F18	3.060	83,200	2.32	36.1
Mean		79,980	2.22	36.0
Std. Dev.		10,490	.21	1.5
Max.		91,090	2.37	37.6
Min.		63,800	1.86	34.5

Avg. Surf. Finish = 7 μin RMS
Avg. Bulk Density = 3.05 gm/cc
Avg. Theo. Density = 95.4%
Avg. Total Porosity = 4.6%
Avg. Open Porosity (meas) = .04%
Avg. Closed Porosity (by Difference) = 4.56%

Table B-47

FLEXURAL TEST RESULTS

SUPPLIER: KYOCERA
MATERIAL: SN-3, HP Si_3N_4
TEMPERATURE: 1000°C
ATMOSPHERE: Air

Sample	Bulk Density (gm/cc)	Strength (psi)	Strain-To-Failure (in/in x 10^{-3})	Secant Modulus (10^6 psi)
A1F9	3.073	34,980	2.18	17.3
A1F10	3.071	38,690	2.22	18.8
A1F11	3.044	35,320	2.32	17.0
A1F12	3.075	35,020	2.08	18.7
A1F13	3.055	38,300	2.33	17.8
Mean		36,460	2.23	17.9
Std. Dev.		1,860	.10	.80
Max.		38,690	2.33	18.8
Min.		34,980	2.08	17.0

Avg. Surf. Finish = 8 µin RMS
Avg. Bulk Density = 3.06 gm/cc
Avg. Theo. Density = 95.7%
Avg. Total Porosity = 4.3%
Avg. Open Porosity (meas) = 0.1%
Avg. Closed Porosity (by Difference)= 4.2%

Table B-48

FLEXURAL TEST RESULTS

SUPPLIER: KYOCERA
MATERIAL: SN-3, HPSI $_3N_4$
TEMPERATURE: 1125°C
ATMOSPHERE: Air

Sample	Bulk Density (gm/cc)	Strength (psi)	Strain-To-Failure (in/in x 10^{-3})	Secant Modulus (10^6 psi)
A1F21	3.059	22,230	2.05	14.1
A1F22	3.059	22,490	2.32	13.2
Mean	3.059	22,360	2.19	13.7
Std. Dev.				
Max.				
Min.				

Avg. Surf. Finish = 5 µin RMS
Avg. Bulk Density = 3.06 gm/cc
Avg. Theo. Density = 95.6%
Avg. Total Porosity = 4.4%
Avg. Open Porosity (meas) = .1%
Avg. Closed Porosity (by Difference) = 4.3%

Table B-49

FLEXURAL TEST RESULTS

SUPPLIER: KYOCERA

MATERIAL: SN-3, $HPSi_3N_4$

TEMPERATURE: $1250^{o}C$

ATMOSPHERE: Air

Sample	Bulk Density (gm/cc)	Strength (psi)	Strain-To-Failure (in/in x 10^{-3})	Secant Modulus (10^6 psi)
A1F8	3.074	8,700	3.92	8.9
A1F19	3.054	9,300	5.22	10.0
A1F20	3.058	6,390	2.94	8.6
Mean		8,130	4.0	9.2
Std. Dev.				
Max.				
Min.				

Avg. Surf. Finish = 9 μin RMS

Avg. Bulk Density = 3.06 gm/cc

Avg. Theo. Density = 95.7%

Avg. Total Porosity= 4.3%

Avg. Open Porosity (meas) = .1%

Avg. Closed Porosity (by Difference) = 4.2%

Table B-50

FLEXURAL TEST RESULTS

SUPPLIER: KYOCERA
MATERIAL: SN-201, Sintered Si_3N_4
TEMPERATURE: 25°C
ATMOSPHERE: Air

Sample	Bulk Density (gm/cc)	Strength (psi)	Strain-To-Failure (in/in x 10^{-3})	Secant Modulus (10^6 psi)
B1F1	3.002	46,160	1.35	34.3
B1F2	3.007	36,900	1.11	34.9
B1F3	3.005	50,120	1.43	33.3
B1F4	3.001	51,350	1.43	34.4
B1F5	3.005	53.670	1.46	35.4
B1F6	3.004	52.670	1.56	32.7
B1F7	3.012	56,410	1.60	35.7
Mean		49,610	1.42	34.4
Std. Dev.		6,440	.16	1.1
Max.		56,410	1.60	35.7
Min.		36,900	1.11	32.7

Avg. Surf. Finish = 16 µin RMS
Avg. Bulk Density = 3.01 gm/cc
Avg. Theo. Density = 93.9%
Avg. Total Porosity = 6.1%
Avg. Open Porosity (meas) = .1%
Avg. Closed Porosity (by Difference) = 6%

Table B-51

FLEXURAL TEST RESULTS

SUPPLIER: KYOCERA
MATERIAL: SN-201, Sintered Si_3N_4
TEMPERATURE: 750°C
ATMOSPHERE: Air

Sample	Bulk Density (gm/cc)	Strength (psi)	Strain-To-Failure (in/in x 10^{-3})	Secant Modulus (10^6 psi)
B1F14	2.999	53,530	1.53	35.4
B1F15	2.999	56,630	1.49	36.9
B1F16	2.999	61,430	1.72	36.0
B1F17	3.001	63,000	1.76	36.1
B1F18	3.000	52,340	1.56	33.3
Mean		57,390	1.61	35.5
Std. Dev.		4,710	.12	1.4
Max.		63,000	1.76	36.9
Min.		52,340	1.49	33.3

Avg. Surf. Finish = 15 µin RMS
Avg. Bulk Density = 3.00 gm/cc
Avg. Theo. Density = 93.7%
Avg. Total Porosity = 6.3%
Avg. Open Porosity (meas) = 0.1%
Avg. Closed Porosity (by Difference) = 6.2%

Table B-52

FLEXURAL TEST RESULTS

SUPPLIER: KYOCERA
MATERIAL: SN-201, Sintered Si_3N_4
TEMPERATURE: 1000°C
ATMOSPHERE: Air

Sample	Bulk Density (gm/cc)	Strength (psi)	Strain-To-Failure (in/in x 10^{-3})	Secant Modulus (10^6 psi)
B1F9	3.004	32,080	1.34	24.4
B1F10	2.963	35,040	1.41	25.2
B1F11	3.011	37,140	1.57	23.5
B1F12	2.996	37,100	1.45	25.9
B1F13	2.996	35,560	1.50	24.3
Mean		35,380	1.45	24.7
Std. Dev.		2,070	.09	.9
Max.		37,140	1.57	25.9
Min.		32,080	1.34	23.5

Avg. Surf. Finish = 16 µin RMS
Avg. Bulk Density = 2.99 gm/cc
Avg. Theo. Density = 93.6%
Avg. Total Porosity = 6.4%
Avg. Open Porosity (meas) = 0.3%
Avg. Closed Porosity (by Difference) = 6.1%

Table B-53

FLEXURAL TEST RESULTS

SUPPLIER: KYOCERA

MATERIAL: SN-201, Sintered Si_3N_4

TEMPERATURE: 1125°C

ATMOSPHERE: Air

Sample	Bulk Density (gm/cc)	Strength (psi)	Strain-To-Failure (in/in x 10^{-3})	Secant Modulus (10^6 psi)
B1F20	2.996	30,900	1.89	21.7
B1F21	2.986	30,670	1.81	23.1
B1F22	2.989	30,700	1.64	23.8
Mean		30,760	1.78	22.9
Std. Dev.				
Max.				
Min.				

Avg. Surf. Finish = 15 µin RMS

Avg. Bulk Density = 2.99 gm/cc

Avg. Theo. Density = 93.4%

Avg. Total Porosity = 6.6%

Avg. Open Porosity (meas) = .3%

Avg. Closed Porosity (by Difference) = 6.3%

Table B-54

FLEXURAL TEST RESULTS

SUPPLIER: KYOCERA
MATERIAL: SN-201, Sintered Si_3N_4
TEMPERATURE: 1250°C
ATMOSPHERE: Air

Sample	Bulk Density (gm/cc)	Strength (psi)	Strain-To-Failure (in/in x 10^{-3})	Secant Modulus (10^6 psi)
B1F8	3.015	10,270	8.05	14.0
B1F19	2.991	11,800	3.85	22.8
Mean		11,040	6.0	18.4
Std. Dev.				
Max.				
Min.				

Avg. Surf. Finish = 13 µin RMS
Avg. Bulk Density = 3.00 gm/cc
Avg. Theo. Density = 93.8%
Avg. Total Porosity = 6.2%
Avg. Open Porosity (meas) = 0.1%
Avg. Closed Porosity (by Difference) = 6.1%

Table B-55

FLEXURAL TEST RESULTS

SUPPLIER: KYOCERA
MATERIAL: SN-205, Sintered Si_3N_4
TEMPERATURE: 25°C
ATMOSPHERE: Air

Sample	Bulk Density (gm/cc)	Strength (psi)	Strain-To-Failure (in/in x 10^{-3})	Secant Modulus (10^6 psi)
21F1	2.870	37,000	1.31	27.9
21F2	2.805	41,670	1.55	27.4
21F3	2.787	36,340	1.34	27.5
21F4	2.804	39,920	1.53	27.5
21F5	2.800	33,340	1.32	26.3
21F6	2.812	40,210	1.38	29.5
21F7	2.729	35,900	1.10	28.9
Mean		37,770	1.36	27.9
Std. Dev.		2,930	.15	1.1
Max.		41,670	1.55	29.5
Min.		33,340	1.10	36.3

Avg. Surf. Finish = 20 μ in RMS
Avg. Bulk Density = 2.80 gm/cc
Avg. Theo. Density = 87.5%
Avg. Total Porosity = 12.5%
Avg. Open Porosity (meas) = 6.7%
Avg. Closed Porosity (by Difference) = 5.8%

Table B-56

FLEXURAL TEST RESULTS

SUPPLIER: KYOCERA

MATERIAL: SN-205, SINTERED Si_3N_4

TEMPERATURE: 750°C

ATMOSPHERE: Air

Sample	Bulk Density (gm/cc)	Strength (psi)	Strain-To-Failure (in/in x 10^{-3})	Secant Modulus (10^6 psi)
21F14	2.801	34500	1.45	26.5
21F15	2.808	44600	1.54	28.6
21F16	2.814	42940	1.49	29.0
21F17	2.815	40670	1.47	27.8
21F18	2.805	38120	1.51	25.0
Mean		40170	1.49	27.4
Std. Dev.		4000	.04	1.6
Max.		44600	1.54	29.0
Min.		34500	1.45	25.0

Avg. Surf. Finish = 17 µin RMS

Avg. Bulk Density = 2.81 gm/cc

Avg. Theo Density = 87.8%

Avg. Total Porosity = 12.2%

Avg. Open Porosity (meas) = 6.8%

Avg. Closed Porosity (by Difference) = 5.4%

Table B-57

FLEXURAL TEST RESULTS

SUPPLIER: KYOCERA
MATERIAL: SN-205, Sintered Si_3N_4
TEMPERATURE: 1000°C
ATMOSPHERE: Air

Sample	Bulk Density (gm/cc)	Strength (psi)	Strain-to-Failure (in/in x 10^{-3})	Secant Modulus (10^6 psi)
21F9	2.815	32,040	1.87	17.9
21F10	2.786	20,160	1.65	13.3
21F11	2.805	26,840	1.63	17.5
21F12	2.820	27,840	1.78	16.3
21F13	2.842	26,170	2.14	14.7
Mean		26,610	1.81	16.0
Std. Dev.		4,270	.21	1.9
Max.		32,040	2.14	17.9
Min.		20,160	1.63	13.3

Avg. Surf. Finish = 17 μin RMS
Avg. Bulk Density = 2.81 gm/cc
Avg. Theo. Density = 87.9%
Avg. Total Porosity = 12.1%
Avg. Open Porosity (meas) = 6.7%
Avg. Closed Porosity (by Difference) = 5.4%

Table B-58

FLEXURAL TEST RESULTS

SUPPLIER: KYOCERA
MATERIAL: SN-205, Sintered Si_3N_4
TEMPERATURE: 1125°C
ATMOSPHERE: Air

Sample	Bulk Density (gm/cc)	Strength (psi)	Strain-to-Failure (in/in x 10^{-3})	Secant Modulus (10^6 psi)
21F20	2.824	17880	1.51	15.1
21F21	2.799	15650	1.76	12.1
21F22	2.811	17950	1.92	13.1
Mean		17160	1.73	13.4
Std. Dev.				
Max.				
Min.				

Avg. Surf. Finish = 28 µin RMS
Avg. Bulk Density = 2.81 gm/cc
Avg. Theo. Density = 87.9%
Avg. Total Porosity = 12.1%
Avg. Open Porosity (meas) = 6.8%
Avg. Closed Porosity (by Difference) = 5.3%

Table B-59

FLEXURAL TEST RESULTS

SUPPLIER: KYOCERA
MATERIAL: SN-205 Sintered Si_3N_4
TEMPERATURE: 1250°C
ATMOSPHERE: Air

Sample	Bulk Density (gm/cc)	Strength (psi)	Strain-To-Failure (in/in x 10^{-3})	Secant Modulus (10^6 psi)
21F8	2.796	3690	6.05	1.7
21F19	2.803	2990	5.66	2.3
Mean		3340	5.86	2.0
Std. Dev.				
Max.				
Min.				

Avg. Surf. Finish = 16 µin RMS
Avg. Bulk Density = 2.80 gm/cc
Avg. Theo. Density = 87.5%
Avg. Total Porosity = 12.5%
Avg. Open Porosity (meas) = 6.8%
Avg. Closed Porosity (by difference) = 5.7%

TABLE B-60

FLEXURAL TEST RESULTS

SUPPLIER: CARBORUNDUM
MATERIAL: SINTERED α-SiC
TEMPERATURE: 25°C
ATMOSPHERE: Air

Sample	Bulk Density gm/cc	Strength (psi)	Strain-To-Failure (in/in x 10^{-3})	Secant Modulus (10^6 psi)
81F1	3.136	53,170	.80	60.5
81F2	3.147	44,750	.90	52.1
81F3	3.133	37,710	.65	57.9
81F4	3.184	50,700	.85	59.7
81F5	3.142	38,730	.68	58.2
81F6	3.171	40,210	.68	61.4
81F7	3.198	44,310	.75	57.4
Mean	3.159	44,230	.76	58.2
Std. Dev.		5,930	.10	3.0
Max.		53,170	.90	61.4
Min.		37,710	.65	52.1

Avg. Surf. Finish = 11 μin RMS
Avg. Bulk Density = 3.16 gm/cc
Avg. Theo. Density = 98.7%
Avg. Total Porosity = 1.3%
Avg. Open Porosity (meas) = ~0%
Avg. Closed Porosity (by Difference) = 1.3%

TABLE B-61

FLEXURAL TEST RESULTS

SUPPLIER: CARBORUNDUM
MATERIAL: SINTERED α-SiC
TEMPERATURE: 1000 C
ATMOSPHERE: Air

Sample	Bulk Density gm/cc	Strength (psi)	Strain-To-Failure (in/in x 10^{-3})	Secant Modulus (10^6 psi)
81F15	3.134	62,840	1.03	60.3
81F16	3.196	53,170	.82	63.0
81F17	3.138	58,240	.88	66.2
81F18	3.150	53,920	.81	66.6
81F19	3.143	47,790	.69	69.0
81F20	3.138	60,110	.87	69.5
81F21	3.197	51,830	.71	74.2
Mean	3.157	55,410	.83	67.0
Std. Dev.		5,220	.11	4.5
Max.		62,840	1.03	74.2
Min.		47,790	.69	60.3

Avg. Surf. Finish = 10 μin RMS
Avg. Bulk Density = 3.16 gm/cc
Avg. Theo. Density = 98.7%
Avg. Total Porosity = 1.3%
Avg. Open Porosity (meas) = ~0%
Avg. Closed Porosity (by Difference) = 1.3%

TABLE B-62

FLEXURAL TEST RESULTS

SUPPLIER: CARBORUNDUM
MATERIAL: SINTERED α-SiC
TEMPERATURE: 1250°C
ATMOSPHERE: Air

Sample	Bulk Density gm/cc	Strength (psi)	Strain-To-Failure (in/in x 10^{-3})	Secant Modulus (10^6 psi)
81F8	3.154	49,560	.78	63.6
81F9	3.129	67,820	1.10	60.5
81F10	3.154	64,350	.92	69.9
81F11	3.186	36,010	.50	71.5
81F12	3.157	72,030	1.22	58.7
81F13	3.146	50,280	.80	62.5
81F14	3.147	59,210	1.05	56.1
Mean	3.153	57,040	.91	63,3
Std. Dev.		12,540	.24	5.7
Max.		72,030	1.22	71.5
Min.		36,010	.50	56.1

Avg. Surf. Finish = 6 μin RMS
Avg. Bulk Density = 3.15 gm/cc
Avg. Theo. Density = 98.5%
Avg. Total Porosity = 1.5%
Avg. Open Porosity (meas) = ~o%
Avg. Closed Porosity (by Difference) = 1.5%

Table B-63

FLEXURAL TEST RESULTS

SUPPLIER: GE
MATERIAL: Sintered (β) SiC, boron doped
TEMPERATURE: 25°C
ATMOSPHERE: Air

Sample	Density (gm/cc)	Strength (psi)	Strain-To-Failure (in/in x 10^{-3})	Secant Modulus (10^6 psi)
G1F1	2.993	64,040	1.28	49.5
G1F2	3.044	64,110	1.15	55.8
G1F3	2.999	--	---	51.9
G1F4	3.037	75,840	1.22	54.0
G1F5	3.019	61,350	1.09	56.3
G1F6	3.055	52,340	.92	56.2
G1F7	3.041	64,910	1.15	56.8
Mean		63,770	1.14	54.4
Std. Dev.		3,080	.12	2.8
Max.		75,840	1.28	56.8
Min.		52,340	.92	49.5

Avg. Surf. Finish = 12 μin RMS
Avg. Bulk Density = 3.03 gm/cc
Avg. Theo. Density = 94.6%
Avg. Total Porosity = 5.4%
Avg. Open Porosity (meas) = 0.9%
Avg. Closed Porosity (by Difference) = 4.5%

TABLE B-64

FLEXURAL TEST RESULTS

SUPPLIER: GE

MATERIAL: Sintered (β) SiC, boron-doped

TEMPERATURE: 1000°C

ATMOSPHERE: Air

Sample	Bulk Density (gm/cc)	Strength (psi)	Strain-To-Failure (in/in x 10^{-3})	Secant Modulus (10^6 psi)
G1F8	3.025	79,380	1.34	59.1
G1F9	3.039	94,690	1.44	66.3
G1F10	3.031	83,810	1.29	65.0
G1F11	3.035	78,850	1.16	67.8
G1F12	3.051	71,340	1.15	61.7
G1F13	3.057	48,380	.78	62.2
G1F14	3.040	69,780	1.15	60.4
Mean		75,180	1.19	63.2
Std. Dev.		14,420	.21	3.2
Max.		94,690	1.44	67.8
Min.		48,380	.78	59.1

Avg. Surf. Finish = 11 µin RMS.
Avg. Bulk Density = 3.04 gm/cc
Avg. Theo. Porosity = 95.0%
Avg. Total Porosity = 5%
Avg. Open Porosity (meas) = 0.6%
Avg. Closed Porosity (by Difference) = 4.4%

TABLE B-65

FLEXURAL TEST RESULTS

SUPPLIER: GE

MATERIAL: Sintered (β) SiC, boron-doped

TEMPERATURE: 1250°C

ATMOSPHERE: Air

Sample	Bulk Density (gm/cc)	Strength (psi)	Strain-To-Failure (in/in x 10^{-3})	Secant Modulus (10^6 psi)
G1F15	3.001	55,000	1.01	54.1
G1F16	3.034	73,560	1.34	54.5
G1F17	3.096	85,890	1.57	54.3
G1F18	3.026	77,060	1.39	55.8
G1F19	3.027	82,890	1.35	61.5
G1F20	3.026	59,060	1.02	58.2
G1F21	3.040	57,340	.94	61.3
Mean		70,110	1.23	57.1
Std. Dev.		12,820	.24	3.2
Max.		85,890	1.57	61.5
Min.		55,000	.94	54.1

Avg. Surf. Finish = 11 μin RMS.
Avg. Bulk Density = 3.04 gm/cc
Avg. Theo. Density = 94.9%
Avg. Total Porosity = 5.1%
Avg. Open Porosity (meas) = 1.4%
Avg. Closed Porosity (by Difference) = 3.7%

APPENDIX C

THERMAL SHOCK

APPENDIX C

C.1 Thermal Shock

Fracture of brittle ceramics due to thermally induced stresses or thermal shock has received considerable attention[1,2]. Earlier work[1] focused on the conditions necessary to avoid catastrophic failure initiation. More recent investigations[2] have centered on also avoiding or reducing post-shock damage and understanding failures due to thermal fatigue[3]. A variety of testing methods have been developed for measuring thermal shock but results are often difficult to apply to actual engineering designs. This is because thermal shock is a complex phenomenon that depends on materials characteristics, test method, sample geometry, and environment. Although not always practiced, it is generally recognized that the most meaningful results are obtained by simulating as closely as possible the conditions that will apply to a material or component in actual service.

C.1.1 Thermal Shock Theory

Understanding of thermal shock has improved significantly from the application of fracture mechanics to determine when critical fracture conditions have been reached and how much damage has occurred before propagating cracks are arrested[2,4-6]. Advances in understanding subcritical crack propagation have also been applied to thermally induced stress situations.

Although actual component geometries and thermal environments are often complex, thermal-elastic theory has been used to establish stress distributions in simple shapes for a variety of heat transfer conditions[1*]. These have been used for analysis of thermally initiated fracture. For an unconstrained component subjected to a rapid temperature change, ΔT, the surface stress as a function of time may be represented as in Figure C.1.

*Appendix references found at end of Appendix.

The peak stress developed is[1,5]:

$$\sigma_m^p = \frac{E\ \alpha\ \Delta T}{(1 - \mu)}\ B\ (\beta) \qquad (1)$$

where σ_m^p = peak stress

E = Young's modulus

α = thermal expansion coefficient

μ = Poission's ratio

β = a h/k = Biot's modulus = heat transfer or quench severity parameter.

$B(\beta)$ = function dependent on sample and heat transfer configurations.

a = size factor or heat transfer distance, i.e. radius or half plate thickness, etc.

h = heat transfer coefficient

k = thermal conductivity

As the severity of quench is increased the peak stress magnitude increases and the time to reach this peak decreases, as shown in Figures C.2 and C.3. Initial thinking considered failure to occur when σ_m^p equaled the "breaking stress" of the ceramic and the largest Griffith microcrack became critical. Manson and Smith[7] suggested improved agreement between theory and experiment might be achieved by incorporating the distribution of strengths measured on ceramics using the Weibull modulus. This view emphasized that the most critical flaw might not be at the surface and that volume effects of flaw distribution could also influence thermal shock results. Their data on steatite did not show sufficient variability to clearly establish this view but cognizance of the flaw distribution was retained in latter development.

In a theory[2] which combined considerations of crack initiation and crack propagation, Hasselman assumed a body containing a uniform distribution of N isolated (non interacting stress fields) circular Griffith cracks per unit volume, which propagate radially under uniform thermal stress. The total energy per unit volume is obtained from the sum of elastic plus fracture contributions:

$$W_t = \frac{3(\alpha\ \Delta T)^2 E_o}{2(1-2\mu)} \left[1 + \frac{16(1-\mu^2)\ N\ell^3}{9(1-2\mu)} \right]^{-1} + 2\pi N\ell^2 G \qquad (2)$$

where W_t = total energy per unit volume

E_o = Young's modulus of crack free material

ℓ = crack length

G = strain energy release rate or fracture surface energy

Following the lead of Berry[8], the creation of a crack by thermal shock is considered to lower the effective Young's modulus, which in turn causes the thermal stresses to relax and this reduces the driving force for crack propagation. Therefore a propagating crack is unstable until no more strain energy can be released by further lengthening:

$$\frac{dW_t}{d\ell} = 0 \qquad (3)$$

Using Equation (3) Equation (2) may be rearranged to give the critical temperature difference needed for crack instability as a function of crack length or crack density. This is shown in Figure C.4 as thermal strain vs. crack length. For special cases of short or long cracks simplified expressions for the critical temperature difference, ΔT_c, maybe obtained:

$$\Delta T_c = \left[\frac{\pi G\,(1-2\mu)^2}{2E_o\alpha^2(1-\mu^2)\ell}\right]^{1/2} \cong \left[\frac{G}{E_o\alpha^2\,\ell}\right]^{1/2} \quad \text{Short Crack} \quad (4)$$

$$\Delta T_c = \left[\frac{128\pi G(1-\mu^2)N^2\ell^5}{81\alpha^2E_o}\right]^{1/2}$$

$$\cong \left[\frac{GN^2\ell^5}{\alpha^2E_o}\right]^{1/2} \quad \text{Long Crack} \quad (5)$$

These show the influence of the different materials parameters. For short crack lengths ΔT_c is independent of crack density, N, while for long cracks a direct proportionality to N is found. The $\ell^{5/2}$ dependence is for penny shaped cracks in a solid body; an $\ell^{3/2}$ relation was determined for surface flaws in a flate plate[9].

The minimum in Figure C.4 indicates there is some crack geometry that is least stable to thermally created stresses while for shorter or longer cracks greater values of temperature difference are needed to inititate (further) propagation. The above is based on a static energy balance between released strain energy and the fracture energy of newly created cracks. However, for short cracks the strain energy release rate may exceed the fracture surface energy and the excess is kinetic energy directed to propagating these cracks. In general this occurs when:

$$\frac{d^2Wt}{d\ell^2} \geq 0 \quad (6)$$

This additional energy causes greater crack lengths to form before a static energy balance is restored. This is shown as dashed lines in Figure C.4, where it may be seen that for a given crack density, thermal strain is stabilized at a longer crack length. For short initial cracks the final crack length is:

$$\ell_f = \left[\frac{3(1-2\mu)}{8(1-\mu^2)\ell_o N}\right]^{1/2} \cong (\ell_o N)^{-1/2} \qquad (7)$$

where ℓ_f = final crack length

ℓ_o = initial crack length

This relation is independent of any significant material property except initial crack density and length, i.e., the total flaw structure.

Alternatively, an expression for critical fracture stress, S_t,

$$S_t = \left[\frac{GE_o}{2\ell_o(1-\mu^2)}\right]^{1/2} \qquad (8)$$

may be used in the final crack length expression:

$$\ell_f = \left[\frac{3(1-\mu^2)\ S_t^{\,2}}{4\pi NGE_o}\right]^{1/2} \qquad (9)$$

This implies the extent of crack propagation or degree of thermal shock damage is proportional to the elastic strain energy in the body at fracture, $S_t^{\,2}/E$, and inversely related to the surface fracture energy G. This idea had been presented previously[4]. A higher strength material would show greater crack propagation during thermal shock. Since strength is inversely related to flaw size, the after shock strength of this material would be even lower than another material which exhibited less crack propagation because it has a lesser original strength. This idea led to the definition of a thermal shock damage resistance parameter, R'''', which is inversely proportional to after shock crack area^2.

$$R'''' = \left[\frac{S_t^{\,2}(1-\mu)}{GE_o}\right] \cong \left[\pi\ell_f^{\,2}\right]^{-1} = A^{-1} \qquad (10)$$

A "thermal stress crack stability" parameter was also suggested[2] to select materials that minimize the probability of fracture and subsequent damage should cracks be propagated as a result of thermal stress.

$$R_{st} = \left[\frac{G}{\alpha^2 E_o}\right]^{1/2} \qquad \text{severe quench} \qquad (11)$$

$$R'_{st} = \left[\frac{k^2 G}{\alpha^2 E_o}\right]^{1/2} \qquad \text{mild quench} \qquad (12)$$

The ideas developed from this theory are summarized in a Hasselman thermal shock plot, where (residual) strength is considered as a function of temperature difference, Figure C.5. Recommendations[9] to improve resistance to thermal shock damage included increasing grain size or porosity to increase effective crack length, increase crack density by using composites of materials with mismatched thermal expansion coefficients, deliberate flaw generation by abrasion or cutting, and increasing surface fracture energy by incorporation of plastic or viscous phases into the material or increasing grain size through overfiring and grain growth. Creating a compressive surface layer, especially for materials with low thermal expansion coefficients, also improves failure initiation resistance[10,11]. Thus, where crack initiation could not be avoided, the prospect was offered that materials could be selected or created with strengths that showed less change during thermal cycling and whose strength level was greater than that of a material that had undergone catastrophic failure from an initially higher value. Hasselman cited a number of investigations[12-15] in support of his theory and several later studies[16-21] further substantiated the basic qualitative ideas, especially for tests using a severe water or oil quench. Reports that did not show the sharp decrease in strength at a critical temperature quench interval could usually be explained as cases where a suitable flaw structure already existed and only quasi-static crack propagation and a gradual loss of strength occurred.

Additional experience showed that postshock strength testing variables such as strain rate, sample size, sample machining, stress distribution (4 point bend test preferred over 3 point loading), and environment deserved more attention. The desireability of obtaining reliable fracture surface energy measurements as a function of environment and mechanical and thermal history was also reiterated. Several thermal shock merit indices were subsequently summarized[6].

C.1.2 Thermal Fatigue

The concepts of thermal shock crack initiation and propagation were extended to the case of thermal fatigue or slow crack growth at subcritical thermal stress[22]. Stress corrosion cracking was enhanced by quenching glass cylinders into water. A sophisticated analytical and numerical technique was used to divide the transient thermal pulse (Figure C.1) into a series of small time intervals and thus permit calculation of a given temperature and stress state as a function of time. Thermal shock failure was assumed to occur when the thermal stress intensity reached K_{IC} and the crack had grown to a critical value. Results showed that knowledge of the K_I-V data at the initial sample temperature was not needed since the surface temperature decreased very rapidly (as long as $\beta > \sim 0.1$). It was foumd that for $\Delta T < \Delta T_c$, significant crack growth occurs in a relatively narrow temperature range since the thermal stress intensity also decreases as the temperature is decreased (Figure C.6). Thus loss of strength prior to a ΔT_c quench may only be seen within $\simeq 10^{o}C$ of ΔT_c for glass, but in this temperature range the crack may be unstable even at a thermal stress intensity less than K_{IC}. Similar results may also apply to Si_3N_4[3]. The time to failure was longer than the interval needed to reach maximum surface stress; this was attributed to a continued increase in thermal stress intensity factor with increasing crack depth even though the thermal stress had peaked

and was decreasing. Thus crack extension during a quench is a function of the total time over which the stress intensity is greater than the fatigue limit value, K_o. To keep this time to a minimum it was suggested materials with high thermal diffusivites were desired.

Slow crack growth also implies ΔT_c is less sensitive to β, so less exact knowledge of thermal conductivity and heat transfer coefficient are needed for reliable estimates of ΔT_c. However, the temperature dependence of conductivity[23] should not be ignored. Lower values of β (mild quench) at high temperatures also require much better determination of K_I-V data, especially of the fatigue limit value of stress intensity, K_o. Estimates of ΔT_c based on $K_{failure} = K_{I_C}$ could give serious errors. Similarly, caution must be exercised when using strength data to evaluate thermal stress resistance since strength testing is not likely to have been performed under conditions of temperature and slow crack growth identical to that experienced by a material during thermal quenching or cycling. Considerations of thermal stress intensity also suggest increasing the strength of the material by decreasing initial flaw size will not improve thermal shock resistance in stress corrosion environments significantly, although possible improvements may be affected by surface-compression strengthening[10,11]. For these reasons thermal-stress resistance parameters[6] should contain the appropriate stress intensity factors[22]:

$$F = \frac{K_{I_C}(1-\mu)}{\alpha E \ell^{1/2}} \qquad \text{slow crack growth absent} \qquad (13)$$

$$F' = \frac{K_{I_C}(1-\mu)k}{\alpha E \ell^{1/2}} \qquad \text{slow crack growth absent} \qquad (14)$$

$$F_{sc} = \frac{K_o(1-\mu)}{\alpha E \ell^{1/2}} \qquad \text{slow crack growth present} \qquad (15)$$

$$F'_{sc} = \frac{K_o (1-\mu)k}{\alpha E \ell^{1/2}} \qquad \text{slow crack growth present} \qquad (16)$$

Analysis of thermal fatigue is complicated by the data scatter for ceramics and the number of variables that influence predictive calculations. Qualitative results show an increase in fatigue life with decreasing stress state, as expected [24]. Accurate predictions of such life are more difficult [3]. Understanding of crack propagation is making progress but much remains to be done. For example, the K-V relation:

$$V = AK^n \exp(-Q/RT) \qquad (17)$$

is very sensitive to the value of activation energy Q. Changes of 5 or 6%, which are often less than the experimental error, can significantly influence the interpretation of thermal fatigue results [3,25]. Predictions are also sensitive to the assumed initial flaw size, which once again demonstrates the influence of total flaw structure and strength variability pointed out by Manson and Smith [7].

B.1.3 Thermal Shock Practice

A variety of thermal shock testing methods are available. Quenching into liquids such as water, oil, or molten metals have been used, as well as air and fluidized bed quenches. The results and correlations of these tests have often been of little value for engineering design purposes. This has prompted suggestions that all the constitutive materials properties, i.e., E, σ, α, K, h, ε, μ, η, etc., should be evaluated as functions of temperature and environment for use in the appropriate merit index [26], to the other view that nothing short of prototype testing has any substantive meaning [27]. Recent reports often offer qualifications that the laboratory results presented

may be less valid for a different geometry or thermal/mechanical environment.

As discussed by Manson [28], consideration of the quench conditions is very important in evaluating thermal shock tests and results. For example, a severe quench (large β) implies a large sample size (a) and/or large heat transfer coefficient (h) and small thermal conductivity (k). Thus a water quench test gives a high h value (~1000 Btu/hr $ft^{2o}F$) and usually may be considered a severe thermal shock test. However, if such a quench is not indicative of actual use conditions (i.e., small component, air quench, or high conductivity material) then interpretation of results for design purposes may be in error. Manson [28] has shown that even a relative ranking between BeO and Al_2O_3 was reversed between different quenching conditions and due to differences in thermal conductivity. Similar considerations may also apply to various SiC or Si_3N_4 materials, depending on the behavior of K_{I_C} and K_o as a function of temperature for different test situations [29]. In comparing the thermal fatigue behavior of SiC and Si_3N_4 Chen and Hasselman [29] conclude their work "clearly illustrates that no general rules for the comparative thermal fatigue behavior of 2 materials can be made without detailed knowledge of the thermal environment, temperature levels, nature of crack growth, and other possible variables."

These comments indicate the most reliable thermal shock and thermal fatigue predictions of ceramic turbine components will be obtained from tests which most closely simulate actual engine environments and conditions. Unfortunately these conditions vary with location in the engine, intended use, thermodynamic cycle, fuel used, and operating loads. Therefore no one test is suitable for all turbine applications. Experimental thermal stress work has centered on evaluating material for use as vanes or stators since these applications appear to be the

most troublesome. Figure C.7 shows the heat transfer coefficient as a function of position on a vane during emergency shutdown, as determined by two different groups for different engines [30]. Considerable variation is evident. Table C.1 shows the characterizations of several types of quench [31].

In spite of these difficulties, practical design necessitates some form of test. Transfer of samples between a torch flame and air blast [31,32] or between an isothermal furnace and fludized bed [30,33] have been used to approximate conditions of an engine ignition or flame-out

TABLE C.1 Thermal -Stress-Inducing Tests for Ceramic Prototypes and Specimens (41)

Media	ΔT ^{o}F	h, Btu/hr-sq-ft-^{o}F	Characteristics
Engine	2500-100	300-1200	ΔT and h vary with location
Fluidized Bed	2400-100	125-175	h constant
Oil-Water	200-100	300-2000	h varies with temperature
Liquid Metal	2900-250	1200	Unsuited to cycling
Burner/Air Blast	2500-100	50-400	h varies with location

Exposure to actual turbine combustor flame has also been reported.[34] An analysis of the strain at the top of a wedge cycled into a fludized bed has been reported to approximate the strain at a vane leading edge during shutdown[33]. A comparision of the two is given in Figure C.8. Figure C.9 shows a typical temperature-time measurement on a vane entering and leaving a flame with forced air cooling[31].

C.2 Internal Friction

The measurement of residual strength as an indicator of the critical quench conditions in thermal shock studies is well established (Figure C.5). However, since the feature of interest is the total flaw structure as a function of quench conditions rather than merely the critical strength limiting flaw, the use of internal friction or specific damping capacity to evaluate post-shock condition has increased. Whereas the modulus and strength may change by up to 15 and 80%, respectively, after shocking, the value of internal friction may change by several hundred percent. It is a more sensitive measuring method and often shows the onset of ΔT_c at lower values of ΔT than as determined from residual strength measurements. It is also non-destructive.

Zener[35] and others[36-38] have provided excellent reviews of internal friction. Hookean elastic theory implies a direct and instantaneous linear relation between low level force application and resultant deformation. However, as the rate of loading and unloading is increased there appears a phase lag between stress and strain which results in the absorption of energy. This time dependent elastic behavior is termed anelasticity. Internal friction may be defined as the amount of energy absorbed during deformation compared to the maximum amount of energy applied initially. As the number and extent of flaws in a body increases the amount of energy absorbed through flaw surface friction, plastic zone dislocation motion, etc. also increases.

There are at least five methods for determing internal friction of solids:[36]

1) determination of the amplitude decay in free vibration (log decrement method).

2) determination of the hysteresis loop in stress-strain curve during vibration.

3) determination of the resonant peak half-width in forced vibration.

4) measurement of energy absorbed during cyclic forced vibration.

5) determination of sound wave propagation parameters.

Each method has advantages and disadvantages, depending on the mechanisms responsible for energy absorption, test environment, sample geometry, frequency range, and vibration mode (torsion, longitudinal, flexural) of interest.

For the first method consider a sample undergoing forced cyclic or impact loading. When this loading is stopped the vibrations will decay at some natural frequency. The log decrement is defined as the logarithim of the ratio of successive amplitudes:

$$L.\ D. = \ln \frac{Z_{n-1}}{Z_n} = \ln \left(1 + \frac{\Delta Z}{Z_n}\right) \simeq \frac{\Delta Z}{Z_n} \qquad (18)$$

In practice improved accuracy is obtained by counting the number of cycles to obtain a 50% decrease in amplitude:

$$L.\ D = \frac{1}{n} \ln 2 \qquad (19)$$

This method is simple and better suited to measuring very low values of internal friction. There are problems associated with dissipating energy at a non-rigid support and operation at high frequency requires use of sophisticated electronic storage and display equipment.

The precision of the hysteresis loop method is low since most cases give small loop dimensions on the strain axis. It is better suited to measures of large values of internal friction,

where the loop width (strain) increases, and to cases where high stress amplitudes may be applied. However, the frequency range is limited and the equipment fairly complex.

The determination of internal friction from the width of the resonance peak at half amplitude (or half power) is favored by many investigators. Measurements may be made over a wide range of frequencies and a variety of methods exist to impart the forced vibrations to the sample. Using suitable driver transducers, measurements may be made as a function of temperature and atmosphere (including vacuum). The formulation due to Zener is:[35]

$$Q^{-1} = \frac{\Delta f}{\sqrt{3}\, f} \tag{20}$$

where Q^{-1} = internal friction
f = resonent frequency
Δf = peak width at half amplitude

This method is useful for measuring the range of internal friction normally found in ceramic materials (10^{-2} - 10^{-6}). Elastic moduli may also be obtained from these resonant frequency measurements at the same time.[39]

The energy provided by the oscillator may also be monitored as a function of the vibration cycle to obtain a measure of internal friction. The result follows from the definition of specific damping capacity:

$$Q^{-1} = {}^{Eabs}/_{Emax} \tag{21}$$

It may be seen that this method is more difficult for low damping materials, such as ceramics, and has appearently not been used much in this field.

The determination of internal friction from sonic and ultrasonic pulsed wave propagation and attenuation has many similarities with both the log decrement and bandwidth methods. The pulse amplitude is monitored as a function of time (or prop-

agation velocity and distance). The method is suitable for very high frequencies and can give high accuracy. However, the equipment is complicated and the necessity of properly coupling the transducer and the sample limit the range of environments and temperatures that can be used.

The versatility and applicability to ceramics of the bandwidth technique explains its popularity as a means of evaluating thermal shock damage. A variety of methods exist for vibrating the sample, including acoustic air coupling, probes or wire suspension coupling driven by piezoelectric transducers, electromagnetic and magnetostrictive coupling, and electrostatic coupling.

Similar techniques are used to detect the vibration amplitude at the other end of the sample. Samples are usually supported at or near vibration nodal points on foam pads, knife edges, or suspended in wire loops (which may or may not be connected to driver and pickup transducers). High temperature measurements may be made using suitable probes or suspending fibers. Graphite and silica yarn and Pt, W, Mo, and other refractory metal wires have been used sucessfully, depending on furnace atmosphere. Cotton thread is satisfactory at room temperature. Most of the considerations that affect dynamic modulus measurements also apply to determinations of internal friction.[39]

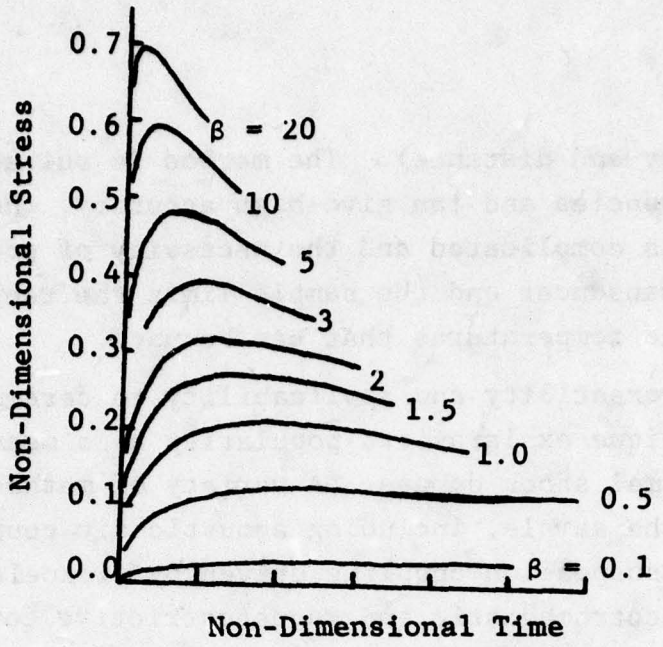

Figure C.1 VARIATION OF DIMENSIONLESS STRESS WITH DIMENSIONLESS TIME FOR AN INFINITE FLAT PLATE

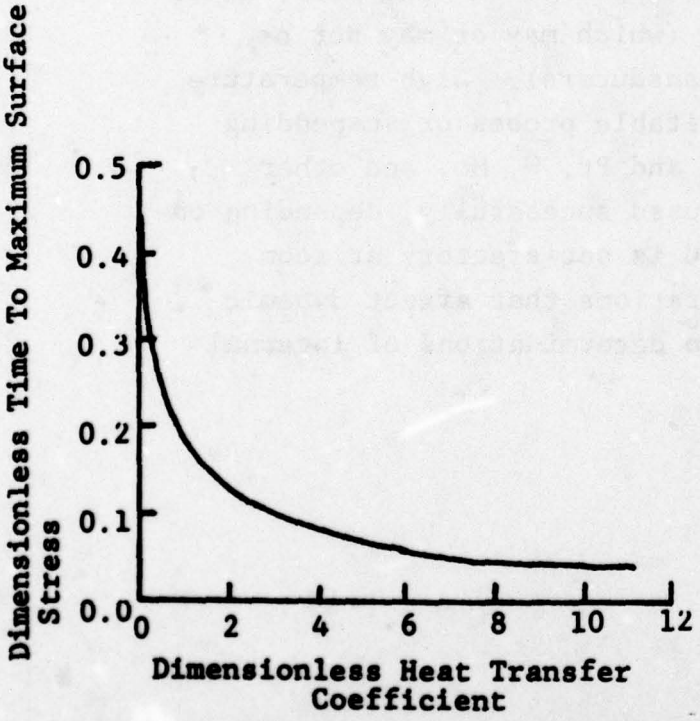

Figure C.2 Variation of dimensionless time to maximum surface stress with relative heat transfer rate[1].

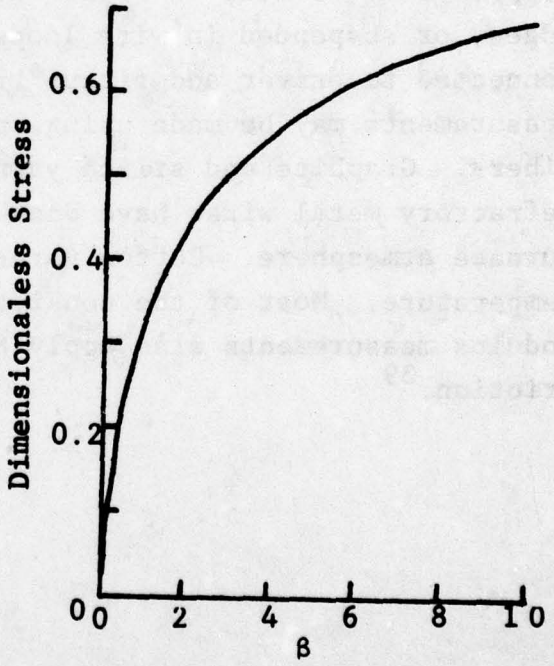

Figure C.3 Variation of dimensionless stress with relative heat transfer rate for an infinite flat plate[1].

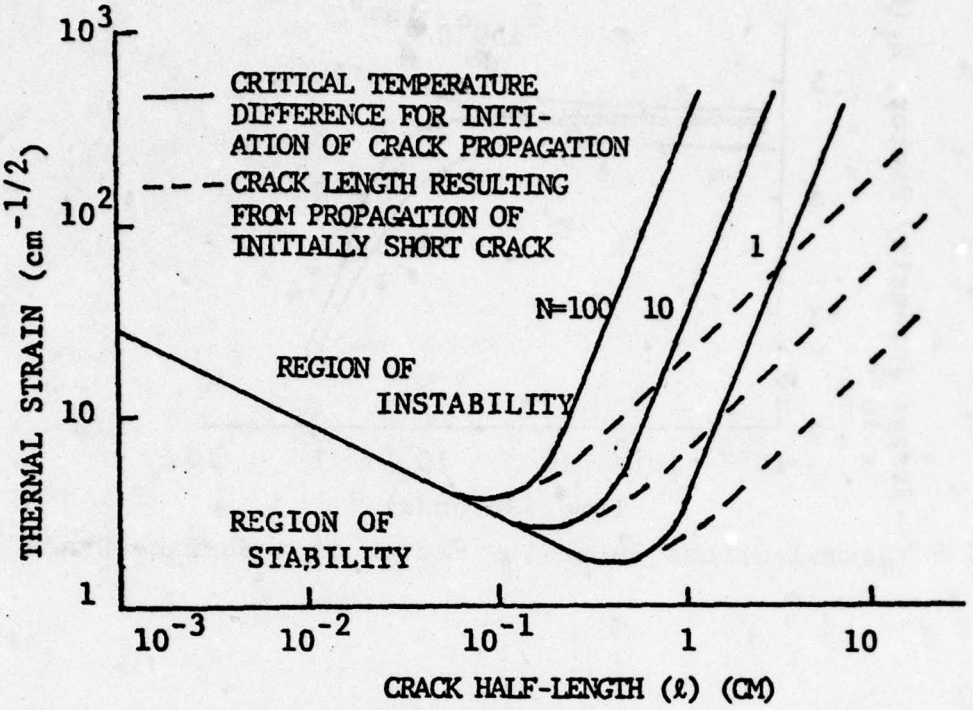

Figure C.4 MINIMUM THERMAL STRAIN REQUIRED TO INITIATE CRACK PROPAGATION AS A FUNCTION OF CRACK LENGTH AND CRACK DENSITY N. (Poisson's ratio = 0.25.)[2]

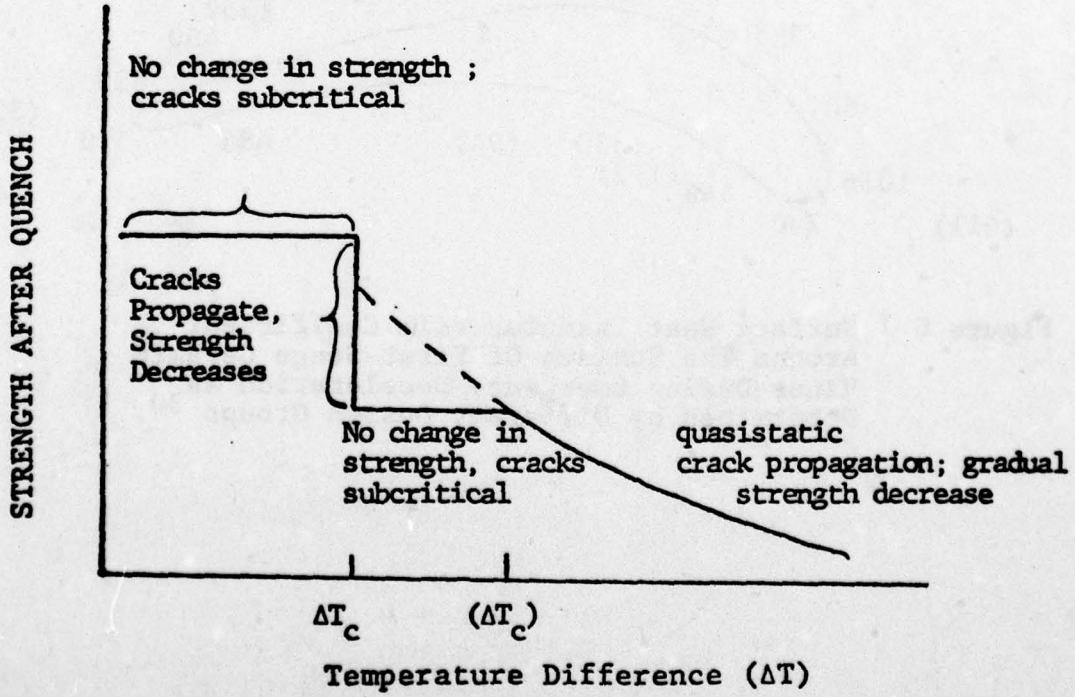

Figure C.5 STRENGTH AS A FUNCTION OF THERMAL HISTORY[2].

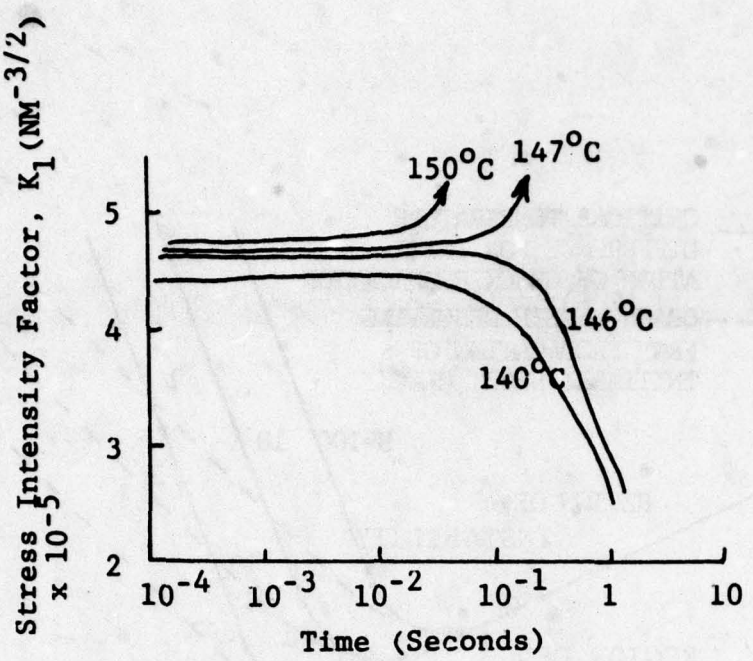

Figure C.6 Thermal Stress Intensity Factor of a Surface Crack[22].

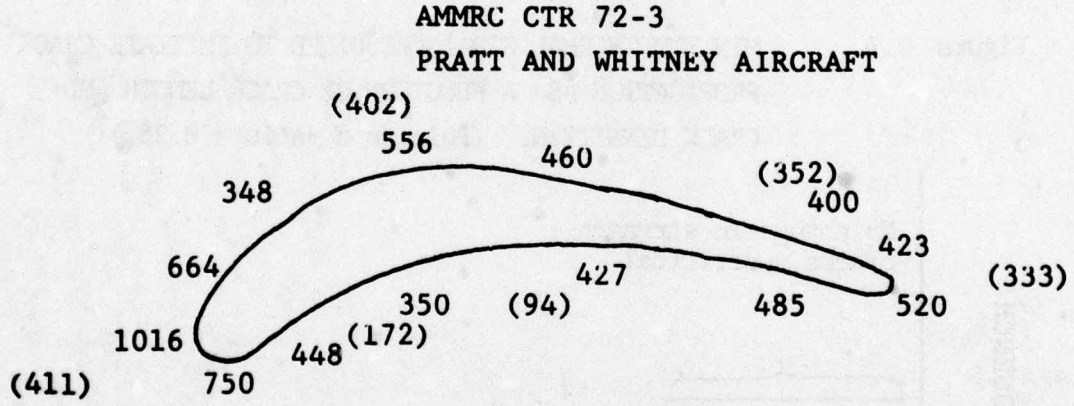

Figure C.7 Surface Heat Transfer Film Coefficient Around The Surface Of First-Stage Ceramic Vanes During Emergency Deceleration as Determined by Different Design Groups [30].

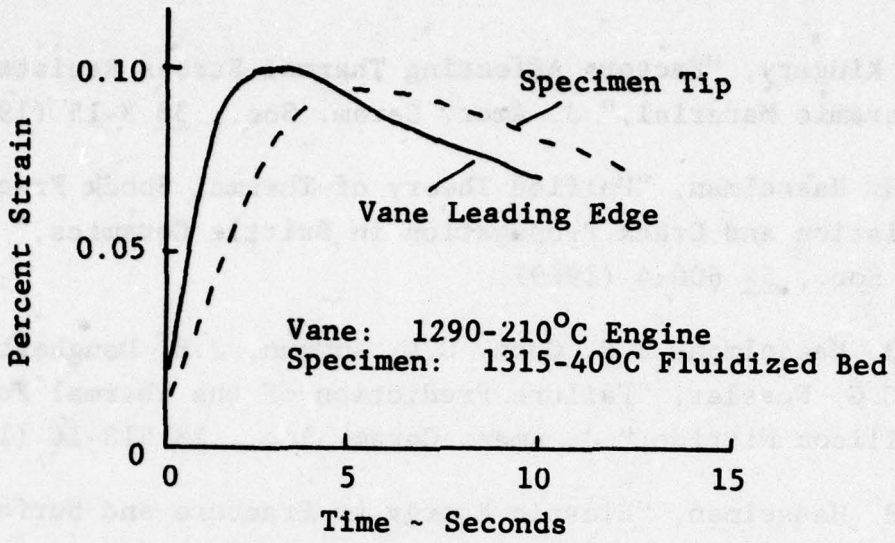

Figure C.8 The strain-time history of the leading edge of a vane in a gas turbine after sudden shutdown compared with the tip of a quenched specimen[33].

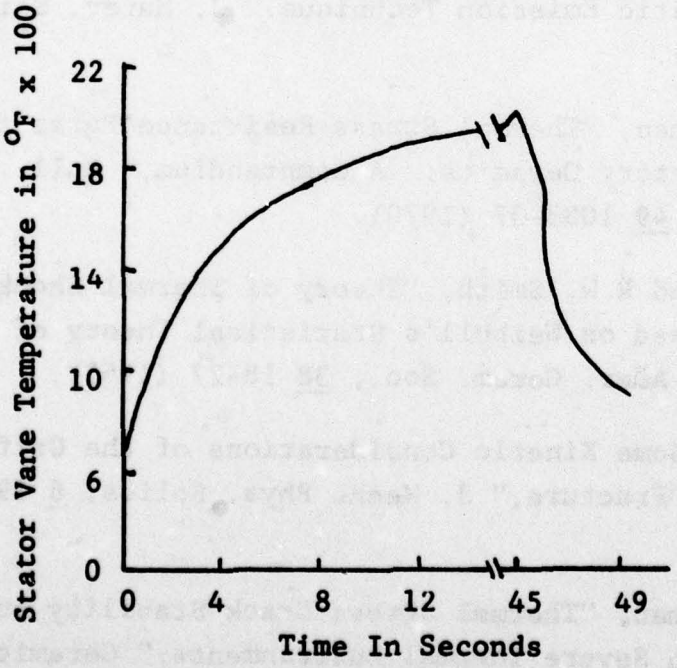

Figure C.9 Vane Temperature Versus Time During Ignition and Flame-Out[31].

APPENDIX REFERENCES

1. W.D. Kingery, "Factors Affecting Thermal Stress Resistance of Ceramic Material," J. Amer. Ceram. Soc., 38 3-15 (1955).

2. D.P.H. Hasselman, "Unified Theory of Thermal Shock Fracture Initiation and Crack Propagation in Brittle Ceramics," J. Am. Cer. Soc., 52 600-4 (1969).

3 D.P.H. Hasselman, E.P. Chen, C.L. Ammann, J.E. Dougherty, and C.G. Nessler, "Failure Prediction of the Thermal Fatigue of Silicon Nitride," J. Amer. Ceram. Soc., 58 513-16 (1975).

4. D.P.H. Hasselman, "Elastic Energy at Fracture and Surface Energy as a Design Criteria for Thermal Shock," J. Ceram. Soc., 46 535-40 (1963).

5. A.G. Evans, M. Linzer, H. Johnson, D.P.H. Hasselman, and M.E. Kipp, "Thermal Fracture Studies in Ceramic Systems Using an Acoustic Emission Technique," J. Mater. Sci., 10 1608-15 (1975).

6. D.P.H. Hasselman, "Thermal Stress Resistance Parameter for Brittle Refractory Ceramics: A Comprendium," Bull. Amer. Ceramic Soc., 49 1033-37 (1970).

7. S.S. Manson and R.W. Smith, "Theory of Thermal Shock Resistance Based on Weibull's Statistical Theory of Strength," J. Amer. Ceram. Soc., 38 18-27 (1955).

8. J.P. Berry, "Some Kinetic Considerations of the Griffith Criterion for Fracture," J. Mech. Phys. Solids, 8 194-206 (1960).

9. D.P.H. Hasselman, "Thermal Stress Crack Stability and Propagation in Severe Thermal Environments," Ceramics

in Severe Environments, ed. W.W. Kriegel and H. Palmour III, Plenum Press, New York, 1971.

10. J. Gebauer, D.A. Krohn, and D.P.H. Hasselman, "Thermal Stress Fracture of Thermomechanically Strengthened Aluminosilicate Ceramic," J. Amer. Ceram. Soc., 55 198-201 (1972).

11. M.E. Kipp, D.A. Krohn, and D.P. H. Hasselman, "Effect of Surface-Compressive Strengthening vs. Reduction in Flaw Size on Thermal Stress Resistance of an Na_2O-CaO-SiO_2 Glass," J. Amer. Ceram. Soc., 57 432-36 (1974).

12. M.S. Tocvorian, "Heat Shock Resistance of Certain Sintered Refractories," Bull. Soc. Franc. Ceram., 29 20-40 (1955).

13. J. Jakayama and M. Ishizuka, "Experimental Evidence for Thermal Shock Damage Resistance," Bull. Amer. Ceram. Soc., 45 666-69 (1966).

14. R.W. Davidge and G. Tappin, "Thermal Shock and Fracture in Ceramics," Trans. Brit. Ceram. Soc., 66 405-22 (1967).

15. H.W. Hennike and H. Sturhahn, "Measurement and Calculation of the Thermal Shock Resistance of Twin Tiles," Ber. Deut. Keram. Ges., 45, 167-73 (1968).

16. T.K. Gupta, "Strength Degradation and Crack Propagation in Thermally Shocked Al_2O_3," J. Amer. Ceram. Soc., 55 249-53 (1972).

17. T.K. Gupta, "Strength Behavior of Thermally Shocked ZnO," J. Amer. Ceram. Soc., 55 429 (1972).

APPENDIX REFERENCES (Cont'd)

18. J.H. Ainsworth and R.E. Moore, "Fracture Behavior of Thermally Shocked Al_2O_3," J. Amer. Ceram. Soc., 52 628-29 (1969).

19. D.P.H. Hasselman, "Strength Behavior of Polycrystalline Alumina Subjected to Thermal Shock," J. Amer. Ceram. Soc., 53 490-95 (1970).

20. F.J.P. Clark, H.G. Tattersall, and G. Tappin, "Toughness of Ceramics and Their Work of Fracture," Proc. Brit. Ceram. Soc., 163-72 (1966).

21. D.R. Larson, J.A. Coppola, D.P.H. Hasselman, and R.C. Bradt, "Fracture Thoughness and Spalling Behavior of High-Al_2O_3 Refractories," J. Amer. Ceram. Soc., 57 417-21 (1974).

22. R. Badaliance, D.A. Krohn, and D.P.H. Hasselman, "Effect of Slow Crack Growth on the Thermal Stress Resistance for an Na_2O-CaO-SiO_2 Glass," J. Amer. Ceram. Soc., 57 432-36 (1974).

23. B.K. Ganguly, K.R. McKinny, and D.P.H. Hasselman, "Thermal Stress Analysis of Flat Plate with Temperature-Dependent Thermal Conductivity," J. Amer. Ceram. Soc., 58 455-56 (1975).

24. D.A. Krohn and D.P.H. Hasselman, "Static and Cyclic Fatigue Behavior of a Polycrystalline Alumina," J. Amer. Ceram. Soc., 55 208-11 (1972).

25. D.P.H. Hasselman and E.P. Chen, "Role of Activation Energy of Slow Crack Growth in the High-Temperature Thermal Fatigue of Silicon Nitride," J. Amer. Ceram. Soc., 60 76-77 (1977).

26. W.R. Buessem, "Thermal Shock Testing," J. Amer. Ceram. Soc., 38 15-17 (1955).

APPENDIX REFERENCES (Cont'd)

27. R.L. Newman, "Prediction of Thermal Shock Resistance During Heating at Very High Rates," J. Amer. Ceram. Soc., 55 464-69 (1972).

28. S.S. Manson, Thermal Stress and Low Cycle Fatigue, McGraw-Hill, Inc. New York, 1966.

29. E.P. Chen and D.P.H. Hasselman, "Comparison of the High-Temperature Thermal Fatigue Resistance of Hot-Pressed Silicon Nitride and Silicon Carbide," J. Amer. Ceram. Soc., 59 525-26 (1976).

30. C.G. Nessler, "Prototype Ceramic Vanes," Ceramics for High Performance Applications," ed. J.J. Burke, A.E. Gorum, and R.N. Katz, Brook Hill Publishing Co., Chestnut Hill, Mass., 1974.

31. C.F. Johnson and D.L. Hartsock, "Thermal Response of Ceramic Turbine Stators," Ibid.

32. S. Prochazka, C.A. Johnson, and R.A. Giddings, "Investigation of Ceramics for High Temperature Turbine Components," Final Report Contract No. N62269-75-C-0122, 1975.

33. C.L. Ammann, J.E. Dougherty, and C.G. Nessler, "The Thermal Fatigue Behavior of Hot Pressed Silicon Nitride," Materials Science and Engineering, 22 15-22 (1976).

34. W.A. Sanders and H.B. Probst, "Behavior of Ceramics at 1200°C in a Simulated Gas Turbine Environment," S.A.E. Paper 740240, 1974.

APPENDIX REFERENCES (Concluded)

35. G. Zener, Elasticity and Anelasticity of Metals, Univ. of Chicago Press, 1948.

36. D. F. Moore, "Internal Friction," Principles and Applications of Tribology, Permgamon Press, New York, 1975.

37. N. F. Astbury and W. R. Davis, "Internal Friction in Ceramics," Trans. Brit. Ceram. Soc., 63 1-18 (1964).

38. H. Kolsky, Stress Waves in Solids, Oxford-Clarendon Press, 1953.

39. S. Spinner and W. E. Teft, "A Method for Determining Mechanical Resonance Frequencies and for Calculating Elastic Moduli from These Frequencies," ASTM Proceedings, 61 1221-38 (1961).

ERRATA

The attached pages have been reproduced more legibly than those bound in the text.

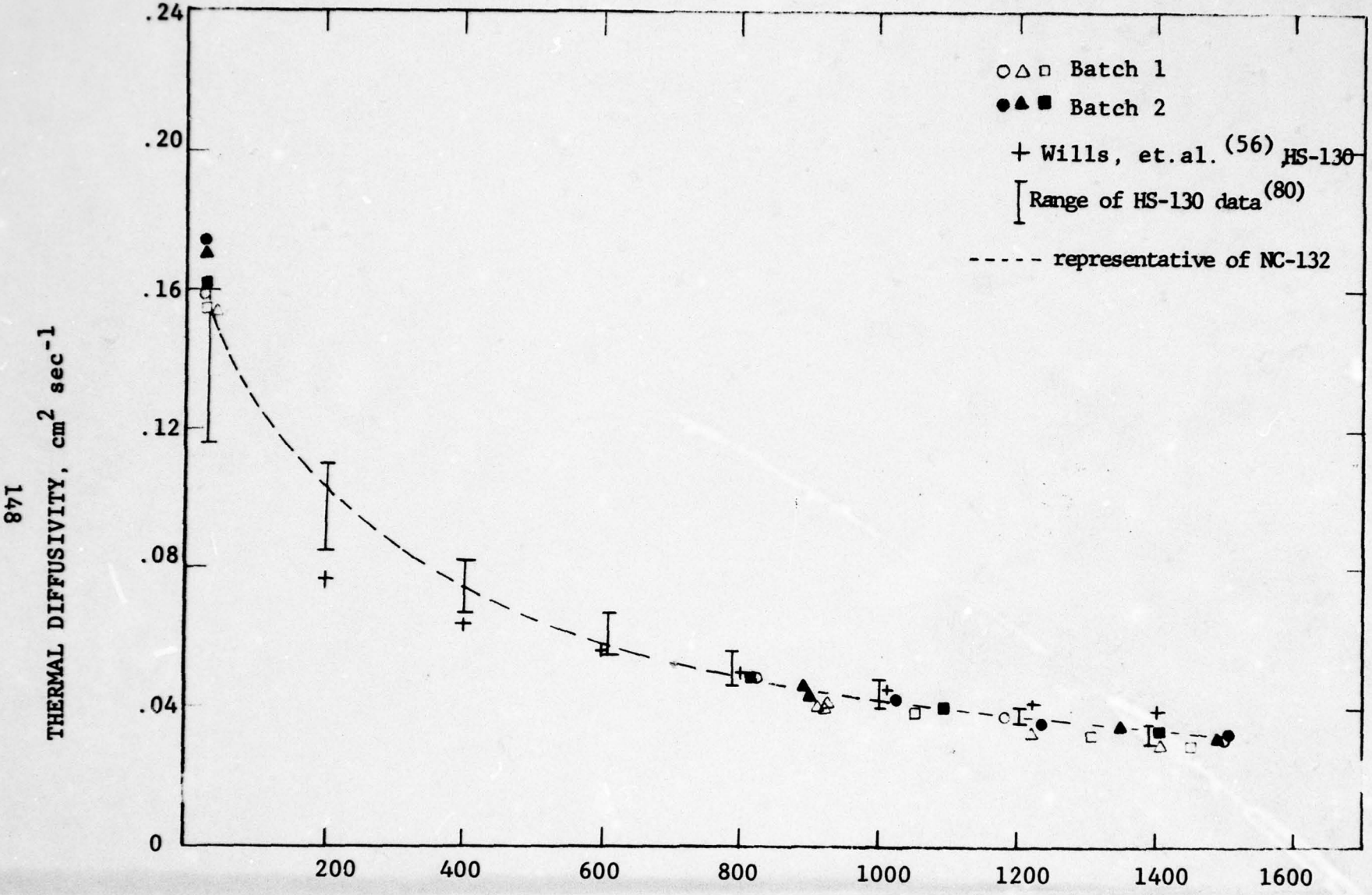

FIGURE 6.12 THERMAL DIFFUSIVITY OF NC-132 HOT-PRESSED Si_3N_4 (HEAT FLUX PARALLEL TO PRESSING DIRECTION)

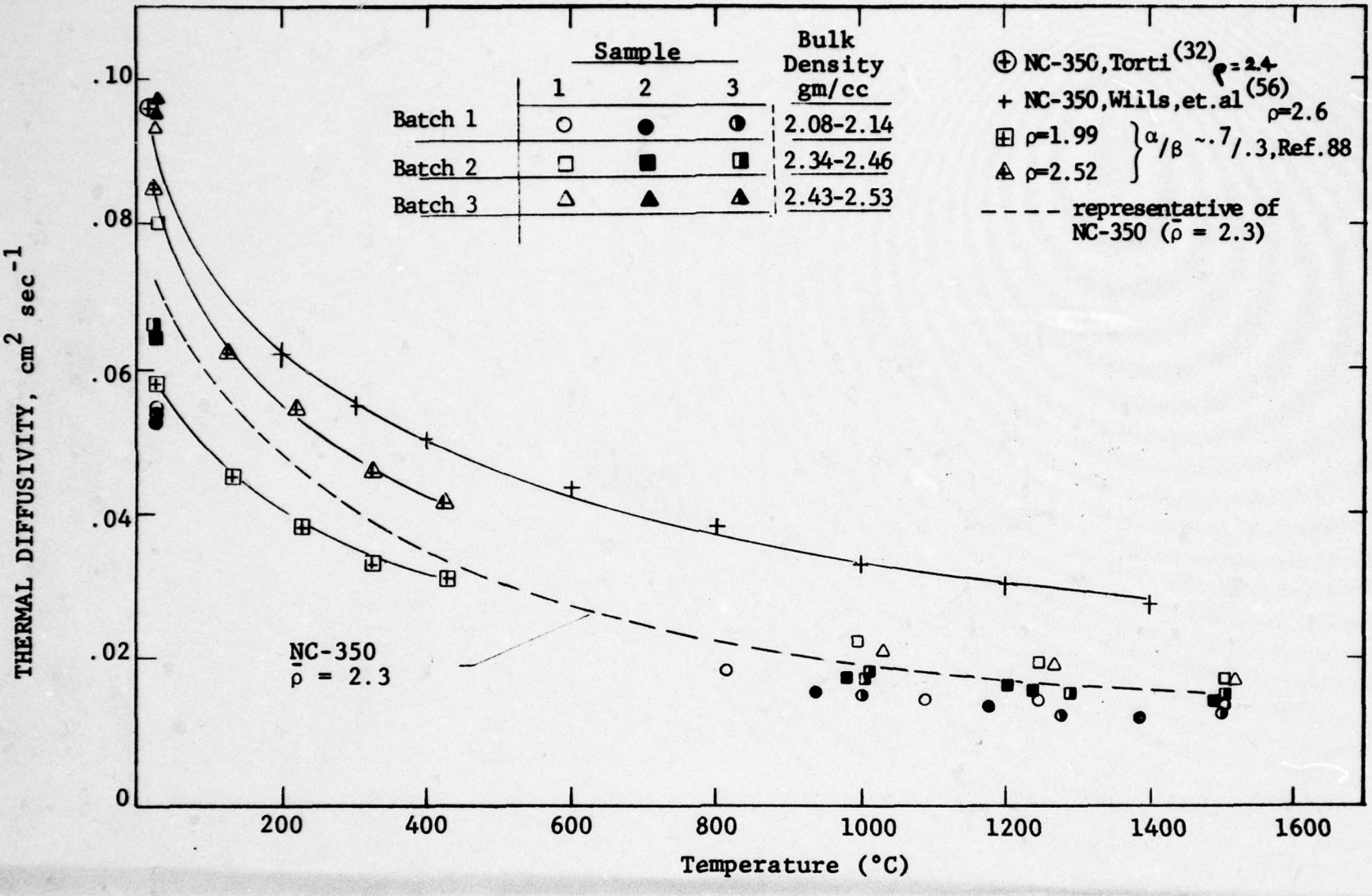

FIGURE 6.14 THERMAL DIFFUSIVITY OF NC-350 REACTION SINTERED Si_3N_4

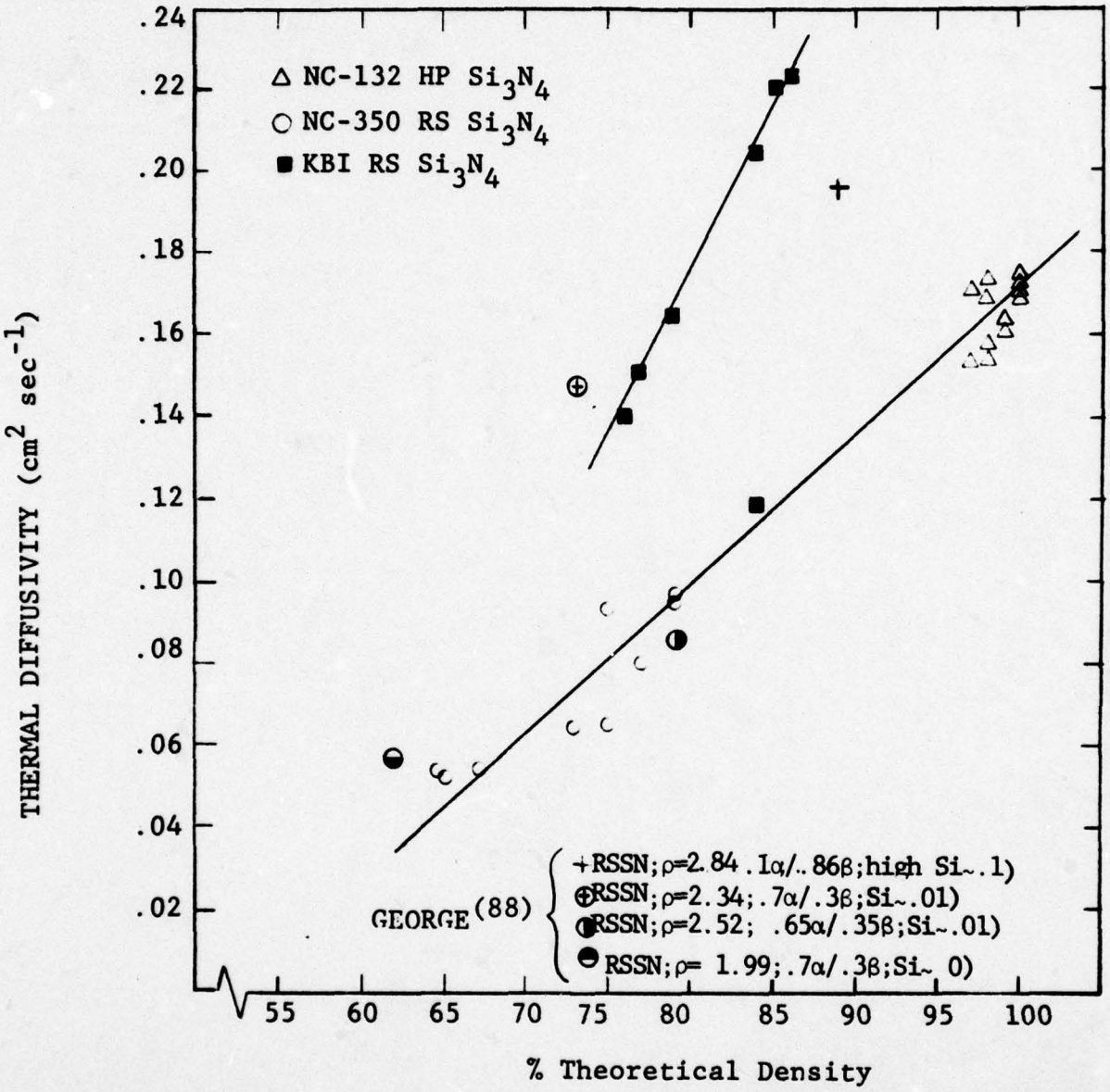

FIGURE 6.15 CORRELATION OF ROOM TEMPERATURE THERMAL DIFFUSIVITY WITH DENSITY

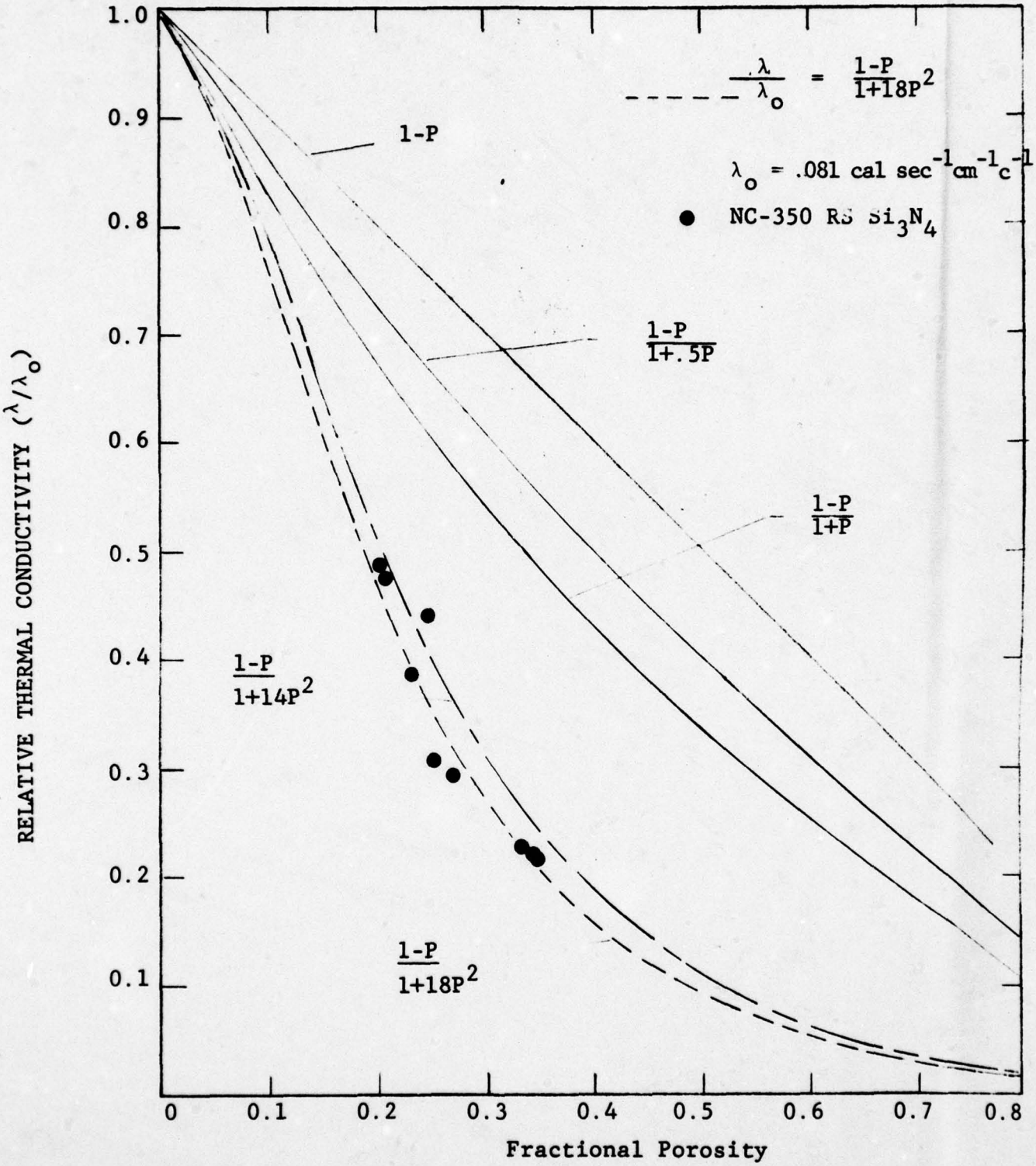

FIGURE 6.16 CORRELATION OF ROOM TEMPERATURE THERMAL CONDUCTIVITY OF NC-350 RS Si_3N_4 WITH POROSITY